In Vitro Experimental Investigation Into the Effect of Compliance on Models of Arterial Hemodynamics

Patrick Henry Geoghegan

A thesis presented for the degree of
Doctor of Philosophy
in
Mechanical Engineering
at the
University of Canterbury,
Christchurch, New Zealand.
2012

To my parents who have supported me
at university from the first day of my undergraduate
degree through to the submission of my Ph.D. thesis.

Acknowledgements

To get to the point where it was possible to submit this Ph.D. thesis, would not have happened if it wasn't for the support and guidance of many people.

Firstly I would like to thank my supervisor Dr. Mark Jermy who over the duration of this work provided constant guidance and advice whenever it was needed. His patience and what seemed to be infinite optimism, was much appreciated in times when things could seem to be getting a bit too much. As I move forward with my career I hope that I will keep continual strong links with him and the university.

I thank all my work colleagues and friends past and present from the bioengineering centre, Mechanical Engineering and the College of Engineering. Special gratitude has to go to Dr. Nicolas Buchmann who provided me with much insight into PIV analysis during his time at Canterbury University and since he assumed his post-doc position has been invaluable in helping me with producing the quality of data analysis that is presented in this work. Also thanks go to Dr. Callum Spence who during his Ph.D. studies provided me with a wealth of knowledge that helped me develop the model construction techniques that were integral to my experimental studies.

Funding was provided by the UC Doctoral Scholarship scheme, New Zealand Postgraduate Study Abroad Awards and my parents all of which was greatly appreciated.

A thanks also goes to the Academic staff and technicians of the University of Canterbury Mechanical Engineering department, many of whom I have interacted with over the course of my studies. A special acknowledgement must go to Julian Phillips, Eric Cox and Graeme Harris who over the years have provided much needed technical assistance. Thanks also go to Prof. David Nobes for providing his facilities at the University of Alberta Canada for my

research and Dr. John Cater who spent time with me in the lab, providing a vast knowledge of PIV.

To all of my friends and family in all corners of the globe, who are far too many to mention individually by name, I thank you for all the entertainment and enjoyment that you have provided me with over these years. It helps to counter balance the stress that can come from Ph.D. research. A special mention must go to Louise Murphy, who over the last 6 months has helped support, entertain and encourage me when it was needed most.

The final thanks go to the most important people of all my parents Joseph and Janet and my brother Niall; I love them dearly. They have been a constant source of support throughout my university career. Without these three there is no way I would have ever finished this Ph.D.

On a final note I wish to point out that I do not acknowledge Mother Nature who's untimely mood swing brought a great deal of chaos to all our lives in Christchurch for far too long.

Abstract

Compliant (flexible) structures play an important role in several biofluid problems including flow in the lungs, heart and arteries. Atherosclerosis is a vascular disease which causes a remodelling of the arterial wall causing a restriction (stenosis) by thickening the intima and the formation of vascular plaque by the deposit of fatty materials. This remodelling alters the compliance of the artery stiffening the arterial wall locally. A common location for this to occur is in the carotid artery which supplies blood to both the brain and the face. It can lead to complete occlusion of the artery in the extreme case and is a major cause of stroke and ischemic infarction. Stroke is the third largest cause of death in the U.S.A., but even if not fatal it can cause coma, paralysis, speech problems and dementia. Atherosclerosis causes a change in the local hemodynamics. It can produce areas of flow separation and low wall shear stress, which can lead to endothelial dysfunction and to promotion of plaque growth.

In-vitro modelling with artificial flow phantoms allows the fluid mechanics of the circulatory system to be studied without the ethical and safety issues associated with animal and human experiments. Extensive work has been performed using both experimental and computational techniques to study rigid models representing the arterial system. Computational methods, in which the equations governing the flow and the elastic walls are coupled, are maturing. There is a lack of experimental data in compliant arterial systems to validate the numerical predictions. This thesis sets out to address the problems associated with the in vitro experimental analysis of compliant structures representing the human vasculature.

A novel construction technique that produced idealised compliant geometries representing both a healthy and stenosed carotid artery from transparent silicone material was developed. A complete analysis was performed of the circumferential and longitudinal response of the geometry, which allowed for dynamic similarity between in vitro and in vivo conditions to be

achieved. Inherent difficulties associated with thin walled phantom construction were overcome, which included the design of a novel endplate that allowed for a smooth transition from the flow system to the flow phantom and a bottom up silicone injection system that ensured the phantom was free of bubbles. The final phantom evolution had a wall thickness that could be produced to within a tolerance of 5%. The constructed flow phantom was ported to a flow system producing a physiological inlet flow waveform scaled to in vitro conditions via Reynolds and Womersley number matching.

Experimental analysis was performed using a laser based optical technique, particle image velocimetry (PIV). A novel Light Emitting Diode (LED) illumination system was also implemented to obtain to obtain high speed planar PIV measurements. The combined set up of the LED light source, driver unit components and fibre optics for high speed imaging costs in the region of $US 650 which provides a far cheaper option in comparison to the pulse laser system (In the region of $US 50,000).

Results obtained in the healthy geometry were compared to a rigid geometry with the same dimensions. It was found that compliance reduced the peak velocity experienced. It also caused a reduction in wall shear stress (WSS) observed and acted to ameliorate the magnitude of the WSS. This is physiologically significant as high WSS can promote atherosclerosis. The introduction of a stenosis caused an increase in the peak velocity observed over the cardiac cycle. A large increase in WSS can be seen to occur in the stenosis throat in both a symmetric and asymmetric stenosed geometry. It is also evident that stenosis eccentricity is important, with asymmetry (where the centre of the stenosis does not coincide with the centre of the artery) producing a major change in WSS and flow field. The study of the flow field downstream of a symmetric stenosis exit showed a Kelvin-Helmholtz vortex ring system to occur between the jet exiting the stenosis throat and the low velocity reverse flow region that surrounded it. The strength of these vortices varied between the acceleration and deceleration phase, demonstrating the failings of a quasi-steady assumption. It was shown that varying the external pressure applied to the flow phantom, along with stenosis eccentricity, affected the inlet flow and pressure waveform and the failings of the common assumption to idealise the physiological flow wave with a sinusoidal input was presented.

Publications Arising from this Research

Journal Papers

Published

1. **Geoghegan PH**, Buchmann N, Spence C, Moore S, Jermy M (2012) Fabrication of rigid and flexible refractive-index-matched flow phantoms for flow visualisation and optical flow measurements. *Experiments in Fluids*

In Review

1. **Geoghegan PH**, Buchmann N, Soria J, Jermy M Time-resolved PIV measurements of the flow field in a stenosed, compliant arterial model. *Submitted to Experiments in Fluids*

Conference Proceedings

1. **Geoghegan PH**, Buchmann N, Soria J, Jermy M (2012) High-speed LED-illuminated PIV measurements of the time-dependent flow field in a stenosed, compliant arterial model. In: *16th International Symposium of Laser Techniques to Fluid Mechanics*, Lisbon, Portugal, 9th-12th July.

2. **Geoghegan PH**, Spence C, Ho WH, Jermy M, Hunter P, Cater JE (2012) Stereoscopic PIV measurement of airflow in human speech during pronunciation of fricatives. In: *16th International Symposium of Laser Techniques to Fluid Mechanics*, Lisbon, Portugal, 9th-12th July

3. **Geoghegan PH**, Jermy M, Nobes D, Buchmann N (2010) PIV and image correlation measurements of surface displacement during pulsatile flow in models of compliant, healthy and stenosed arteries. Abstract In: *17th Australasin Fluids Mechanics Conference*, Auckland, New Zealand

4. Spence C, **Geoghegan PH**, Lu XB, Jermy M, Hunter P, Cater JE (2010) Stereoscopic Particle Image Velocimetry Measurement of Articulatory Airflow for Validation of a Computer Model of Speech. In: *17th Australasin Fluids Mechanics Conference*, Auckland, New Zealand, 5-9 December

5. **Geoghegan PH**, Buchmann N, Jermy M, Nobes D, Spence C, Docherty PD (2010) SPIV and image correlation measurements of surface displacement during pulsatile flow in models of compliant, healthy and stenosed arteries. In: *15th International Symposium of Laser Techniques to Fluid Mechanics*, Lisbon, Portugal, 5th-8th July

6. **Geoghegan PH**, Jermy MC, Buchmann NA, Spence CJ, Freitag T (2009) Experimental investigation of flow in a compliant tube using particle image velocimetry. In: *8th International Symposium on Particle Image Velocimetry*, Melbourne Australia,

7. **Geoghegan PH**, Jermy MC, Buchmann N, Spence CJ (2009) Experimental investigation of flow in compliant tubes to validate numerical models of aneurysms. In: *4th Asia Pacific Conference on Biomechanics,* Christchurch, New Zealand

Table of Contents

List of Figures

List of Tables

1 Introduction

Several common diseases involve the flow of a fluid in a compliant (distensible) vessel. Atherosclerosis is a vascular disease which causes a remodelling of the arterial wall causing a restriction (stenosis) by thickening the intima and the formation of vascular plaque by the deposit of fatty materials (Widmaier et al. 2004). This remodelling alters the compliance of the artery stiffening the arterial wall locally (Martini et al. 2006). It is expected that wall movement has significant effect on the flow field developed within the structures.

Coronary heart disease (CHD), which is a major cause of death in the U.S.A with approximately 650,000 fatalities a year (Mautner et al. 1994), involves the progressive constriction of the coronary artery by atherosclerosis. Blood flow is reduced and when under stress the heart muscle is deprived of oxygen and nutrients. The flow field in the coronary artery is strongly influenced by the flexing of the artery as the heart muscle contracts during systole. Atherosclerosis also occurs in the Carotid artery (CA), it can lead to complete occlusion of the artery in the extreme case and is a major cause of stroke and ischemic infarction (Martini et al. 2006).

Arterial remodelling also occurs in expansive diseases like aneurysms with arterial compliance playing an important part in the flow field dynamics. An abdominal aortic aneurysm (AAA) is a balloon like dilation of the aortic artery which is classed as the 13^{th} most common cause of fatality in the U.S.A. (Vorp (2006)). At an advanced state they often pulse strongly enough that they can be palpated. The changing configuration of the blood vessels affects the internal pressure and wall shear stress (WSS). Other common sites for aneurysm formation are the cerebral arteries. It is estimated up to 8% of the current general population are carrying a cerebral aneurysm and 90% of these will have a subarachnoid Haemorrhage (SAH). The death rate of patients suffering an SAH is 40 to 60%, with 10 to

20% of survivors becoming severely disabled. If untreated up to a further 35% will die from a future SAH (Heros and Kistler 1983; Mayer et al. 1995).

The aim of this thesis is to experimentally study in vitro (in an artificial environment outside the living organism) the fluid dynamics within compliant flow phantoms representing the CA in both a healthy and stenosed state. Particle image velocimetry (PIV) is used non-invasively to study the internal flow field and WSS. This work contributes to the necessary experimental techniques and theoretical background required to produce a better understanding of the fluid mechanic phenomena that occur over a cardiac cycle in the CA. It also develops the technique required for production of flexible flow phantoms required for experimental study to be achieved.

1.1 Arterial Structure

The main arteries of interest for this thesis are the elastic arteries, which include the two major trunks that exit the heart known as the Aorta, the pulmonary trunk (the aorta's major initial branches) and the CA. The elastic arteries perform the function of propelling blood while the ventricles (pumping chambers of the heart) are relaxing. As blood enters the elastic arteries they expand and accommodate the influx of blood. The stretching of the wall stores mechanical energy. The elastic fibres in the wall then contract and change the potential energy of the wall into mechanical energy of the blood. This means blood will continue to move through the system when the ventricles are relaxed. There are three layers of the artery wall, which are known as the tunica intima, tunica media and tunica adventitia (Figure 1) (Seeley et al. 2003).

The tunica intima is in direct contact with the blood that flows through the lumen (which in biological terminologies is the internal space in a tubular structure). There are multiple parts to this layer, but it has minimal contribution to the thickness of the wall. Firstly there is the endothelium (Section 1.1.1), which is a thin layer of flattened cells that covers the entire inner layer of the cardiovascular system. These cells perform functions that include depositing locally acting chemical mediators that influence the elastic state of the vessels smooth muscle and also assist with capillary permeability. The next part of the tunica intima is a basement membrane that physically supports the endothelium, which is a framework of collagen fibres known as the basal lamina. The external part of the tunica intima is the

internal elastic lamina. This is a thin sheet of elastic fibres which has a porous nature that allows diffusion of materials through the tunica intima to the next layer of the artery (Caro et al. 1978).

The tunica media is a thick layer of smooth muscle cells and a large amount of elastic fibres. The smooth muscle cells form concentric rings around the lumen and the main function is to control the diameter of the lumen. This layer essentially controls the rate of blood flow and regulates blood pressure through its rate of contraction. The tunica media is covered in a network of elastic fibres known as the external elastic lamina and this separates it from the tunica adventitia (Tortora and Derrickson 2009).

The tunica adventitia is the external covering of the artery and consists of elastic and collagen fibres. It contains a number of nerves and tiny blood vessels that supply the tissue of the vessel wall, known as vasa vasorum. The tunica adventitia also helps anchor the artery to the surrounding tissue (Tortora and Derrickson 2009).

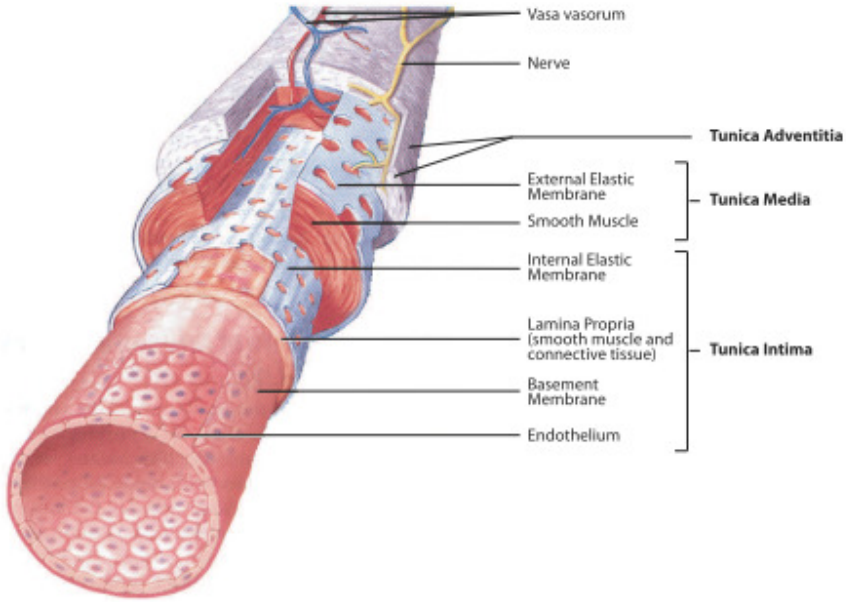

Figure 1 Arterial wall structure. Figure adapted from Seeley et al. (2003)

1.1.1 Endothelium

The endothelial cells in the endothelium are important in the development of atherosclerosis. The endothelium is a single layer of cells, which are quite fragile mechanically and can be damaged by high shear stress. It also has the ability to regenerate or grow. It continuously

regenerates and can form a lining over living or synthetic grafts that are inserted surgically (Caro et al. 1978). It provides an interface between the circulating blood and the rest of the vessel wall. It performs several functions in the vascular system including fluid filtration, blood vessel tone and hemostasis. The health of the endothelium is important to normal vascular physiology and any dysfunction can be a major factor in the pathogenesis of vascular disease (Gimbrone et al. 2000).

1.2 Carotid Artery

As previously discussed, a region where atherosclerosis can occur is in the carotid artery (CA) (Figure 2). Two common carotid arteries (CCA's) ascend into either side of the neck from the aortic arch. They can easily located by pressing either side of the windpipe until a strong pulse is felt (Martini et al. 2006). This is a common site used when pulse rate is recorded. Each CCA then divides into the internal CA (ICA) and the external CA (ECA) at a region known as the CA bifurcation. The ECA provides blood to structures in the neck, oesophagus, pharynx, larynx, lower jaw and face (Martini et al. 2006). The ICA supplies the anterior part of the brain, the eye and its appendages, and sends branches to the forehead and the nose (Gray 1918). Any change in circulatory supply to the brain can be dangerous. If blood flow to the brain is interrupted for several seconds it can lead to unconsciousness and after four minutes it can cause permanent neural damage (A stroke) (Martini et al. 2006). A stroke caused by the restriction of blood flow is known as an ischemic stroke (opposed to a stroke caused by haemorrhage). A stroke can be fatal, but even if this does not occur it can cause coma, paralysis, speech problems and dementia. It is the third largest cause of death in the U.S.A., claiming 139,000 lives in 2002. This is predicted to increase to 275,000 in 2032 due to an aging population (Elkins and Johnston 2003). It is therefore evident that a restriction caused by atherosclerosis, or a complete occlusion in the CA can cause severe damage to the body.

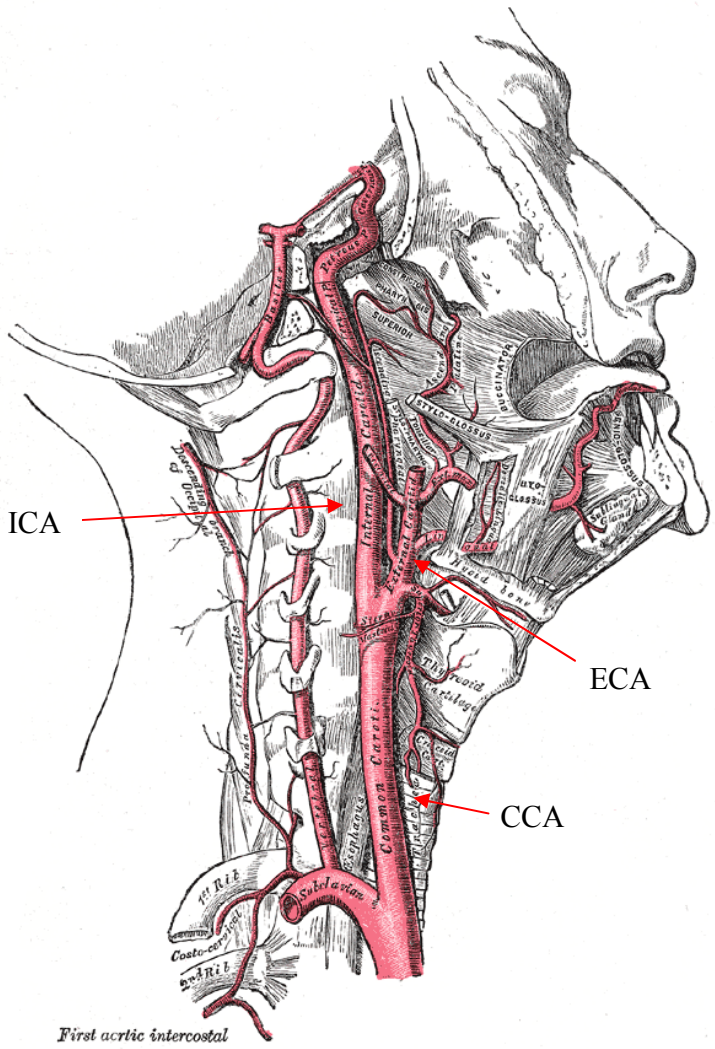

Figure 2 Arteries in the human neck. Figure adapted from Gray (1918)

1.3 Homeostasis

Homeostasis is important to the understanding of the workings of the biological system. Homeostasis is the process of regulating a living system so it maintains a normal operating condition. As discussed previously the endothelium promotes homeostasis in a couple of ways. It can be through muscle tone, causing the contraction or dilation of the surrounding smooth muscle. With an increase in flow rate arteries can dilate through endothelial-dependent release of nitrous oxide (NO) (Ku 1997). It can also be through activating hemostasis when a trauma occurs, which is process which causes bleeding to stop. When an artery is damaged and blood exits through a hole quickly there is a high wall shear stress (Section 1.4.1) incurred in the endothelium. When this happens hemostasis is activated

(along with a rapid contraction of the artery) through platelet activation and adherence, for high shear stress platelet deposition can increase by a factor of 100 (Ku 1997).

1.4 Atherosclerosis

In the arterial wall, certain consequences of endothelial dysfunction and the breakdown of homeostasis are directly related to the pathogenesis of atherosclerosis (Gimbrone et al. 2000). The main result of atherosclerosis is the thickening of the artery wall and a loss of its elasticity (Figure 3). This disease occurs progressively over time where lesions form on the artery wall known as atherosclerotic plaques. Cholesterol doesn't dissolve in water and must be made water soluble to be transported in blood; this is done by combining it with lipoproteins produced by the liver and small intestine. There are two main kinds of lipoproteins, low-density lipoproteins (LDL) and high-density lipoproteins (HDL). LDL takes the cholesterol from the liver to the cells in the body with the purpose of cell membrane repair, the production of steroid hormones and bile salts. On the other hand HDL removes excess cholesterol from the cells and returns it to the liver. If there is an imbalance in these two lipoproteins with an excess of LDL compared to HDL then the excess deposits of cholesterol causes the formation of atherosclerotic plaque (Tortora and Derrickson 2009).

There are three ways atherosclerosis can increase the chance of stroke. Firstly it narrows the artery forming a stenosis (restriction) through a build-up of plaque on the artery wall, which in turn reduces the flow of blood to the brain. Secondly a blood clot or thrombus can form in the stenosis region, which can completely block the flow of blood to the brain. Thirdly plaque can break away from the stenosed region, travel downstream and block a smaller artery (Lovald et al. 2009). It is often recommended that a stenosis that has an occlusion of 70% or more be given surgical attention, to reduce the probability of stroke (Collaborators 1991).

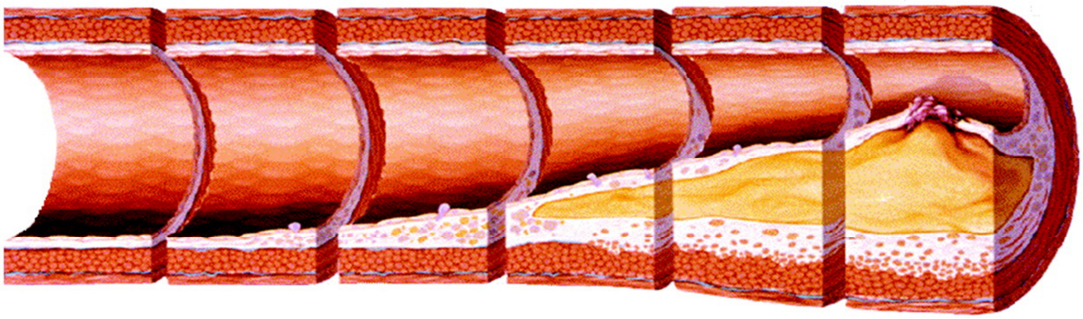

Figure 3 Progression of atherosclerosis over time. Figure adapted from Koenig and Khuseyinova (2007).

1.4.1 Wall Shear Stress

As blood flows through a vessel it exerts a force known as wall shear stress (WSS) on the endothelium. WSS (τ_w) is defined by Equation 1, where μ is the dynamic viscosity of the fluid and the second term is the velocity gradient at the wall.

$$\tau_w = \mu \frac{\partial u}{\partial y}\bigg|_{y=0} \qquad \textbf{Equation 1}$$

The relationship it has with the progressive development of atherosclerosis has been widely investigated (Zarins et al. 1983; Ku et al. 1985). Zarins et al. (1983) initially studied scale models of the CA obtained from autopsy using LDA under steady flow conditions using flow data obtained to create a correlation with low WSS and intima thickening. Ku et al. (1985) then went on to perform pulsatile flow analysis on the same geometry obtaining a correlation between oscillating WSS and thickening. Biologically, WSS is a major control factor in the structure of the endothelium (Chatzizisis et al. 2007; Traub and Berk 1998). In the main vasculature, in regions void of arterial geometry change, the arterial vessel diameter changes to maintain a normal physiological WSS ~1-2Pa (Traub and Berk 1998). Endothelial cells are oriented with their longitudinal axis parallel to the flow, which presents athero-protective characteristics. In regions of low WSS and disturbed flow (WSS<0.4Pa), endothelial cells do not align their longitudinal axis with the flow direction which makes them more exposed to endothelial dysfunction and more likely to promote plaque growth (Traub and Berk 1998). The cells then present an environment more suited to the progression of atherogenesis such as increased permeability of the endothelium and impaired NO synthesis.

Arteries can adapt to long term changes in WSS. If an increased WSS is experienced the artery responds through vasodilation followed by a remodelling to a larger diameter with the

same arterial structure. If a low WSS is observed it causes a thickening to the intimal layer to re-establish a normal WSS (Ku 1997).

1.5 Blood

An important factor when modelling a cardiovascular system is an understanding of the composition of blood and its mechanical response. Blood is a mixture of cells, proteins, lipoproteins and ions. This transports nutrients and waste through the arterial system (Ku 1997). It is a suspension of formed elements in plasma. The formed elements comprise 37-54% of the whole blood, of which 99.9% are red blood cells and the other 0.1% are platelets and white blood cells (Martini et al. 2006). Plasma is mainly water based (92%) with the final portion containing plasma proteins. Blood is considered a non-Newtonian fluid; its viscosity varies with shear rate. The non-Newtonian behaviour of blood is highly dependent on shear rate and haematocrit level (Guyton and Hall 2000) and is most prevalent when very low shear rates are experienced and the red blood cells group together, which gives the blood its non-Newtonian behaviour. It is also a major factor in the microcirculatory system when the capillary diameters are so small that only single blood cells can pass through (Ku et al. 1985). As shear rate increases the red blood cells separate and the viscosity of blood reduces.

The non-Newtonian behaviour of blood is neglected in this study. This assumption is common place in experimental and numerical modelling of arterial fluid dynamics in medium to large arteries. In these geometries the shear rates are regularly above $100s^{-1}$ which is large enough that the groups of red blood cells have separated so much that they no longer affect the blood viscosity Fung (1993). The WSS in the carotid artery can be estimated as 0.75Pa at a mean Re of 290 (Buchmann et al. 2010), using an estimated blood viscosity of 0.004kg/ms gives a WSR of $187.5s^{-1}$, allowing for the viscosity of blood to be considered constant and validating a Newtonian assumption (Yamamoto 2011).

In this work blood is assumed to be homogenous. Even though blood is a suspension of the blood cell, platelet and leukocyte particles in plasma, these are all at least three orders of magnitude smaller than the diameter of the carotid artery (7.5µm to 6mm), therefore making this a reasonable assumption. It is also assumed that it is incompressible due to the relatively low pressure variation that actually occurs in the human arterial system in relation to the density of blood.

1.6 Conclusion and Thesis summary

This section has provided a brief discussion of the medical background that drives the purpose of this thesis. It has shown WSS is a major factor in the development of atherosclerosis. For a more in-depth understanding of the medical theory several references are suggested (Gray 1918; Martini et al. 2006; Tortora and Derrickson 2009), further elaboration within this body of work is out with the scope of its intended study. Each chapter will provide its own literature review of the relevant computational and experimental studies.

The aim of this thesis is to develop a greater understanding of the flow field dynamics and WSS experienced in both a healthy CA and one that is experiencing a restriction due to stenosis. Experimental analysis will be performed in vitro in a lab environment with custom made compliant flow phantoms that are representative of the CA. This requires development of a moulding technique to produce such geometries. Experimental analysis will be performed using a non-invasive technique known as particle image velocimetry (PIV), which has been previously used to study similar geometries e.g. (Buchmann 2010). It will be shown that analysis of this nature has previously been performed in rigid geometries both experimentally and computationally, but work with compliant geometries that experience fluid-structure interactions (FSI) is far scarcer. In addition, this thesis presents, to this authors knowledge, the first results obtained with a physiologically representative flow waveform input into a compliant phantom representing the CA. A comparison is also made to results obtained in an equivalent rigid geometry, providing the effect compliance plays on the flow field and WSS.

The thesis has the following structure. Chapter 2 describes the construction method developed that can produce a flow phantom for use in experimental analysis that preserves dynamic similarity between in vivo and in vitro conditions. The work in this chapter has been published in *Experiments in Fluids* (Geoghegan et al. 2012a). Chapter 3 presents a review of the PIV experimental technique applied in this thesis, with a discussion on both the hardware and software components required to perform analysis in a compliant structure. Chapter 4 describes the flow system setup required to produce a physiologically realistic inlet waveform in a compliant phantom. It also provides a discussion on the liquid used to mimic blood within the arterial geometry. Chapter 5 presents a study of the flow field and WSS in an idealised compliant phantom representing the CA experiencing a physiologically

representative flow input. It compares results obtained in an equivalent rigid geometry, which provides further confirmation that the assumption of rigid walls is not valid. Chapter 6 provides an analysis of the effect compliance has on the experimental results providing a validation into the purpose of producing the more complex compliant flow phantom geometries compared to the rigid counterparts. This work in part (Section 6.4) is currently under review for publication in *Experiments in Fluids*. Chapter 7 provides a study of the flow field and WSS observed in a compliant stenosed geometry representing the CA. It provides analysis of both a symmetric and asymmetric stenosis axial location. Some of the results were presented in the Proceedings of the 15th International Symposium of Laser Techniques to Fluid Mechanics held in Lisbon, Portugal (Geoghegan et al. 2010). Chapter 8 presents time resolved measurements of the flow field downstream of a symmetric stenosis using a novel illumination technique that replaces the conventional expensive laser used in PIV experimentation with a relatively low cost light emitting diode (LED) system. This work is currently under review for publication in *Experiments in Fluids*. Chapter 9 provides a final conclusion to the key outcomes of the research within this thesis and provides possible developments that can be used in future work.

2 Phantom Construction

To obtain usable data from particle image velocimetry (PIV) (Chapter 3) experimentation in a compliant model of the carotid artery (CA) there are two main areas of study that have to be investigated. The first consideration and the basis of this chapter is the construction of an optically transparent physical model (commonly called a flow phantom), the assumptions made and the methods used to preserve the mechanical properties between the real world in-vivo problem and in-vitro experimental analysis. The second consideration is how to physically represent blood, which includes assumptions made, preserving dynamic similarity in the fluid system and representing the oscillatory nature of the cardiovascular system. This second consideration is further investigated in (Chapter 4). The technique for construction of compliant flow phantoms used in this body work was continually developed throughout its duration. As such, three different flow phantom geometries were produced, designated as Mark (Mk.) I, II and III, with continual improvement to the casting technique and the physiological relevance of the phantom geometry occurring with each evolution.

The first part of this chapter provides a background to previous methods of construction used to produce compliant flow phantoms. The second section reviews the method used to ensure dynamic similarity in the mechanical properties between the flow phantom and the arterial geometry. The third section then outlines the manufacturing method employed in the current work to produce a compliant flow phantom.

2.1 Background

There are several key points that have to be addressed when constructing a thin walled optically transparent flow phantom for PIV. Firstly there is the ability to produce a phantom with well-controlled internal geometry and wall thickness. Secondly the phantom material has to have well defined mechanical properties that can preserve dynamic similarity and

thirdly, the phantom material has to have a refractive index that can easily be matched by the working fluid (Chapter 4).

Several methods for constructing compliant flow phantom geometries have been reported. Gawenda et al. (2004) produced latex phantoms of fusiform aneurysms by painting a glass female mould with liquid latex. The number of layers applied controlled the elasticity of the resulting model. This technique provides minimal control of the uniformity of wall thickness and the opaqueness of the latex material makes it unusable for flow visualization techniques. O'Brien et al. (2005) and Doyle et al. (2008) used a technique involving a two stage investment casting process to produce flow phantoms representing the abdominal aortic aneurysm (AAA). Two part Aluminium female moulds were constructed using a computer numerical control (CNC) milling process. A casting wax was inserted into the first mould to produce a representation of the internal geometry of the AAA. This was used as a sacrificial negative model. The wax negative was then placed in the second aluminium female mould with silicone injected into the space between the wax and the aluminium to produce the thin walled phantom. After the silicone cured the wax was melted out and the aluminium cast removed. This technique has the advantage that CNC milling can produce a variety of different phantom geometries, but a drawback to the system is that when wax sets it can shrink introducing an error into the original geometry. Yagi et al. (2009) use a similar lost wax method to produce a phantom of a physiologically realistic cerebral aneurysm from silicone rubber. Burgmann et al. (2009) developed a method using a rotating hollow cylinder to produce a straight cylindrical compliant flow phantom. Silicone was injected into the rotating cylinder and rotated at 1500rpm until the silicon elastomer cured. This method has several drawbacks. Firstly, to ensure uniform distribution of the silicone elastomer the internal diameter of the rotating cylinder has to be machined to a high precision and any deviation in the horizontal position would cause the silicone to gather at one end. Secondly, this method is very difficult to apply to more complex geometries.

A technique that can be adapted to compliant phantom construction that has been widely used in the construction of rigid wall flow phantoms is rapid prototyping of the sacrificial negative model. This can be achieved with materials such as plaster starch or acrylonitrile butadiene styrene (Buchmann et al. 2011; Spence et al. 2011b; Hopkins et al. 2000). There is

minimal restriction on the geometry that can be constructed and once the phantom material has cured the negative model can easily be dissolved out.

It is important that the material of a phantom constructed for flow visualisation analysis is optically transparent and has a low refractive index that can be easily matched to the working fluid (aqueous glycerol solution). It is also desirable that the properties are homogeneous and that they can be repeated for every phantom, producing a high quality, safe and stable construction. In this work the silicone elastomer Sylgard 184 was used for phantom construction as the casting technique and quality of results were well documented in concurrent and previous work (Geoghegan et al. 2012a; Spence 2011; Buchmann 2010) along with the refractive matching technique.

A basic overview of the construction method employed in this body of work is as follows

1. Produce a three dimensional (3D) solid computer model of the internal artery geometry
2. Rapid prototype a negative of the flow phantom geometry in a water soluble material
3. CNC machine a mould of the external wall of the artery geometry
4. Inject silicone between external and internal mould
5. Remove moulds after the silicone cures.

2.2 Material Properties

To ensure the flow physics in the phantom was representative of the real-world problem, the fluid properties of the working liquid and mechanical properties of the physiological model have to be scaled to preserve dynamic similarity. This was achieved through the use of dimensionless scaling factors. The phantom must be large enough that the spatial resolution of measurement technique was not limiting, but small enough that the flow rate was feasible, and the materials affordable. Chapter 4 explains the process for matching fluid properties and the inherent dimensionless parameters associated with the problem this section defines the method for matching material properties. When considering a thin walled phantom that is required to dilate and contract, the main difference compared to a rigid phantom is the thin walled fluid system will have a variable boundary depending on fluid pressures. To obtain dynamic similarity it was important to match material properties. Two important factors

have to be considered to achieve this. Firstly the circumferential response of the vessel wall to the fluid pressure change during an oscillatory flow cycle and secondly the longitudinal response of the vessel to the same input.

2.2.1 Circumferential Response

To ensure dynamic similarity for the circumferential response of in vitro experimentation for arterial structures it was important to match the distensibility. The explanation of this term was developed by Caro et al. (1978). The first thing requiring definition is the Young's modulus of elasticity (E). This is a characteristic quantity of a material and in the simplest materials is independent of the manner in which the stresses are applied. The value of E can be calculated by Equation 2.

$$E = \frac{\Delta p_i}{\Delta D_e} \cdot \frac{2 D_e D_i^2 (1 - \sigma^2)}{D_e^2 - D_i^2} \qquad \textbf{Equation 2}$$

p and D represent pressure and diameter respectively. Subscript e and i represent the external and internal location. Finally σ is the Poisson's ratio which for incompressible materials (which all biological materials effectively are) this value is a ½ (this is true of most biological materials). If the wall thickness (h) of a cylindrical vessel is significantly less than the diameter (which is the case for major vessels in the cardiovascular system) all diameters can be denoted as D thus reducing Equation 2 to

$$\frac{2\Delta D}{D\Delta p} = \frac{D(1 - \sigma^2)}{Eh} \qquad \textbf{Equation 3}$$

For small changes in D the left hand side of Equation 3 can be written as

$$\frac{2\Delta D}{D\Delta p} \approx \frac{1}{A}\frac{\Delta A}{\Delta p} = d \qquad \textbf{Equation 4}$$

This is known as distensibility (d) where A is the cross-sectional area of the cylindrical vessel. It can also be shown for materials where σ^2 is small compared to 1 the equation for d can also be written as

$$d = \frac{1}{E(h/D)} \qquad \textbf{Equation 5}$$

Combining Equation 4 and Equation 5 the following dimensionless parameter can be obtained.

$$\frac{\Delta A}{A} = \frac{\Delta p D}{E h} \quad \textbf{Equation 6}$$

To further validate this equation provided similitude between the experimental setup and in vivo conditions the Buckingham π-theorem was applied to the physical problem. A full explanation of this theorem can be found in standard texts such as Potter and Wiggert (2002), but basically the Buckingham π-theorem states: for a physical problem that has n variables that contain m basic dimensions, Equation 7 holds true.

$$x_1 = f(x_2, x_3 \ldots\ldots x_n) \quad \textbf{Equation 7}$$

Equation 8 which relating all the variables, has n-m dimensionless groups known as π-terms

$$\pi_1 = f(\pi_2, \pi_3 \ldots\ldots \pi_{n-m}) \quad \textbf{Equation 8}$$

The π_1 term includes the dependent variable and the remaining π-terms including only independent variables. To produce dimensionless numbers there need to be m repeating variables that are combined with the remaining variables. It is important that the repeating variables contain all of the basic dimensions but do not create a dimensionless number themselves.

For the case in question the dependent variable of a compliant artery is the change in diameter (ΔD) of the artery which is dependent on the change in pressure (Δp), E, h, dynamic viscosity of the fluid (μ), angular frequency of the flow (ω), D, density (ρ) and fluid velocity (U)

$$\Delta D = f(\Delta p, E, h, \mu, \omega, D, \rho, U) \quad \textbf{Equation 9}$$

Equation 9 gives a total of eight variables with three basic dimensions (mass, length, time), resulting in 5 dimensionless groups. The repeating variables for this case are D, ρ and U. Applying the theorem, Equation 9 produces Equation 10.

$$\frac{\Delta D}{D} = f_1\left(\frac{\Delta p}{\rho U^2}, \frac{E}{\rho V U^2}, \frac{D}{h}, \frac{\rho U D}{\mu}, \frac{l\omega}{V}\right) \quad \textbf{Equation 10}$$

It is also known that Δp is dependent on D, V, ρ, μ, gravity (g), speed of sound (c), ω and surface tension σ_s. (Equation 11).

$$\Delta p = f(D, U, \rho, \mu, g, c, \omega, \sigma_s) \quad \textbf{Equation 11}$$

Applying the Buckingham π-theorem Equation 12 is obtained.

$$\frac{\Delta p}{\rho U^2} = f_1\left(\frac{\rho U D}{\mu}, \frac{D\omega}{U}, \frac{U^2}{Dg}, \frac{U}{c}, \frac{U^2 \rho D}{\sigma_s}\right) \quad \textbf{Equation 12}$$

The left hand term is known as the Euler number (Eu) and the parameters 1-5 on the right hand side are the Reynolds number (Re), Strouhal number (St) (both Re and St will be discussed further in Chapter 4), Froude number (Fr), Mach number (M) and Weber number (W) respectively. M can be ignored due to the low velocities experienced in the artery system; W can be ignored in the major arteries as the force of surface tension is negligible compared to all other forces experienced by the working fluid and Fr can be ignored by the negligible change in gravitational potential energy in the system. Therefore Equation 12 can be rewritten as Equation 13).

$$\frac{\Delta p}{\rho U^2} = f_1\left(\frac{\rho U D}{\mu}, \frac{D\omega}{U}\right) \quad \textbf{Equation 13}$$

This shows the Euler number accounts for the effect of Re and St (any change in Re and St will be caused by a change in the Euler number, therefore including them would be redundant) reducing Equation 10 to Equation 14.

$$\frac{\Delta D}{D} = f_1\left(\frac{\Delta p}{\rho U^2}, \frac{E}{\rho U^2}, \frac{D}{h}\right) \quad \textbf{Equation 14}$$

Referring back to Equation 5 and Equation 6; they are essentially a combination of the non-dimensional numbers above. The upshot is that to get an equivalent response in diameter change between in vivo and in vitro cases each of the dimensionless parameters on the right hand side of Equation 14 are required to be matched.

2.2.2 Longitudinal Response

The second important property characterising a thin walled model is the wave propagation length λ, which relates to the longitudinal response of the vessel wall. For oscillatory flow in a compliant tube there are oscillations in both time and space. Both have the same time period T.

$$T = \frac{2\pi}{\omega} \quad \textbf{Equation 15}$$

In one time period the input oscillatory pressure completes one cycle in time and the pressure inside the tube completes one cycle in space (Zamir 2000). The propagation wavelength is the length of tube that one of these cycles occupies and can be calculated by Equation 16.

$$\lambda = Bc_0T \qquad \textbf{Equation 16}$$

The propagation wave speed in inviscid flow c_0 is obtained using the Moens-Korteweg formula (Burgmann et al. 2009; Zamir 2000) and is given as:

$$c_0 = \sqrt{\frac{Eh}{D\rho}} \qquad \textbf{Equation 17}$$

The dispersion coefficient B is represented by the solid line shown in Figure 4 and can be found through calculation of the frequency parameter also known as the Womersley number (Equation 18).

$$\Omega = \sqrt{\frac{\rho\omega}{\mu}}\frac{D}{2} \qquad \textbf{Equation 18}$$

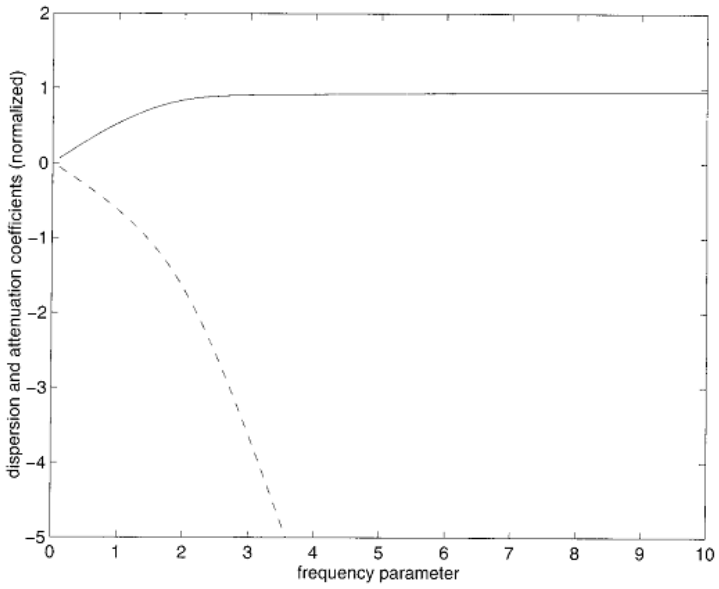

Figure 4 The dispersion coefficient is represented by the solid line. Figure adapted from Zamir (2000).

To observe large differences between flows in elastic and rigid tubes requires a complete wavelength within the tube, if a tube is shorter than this the difference between the two will be damped. In the arterial system of the body the tube lengths (L) vary between λ and λ/100.

For example the wave speed in the aorta is roughly 5m/s and a frequency of $1.2s^{-1}$ giving a wavelength of 4m. The aorta itself is only about 0.5m for a fully grown man (Caro et al. 1978).

To calculate the length of model required for an accurate analysis of the effect of compliance the ratio of length of model L_{model} to λ_{model} has to be matched to real world values (Equation 19).

$$\frac{L_{model}}{\lambda_{model}} = \frac{L_{RW}}{\lambda_{RW}} \qquad \textbf{Equation 19}$$

To interpret the results obtained from compliant models, the Young's modulus (E) of the material must be known and can be determined experimentally.

2.3 Young's modulus

The Young's modulus of the cured silicone was affected by the percentage of catalyst and the temperature during curing. The relationships were not quantified in the product literature and experiments were carried out to elucidate them. A tensile test was performed on silicone samples using the gallows shown in Figure 5. Known weights were used to apply an incremental uniaxial tensile load to samples. A Canon PowerShot A480 10 megapixel camera with 300mm standoff was used to track the change in length of the sample. The centres of the blue marks were tracked manually. Pixel displacement was then converted to millimetre displacement 1 pixel = 0.08mm with a measurement accuracy of ±2 pixels (resting separation was 124±3 pixels between samples). Samples were tested with 10% ± 0.01% hardener cured at 20±1, 40±3, 100±3, 150±5°C[1]. The gradient of the linear portion of a graph of stress σ versus strain ε gives the Young's modulus E of each individual sample, the results of which can be seen in Figure 6. Error bars show the difference between the maximum and minimum of three different samples cured at the same conditions at different times from different batches of silicone. Samples for tensile testing may be poured from the same batch, and cured alongside flow phantoms, then used to obtain the exact Young's modulus of these models. Increasing the curing temperature decreases the time required for the silicone to harden, in turn reducing the time for entrained air bubbles to rise to the surface and break.

[1] Temperatures were obtained with a Maxim DS19121G Thermochron® iButton®, which has an accuracy of ±1°C and a resolution of 0.5°C.

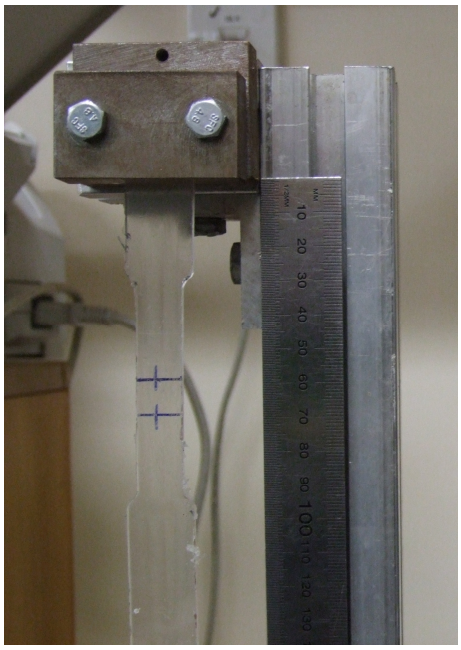

Figure 5 Silicone sample in gallows

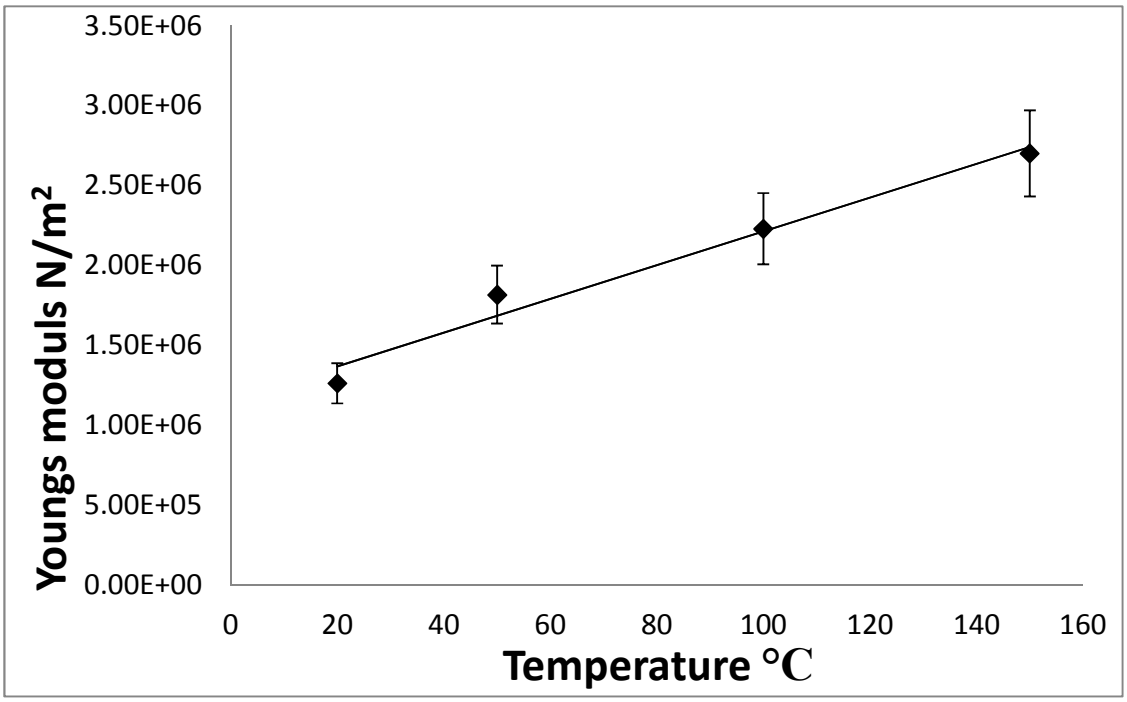

Figure 6 Young's Modulus versus change in temperature for Dow Cornings Sylgard 184

Young's modulus measured on post-mortem samples can differ from the in-vivo values. Some example values are shown in Table 3. Using this information and the formulation discussed in section 2.2 a flow phantom that was physiologically realistic was produced.

Table 1 Young's Modulus values for commonly investigated vessels. Table adapted from Steiger et al. (1989); Riley et al. (1992); Isnard et al. (1989)

Structure	Test condition	Young's Modulus (N/m^2)
Cerebral aneurysm wall	In-vitro	$1.7x10^6$
Cerebral aneurysm neck	In-vitro	$3.1x10^6$
Intracranial artery	In-vitro	$2.5x10^6$
Carotid artery	In-vivo	$0.7\text{-}0.98x10^6$
Aorta	In-vivo	$0.526\text{-}1.071x10^6$

2.4 Phantom Geometries

The structure of the CA varies widely throughout the general population (Ding et al. 2001). The physiological relevance of the geometries used within this thesis should be considered. Idealised geometries can be used to study the general flow field and WSS experienced and help develop an understanding of the results expected across the general population. Physiologically realistic geometries are becoming common in studies using rigid flow phantoms (Buchmann et al. 2011; Spence 2011; Tateshima et al. 2003b). The construction process becomes inherently more complex when the flow phantom wall is compliant. Using the assumption of an idealised geometry alleviates the increase in complexity. The work in this thesis is also in part, meant as a source of validation for current and future computational studies. Many of these have used idealised representations of arterial geometries (Long et al. 2001; Sherwin and Blackburn 2005; Varghese et al. 2007b; Mao et al. 2011). As this work is one of the first studies to study compliant geometries experimentally it was decided only to use idealised geometries, to reduce construction complexity. That being said, it is acknowledged that geometric variation from person to person will have an influence on hemodynamic factors, especially when study progresses from a healthy artery, to an artery with atherosclerosis. This issue should be addressed in future work and methods to achieve this will be discussed further in Chapter 9.

As discussed previously three geometries of idealised flow phantoms representing the common carotid artery (CCA) under healthy and atherosclerotic conditions were constructed. Table 2 provides an overview of both the properties of the CCA and the Mk. I, II and III flow phantoms. This section provides an explanation and justification for the selection of the properties for the compliant flow phantoms.

Table 2 CCA (Buchmann 2010; Riley et al. 1992) and flow phantom properties

Property	CCA	Mk. I	Mk. II	Mk. III
Wall Thickness (m)	0.000617	0.00128	0.00128	0.00128
Internal Diameter (m)	0.0062	0.02	0.02	0.02
Density(blood, glycerol) (kg/m^3)	1060	1140	1140	1140
Young's Modulus (N/m^2)	776 000	1 320 000	1 320 000	1 320 000
Time Period Oscillation (s)	1	2.92	2.92	2.92
Propagation wavelength (m)	8.25	27.26	27.26	27.26
Length (m)	0.1	0.21		0.33
Symmetric Stenosis (% by diameter)	N/A	N/A	30%	50%
Asymmetric Stenosis (% by diameter)	N/A	N/A	30%	50%
Asymmetric Stenosis offset (m)	N/A	N/A	0.003	0.005

The average human CCA has a diameter of 6.2mm(±0.15mm) (Riley et al. 1992), all the phantoms constructed had the internal diameter scaled to 3.2 times life size (20mm), this increased the effective spatial accuracy in model construction and gave an increased temporal resolution due to dimensional scaling requiring slower flow velocities per flow wave. It also allowed for a larger field of view to perform PIV analysis and the internal diameter conformed to standard pipe fittings that were used for constructing the flow system.

Wall thickness was calculated using Equation 5, which matched the distensibility of the phantoms to that of the CCA. It was calculated with an estimation of E obtained from Figure 6, but as previously stated in section 2.3 the Young's modulus varies with both percentage hardener and curing temperature. This meant that even with due diligence in the mixing process and a well-controlled curing temperature there was a variation in E obtained, resulting in a variation in distensibility between phantom and CCA. All phantoms were cured at a temperature of 20±1ºC; this gave an estimated E of 1.2×10^6N/m^2. Using the data from Table 2 and Equation 5 this gave a wall thickness of 1.28mm.

All internal geometries for use as the sacrificial negative model were constructed using SolidWorks[2]. The Mk. I flow phantom served as a feasibility study into the construction method of producing a compliant flow phantom and experimental analysis in a compliant structure. The internal geometry of the Mk. I is shown in Figure 7(a), it represents a healthy carotid artery produced by extruding a simple circular sketch along the longitudinal axis. For

[2] SolidWorks, Concord, MA, USA

simplicity in the initial moulding process the longitudinal response was not taken into account for this phantom. It was constructed with a length of 210mm as increasing phantom length created an increased difficulty in ensuring uniformity in wall thickness along the length of the mould.

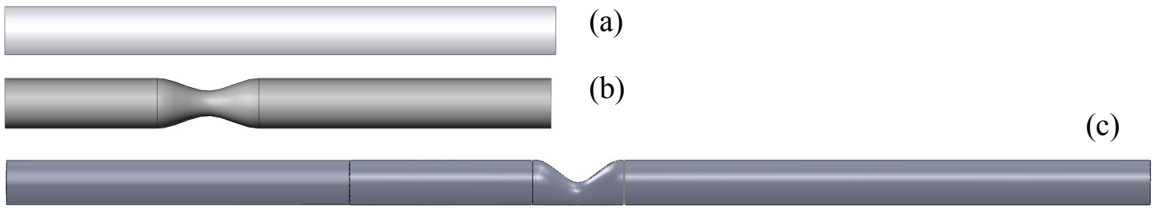

Figure 7 Internal phantom geometries for the Mk. I healthy artery (a), Mk. II 30% symmetric stenosis by diameter (b) and Mk. III 50% asymmetric stenosis by diameter (c).

Two versions of the Mk. II phantom (Figure 7(b)) were constructed with a length of 210mm. Both were constructed with a constriction located at 1/3 the length of the phantom which represented a stenosis. Two stenosis were produced, firstly a symmetric stenosis (Figure 8(b)) which was characterised by having the centre of the restriction concentric with the centre of the main phantom in the axial plane. The second was an asymmetric stenosis (Figure 8(a)) which was characterised by having the centre of the restriction offset radially from the centre of the main phantom. The common method of quantifying a stenosis is by the reduction in diameter at its peak constriction. The Mk. II geometries had a 30% stenosis (for reference 51% by area) therefore the internal diameter at the peak reduction is 70% of that in the main phantom geometry; this gave the stenosis a diameter of 14mm. The asymmetric stenosis was offset from the centre of the main phantom by 3mm.

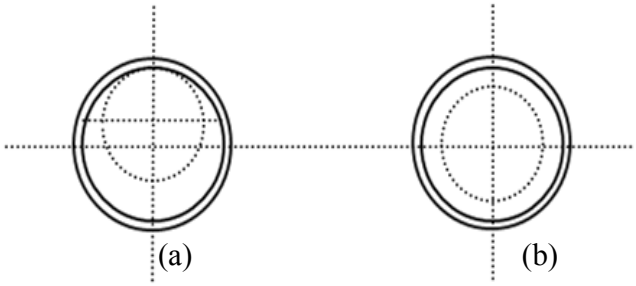

Figure 8 Stenosis placement (a) asymmetric (b) symmetric

Both symmetric and asymmetric stenosis were constructed with a length of 40mm and in the plane of symmetry as shown in Figure 9 the symmetric stenosis can be described using Equation 20(a) and the asymmetric stenosis by Equation 20(b).

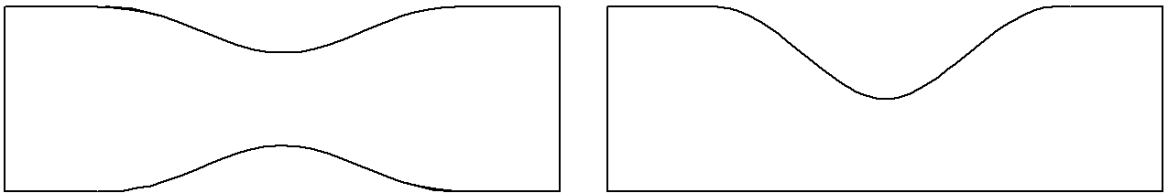

Figure 9 Cross section in the plane of symmetry for a stenosis that is (a) axial symmetric (b) axial asymmetric

$$y = 1.5\cos\frac{\pi}{20}x \qquad \text{(a)}$$

$$y = 3\cos\frac{\pi}{20}x \qquad \text{(b)}$$

Equation 20

The Mk. III phantoms (Figure 7(c)) were designed to incorporate dynamic similarity in the longitudinal response of the flow phantom. To obtain the phantom length using the method described in section 2.2.2 requires an understanding of the blood mimicking fluid (aqueous glycerol solution) used in the experimental set up and the oscillating nature of the representative physiological flow wave. A full explanation of this can be found in Chapter 4, but the important data for phantom length calculation is provided in Table 2 giving a phantom length of 330mm. A symmetric and an asymmetric Mk. III phantom were produced with a 50% stenosis (75% by area). The stenoses were again 40mm in length and were mathematically described by Equation 21(a) and Equation 21(b) respectively.

$$y = 2.5\cos\frac{\pi}{20}x \qquad \text{(a)}$$

$$y = 5\cos\frac{\pi}{20}x \qquad \text{(b)}$$

Equation 21

Once the sacrificial negative geometry had been constructed in SolidWorks it was exported to a stereo-lithography (STL)[3] file. 3D rapid prototype printing was used to create a negative mould from the scaled digital STL file (discussed further in section 2.5.1).

2.5 Casting Procedure

The casting technique implemented in this body of work has largely been reported in Geoghegan et al. (2012a) and draws on some methods that were used to construct thick-walled, rigid flow phantoms in concurrent and previous projects (Spence 2011; Buchmann

[3] A common file type used in 3D graphics applications compatible with rapid prototyping machines

2010). Previous studies involving compliant flow phantoms often fail to give a full description of casting techniques (Pielhop et al. 2012; Deplano et al. 2007; Bertram and Tscherry 2006), or when reported they are often overly complex methods with certain key pieces of information omitted (Burgmann et al. 2009; Yagi et al. 2009; Doyle et al. 2008). This therefore led to a significant period of development being required to produce an adequate phantom for use in experimental analysis.

2.5.1 Rapid Prototyping of Sacrificial Models

There are a number of possible materials for the negative mould. Wax, gelatine and chocolate were trialled. These can reproduce fine detail, but shrink on cooling. Low melting point alloys are available, which can be melted and flushed out with hot water. These can leave residues which are difficult to remove. It is desirable to use a material which can be 3D printed directly, without the use of an intermediate positive mould to form the negative (Yagi et al. 2009; Doyle et al. 2008). Finally a plaster powder was chosen, which can be 3D printed and is dimensionally stable.

The Mk. I phantoms were constructed in a ZPrinter 310 Plus[4] using ZP130[4] powder and binder. The Mk. II and III phantoms were printed by a Spectrum Z510[4] printer using ZP150[4] powder and binder. Specifications of the two 3D printers used are given in Table 2. These machines build up the model in layers of a water-dissoluble plaster powder. The resulting prototype was brittle and porous and in normal practice was filled with wax or epoxy to increase its strength. Since this renders the material insoluble, the flow phantom moulds are produced without filler. The updated Z510 printer was found to produce a smoother surface finish with a finer resolution and also provided a larger build size.

[4] 3D Systems Corporation (Previously Z Corporation)

Table 3 Rapid prototyping specifications (adapted from (Geoghegan et al. 2012a))

	ZPrinter 310 Plus	Spectrum Z510
Max Build Size (mm)	203×254×203	254×356×203
Layer thickness (mm)	0.089–0.203	0.089–0.203
Resolution (dpi)	300×450	600×540
Number of print heads	1	4
Number of jets	304	1216
Build Speed	2–4 layers per minute	2–4 layers per minute

The accuracy of the rapid prototyping printers was quantified using a straight plaster cylinder with an original diameter of 20mm. Digital callipers with a measurement accuracy of ±0.005 were used to measure the tube diameter 3 consecutive times at 10 points along the surface of the untreated rapid prototyped cylinder. This resulted in an average of 20.22mm with a standard deviation (SD) from the mean of 0.02mm. This was a 1% increase in diameter from the STL geometry or equivalent to a 2% increase in cross sectional area. The material cost was \$0.3/cm^3 for the powder and \$0.4/ml for the binder.

Figure 10 Rapid prototyped Mk. II geometries

2.5.2 Model Surface treatment

Without filler added at the rapid prototyping stage the models are fragile so need to be handled with care. They are also porous and water soluble so rubber gloves are required when handling due to sweat causing degradation of the plaster surface. Before casting can commence the plaster surface must be sealed to prevent silicone from perfusing through the model in the curing stage. The models are coated with several layers of dilute polyvinyl acetate (PVA), rendering them impermeable to the liquid casting resin. Woodworking PVA glues sold for outdoor use often contain water resistant additives, so the PVA glues sold as school glue are favoured. The PVA coating improves the strength of the prototype and provides a physiologically realistic smooth surface to the model. Concurrently during the

process of PVA application the surfaces are lightly sanded with 400 to 1200 grit sand paper to produce a smooth finish.

The effect of PVA coating on the model geometry was tested in the same manner as the plaster models (section 2.5.1) using a straight plaster cylinder with an original diameter of 20mm. The first coat of PVA was partially absorbed by the plaster surface, for a PVA solution with 10% water added by mass there was 0.02mm increase in surface diameter (SD of 0.01mm) after sanding (sanding started with 400 grade paper sanding was repeated with increasing grade in increments of 200 to 1600). Subsequent coats of 90:10 PVA:water solutions gave an increase in diameter of 0.03mm (SD of 0.01mm). A PVA:water solution of 80:20 by mass gave a 0.01mm increase in diameter (SD 0.009). Differences in PVA composition from model to model would also affect the final cross sectional area.

2.5.3 Flow Rig Attachment

It was important to have a homogeneous transition from the rigid cylindrical pipe exit of the flow system to the entrance of the compliant flow phantom and vice versa at the opposite end. The Mk. 1 phantom employed a custom designed adapter similar to Burgmann et al. (2009) as shown in Figure 11. A conical adapter was attached to the exit of the rigid pipe. The adapter had an internal diameter of 20mm with the external wall increasing in diameter at an angle of 26º. The phantom was sheathed over the conical adapter. An external clamp (only one half is shown in Figure 11) secured the phantom into place. A major drawback of this mating assembly design was that it was prone to leakage and if the phantom experienced an excessive internal force it could break free from the clamp. Applying room temperature vulcanising rubber (RTV) between the conical adapter and the phantom minimised the occurrence of these flaws but with RTV having a curing time of 24 hours, this adaption hindered experimental progress when changing flow phantoms.

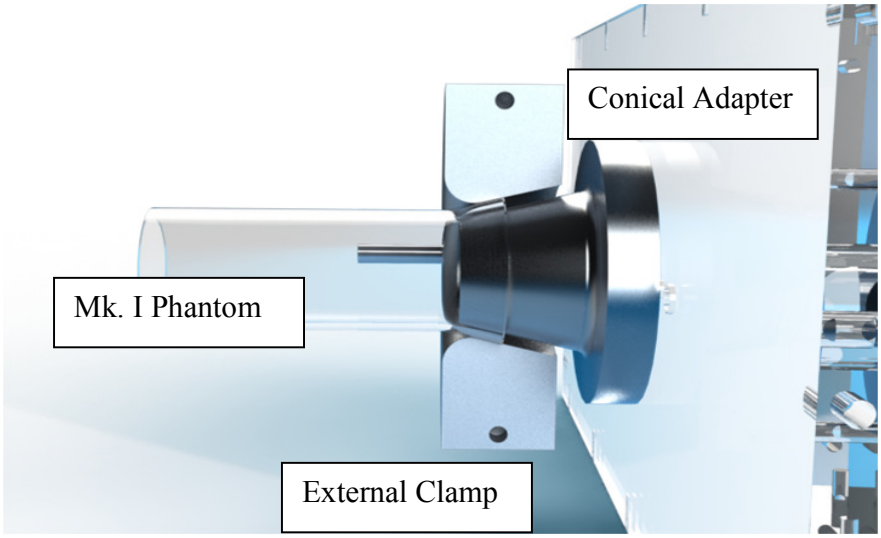

Figure 11 Mk. I phantom to flow circuit mating assembly

To overcome this flaw in experimental set up, the Mk. II and III phantoms incorporated a custom designed endplate attachment into the silicone phantom design. An end piece mould machined from Poly (methyl methacrylate) (PMMA) plate was attached to either end of the main phantom mould and produced a silicone block after the phantom cured (Figure 12(a)). Initial endplate designs had a right angle joint between phantom and endplate. This joint was prone to failure as bubbles that formed during pouring were trapped at the joint (this was accentuated by the high viscosity of the liquid silicone base slowing the bubbles). To counteract this, the final design had a transition zone from the compliant phantom to the silicone endplate. The geometry of this is shown in Figure 12(b) with all sharp edges filleted to reduce the possibility of points of failure. The join in the mould construction was also placed part way down the transition zone so that any bubbles were caught in a thicker region, thus were less likely to pierce the model.

To provide attachment to the flow rig system a square PMMA plate was glued to the end of each silicone block with an o-ring set in a machined groove to provide a seal when the phantom was clamped in. This system allowed phantoms to be exchanged in less than 10 minutes compared to the previous 24 hours. There was also a smoother transition from rigid to compliant system as there was no longer the lip of the conical adapter impinging on the flow.

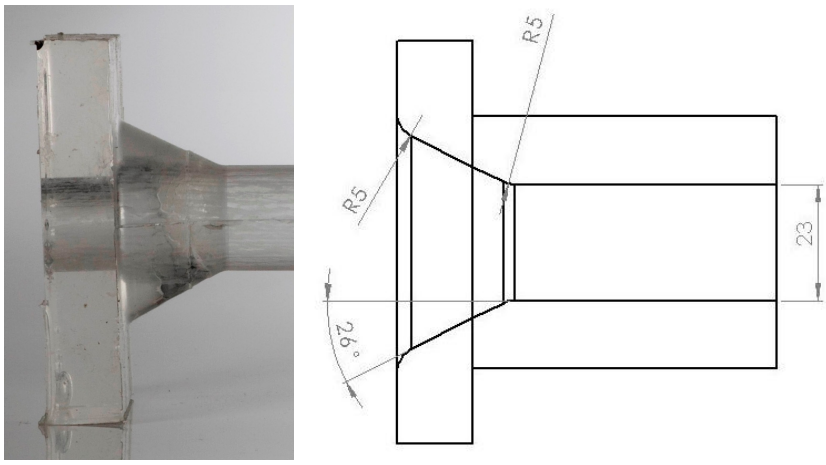

(a) (b)

Figure 12 Mk II and III (a) silicone endplate and (b) endplate to model connection design

2.5.4 Model casting

An optically transparent silicone elastomer (Sylgard 184, Dow Corning) was chosen as the material for the final flow phantoms because it has a low refractive index (n=1.43) that could be matched by a glycerol in aqueous solution, and has a proven track record (Spence et al. 2011b; Buchmann et al. 2009; Hopkins et al. 2000). The two part mixture of base and hardener required vigorous mixing to ensure uniform distribution of hardener throughout the base as variation in this affects Young's Modulus and refractive index. The pot life of the final mixture was approximately 4 hours. Sufficient silicone was prepared to cast the model using a single batch. Due to the high viscosity of the silicone (6.2±0.2 Pa.s at 20°C) numerous air bubbles were entrained during mixing. A vacuum chamber (a basic water aspirator connected to a faucet and plastic dessicator) was consequently used to degas the silicone at -75 kPa gauge pressure before pouring. Air bubbles rose out of the mixture and burst on the surface upon opening the dessicator to atmosphere. Four cycles were sufficient to completely degas the silicone up to a depth of 150 mm. This degassing procedure took approximately 45 minutes in total.

Each generation of phantom had its own final casting mould. Figure 13(a) shows the Mk. I mould with one half of the female external mould removed. The external female mould was produced from aluminium using a CNC mill with a diameter of 23mm. With an ideal rapid prototyped internal mould this would give a wall thickness of 1.5mm, but with increase in internal model from machining and PVA treatment it will produce a phantom closer to

1.28mm thick (the required thickness). This mould formed the outer wall of the compliant silicone phantom. A base was also machined in aluminium that located the plaster model in the centre of the aluminium mould. The mould was fastened and sealed with pan head screws and PVA glue. Silicone was injected into the space between the plaster and aluminium mould, taking great care not to entrain bubbles during this phase and was cured for 48 hours. Once cured, the model was immersed in water to disperse the plaster prototype and dissolve the PVA coating. Additionally, the plaster could be eroded with a soft scraper or a water jet to remove any plaster parts requiring mechanical effort to break adhesion. The final Mk. I flow phantom obtained is shown in Figure 13(b).

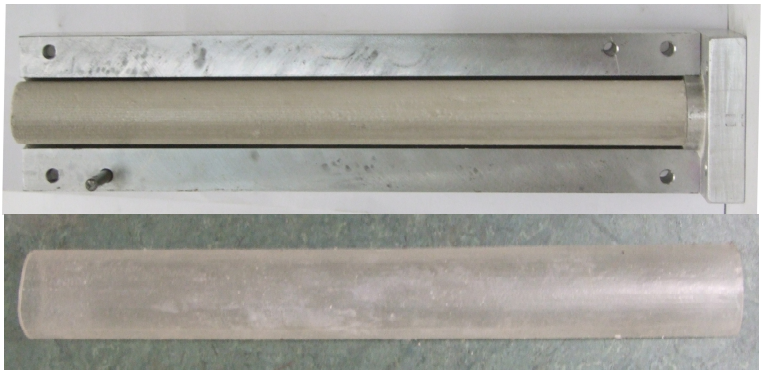

(a)

(b)

Figure 13 (a) Mk. I mould with one half of the female mould removed. The image is rotated 90º for ease of viewing. The mould sits on a square metal base with silicone injected at the open end. (b) Mk I. Flow phantom

As stated in section 2.5.3, the Mk. II phantom incorporated a custom endplate design. The external mould is shown in Figure 14(a). The mould adapted the Mk. I CNC machined aluminium female mould with attached PMMA plate endplate moulds. The base of the endplate moulds had a drilled-through 20mm diameter hole that was concentric with the internal drilled-through cylinder of the aluminium mould. These holes located the plaster phantom centrally in the external mould. Silicone was injected through an opening in the top endplate mould with the same curing and mould removal process used for the Mk. I phantom construction applied. The final Mk. II flow phantom obtained is shown in Figure 14(b).

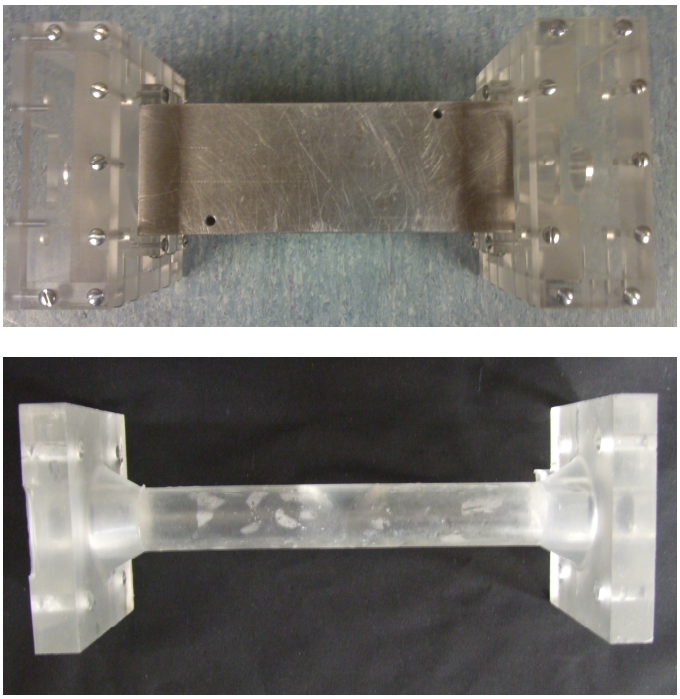

(a)

(b)

Figure 14 (a) Mk. II mould with PMMA endplate moulds attached. (b) Mk II Flow phantom

The Mk. III phantom had an increased length of compliant section at 330mm to incorporate longitudinal response matching (Section 2.2.2). Figure 15(a) shows a treated plaster model sitting in the female external mould. It was found with a set up similar to the Mk. II mould rig, where the endplates were used to locate the plaster mould centrally, a slight misalignment in endplate attachment would cause a large variation in wall thickness along the phantom. To counteract this, an alignment rig was constructed so that the plaster model location could be finely adjusted independently of the mould to insure uniform thickness along the length of the phantom.

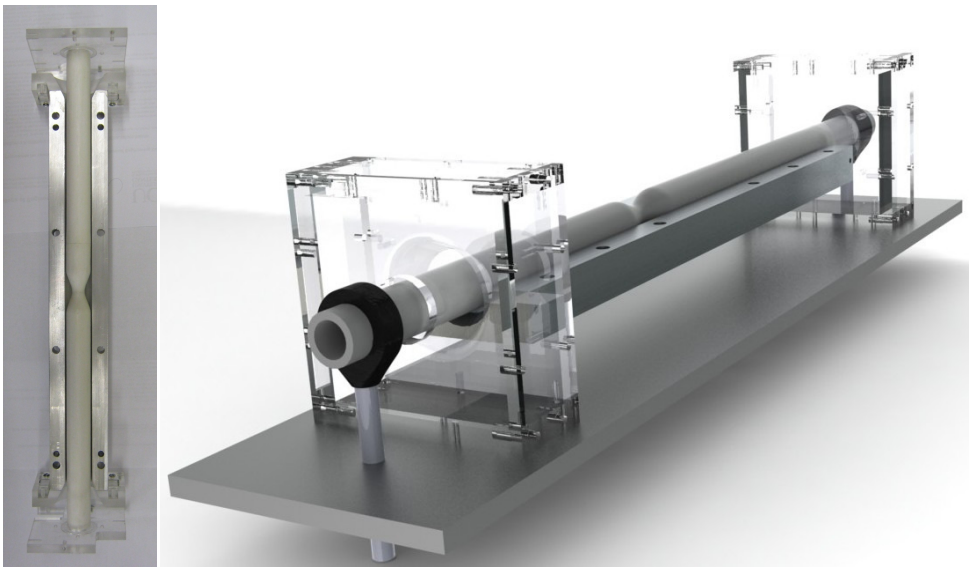

(a) (b)

Figure 15 (a) plaster model located in female aluminium mould (b) alignment rig assembly used to ensure uniform wall thickness.

With the top down silicone injection method used in the Mk. II phantom construction it was found that on occasion bubbles would form as the silicone filled the bottom endplate section and could settle in the main aluminium section of the mould system degrading the wall integrity of the compliant phantom. To counteract this, the Mk. III mould system incorporated a 45º plunger system shown in Figure 16 and injected into the mould from the bottom up. The angled plunger ensured that silicone did not fall as a free jet during the pouring phase, preventing aeration and the formation of bubbles.

Figure 16 Image of the silicone injection plunger system

The 50% symmetric stenosis Mk. III phantom with endplate attachments is shown in Figure 17. Figure 18 shows magnified images of the 50% symmetric and asymmetric stenosis. The striations seen in Figure 17 and Figure 18 might be explained as shallow grooves occurring during the PVA coating or partial variations in refractive index. The surface was smooth to the touch and the striations cannot be felt with the finger.

Figure 17 Silicone flow phantom representing the carotid artery with symmetric stenosis 330mm long

(a) (b)

Figure 18 Magnification of the flow phantom with a (a) 50% symmetric stenosis and a (b) 50% asymmetric stenosis

2.5.4.1 Rigid Phantom Casting

To analyse the affect of compliance on the flow field within a phantom geometry a rigid flow phantom was constructed with the same internal geometry as the Mk. I flow phantom representing a straight healthy CA. To create the rigid flow phantom a PMMA casting box was constructed around each model, fastened and sealed with pan-head machine screws and PVA glue. The phantom was constructed from the same silicone elastomer as the compliant phantoms. The casting box fitted around the negative mould such that the resulting model minimum wall thickness was 12 mm, which was found sufficient for an effectively rigid model. The silicone was prepared and cured by the same method applied to the compliant flow phantom.

2.6 Wall Thickness Verification

Wall thickness verification was achieved by dissecting sample flow phantoms physically measuring the wall thickness. Axial slices were removed periodically along the length of a phantom. Wall thickness was measured optically using a cannon PowerShot A1200 12.1 megapixel camera with 1 pixel equivalent to 0.06mm, the surface of the slices were spray painted matt black to allow better contrast for image processing with an example image shown in Figure 19. It was important to ensure slices were removed perpendicular to the longitudinal axis as misalignment would increase projected area which would skew the obtained results

Figure 19 Example image of axial slice removed from flow phantom

Wall thickness was recorded at 0º, 90º, 180º and 270º around the circumference. Measurement accuracy was within ±1 pixel. For the Mk. I, 3 phantoms were dissected. The average wall thickness was 1.31±0.05mm. The wall thickness was shown to vary 1.34-8.05% with a standard deviation of 5.02%. The Mk. II phantom as stated before was susceptible to misalignment of the internal mould so over 3 phantoms the average wall thickness was found to be 1.39±0.08mm. The wall thickness was shown to vary 0.99-11.24% from the calculated mean at a standard deviation of 5.76%. For the Mk. III phantom over 3 phantoms the wall thickness was found to be 1.3±0.05mm. The wall thickness was shown to vary 1.44-8.00% with a standard deviation of 4.99%. An overview of this data is provided in Table 4. For comparison Doyle et al. (2008) analysed four of their models with an average wall thickness of 2.21±0.8mm with standard deviation ranging between 4.24-11.09%. Burgmann et al. (2009) found there phantom wall thickness to vary between 4-7% from the calculated mean.

Table 4 Overview of variation in wall thickness

Property	Mk. I	Mk. II	Mk. III
Average Wall thickness (mm)	1.31	1.39	1.30
Minimum deviation (%)	1.34	0.99	1.44
Maximum Deviation (%)	8.05	11.24	8.00
Standard Deviation (%)	5.02	5.76	4.99

2.7 External Pressurisation Chamber

When porting the phantom to the flow system it was important to control the transmural pressure across the phantom wall (discussed further in Chapter 6). This was achieved by means of encasing the compliant phantom in an external pressurisation chamber (EPC). The EPC shown in Figure 20 was constructed from PMMA plate. Five sides were permanently fixed with pan-head machine screws and the seams were sealed with RTV to make it water tight. The final surface was removable to allow easy access to the phantom. It was held in place with threaded rod and wing nuts and had an inset o-ring running around the perimeter to create a seal. A header tank was attached to the EPC via a flexible tube and transmural pressure was varied by varying the height of the fluid in the EPC header tank system.

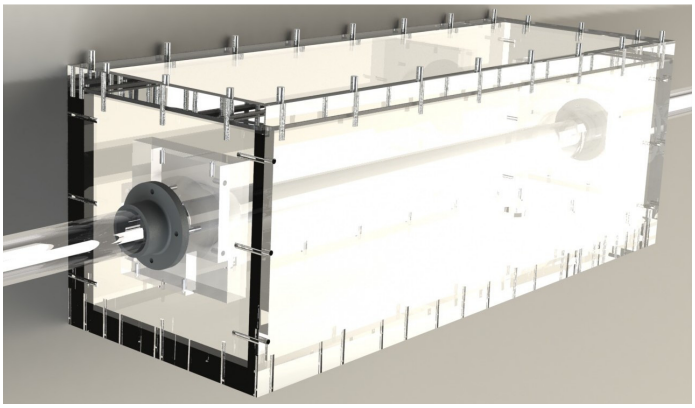

Figure 20 External pressurisation chamber (EPC)

2.8 Conclusions

This section has provided a progressive development of a unique moulding technique for producing thin walled compliant flow phantoms of idealised artery geometries. It provides the necessary formulation to match the in vitro material properties of the flow phantom to the in vivo properties of arteries. It was found to ensure a good connection with a smooth transition between the flow system and the compliant phantom, silicone endplates should be

cast onto the compliant phantom. The final phantom evolution (Mk. III) had an inner radius of 20.22mm and a wall thickness of 1.3±0.05mm. To ensure the final cured phantom was free of bubbles a bottom up silicone injection system should be employed. An external pressurisation chamber was designed to allow for full control of external pressure. It was also designed, along with the PMMA endplates attached to the phantom, to allow for a quick turn around when switching between phantoms. Other methods of phantom construction are available, but it should be noted that the research group that produced a compliant phantom using a rotating hollow cylinder (Burgmann et al. 2009) have since transferred to a core casting technique to produce more complex geometries like stenosis (Pielhop et al. 2012) since the work of this thesis became available (Geoghegan et al. 2010).

3 Particle Image Velocimetry

Particle Image Velocimetry (PIV) is a quantitative laser based optical technique that can be used to obtain non-intrusive, near instantaneous flow field measurements. It provides a velocity field in the region of interest, this can then be used to determine other quantities which require velocity derivatives including vorticity and shear rate. The non-intrusive nature of the technique gives it an advantage over the likes of hot wire anemometry and other probe techniques, as it allows for the production of results that are more faithful to the flow regime. The reason for this is that intrusive techniques like hot wire anemometry require probes to be inserted into the flow regime being studied, which produces an artificial deviation in the flow field. PIV is similar to Particle Tracking Velocimetry (PTV), both methods track particles (seeding) within a fluid flow. The difference between the two methods is that PIV tracks groups of particles within a pre-defined interrogation region (window) and PTV tracks individual particles. Both methods are useful in different scenarios. PTV works best when there is a low seeding density in the fluid system and each particle and its displacement is easily identified. As the fluid structure being analysed becomes more complex the seeding density needs to be increased to give a better resolution of the fluid flow. Identification of individual particles becomes more complex and PIV becomes the method of choice.

Adrian (2005) provides a review of how PIV developed from initial inception to current state of the art. The initial PIV technique (Adrian 1984) was born out of a technique known as laser speckle velocimetry (Meynart 1983) and used one camera to provide two components of velocity in a two dimensional plane (2D2C). The PIV technique shifted from using photographic film to digital cameras most notably in works by Willert and Gharib (1991) and Westerweel (1993). The technique has been developed into a method known as stereoscopic PIV (SPIV) which uses two cameras to provide, three components of velocity in a two

dimensional plane (2D3C) (Willert 1997). It then developed into a technique known as Tomographic PIV (tomoPIV), which uses multiple cameras to obtain three components of velocity in a three dimensional volume (3D3C) (Elsinga et al. 2006).

A basic set up of a planar PIV system providing a 2D2C measurement of a fluid displacement is shown in Figure 21. The basic principle of planar PIV and its general application is; a light sheet produced when a high power laser beam passes through an optical system illuminates seeded particles, which are usually artificially placed in the fluid system. A digital camera captures sequential images in image pairs with a pre-defined time difference (Δt) between the individual images of the image pair. A computer system is then used to analyse the digital images. The image pairs are divided into a grid of interrogation windows and a process known as cross-correlation (section 3.6) is applied to matching windows between the images.

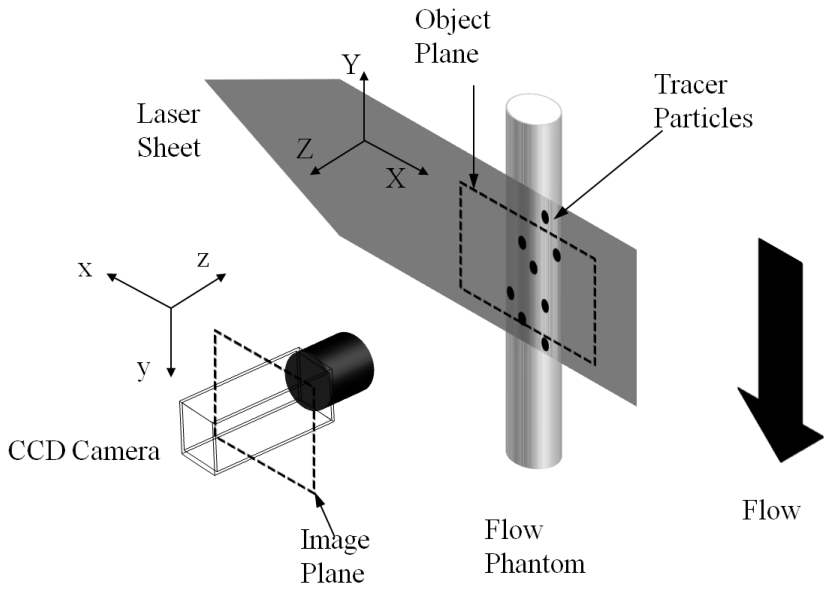

Figure 21 Basic planar PIV set up

Figure 22 graphically shows the cross-correlation process which essentially slides window two over window one until the best match of particle pattern is obtained. The resultant displacement of the window gives the particle displacement for that region in pixels. Using a calibration image to convert pixel size into an object plane measurement, the pixel displacement $\Delta \underline{s}$ can then be easily converted into velocity $\Delta \underline{v}$ using Equation 22.

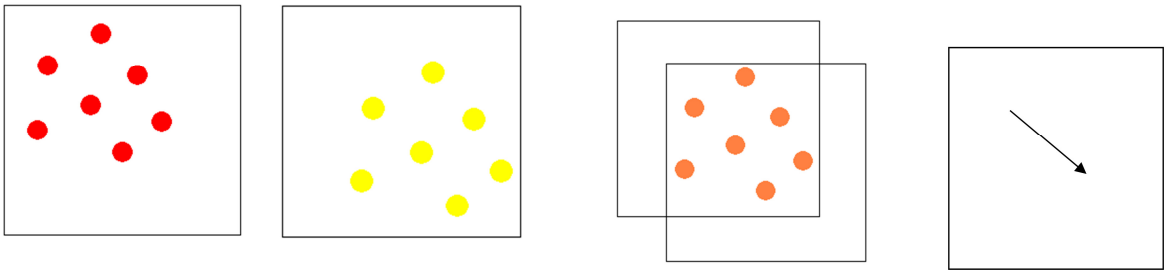

Figure 22 (a) Window image one (b) matching window image two (c) particle pattern matching (d) resultant vector

$$\underline{U} = \lim_{\Delta t \to 0} \frac{\Delta \underline{s}}{\Delta t} \qquad \textbf{Equation 22}$$

As mentioned previously, the setup in Figure 21 provides only a two dimensional representation of the fluid flow. This method of analysis is perfectly applicable for a flow regime with very little out of plane displacement, for example a laminar steady flow through a straight cylinder; however this is not the case for a vast amount of different fluid flow problems. SPIV can be used to obtain 2D3C measurements of a fluid displacement. This method will be outlined in greater detail in Section 3.8.

There is a large amount of literature that discusses PIV (Raffel et al. 2007; Stanislas and Monnier 1997; Westerweel 1997) and SPIV (Wieneke 2005; Prasad 2000; Willert 1997; Soloff et al. 1997) theory and the experimental apparatus required for its application. With the basis of this thesis being on the application of the process rather than the theoretical advancement of the experimental process this chapter will provide a brief explanation of the theoretical background only. The experimental work implemented in this thesis is an extension of previous and concurrent work by Buchmann (2010) and Spence (2011).

3.1 Tracer Particles

The difference between flow visualization and PIV is that seeding is introduced inhomogeneously in flow visualization to make flow structures visible. PIV requires a homogenous distribution of seeding to allow for analysis of a full flow field (Westerweel 1997). When performing PIV it is the velocity of the seeding that is measured. Therefore the relationship between the fluid and the tracer velocity has to be fully understood so the accuracy of the experiment can be verified and errors quantified. The ideal particles will exactly follow the fluid motion without interacting with each other and altering the flow or

properties of the fluid (Westerweel 1997). A compromise for particle size is required between this and a high signal-to-noise ratio (SNR) of the scattered light (Melling 1997).

3.1.1 Particle Fluid Interaction

Raffel et al. (2007) show that the velocity lag $\underline{U_s}$ of a particle in a continuous accelerating fluid can be calculated by

$$\underline{U_s} = \underline{U_p} - \underline{U} = D_p^2 \frac{(\rho_p - \rho)}{18\mu} \underline{a} \qquad \textbf{Equation 23}$$

$\underline{U_p}$, D_p and ρ_p are the particle velocity, diameter and density respectively. $\underline{U}$, $\underline{a}$, ρ, μ are the fluid local velocity, acceleration, density and dynamic viscosity respectively. For this thesis in which the experimentation is predominantly based on time varying flow rates, it is important to understand the response of a particle to an acceleration of the fluid. A good marker for this is the relaxation time τ_s, which is the measure of the particle to obtain velocity equilibrium with the fluid.

$$\tau_s = D_p^2 \frac{\rho_p}{18\mu} \qquad \textbf{Equation 24}$$

A final factor to consider, especially for complex flow systems, is the response to centrifugal forces occurring from fluid rotation. The force experienced by a particle in a rotating fluid is the pressure gradient normal to the fluid stream lines which can be calculated by

$$\frac{\partial p}{\partial r} = \rho \frac{U_\theta^2}{r} \qquad \textbf{Equation 25}$$

U_θ is the tangential velocity and r is the radius to the centre of rotation. To keep a particle on a circular path around the centre of rotation the pressure gradient needs to match the radial acceleration of the particle multiplied by the mass (Equation 26), if not the particle will accelerate radially, which will occur if $\rho_p \neq \rho$ or D_p is large.

$$\frac{\pi \rho_p D_p^3}{6} \frac{U_\theta^2}{r} \qquad \textbf{Equation 26}$$

From this section it can be seen the ideal particle would be neutrally buoyant i.e. $\rho_p = \rho$. For gas flows this can't be achieved and presents a large challenge in the PIV process (Raffel et al. 2007; Melling 1997). For experimental analysis using liquid flow it is much easier to

obtain near neutral buoyancy so errors due to tracer particles are greatly reduced. Table 5 presents an overview of several seeding particles available. The Sphericel 110P18 hollow glass spheres were finally selected due to their good match in density to the working fluid (1.14g/cm^3) and their favourable cost compared to other choices.

Table 5 Overview of tracer particles considered for use in experiments. Table adapted from Spence (2011).

Tracer Particles	Diameter (μm)	Density (g/cm^3)	Reference
Sphericel 110P18	16.2	1.1	Potter Industries Inc., http://www.pottersbeads.com/
Polyamide	5, 20, 50	1.03	
Silver-coated hollow glass spheres	10	1.4	Dantec Dynamics, http://www.dantecdynamics.com
Fluorescent polymer	10, 30, 75	1.5	

3.1.2 Particle Optical Properties

The scattering of light from particles that have a D_p which is larger than the laser light wavelength (λ) are subject to Mie's scattering theory which essentially states that most the light is scattered in the forward and backward direction as shown in Figure 23.

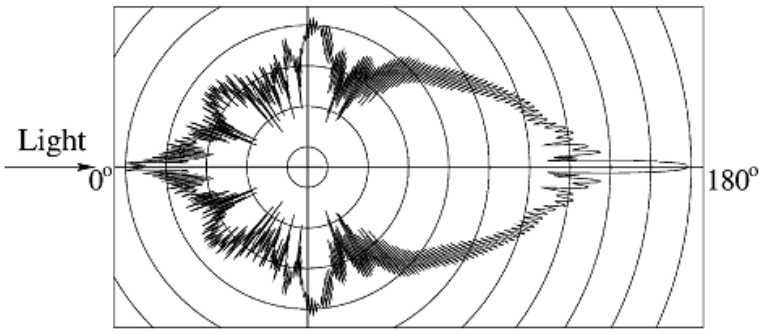

Figure 23 Light scattering by a 10 μm glass particle in water. Figure adapted from Raffel et al. (2007).

This is a logarithmic scale plot with neighbouring contours differing by a factor of 100 in intensity. Ideally planar PIV analysis would be performed in forward scatter, but due to the depth of field available a 90º viewing angle is most commonly used. An important parameter to consider is the scattering efficiency, which is the ratio of the refractive index (n) (Appendix A – Refractive Index) of the particles to that of the fluid. This means that the scattering of light in water is far weaker than in air. To counteract this effect particle size can be increased. With the particle to fluid density ratio being small for liquid flows, increasing

particle size still satisfies the inequalities in section 3.1.1. It is also possible to use metallic coated particles in liquid flows, which increases the refractive index ratio.

3.2 Laser

For PIV experimentation the common method of illumination is a laser as they have the ability to emit a high energy density monochromatic light which can be easily manipulated to produce a light sheet without chromatic aberrations (Raffel et al. 2007). The laser used for the majority of this research was a dual cavity Nd:YAG (Neodymium-doped Yttrium Aluminium Garnet, Nd:$Y_3Al_5O_{12}$ is the crystal used as the lasing medium) New wave solo 120XT (specifications in Table 6). It is a pulsed laser using a Q-switch to produce a bright, short, light pulse. The Q-switch gives accurate control of the timing of the laser pulse, which removes the need for the use of a mechanical shutter on the camera and can be controlled externally to allow synchronization with the experimental system. The laser has a fundamental wavelength of 1064nm which is in the infra-red spectrum and invisible to the human eye. The beam has to be passed through a frequency doubler to produce visible (green) light with a wavelength of 532nm. The laser is dual cavity which means it has two light sources that are aligned to exit the laser through the same point and have individual Q-switch controls. The light intensity from both lasers was relatively constant when the lasers warmed up to operating temperature. There was a difference in light intensity between cavities and this had to be accounted for when analysing the results obtained.

Table 6 PIV laser specifications

Specifications	New Wave Solo 120XT
Lasing medium	Nd:YAG
Wavelength (nm)	532
Repetition rate per cavity (Hz)	1 – 15
Maximum pulse energy (mJ)	120
Pulse width (ns)	3 – 5
Energy stability (±%)	4
Beam diameter at laser output (mm)	5
Divergency (mrad)	3

3.2.1 Laser optics

Two optical systems were used for PIV analysis. The first used a combination of adjustable lenses mounted to a lens rail to provide the light sheet required for PIV. Two convex lenses

in a Keplerian arrangement were used to reduce the laser beam from a thickness of 5mm to 0.5mm. It is noted that a focal point occurs, but ionization is avoided by enclosing the beam and protecting it from dust particles. A plano-concave lens is then used to diverge the beam into a laser light sheet. The arrangement can be seen in Figure 24. Uncoated lens surfaces exposed to air produce a slight loss due to refraction of the order of 4% per surface, which can be accepted for most cases in PIV (Raffel et al. 2007).

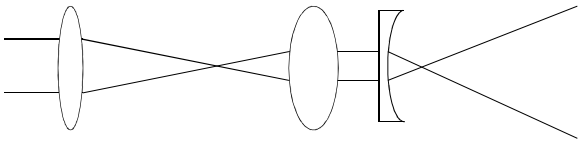

Figure 24 Adjustable optical lens set up

The second set up is a commercial set up provided by Dantec Dynamics. From the laser source an articulated arm with angled mirrors allows for free movement of the laser beam, reducing alignment time between laser and optics and increasing safety from beam exposure. At the end of the arm a light sheet rig containing a base module[5], large angle module[6] and light-sheet thickness adjuster[7] produced the required light sheet for PIV analysis.

3.3 LED Illumination

Two major drawbacks to laser illumination for use with PIV is firstly the danger involved using high powered lasers, with the requirement of safety goggles being worn when the laser is running at full power. The second is cost, with low repetition rate double pulsed lasers costing in the region of $US 50 000. High-power Light emitting diodes (LED's) have become rapidly available due to recent developments in solid-state illumination (Buchmann et al. 2012). Willert et al. (2010) investigated the applicability of using LED illumination as an alternative to laser-based illumination for planar PIV experimentation in mediums of both air and water. Buchmann et al. (2012) further investigated this technique for the application with Tomographic PIV. The uncollimated light of LED's is less dangerous than a laser setup (Willert et al. 2010) and can be operated without the need for goggles. The combined set up of the LED light source driver unit components and fibre optics for high speed imaging costs

[5] Dantec Dynamics 80X74 Base module house a plano-concave lens

[6] Dantec Dynamics 80X75 large angle module contains a plano-concave lens

[7] Dantec Dynamics 80X71 light-sheet thickness adjuster is a Galilean like beam expander or compressor depending on orientation

in the region of 500 Euro (~$US 650) (Willert et al. 2010). This new LED illumination method is applied in Chapter 8 of this work which also provides a full explanation of the system and its operation.

3.4 Camera

Dantec flow sense 2M cameras were used for the bulk of the work in this thesis with the specifications found in Table 7.

Table 7 PIV camera specifications

Specifications	Dantec Flow Sense 2M
Sensor type	CCD progressive scan monochrome
Sensing area (mm)	11.8 × 8.9
Cell size (μm)	7.4 × 7.4
Effective pixels	1608 × 1208
Maximum frame rate (frames/sec)	17.17
Output quantization (bit)	8 or 10
Frame separation (μs)	1.5

They are digital cameras with a charged couple device (CCD) array which contains a large amount of CCD elements known as pixels that convert light into electric charge (Raffel et al. 2007). The camera was fitted with a Nikon AF Micro-Nikkor lens with specifications shown in Table 8. The cameras can capture two images (pair) in quick succession at a rate of 17.17 Hz. The fastest rate possible between images in a pair was restricted by the time it takes for the first image to transfer from the array of photodiodes to the CCD array, which is known as the transfer pulse width (TPW) and for the Dantec cameras is 1.5 μs.

Table 8 PIV lens specifications

Specifications	Nikon AF Micro-Nikkor 60mm f/2.8D
Focal length (mm)	60
f-number[8]	2.8 - 32

A BNC 565 pulse/delay generator was used to synchronize the cameras and laser via TTL (transistor-transformer logic) signals. The Q-switch has a delay (QSD) of 182 μs between laser triggering and the time of fire and is a fixed characteristic due to the laser charge time. The camera has a delay of 4 μs from its trigger point so the trigger for the first exposure is

[8] A small f-number is equivalent to a large lens aperture

offset from the laser to make the pulse occur in the centre of the exposure. The second camera exposure occurs after the TPW and continues until it receives a new signal. The second image in the pairs location in time is controlled by the time delay (Δt) selected for Equation 22. The schematic of the setup is shown in Figure 25.

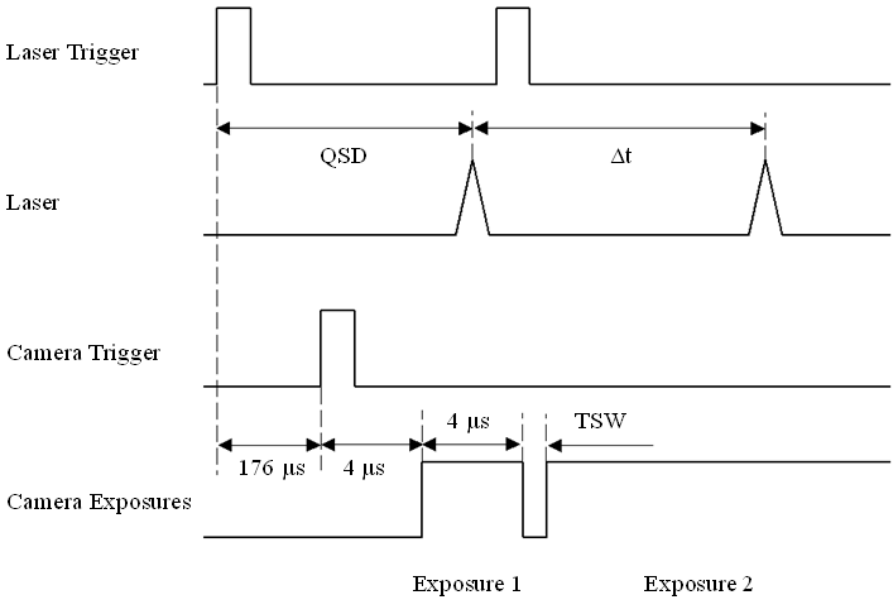

Figure 25 Camera and laser synchronization schematic

3.5 Imaging of Particles

An important practical factor of optical imaging to consider when performing PIV is diffraction limited imaging. Diffraction in a lens is essentially the limiting factor of an optical system's ability to resolve detail. In the next section a brief outline of the theory will be presented; a full explanation of this effect is discussed by Raffel et al. (2007) and Stanislas and Monnier (1997).

With a perfectly aberration free lens in a PIV camera set up, a seeded particle in the fluid flow does not appear as a point source in the image, but will form a Fraunhofer diffraction pattern, A circular pattern (Airy disk) with surrounding rings (Airy rings) is obtained. The Airy function represents the point spread function (PSF), which is essentially the quantification of the amount of blur (spread) of a point light caused by all physical optical

systems and is determined by the quality of the optical components (Gonzalez and Woods 2009). The Airy function is equivalent to the square of the Bessel function and can be used to calculate the size of the Airy disk with the first zero of the function representing the size of the disk.

The smallest particle image that can be obtained with an imaging system is limited by the size of the diameter of the Airy disk (diffraction limiting diameter) D_{diff}. Raffel et al. (2007) show that D_{diff} can be calculated as follows

$$D_{diff} = 2.44(M + 1)f_{\#}\lambda \qquad \textbf{Equation 27}$$

Where M is the magnification factor of the lens and $f_{\#}$ the f-number of the lens, which is the ratio of the focal length to the aperture diameter and λ the wavelength of the light source used.

As imaged particle size increases (magnification or particle diameter increase) geometric imaging dominates the PSF to predict the particle image size and Equation 28 is used

$$D_{\tau} = \sqrt{\left(Md_p\right)^2 + d_{diff}^2} \qquad \textbf{Equation 28}$$

3.6 Cross-Correlation

This section provides a brief overview of the essential aspects required to understand the cross-correlation process and how it is applied to the experimental work in this thesis. Raffel et al. (2007) and Westerweel (1997) provide the basis for this section and a more in-depth explanation of the cross-correlation application can be found in their work. The cross-correlation algorithm used was implemented by Buchmann (2010) using MATLAB[9].

3.6.1 Background

As stated previously to perform a cross-correlation the image pairs need to be discretized into a grid of interrogation windows with the correlation being performed on each window pair. Mathematically the image of a particle can be described as the convolution of the geometric image and the PSF. The image intensity field of the first exposure is then given by

[9] MATLAB, MathWorks® Inc.

$$I(\underline{x},\underline{\Gamma}) = \tau(\underline{x}) * \sum_{i=1}^{N} V_0\left(\underline{X_i}\right)\delta\left(\underline{x} - \underline{x_i}\right) \quad \textbf{Equation 29}$$

Where $\underline{\Gamma}$ describes the location of the ensemble of particles at a given time in the interrogation window, the vectors $\underline{x}$ and $\underline{X}$ give locations of the particles with the co-ordinate system corresponding to Figure 21. They are related by Equation 30.

$$\underline{X_i} = \frac{x_i}{M} \quad \textbf{Equation 30}$$

N is the number of tracer particles in the image, $\tau(\underline{x})$ is the PSF assumed to have a Gaussian shape, $\delta\left(\underline{x} - \underline{x_i}\right)$ describes the geometric part with a Dirac delta-function shifted to location $\underline{x_i}$ and $V_0\left(\underline{X_i}\right)$ is a transfer function that gives the light energy of the image of the i'th particle inside the interrogation volume in the object plane and its conversion into an electronic signal. The definition of the Dirac delta-function is

$$\tau\left(\underline{x} - \underline{x_i}\right) = \tau(\underline{x}) * \delta\left(\underline{x} - \underline{x_i}\right) \quad \textbf{Equation 31}$$

Therefore Equation 29 can be rewritten as

$$I(\underline{x},\underline{\Gamma}) = \sum_{i=1}^{N} V_0\left(\underline{X_i}\right)\tau\left(\underline{x} - \underline{x_i}\right) \quad \textbf{Equation 32}$$

If it is then assumed that all particles in the object plane move with a constant displacement $\underline{D}$, with a particle displacement of $\underline{d}$ in the image plane, the image intensity field of the second exposure can be written as

$$I'(\underline{x},\underline{\Gamma}) = \sum_{j=1}^{N} V_0{}'\left(\underline{X_j} + \underline{D}\right)\tau\left(\underline{x} - \underline{x_i} - \underline{d}\right) \quad \textbf{Equation 33}$$

$V_0{}'$ is the interrogation volume in exposure two. The cross-correlation of the two interrogation windows can be written as

$$R_{II}(\underline{s},\underline{\Gamma},\underline{\mathrm{D}}) = \frac{1}{W}\sum_{i,j} V_0\left(\underline{X_i}\right)V_0\left(\underline{X_j} + \underline{D}\right)\int_W \tau\left(\underline{x} - \underline{x_i}\right)\tau\left(\underline{x} - \underline{x_i} + \underline{s} - \underline{d}\right) \quad \textbf{Equation 34}$$

$\underline{s}$ is the separation vector in the correlation plane and W is the interrogation area. If the terms representing the correlation of particle images with themselves (i = j) are separated from the terms that represent the correlation of a particle image with a different particle image (i ≠ j); Equation 34 can be represented by

$$R_{II}(\underline{s},\underline{\Gamma},\underline{\mathrm{D}}) = R_C(\underline{s},\underline{\Gamma},\underline{\mathrm{D}}) + R_F(\underline{s},\underline{\Gamma},\underline{\mathrm{D}}) + R_D(\underline{s},\underline{\Gamma},\underline{\mathrm{D}}) \quad \textbf{Equation 35}$$

$R_C(\underline{s},\underline{\Gamma},\underline{\mathrm{D}})$ represents the convolution of the mean intensities and $R_F(\underline{s},\underline{\Gamma},\underline{\mathrm{D}})$ is a fluctuating noise component, both these components relate to i ≠ j. The important term for cross-correlation analysis is $R_D(\underline{s},\underline{\Gamma},\underline{\mathrm{D}})$, which represents the convolution of matching particle pairs between exposure one and two (i = j) and is expressed as

$$R_D(\underline{s},\underline{\Gamma},\underline{\mathrm{D}}) = R_\tau(\underline{s} - \underline{d})\sum_{i=1}^{N} V_0\left(\underline{X_i}\right)V_0\left(\underline{X_j} + \underline{D}\right) \quad \textbf{Equation 36}$$

Raffel et al. (2007) give a full explanation of the term $R_\tau(\underline{s} - \underline{d})$ Which is the correlation of a particle image, the final result for the correlation function in Equation 35 gives a maximum value at $\underline{s} = \underline{d}$.

3.6.2 Application

To practically apply the cross-correlation algorithm to recorded images they firstly have to be split up into a uniform grid of interrogation windows. To optimize the results some criteria should be adhered to (Scarano 2002).

1. Each window requires a minimum number of particles present (≥15 for a valid vector detection of at least 90% (Keane and Adrian 1990))

2. With w representing the interrogation window size, the maximum velocity gradient is given by

$$\left|\frac{\partial u}{\partial x}\right| \Delta t < \frac{d_p}{w}$$

3. To limit the loss of pairs due to in plane motion the one quarter rule is applied, where the maximum displacement of particles between image pairs is kept to ¼ of the interrogation window size (one quarter rule)

Once window size and time delay is selected (typically sizing's of 32 × 32 and 64 × 64 pix^2) the light intensity distribution of each pixel in an interrogation window is cross-correlated between image exposures. A spatially discrete cross–correlation function with an interrogation window size of N × M pix^2 is given by Raffel et al. (2007) as

$$R_{II}(x,y) = \sum_{i=1}^{N}\sum_{j=1}^{M} I(i,j)\, I'(i+x, j+y) \qquad \textbf{Equation 37}$$

I and I' are the intensity values from exposure one and exposure two respectively. The cross-correlation algorithm used in this thesis (Buchmann 2010) employed a normalised cross-correlation (Raffel et al. 2007; Westerweel 1997).

$$R_{II}(x,y) = \frac{\sum_{i=1}^{N}\sum_{j=1}^{M}\left(I(i,j)-\overline{I}\right)\left(I'(i+x,j+y)-\overline{I'}\right)}{\sqrt{\sum_{i=1}^{N}\sum_{j=1}^{M}\left(I(i,j)-\overline{I}\right)^2}\sqrt{\sum_{i=1}^{N}\sum_{j=1}^{M}\left(I'(i,j)-\overline{I'}\right)^2}} \qquad \textbf{Equation 38}$$

$\overline{I}$and $\overline{I'}$ are the mean intensities from exposures one and two respectively and are subtracted to eliminate the R_C and R_F terms (Westerweel 1997). Normalizing the cross-correlation sets the magnitude of the results to be in the range of 0 to 1. The result of the cross-correlation is a correlation map as seen in Figure 26. The largest value obtained from the cross-correlation represents the closest match of particles between the two exposures. The particle displacement vector is calculated as the displacement between the correlation peak and the centre of the interrogation window.

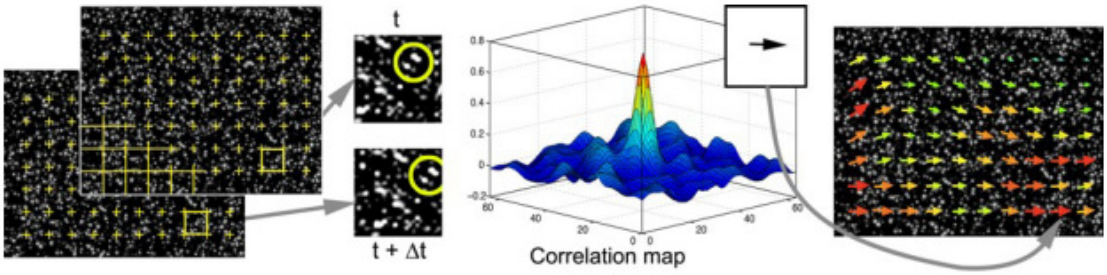

Figure 26 Schematic of the cross-correlation procedure. Figure adapted from Spence (2011).

Using the direct correlation function (Equation 38) can be a very time consuming process. To reduce the processing time the correlation theorem can be used where the cross-correlation of two functions is equivalent to the complex conjugate multiplication of the Fourier Transforms (Raffel et al. 2007). In programming the fastest way to compute the discrete correlation function is using the Fast Fourier Transform (FFT) and the calculation becomes

$$I(i,j) \otimes I'(i,j) \Leftrightarrow FFT^{-1}[FFT(I) \times (FFT(I)')^*] \qquad \textbf{Equation 39}$$

Where $\otimes$ represents the correlation function, * indicates the complex conjugate and $\times$ is the piecewise multiplication of the frequency components.

It can be seen above that the correlation function is evaluated at discrete locations i,j representing the pixels of the CCD chip which means displacement results will be biased towards integer values with an accuracy of ± 0.5 pixel. This can be improved by approximating the sub-pixel location of the correlation peak by using an interpolation function that takes into account the neighbouring peaks (Westerweel 1997). There are several methods available for sub-pixel analysis, the one implemented by Buchmann (2010) in this correlation algorithm is a two-dimensional Gaussian interpolation function (Raffel et al. 2007).

3.6.2.1 Peak Locking

An error that can occur when particle size becomes very small (~<2 pixels) is known as peak locking. With such a small size there is not enough information available on the shape of the particle. This means the displacement is biased towards integer values even after sub-pixel analysis. This is one of the most significant error biases in digital PIV and has to be taken into careful consideration. Mitigation of the problem can be applied by correctly imaging

particles when performing experimentation. Pre-processing of images (section 3.7) can also be applied to optimize particles before cross-correlation is implemented. The Gaussian interpolation function is the current method that is accepted to have the lowest peak locking effect (Raffel et al. 2007)

3.6.2.2 Vector validation

A wild vector that occurs due to a failure in the cross-correlation algorithm (Figure 27) can occur due to a multitude of reasons including, low seeding density in a localized region, high image noise, CCD noise and high velocity gradients.

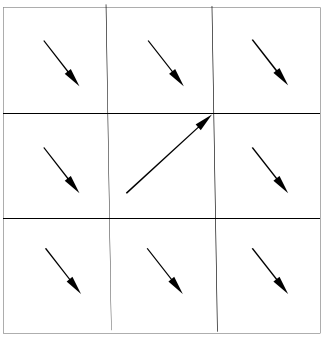

Figure 27 depiction of a wild vector

Visually it is quite simple to locate these wild vectors, but the process is much harder to program. In this work, to obtain a good confidence in the results output from the correlation function, a combination of techniques is used to detect and remove these wild vectors. A modified version of a technique discussed by Keane and Adrian (1990) is implemented where a vector is valid if it exceeds a pre-set value of the ratio of the correlation peak to the mean correlation value. This known as the signal-to-mean ratio (SMR) and is set with a typical value between 1.5 and 2.

$$SMR = \frac{max\left(R_{II}(x,y)\right)}{\frac{1}{W}\int_W R_{II}(x,y)} \qquad \textbf{Equation 40}$$

It differs from the method of Keane and Adrian (1990) where the ratio is between the highest and second highest peak as in this work a second peak may not always be present.

The SMR detection technique will not always capture all the erroneous vectors produced in the cross-correlation especially in areas of low SNR. The normalised median test (NMT) developed by Westerweel and Scarano (2005) is defined by

$$r_0 = \frac{|U_0 - U_m|}{r_m + \varepsilon} \qquad \textbf{Equation 41}$$

For a displacement vector U_0 in the centre of a 3x3 grid, with U_m representing the median of the surrounding 8 vectors U_1 to U_8, r_0 is the normalised displacement residual, r_m the median of the displacement residual r_i=| U_i-U_m| and ε is an acceptable fluctuation level from cross-correlation noise (~0.1 pixels). Threshold values for the NMT usually lie between 2 and 3. Once an invalid vector was located it was removed and replaced. This is performed using a linear interpolation technique (Westerweel 1994).

Other methods of invalid vector detection are available including a method proposed by (Green et al. 2000) where a forward window is slightly offset from the original window in the direction of the vector and a reverse window placed on the same path in the reverse direction. Cross correlation is then performed on the new windows and compared with the original. If a vector is invalid the offset windows will produce a different result and can be used to adjust the original. This method could be implemented in future codes to increase the validity of results, but is noted that it would increase processing time 3 fold.

3.6.2.3 Window Refinement

Several methods of refinement can be introduced after the cross correlation has been performed. A multi-grid window shifting technique was employed in the PIV code implemented in this work (Raffel et al. 2007; Scarano and Riethmuller 2000; Westerweel et al. 1997) which is depicted in Figure 28 and Figure 29. The basic method starts by doing a first pass of the image pair with the window sizes set adhering to the one quarter rule. The resultant displacement is then used as a predictor to offset the window position. The window size is then halved and interrogation is then performed on the reduced window size which will yield an increase match in particles between image pairs and an increased spatial resolution.

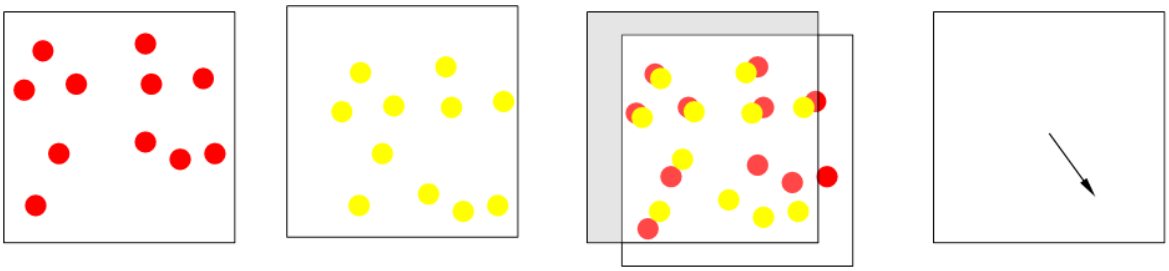

Figure 28 (a) Window image 1 (b) window image 2 (c) closest pattern match (d) resultant vector

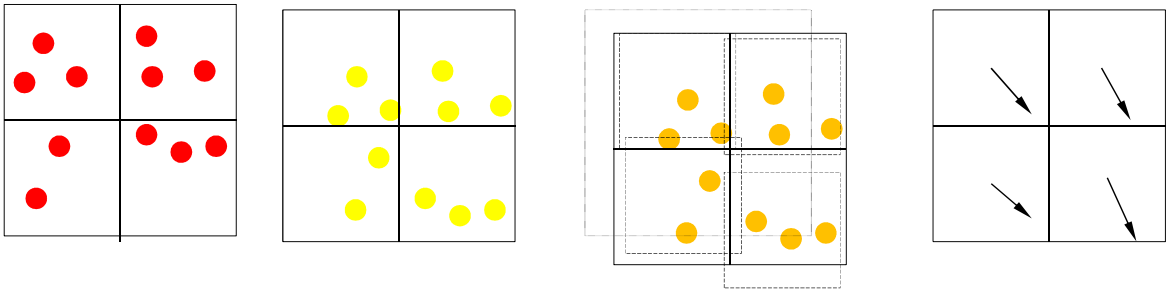

Figure 29 (a) Window image 1 refinement (b) window image 2 refinement (c) window one shifted by closest pattern match vector and refined grid matched (d) resultant vectors

This method enables the application of window sizes smaller than the particle image displacement (Raffel et al. 2007) and means progressive iterations of this refinement aren't limited by the one quarter rule.

The dynamic spatial range (DSR), a limiting factor in window sizing, is the ratio of the largest observable length scale to the smallest observable length scale (usually the window size). In this case it's the maximum measureable velocity to the minimum resolvable velocity (Raffel et al. 2007). Using this refinement the DSR and spatial resolution are decoupled meaning the DSR can be increased. Window sizing can be reduced until ~15 particles are contained within the window. At the final window size a second iteration is completed increasing the SNR approaching the displacement bias to zero (Scarano and Riethmuller 2000). In flow domains with a high dynamic range in displacement, like a stenosis, the multi-grid window shifting technique can improve the fidelity of results markedly.

3.6.2.4 Window Distortion

The PIV method discussed up until now has assumed an approximate uniform motion of the tracer particles in the interrogation window and has been operated on an interrogation window of a regular geometric shape that match between images in a pair. In practical cases this assumption rarely holds true, with the velocity field varying over an interrogation

window. If the displacement calculated is under 3% of the window size (i.e. for a 64 × 64 pix^2 window, the displacement is less than 1.92pix (3%)) the effect on the results can be classed as negligible (yielding 95% valid vectors) (Keane and Adrian 1992). As velocity gradient increases the cross-correlation peak broadens and can split into multiple peaks (Westerweel 2008). This is important when analysing data in high sheared flows occurring in vortices, turbulence and boundary layers. This makes velocity gradients a big problem when analysing a fluid structure like a stenosed artery.

In this work the iterative window distortion technique discussed in detail by several authors (Raffel et al. 2007; Scarano 2002; Keane and Adrian 1990) is employed to reduce the effect of velocity gradients. Figure 30 shows a schematic of the second window distorted to contain all the particles in frame one. The shape of the distorted second window is calculated from the velocity gradient across the interrogation window obtained from a first pass displacement predictor field. To cross-correlate between the two windows they need to be of equal shape and size. Therefore the distorted field is remapped to the original dimension and cross-correlation is performed.

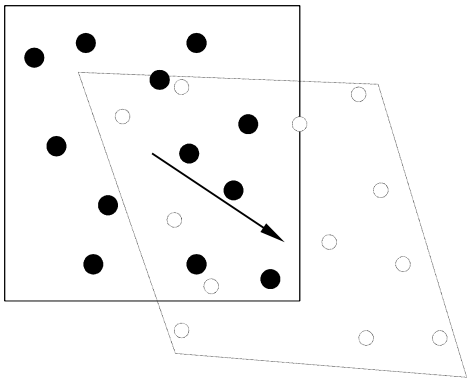

Figure 30 Basic principle of the window distortion technique

3.6.2.5 Ensemble Correlation Averaging

For some sections of this work an averaging process known as ensemble averaging was applied to the results. The purpose of creating averaged results was that certain experimental conditions were unable to produce a good pixel per window ratio and can have a poor SNR. This means that the correlation peak could be weak and hard to distinguish from the surrounding erroneous peaks, increasing the percentage of invalid vectors obtained. Ensemble correlation averaging averaged the coincident correlation planes from a sequence

of images (Raffel et al. 2007). As noise is usually random the correlation peak representing the displacement is amplified to produce a valid vector.

Other averaging methods that can be used to improve results are image averaging where first and second image exposures are averaged and correlated and velocity field averaging where the image pairs are processed and the velocity fields are averaged between image pairs. Raffel et al. (2007) compared averaging techniques on a known test result with increasing image pairs. For a data set containing 8 pairs and above an average correlation produced less than 0.5-1% invalid vectors. Image averaging produced 5% after 4 image pairs which increased with increased image pairs used due correlation between non-paired particles and vector averaging achieved a best value of 125 invalid vectors after 2 pairs then increased. Buchmann (2010) produced a similar analysis with a different test case ensemble averaging again produced less than 1% invalid vectors. Vector averaging this time out performed image averaging, but could only achieve 13% invalid vectors.

It should be noted that the drawback to averaged results is that unsteadiness in the flow cannot be analysed requiring single image pair 'instantaneous' results for turbulence and RMS analysis. Phase averaging can be used for analysing cyclic phenomena, but not turbulence. This will be explained further in the relevant chapters (Chapter 5, 7 and 8).

3.6.2.6 Synthetic Results

To validate the cross-correlation algorithm implemented in this work, synthetic images with known displacement properties were produced and analysed. Images with particles of 2mm diameters and 1/32 particles per pixel, 10% background noise and a moderate velocity gradient of 0.05-0.15 pixel/pixel were generated. These images were interrogated at a window size of 32×32 pixel^2 with discrete window shifting giving the expected total measurement uncertainty at approximately 0.05-0.1 pixel (Buchmann 2010).

3.7 Image Pre-Processing

Image pre-processing techniques can be used to improve the SNR before cross-correlation is performed on an image pair increasing the likelihood of obtaining a valid vector. This does not replace the need to take the best images possible with every care needing to be taken when producing optically transparent models, matching refractive index, focusing cameras and so on. Even with every care taken some imperfections in the images are unavoidable

which include variations in laser cavity strength, trapped air bubbles in the flow (often found trapped in the low flow region behind a stenosis), background illumination, dust particles within the silicone phantom and laser reflections from model surfaces. Pre-processing methods developed in previous work (Raffel et al. 2007; Honkanen and Nobach 2005; Stitou and Riethmuller 2001; Westerweel 1993) which include background subtraction, image intensity stretching, thresholding and low or high pass filtering have been implemented in this work, with modifications made to suit the experimental constraints of work produced for this thesis.

3.7.1 Background Subtraction

For steady flow analysis and rigid phantom analysis the background subtraction method used is similar to that of Buchmann (2010) and Spence (2011). Wereley et al. (2002) proposes the use of a time average image subtraction where an average intensity image is created from all images in the acquisition sequence over a large set of images (>100). This creates a background image as it is assumed due to tracer particles being distributed uniformly, their intensity diminished by averaging and moving quickly through the plane they do not appear in the background image. The background image is then subtracted from each image frame to leave the particles only. It is found though that the average background image still contains a large amount of particle images which results in practice to a loss of usable particles. Wereley et al. (2002) also proposes the use of a minimum background subtraction method where the minimum pixel intensities for the data acquisition set are used to create the background image. This however can underestimate the background noise within the particle images and fail to remove erroneous data.

The background subtraction method employed was first presented by Stitou and Riethmuller (2001) and should be referred to for a full explanation. In summary a local threshold technique separates the image intensity into a mean (first component) and the dispersion of the noise intensity around the mean value (second component).

$$T(x,y) = I_0^*(x,y) + rms\big(I(x,y)\big)k \qquad \textbf{Equation 42}$$

Where T is the local threshold, I_0 is the background model, * represents the mean value, I is the variation of the image intensity within the data set and k is a parameter that is set so that a pixel with an intensity that is higher than the local threshold is highly unlikely to be noise.

Therefore any pixel that is above the threshold value is classed as signal. The value for k can vary between experiments and should be set accordingly. It must also be noted that background subtraction is performed separately for image 1 and image 2 of the image pairs as there is slight variation in light intensity due to length of exposure and laser cavity strength.

For a time varying flow wave within a flexible structure creating a background image from an entire data set will result in a reduced SNR increase compared to a rigid phantom. It can be seen from Figure 31 that the variable boundary of the phantom wall will cause a false background image to be created for all cases as the average image combines all boundary positions of the flow cycle leaving 'ghost images' within the background image.

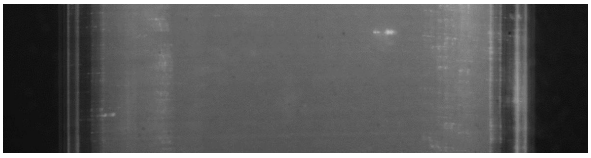

Figure 31 Average Background image over whole data set

The image pairs from a time varying flow cycle has to be separated into matching time steps over the flow cycle before a background image can be calculated. Once the data set is separated into matching time steps the background subtraction can be performed as previously discussed producing individual background images for each time step (Figure 32).

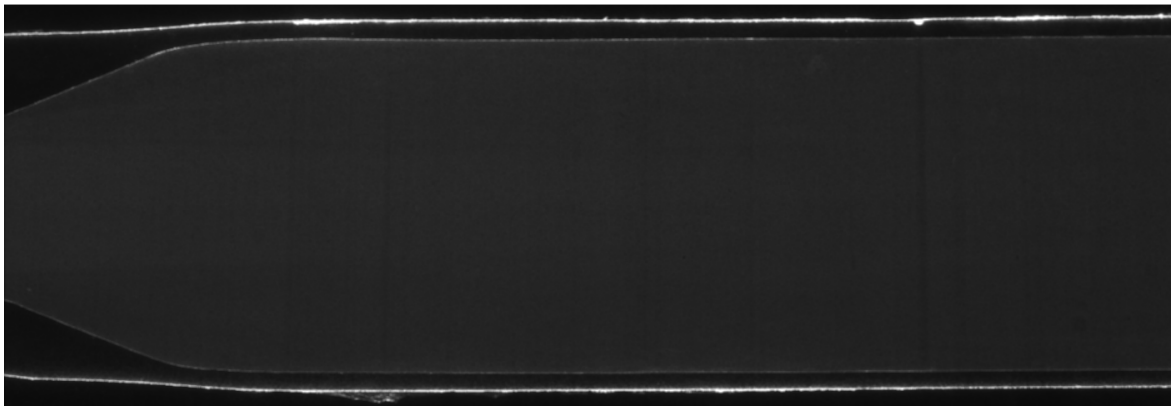

Figure 32 Example of the final background image used for subtraction from the individual image frames

3.7.2 Image intensity stretching and smoothing

Wall reflections can cause large intensity spikes, to preserve a camera CCD chip the camera aperture settings were restricted by these high intensity spikes. Wall reflections were

removed by background subtraction, but the intensity of the reflections was higher than most particles that were imaged. Following background subtraction dynamic histogram stretching was employed on each image pair. The histograms of each image pair were stretched at the lower and upper limits to the minimum and maximum intensity values (0 and 255). For example a setting of 5% and 95% meant every pixel in the first 5% was set to an intensity of 0 and in the last 5% set to an intensity of 255. This increased the SNR ratio by increasing the intensity of particles and reducing the intensity of the background noise. The final pre-processed image is shown in Figure 33.

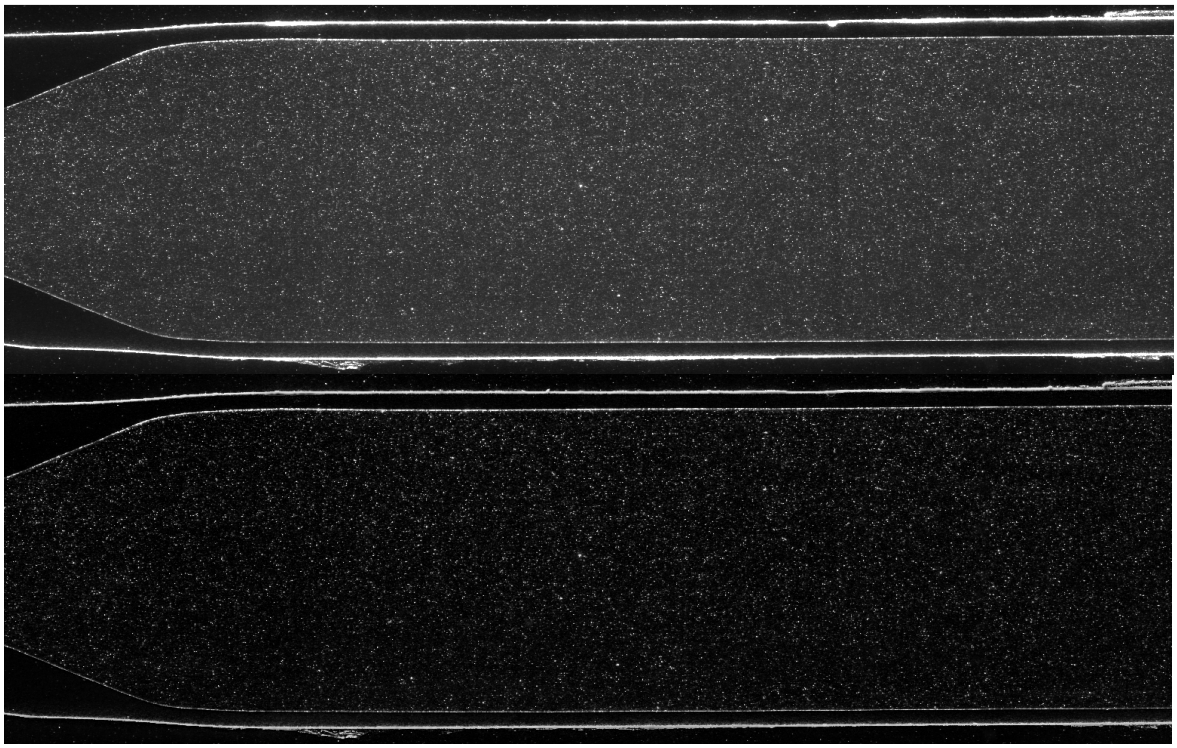

Figure 33 Example image (top) before pre-processing and after (bottom) pre-processing is applied

An image filter can then be applied to 'smooth' the particle images in certain circumstances where cross-correlation is difficult to achieve (Section 8.2). A Gaussian filter kernel (typically 3x3 or 5x5 pixel^2 in size) was passed over final images which is a low pass filter that removed high frequency noise like CCD noise. It can also improve the sub-pixel fitting and peak-locking by widening the correlation peak giving an improved sub-pixel peak fitting.

3.7.3 Masking

The final pre-processing technique employed in this work was image masking where a binary image of flow region was created and imposed a zero flow condition at the fluid wall interface and all external regions in the acquired image. For rigid phantoms a CT scan of the flow phantom was obtained with cross-sections at the image planes extracted using the visualization software Paraview[10] and aligned with maximum images. Masks are then created from the cross-section images using Adobe Photoshop[11]. For stereoPIV (Section 3.8) these images can be warped into the image plane for each camera using the calibration coefficients.

For compliant models this masking process is impossible to implement due to the varying boundary of the flexible wall over a flow cycle. For this a wall detection method was implemented similar to Burgmann et al. (2009). Figure 34 shows an average image of the centre plane with well-defined boundaries.

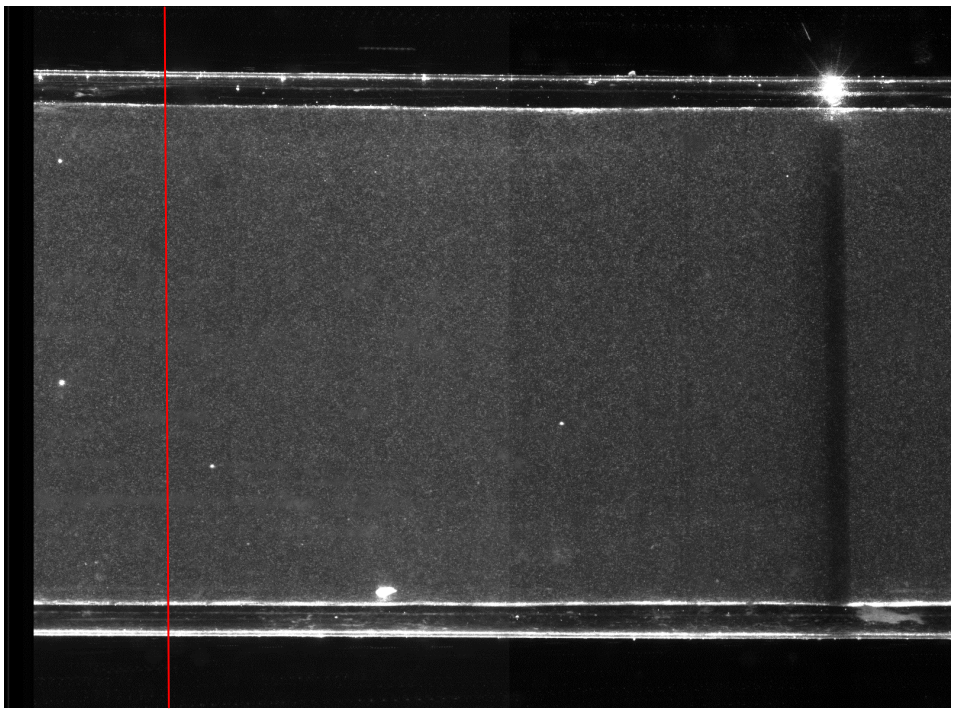

Figure 34 Average image of the flexible flow phantom with well-defined wall boundaries

[10] Open source software http://www.paraview.org/

[11] Adobe Photoshop CS5 Adobe Systems Incorporated

A histogram of the intensities was taken through an axial slice (example shown by red line) of the flow phantom and produced the plot in Figure 35. As can be seen, there are 4 definite peaks and 2 definite troughs. The wall detection code starts from the centre of the graph and cycles left and right to detect the first 2 peaks above a pre-set threshold and 2 troughs below a pre-set threshold. The distance between the trough and peak is calculated, and compared to the threshold set that relates to the wall thickness. If the value is acceptable the wall position has been located. The code cycles to the next axial slice and repeats the process. Once it has located the wall position in the second slice the results are compared with the previous slice to check it is within a pre-set tolerance. If a suspect wall location value is identified it is replaced with an average of the surrounding slice values.

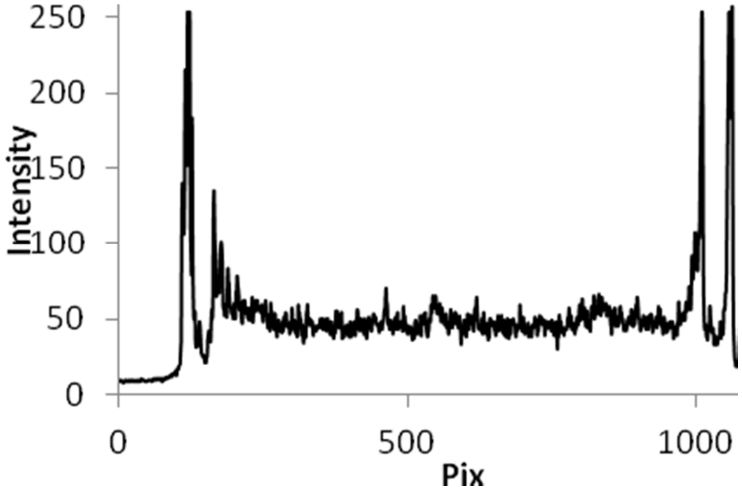

Figure 35 Example axial intensity slice for wall detection

The final result from planar PIV processing can be used for fluid flow analysis (Figure 36).

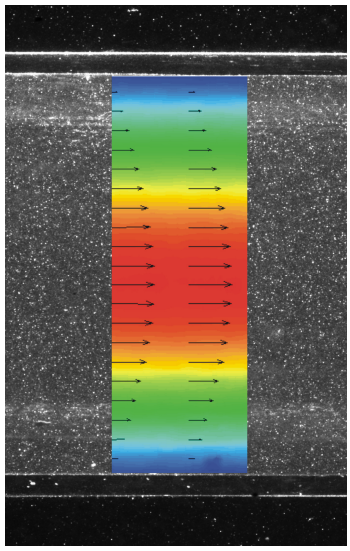

Figure 36 Example result after planer PIV processing is completed

3.8 Stereoscopic Particle Image Velocimetry (SPIV)

Planar PIV uses a single camera in perpendicular orientation to the region of interest (ROI) illuminated by a laser light sheet. The vector field obtained from this setup has two drawbacks. Firstly the out-of-plane velocity component of a vector is lost and secondly the measured in-plane components are affected by a perspective error due to local nonzero out-of-plane components. The error is proportional to the relative magnitude of the out-of-plane component to the in-plane component (Prasad and Jensen 1995). For planar PIV an error in the region of 10% in the in-plane measurement can occur when the in-plane and out-of-plane displacements are similar in magnitude (Prasad 2000).

SPIV (Raffel et al. 2007; Prasad 2000; Willert 1997) overcomes these drawbacks using two cameras positioned at different locations focused on the same ROI to resolve the out of plane motion. This provides a 2D3C measurement of a fluid system (i.e. three components of displacement are resolved in a two dimensional object space). There are two types of basic SPIV setup's, the angular displacement method and the translation method with good full explanations of both being given by Prasad (2000) and Raffel et al. (2007). The angular displacement method will be further discussed (where the two cameras are parallel to each other and orthogonal to the light sheet) as it allows for a larger common ROI to be imaged between the two cameras. A schematic of the angular displacement method is shown in

Figure 37, where the two cameras are not parallel but rotated (typically 30° from the normal) to view the same ROI.

Viewing the light sheet at an angle does create a problem of varied magnification and focus across the image plane. A simple method to obtaining well focused particles is to increase the depth of field of the optics system. This can be achieved by increasing the $f_{\#}$ (reducing the lens aperture), which means a reduction in the intensity of the imaged particles. Another method that can be practically used to ensure all particles are in focus across the image plane is the Scheimpflug condition, where the lens plane and the image plane are rotated so that they are collinear with the object plane (Prasad and Jensen 1995).

In this work the 2D2C vector fields are calculated in the same manner as discussed in Section 3.6 for each camera and the 2D3C vector field is calculated by a stereo reconstruction with a three dimensional camera calibration.

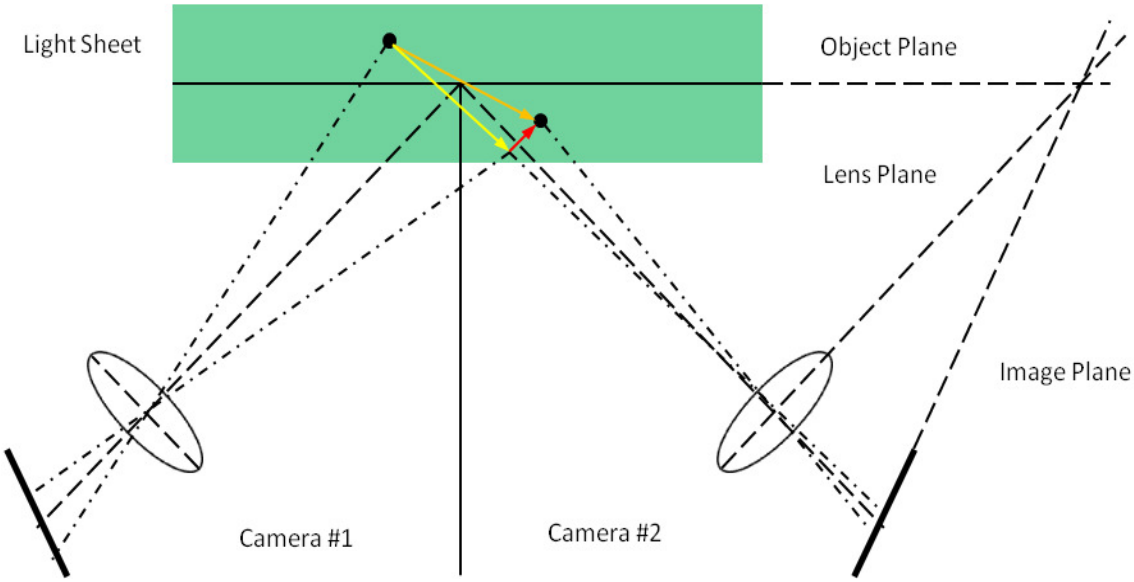

Figure 37 Angular displacement method SPIV setup with Scheimpflug condition (yellow arrow: displacement seen by camera #1, red arrow: displacement seen by camera #2, orange arrow: actual displacement)

3.8.1 Calibration and Disparity Correction

There are two main methods of reconstruction for SPIV. For geometric reconstruction there is a requirement of an accurate knowledge of the recording geometry including focal distance, magnification and camera angle. It does not account adequately enough for lens distortion and variations in experiments. The preferred method that is further explained is a three dimensional calibration based reconstruction method as described by Soloff et al.

(1997). It does not require prior knowledge of the experimental setup and can account for known and unknown distortions experienced during the experimentation.

The method requires the cameras to be calibrated by imaging a calibration target. The calibration target for this experiment was a Cartesian grid pattern of circular calibration markers 1mm in diameter in an array of 76×76 spaced at 2.5mm. The markers were CNC machined into a 200×200×10mm black anodized aluminium plate and filled with white polyfill flush to the plate surface giving a white on black contrast pattern. The calibration target plate was aligned with the object plane in the measurement volume. To ensure the calibration process accounted for distortion due the diffraction of the Perspex external wall and the external glycerol, calibration was performed in the box filled with glycerol with the silicone and the phantom removed. The calibration plate was attached to a micrometer screw that could traverse linearly. For the camera calibration the target plate is imaged by both cameras simultaneously at a minimum of three locations (different z locations in the measurement volume). This consisted of the object plane and a traverse of half the light sheet thickness (1mm) in the forward and reverse z directions. An improvement to the setup used in this experimentation would be the construction of a three dimensional calibration plate with the markers on two levels in the z direction. This would remove the need to translate the target plate through the z positions and removes any errors from the displacement.

The location of the calibration markers are located by local pattern matching (cross-correlation) they are used to calculate the 19 coefficients of the image mapping function ($\underline{F}$) (Equation 43) with a least squares procedure. This third order polynomial accounts for linear distortions, with the linear terms accounting for perspective error and the quadratic and cubic terms tracking adequately the non-linear distortions like barrel and pincushion radial distortions (Soloff et al. 1997). Prasad (2000) has shown that other studies have used higher order functions with little to no increase in accuracy of the vector field. Therefore implementation and increased computational time caused by higher order functions was not deemed necessary.

$$\underline{F}(x,y,z) = a_0 + a_1x + a_2y + a_3z + a_4x^2 + a_5xy + a_6y^2 + a_7xz + a_8yz + a_9z^2 + a_{10}x^3 + a_{11}x^2y + a_{12}xy^2 + a_{13}y^3 + a_{14}x^2z + a_{15}xyz + a_{16}y^2z + a_{17}xz^2 + a_{18}yz^2 \quad \textbf{Equation 43}$$

Equation 44 can be used to relate the three dimensional object field coordinates ($\underline{x}$) to the two dimensional image field ($\underline{X}$) for each camera. Using a Taylor expansion the three component displacement field can then be calculated.

$$\underline{X} = \underline{F}(\underline{x}) \quad \textbf{Equation 44}$$

As discussed the three dimensional calibration method compensates for all image distortions from imperfect lenses and refractive changes of light path, its major drawback is that the calibration plate has to be placed exactly in the same place as the light sheet (object plane) (Wieneke 2005). Willert (1997) showed that a rotation of the calibration plate of 0.6° gave deviations of 10 pixels at the edge of the vector field from the true value although the reconstruction grid overlapped better than 1 pixel. To counteract the obvious constraints this puts on an experimental setup in this work a method proposed by Wieneke (2005) was implemented known as self-calibration or disparity correction. This method does not require the perfect alignment of the calibration plate and light sheet and can be tilted and slightly offset. An iterative process updated the mapping function coefficients by cross correlation images from camera #1 and #2 that have been dewarped into object space creating a final disparity correction to replace the original mapping function. Wieneke (2005) stated that it has been shown that with the disparity correction implemented the z=0 plane of the mapping function lies within 0.1 pixels of the middle of the light sheet.

3.8.2 SPIV Error Validation

To validate the SPIV code for this experiment, a solid body translation experiment similar to that of Parker et al. (2004) was implemented. Two cameras were set up in stereo configuration set at a symmetric 45 ° offset. The same lenses, apertures and similar magnifications were used as in the experimental setup (discussed later). High density seeding particles were simulated by a sheet of 150 grit sand paper attached to a micrometer traverse. A distorting medium of an acrylic panel was placed between the sandpaper and the camera to simulate the distorting medium of the experimental setup. The sandpaper was

traversed through 1mm ± 5μm displacements in the x and z direction resulting in 13 to 14 pixel displacements and was repeated ten times to get the rms error in displacement. Displacement vector field calculations were calculated using a 64 × 64 pixel^2 interrogation window with 50% overlap and no vector validation or filtering. The results of this are shown in Table 9.

With a 1mm displacement there was a total error in the x and z direction of 0.4% and 0.5% respectively. There was no investigation in y direction but it is typically the same as the x direction (Willert 1997). The rms error includes PIV displacement errors, interpolation errors, camera calibration errors, target grid spacing errors and traversing errors.

Table 9 SPIV errors from solid body translation

Traverse	Mean (μm)	RMS (μm)
0mm xyz displacement		
Δx	0.28	0.36
Δy	0.25	0.29
Δz	0.32	0.42
1mm x displacement		
Δx	999.2	3.1
Δy	1.5	1.2
Δz	5.2	4.2
1mm z displacement		
Δx	1.6	2.1
Δy	1.5	1.9
Δz	999.7	2.2

3.9 Interfacial PIV

An important factor in the development of arterial diseases is the wall shear stress (WSS) distribution within the artery. Evaluating this is of great importance if any useful knowledge is to be garnered from PIV analysis. With conventional PIV analysis performed near a wall surface, due to a decreasing concentration of tracer particles and the strong velocity gradients present, the velocity measurements obtained are usually biased (Kähler et al. 2012). The strong light intensities observed in Figure 34 from light reflection on the wall surface, which is commonly more intense than the particles, can also increase the measurement uncertainty and bias in the results. To overcome this, a technique developed by Buchmann et al. (2009)

known as interfacial PIV (IPIV) can be used. A full explanation of the technique and an error analysis of its application can be found in Buchmann (2010), this section provides only a brief overview.

3.9.1 Wall Shear Stress Calculation

Assuming that the flow in the boundary layer travels virtually parallel to the wall interface, the transformed images are discretized into interrogation windows M×N (usually 32×80pixel^2) in size and a 1-D cross-correlation is performed on each horizontal line of the interrogation window. Strong tracer signals produce peaks and are located at a position representing the tracer displacement. The results produce a correlation peak at each horizontal with the location of the peaks lying along the velocity profile.

At the wall the no-slip condition is assumed (U(0) = 0) and the velocity gradient at the wall is extracted by fitting a straight line through the correlation peaks (Figure 38). The line L is swept through the correlation map and the Gaussian weighted sum of correlation values is computed to Equation 45.

$$F\left(grad\left(y\right)\right) \equiv \frac{\sum_{y=-N}^{N} \hat{R}_{U,y} \cdot \Omega\left(y\right)}{\sum_{y=-N}^{N} \Omega\left(y\right)} \qquad \textbf{Equation 45}$$

To impose the no-slip condition the correlation map is reflected around U=0, y=0. Ω is the Gaussian weighting function (Equation 46) and is centred around the current wall normal position

$$\Omega\left(y\right) = \exp\left[-\frac{\left(y-n\right)^2}{2\sigma^2}\right] \qquad \textbf{Equation 46}$$

$2\sigma^2$ is the spread of the Gaussian function. Using the weighting function on the correlation peaks acts like a filter to reduce measurement uncertainty and prevent detection of false or strong peaks further away from the wall. The velocity gradient at the wall is calculated as the slope of the line for which Equation 45 is at its maximum giving wall shear rate (WSR) to be calculated by Equation 47.

$$\left(\frac{\partial u}{\partial y}\right)\Big|_{y=0} = \max\{F(grad(0))\}$$ **Equation 47**

WSS can then be calculated from WSR by Equation 48 ((Buchmann et al. 2009))

$$\tau_w = \frac{\mu \frac{\partial u}{\partial y}}{\Delta t}$$ **Equation 48**

Where μ is the dynamic viscosity of the fluid and Δt is the time delay between image exposures.

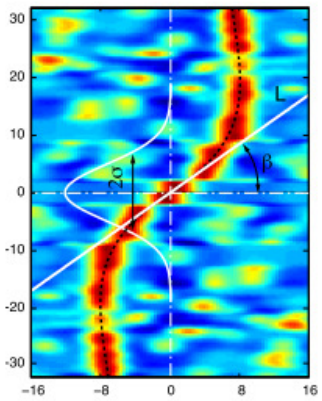

Figure 38 Original and inverted correlation map for wall shear rate estimation. Figure adapted from Buchmann (2010).

3.9.2 Obtaining the Region of Interest

For a region of interest (ROI) with a flat interface the 1-D cross correlation can be applied directly to the image by aligning pixel rows of the camera with the wall interface. For irregular interfaces like the ones investigated within this work this is not possible. Therefore the interface region has to be transformed so that a 1-D correlation can be performed.

To achieve this firstly the interface has to be located in the image. The masked images produced in section 3.7.3, provide the location of the wall interface required for WSS analysis with an accuracy of ±1pix. Following this a wall analysis region in the flow domain with constant height (commonly 80 pixels) in the wall normal direction is defined in physical (x,y) coordinates in the PIV images (Figure 39(a)). This near wall region can then be transformed to a rectangular image in transformed coordinates (ξ,η) (Figure 39(b)) using a

conformal mapping and grid generation algorithm (Nguyen et al. 2010). The Laplace's equations

$$\frac{\partial^2 x}{\partial \xi^2} + \frac{\partial^2 x}{\partial \eta^2} = 0; \frac{\partial^2 y}{\partial \xi^2} + \frac{\partial^2 y}{\partial \eta^2} = 0 \qquad \textbf{Equation 49}$$

are solved using an iterative Poisson solver in MATLAB and produce a curvilinear grid. Pixel intensities in the grid points produced are interpolated at sub pixel locations using a two-dimensional cardinal interpolation function (Scarano 2002) resulting in a rectangular image in mapped coordinates. Equation 47 can then be used to calculate the WSR in the transformed domain ($\partial U/\partial \eta$)

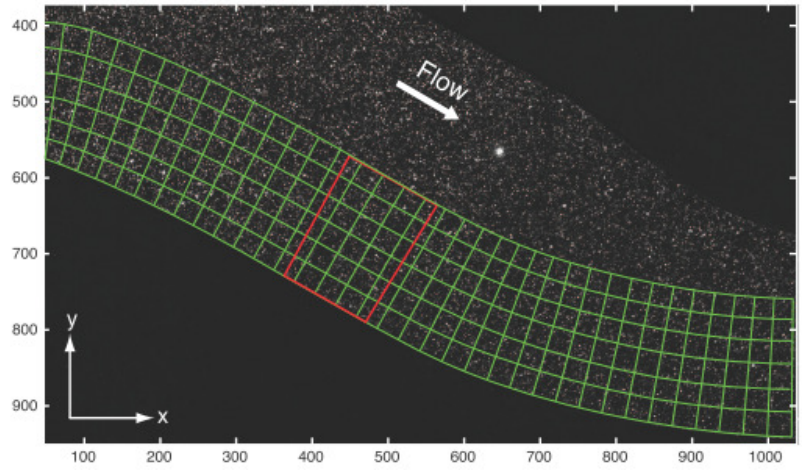

(a)

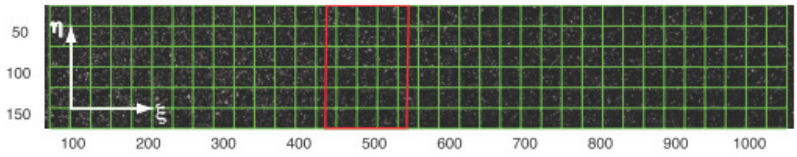

(b)

Figure 39 (a) Orthogonal curvilinear grid in (x,y) space. (b) Image of region re-sampled in transformed space (ξ,η). Figure adapted from Buchmann (2010).

A reverse transformation is then performed to convert the displacement in the transformed domain (U,V) and the physical domain (u,y). The relationship between the two is defined as

$$u = \frac{\partial x}{\partial \xi} U + \frac{\partial x}{\partial \eta}, \qquad v = \frac{\partial y}{\partial \xi} U + \frac{\partial y}{\partial \eta} V \qquad \textbf{Equation 50}$$

In the iPIV technique only horizontal displacement (U) is calculated with V=0, which, in the physical domain, is related to the local wall parallel displacement ($\tilde{u}$) in the coordinate system aligned with the interface ($\tilde{x}, \tilde{y}$) by Equation 51.

$$\tilde{u} = U g_{\varepsilon} \qquad \textbf{Equation 51}$$

The WSR in the physical domain can then be calculated using Equation 52.

$$\frac{\partial \tilde{u}}{\partial \tilde{y}} = \frac{\partial U}{\partial \eta} \frac{g_{\varepsilon}}{g_{\eta}} \qquad \textbf{Equation 52}$$

Where g_ξ and g_η are the coefficients characterising the coordinate transformation and are derived by Equation 53.

$$g_{\xi} = \sqrt{\left(\frac{\partial x}{\partial \xi}\right)^2 + \left(\frac{\partial y}{\partial \xi}\right)^2}, \qquad g_{\eta} = \sqrt{\left(\frac{\partial x}{\partial \eta}\right)^2 + \left(\frac{\partial y}{\partial \eta}\right)^2} \qquad \textbf{Equation 53}$$

This technique provides a reduction in error in near wall velocity estimation. It is however restricted by the use of a single line interrogation, with any large wall normal displacements causing an increase in velocity error. It also improves the data resolution in the wall normal direction at the expanse of the wall parallel direction. The work of Buchmann (2010) (Chapter 4) has shown that for synthetic test results, planar PIV at a window sizing of 16 × 16 pix^2 produced a WSR measurement uncertainty of 9.4%. In comparison iPIV produced an error in WSR of 0.8%.

4 Physiological Flow System

This chapter provides a method to preserve the dynamic similarity between in vitro and in vivo conditions. It takes into consideration the dimensionless parameters Reynolds number (Re) and Womersley number (α). It describes how to produce a refractive matched liquid to enhance particle image velocimetry (PIV) experimental results. A full explanation on setting up a flow system to carry out compliant flow phantom analysis is provided. A method for producing oscillating flow waves and synchronising the input to the PIV analysis is given. Finally an analysis of the precision of the experimental setup is given.

4.1 Fluid Properties

As previously stated in Chapter 2, to preserve the dynamic similarity of the experimental setup, the fluid properties have to be scaled in conjunction with the mechanical and geometrical properties. The dependant variable for a time oscillating flow is the change in pressure (Δp) and has been shown by Equation 13 (Section 2.2.1) to be dependent on Re and St, which therefore have to be matched to ensure similitude between in vivo and in vitro oscillatory flow. To recap, Re which describes the ratio of inertial forces to viscous forces is defined as

$$Re = \frac{\rho U_m D}{\mu}$$ **Equation 54**

Due to the varying boundary condition of the compliant phantom as it expands and contracts the assumption is made that the variation in diameter has minimal effect on Re and St so all fluid dimensionless parameters are calculated for the inlet with a neutral unexpanded phantom diameter. The mean fluid velocity U_m is calculated as the ratio of flow rate to cross-sectional area (Equation 55).

$$U_m = \frac{Q}{A}$$ **Equation 55**

As stated previously μ is the dynamic viscosity and values for blood (Galdi et al. 2008), air, water (Potter and Wiggert 2002) and water/glycerol[12] (section 4.2) mixture are shown in Table 10.

Table 10 Density and dynamic viscosity of blood, air, water and water/glycerol mixture

Property	Blood (37°C)	Air (20°C)	Water (20°C)	61:39 Water/Glycerol mixture (20°C)
Density (kg/m^3)	1060	1.204	998.2	1140
Dynamic Viscosity (Pas)	$3x10^{-3} – 4x10^{-3}$	$1.81x10^{-5}$	$1.005x10^{-3}$	$1.06x10^{-2}$
Kinematic Viscosity (m^2/s)	$2.83x10^{-6} –3.77x10^{-6}$	$1.5x10^{-5}$	$1.01 x10^{-5}$	$9.30 x10^{-6}$

To ensure dynamic similarity in oscillatory flow the Strouhal number St (Equation 56) is widely used in engineering practice; ω is the angular frequency of the oscillation

$$St = \frac{\omega D}{U}$$ **Equation 56**

In biological fluid flow it is more common to use the dimensionless parameter known as the Womersley number (α) (Womersley 1955), which combines St and Re.

$$\alpha = \frac{1}{2}\sqrt{ReSt}$$ **Equation 57**

Combining Equation 54, Equation 56 and Equation 57 gives

$$\alpha = \frac{D}{2}\sqrt{\frac{\omega\rho}{\mu}}$$ **Equation 58**

α quantifies the degree of quasi-steadiness, which supposes that there is an instantaneous response to pressure gradient variation by the fluid flow. α can be interpreted as the ratio of the unsteady inertial forces to the viscous forces i.e. it is the ratio of thickness of the fully developed viscous boundary layer (½d for Poiseuille flow) to the oscillating boundary layer. For a pipe flow, where $\alpha < 1$ the frequency of oscillation is sufficiently small that viscous forces dominate inertial forces giving the flow a near Poiseuille profile (parabolic in shape) and the centreline velocity oscillates in phase with the driving pressure gradient (Womersley

[12] The Viscosity of Water/Glycerol is obtained using a HAAKE Viscometers Rotovisco© RV20 concentric cylinder viscometer

1955). As $1 \leq \alpha \leq 10$ the inertial forces dominate the viscous forces flattening the flow profile and the phase lag between flow and pressure gradient increases until it plateaus at approximately 80° (Figure 40) where the flow rate is only about one-fifteenth of the flow rate expected in a Poiseuille profile experiencing the same pressure gradient (Womersley 1955).

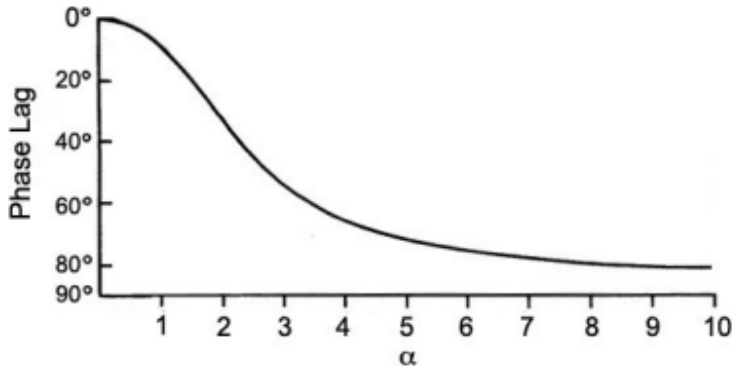

Figure 40 The effect of α on the phase lag between the oscillating pressure and the flow generated (adapted from (Womersley 1955))

In conclusion, to obtain similitude between in vivo and in vitro conditions for a time oscillating flow in a compliant flow phantom the following dimensionless groups should be matched (Equation 59 is the definition of distensibility from Section 2.2.1).

$$d = \frac{1}{E(h/D)} \qquad \textbf{Equation 59}$$

$$Re = \frac{\rho U_m D}{\mu} \qquad \textbf{Equation 60}$$

$$\alpha = \frac{d}{2}\sqrt{\frac{\omega\rho}{\mu}} \qquad \textbf{Equation 61}$$

4.2 Blood Analogue Liquid

Much of this section has previously been investigated by Buchmann (2010), the following discussion provides an overview of the relevant details required for this investigation. Optical refraction has been discussed previously in Chapter 3 and an explanation of refractive index is provided in Appendix A – Refractive Index. As discussed optical refraction occurs at the model/liquid interface where there is a difference in refractive index between the media. For simple geometries refraction can be corrected analytically (Lowe and Kutt 1992) or by performing an image calibration like that presented by Soloff et al.

(1997) (Section 3.8.1). However, in situations where the interface is a complex 3D shape like the highly curved nature of a compliant cylindrical flow phantom, an analytical method is inadequate and image calibration may not be possible. Matching the refractive index between liquid and solid reduces image pre-processing time expenditure due to optical distortions.

Nguyen et al. (2004) provide an in depth review of refractive index matching for cardiovascular flow phantoms with both Newtonian and Non Newtonian blood analogue liquids. Table 11 provides data for potential matching liquids that were suggested in this work.

Table 11 physical properties of liquids for refractive index matching at 20ºC (Nguyen et al. 2004)

	n	μ	ρ
D-limonene	1.473	0.80	0.85
Diethyl Phthalate	1.504	12.00	1.18
Methyl Salicylate	1.526	4.09	1.18
Mineral Oil	1.460	21.20	0.82
Ethanol	1.362	1.17	0.79
Glycerol	1.470	11.50	1.26
Water	1.333	1.00	1.00

One of the most common Newtonian blood analogue liquids used in conjunction with silicone flow phantoms is a combination of water and glycerol (Spence et al. 2011a; Buchmann et al. 2011; Geoghegan et al. 2010; Geoghegan et al. 2009b; Burgmann et al. 2009; Deplano et al. 2007). It allows a range of viscosities and refractive indices (n=1.33 to 1.47) to be achieved by adjusting the mixture proportion and temperature. It is also possible to use aqueous solutions like potassium thiocyanate (KSCN) (Palmen et al. 1993) and sodium iodide (Tateshima et al. 2001). These materials can be hard to work with as they can be hazardous, corrosive and can also be quite expensive. Glycerol has the advantage of being non-toxic, non-corrosive, easy to wash off and relatively cheap (40 litres ~NZ$100). Other studies have also developed non-Newtonian blood analogues for optical measurements such as aqueous solutions of KSCN and Xanthan gum (Gray et al. 2007; Gijsen et al. 1999) or polyacrylamide (Liepsch 2002) to match both the shear thinning behaviour of blood and the refractive index of the phantom. Although blood is a colloidal suspension of particles (including red blood cells, white blood cells and platelets, in plasma), in large arteries such as

the carotid artery the rheological effects of the particles can be ignored and blood treated as a simple continuous viscous fluid (Yamaguchi et al. 2006). The vessels studied in this thesis are large enough in diameter that it can be assumed the non-Newtonian behaviour can be ignored as discussed in Section 1.5.

The blood analogue liquid selected must also allow for dynamic similarity to be adhered to. For a study performed in a 1:1 scale flow phantom the working liquid will generally have a dynamic viscosity similar to that of the high shear plateau in blood (~$3.5x10^{-3}$Pas). The experimentation in this work as discussed in Section 2.4 is performed on flow phantoms that are 3.2 times larger than life-size and it is common to use a liquid with a higher viscosity. The viscosity of a blood analogue must allow, when dynamic similarity is obtained, a flow rate and oscillatory flow time period which are achievable and measureable. The vast majority of this section has previously been presented (Geoghegan et al. 2012a; Spence 2011; Buchmann 2010); this section provides a general overview of this previous work.

4.2.1 Refractive Index calculation

As temperature increases, for most liquids the density decreases and refractive index decreases proportional to this. Perry (1950) gives an empirical relation between the change in refractive index and density as: $\Delta n \approx 0.6\Delta\rho$. Equation 62 provides a relationship between refractive index and temperature for organic liquids (Nguyen et al. 2004).

$$n(T) = a + bT \qquad \textbf{Equation 62}$$

n is the index of refraction, a and b are material constants and T is the absolute temperature. Equation 63 is used to calculate the refractive index of a mixture (subscript mix) of two liquids (subscripts 1 and 2) in proportions P and (1-P).

$$n_{mix} = n_1 P + n_2(1-P) \qquad \textbf{Equation 63}$$

Combining Equation 62 and Equation 63, the proportions of liquid required to achieve a refractive index ($n_{required}$) can be calculated using Equation 64.

$$P = \frac{n_{required} - a_2 + b_2 T}{a_1 - a_2 + (b_1 - b_2)T} \qquad \textbf{Equation 64}$$

The relationship of μ with variation in T can be expressed as

$$ln(\mu) = e + \frac{f}{T}, \qquad e = ln(\mu_0), \qquad f = -\frac{d}{R} \quad \textbf{Equation 65}$$

μ_o is the asymptotic dynamic viscosity at high T, d is the activation energy of the liquid (J/mol), and R is the universal gas constant (8.314 J/mol.K). A Grunberg-Nissan model of type 1 can be used as an estimation of the dynamic viscosity of a liquid mixture (μ_{mix}).

$$ln(\mu_{mix}) = Pln(\mu_1) + (1-P)ln(\mu_2) + P(1-P)d_{12} \quad \textbf{Equation 66}$$

Equation 67 provides an empirical relationship to calculate change in density and the density of a mixture (ρ_{mix}) can be estimated by Equation 68.

$$\rho(T) = \rho_o \left(\frac{T_0}{T}\right)^s = g\left(\frac{h}{T}\right)^s \quad \textbf{Equation 67}$$

$$\rho_{mix} = P\rho_1(T) + (1-P)\rho_2(T) \quad \textbf{Equation 68}$$

s is a material constant for an individual liquid and T_0 = 20°C the reference temperature. The temperature dependency of the kinematic viscosity for a given P of the mixture can then be expressed as the ratio of dynamic viscosity and density, combining Equation 65, Equation 66, Equation 67 and Equation 68 gives

$$\nu_{mix} = \frac{\mu_{mix}}{\rho_{mix}} = \frac{exp\left[P\left(e_1 + \frac{f_1}{T}\right) + (1-P)\left(e_2 + \frac{f_2}{T}\right) + P(1-P)d_{12}\right]}{P\left(g_1\left(\frac{h_1}{T}\right)^{s_1}\right) + (1-P)\left(g_2\left(\frac{h_2}{T}\right)^{s_2}\right)} \quad \textbf{Equation 69}$$

The refractive index of the silicone material used in construction of the flow phantoms is specified by the manufacturer to be 1.43. This value though can be altered in the curing phase of the silicone depending on the percentage of catalyst that is added and the temperature curing occurs at. An aqueous glycerol solution was used to simulate blood flow and match the refractive index to the flow phantoms as there is already good experimental verification of the applicability of this mixture at providing good refraction properties and dynamic similarity when used in conjunction with the silicone material. Glycerol is a clear liquid with a high refractive index and viscosity. It is also inexpensive as it is commonly used in the food industry and it is non-toxic and compatible with the materials commonly used in the phantom, flow circuit and pump.

It should be first noted that for compliant flow phantom study due to the high curvature in the phantoms used, the external pressurisation chamber (EPC) needs to be filled with refractive index matched liquid as well as the internal flow system Due to the static nature of the external liquid and the fact the particles are 'near' neutrally buoyant, over time they can attach to the external wall of the phantom producing unwanted reflections in PIV analysis, therefore the external liquid should be void of seeding particles. Using Equation 64 the value of P that matches an aqueous glycerol liquid to the manufacturer's refractive index for silicone is 69.1% glycerol by weight. As previously stated the refractive index can vary from the guideline value, so an iterative technique similar to Hopkins et al. (2000) was employed to fine tune the mathematical value. A chessboard grid pattern as shown in Figure 40 is placed behind the EPC containing the phantom. A mixture of liquid that has an excess amount of glycerol is circulated through the system and filled in the EPC. An image is recorded of the distortion due to refractive mismatch; water is then added in gradual amounts with an image recorded after each addition. The distortion of the pattern reduces until refractive matching is achieved and the flow phantom 'disappears'. It was found that the optimal mixture was 61% glycerol 39% water by weight. Figure 41 presents some example cases recorded during the refractive matching process. (a) shows a phantom containing a 61:39 mixture with the EPC filled with air, (b) shows both phantom and EPC filled with a 70:30 mixture and (c) shows the phantom and EPC filled with a refractive matched 61:39 solution. A major advantage of employing the technique described by Hopkins et al. (2000) is the ease of adjustment of the refractive index for the whole system if refractive mismatch occurs. Water evaporates at a much higher rate than glycerol which means the refractive index of the liquid system alters over time and should be adjusted on a weekly basis to ensure refractive matching is preserved.

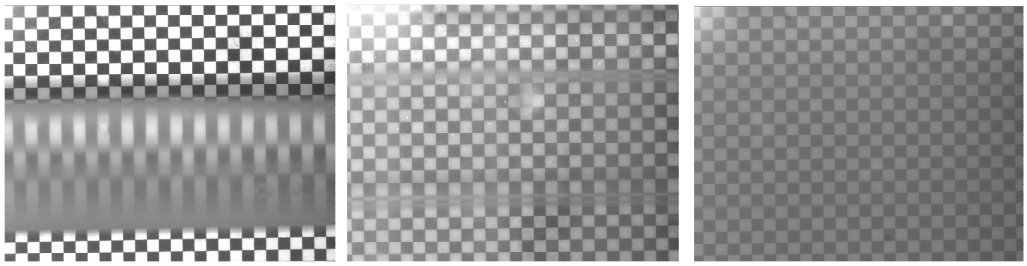

(a) (b) (c)

Figure 41 Distortion of the grid lines seen through a compliant flow phantom when (a) the EPC is full of air (b) the phantom and EPC contain 70% glycerol 30% water and (c) the phantom and EPC contain 61% glycerol 39% water

A full analysis of the physical properties of the aqueous glycerol solution is shown in Figure 42 and compared with the mathematical model for P=61%. Water and glycerol are both Newtonian liquids so the resulting mixture is assumed to have the same property. As shown in the power-law fit, the mixture does not have perfect linearity and a 7.5% increase in viscosity is shown. There is only minor shear thickening behaviour overall and therefore the Newtonian assumption holds true. There is good agreement between the predictions and measurements for the dynamic viscosity, refractive index and density. For a typical operating temperature of 20°C, the measured refractive index (measured with a bench top refractometer) was 1.417 compared to the predicted 1.419 (error= 0.14%) and a mean kinematic viscosity (measured with a rotary rheometer) of $10.2 \times 10^{-6} m^2/s$ compared to the predicted $10.51 \times 10^{-6} m^2/s$ (error= 3.04%). To ensure refractive index and viscosity was kept constant throughout an experimental session, a cooling unit was inserted into the flow system to keep the fluid temperature at a constant 20±0.5ºC.

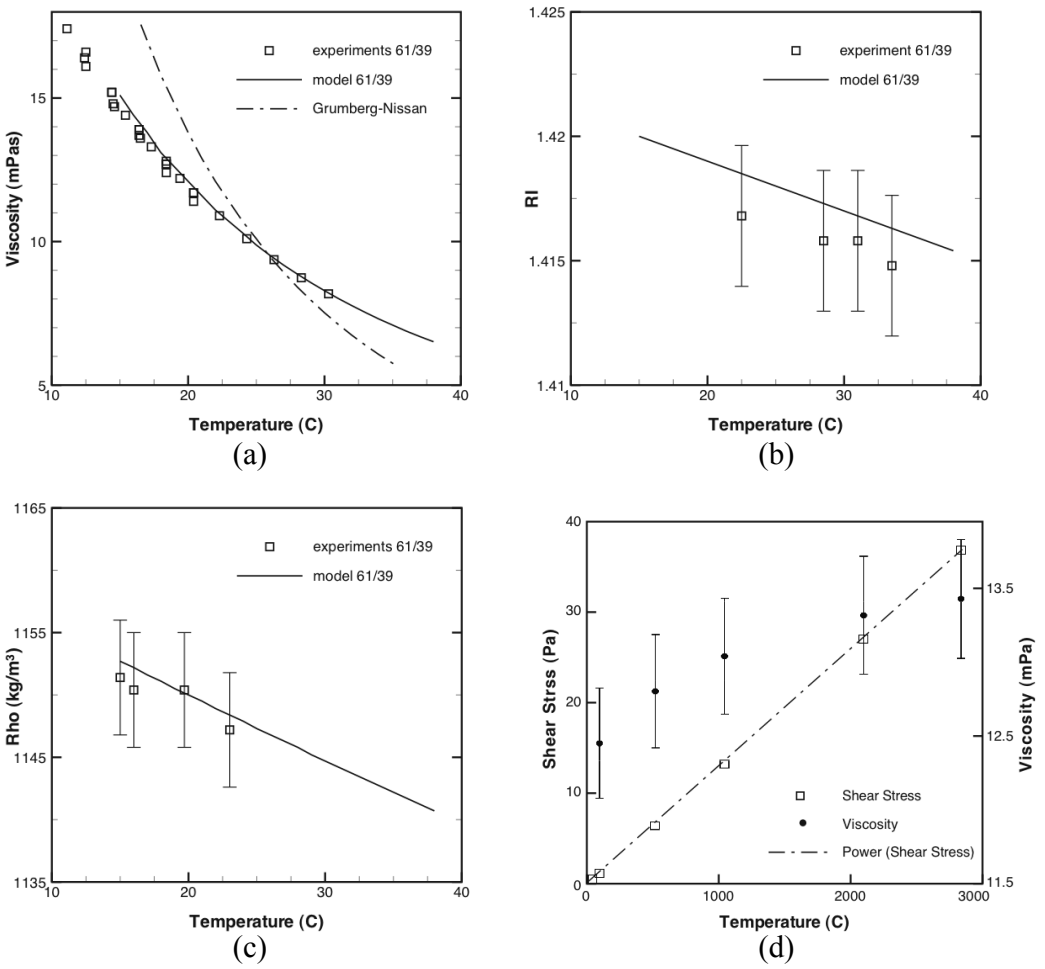

Figure 42 Physical properties of the 39:61 water-glycerol mixture, comparison between measurement and model prediction (a) temperature dependency of the dynamic viscosity, (b) temperature dependency of the refractive index, (c) temperature dependency of the density, (d) shear stress and dynamic viscosity versus shear rate. Figure adapted from Buchmann (2010).

4.3 Physiological Flow Wave

The time-dependent in-vivo flow rate of a healthy male volunteer in the common carotid artery (CCA) was obtained through Phase Contrast (PC) Magnetic Resonance Imaging (MRI) (Buchmann 2010). An explanation of this technique is out with the scope of this work, a full explanation is given by Vlaardingerbroek and Boer (1996). A perpendicular measurement plane obtained the axial component only, with 30 recordings equally spaced during one cardiac cycle. To obtain the cardiac waveform the mean velocity is calculated at each time step as the average pixel value in the phase image. The flow rate for the time step is calculated by multiplying the mean flow rate by the lumen area (Moore 2007). The Physiological waveform can be seen in Figure 43. The in vivo peak and mean Re are 954

and 614 respectively with an α of 4.54 calculated with a density of 1060kg/m^3 and a kinematic viscosity of 3×10^{-6}m^2/s (Table 10). For a 3.2 times scale model this required a peak flow rate of 8.7l/min and a time period of 2.92 seconds at 20ºC.

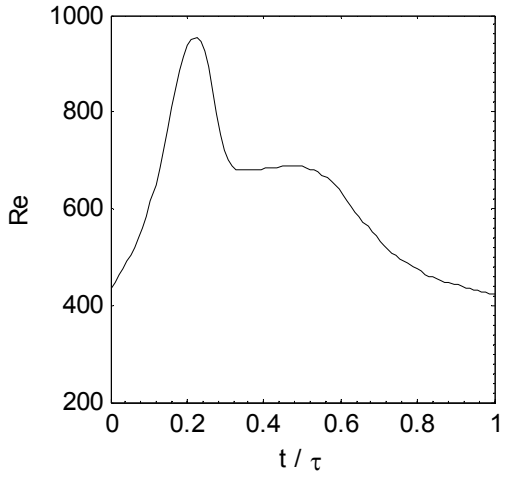

Figure 43 Pulsatile in vivo inlet waveform

4.4 Flow Facility

A schematic of the flow rig system used for experimentation in this work is provided in Figure 44. The compliant phantom and EPC (j) was ported to a flow system that can switch between two flow modes via the three way valve (l). The first mode, steady flow, was provided by a header tank with weir (a1), giving a constant head of pressure with the exit flow being directly returned to the sump and pumped back to the header tank. Flow rate was controlled by two ball valves (b) upstream and downstream of the phantom. The second mode utilises a piston pump (c) to produce unsteady flow. A header tank with weir (a2) was located at a height of 1.72m above the flow phantom at the end of the circuit to keep a constant exit pressure. To ensure a good Poiseuille flow profile entered the flow phantom and remove any effects caused by junctions in the circuit, a honeycomb flow straightener in a settling chamber (d) and a straight rigid acrylic pipe section of 1.5m was located upstream. The length of tube was calculated based on the work of Durst et al. (2005) who developed Equation 70 to give the relationship between pipe length and diameter to guarantee a Poiseuille profile in steady laminar flow entered the phantom. It should be noted that for a time oscillating flow this length requirement reduces by almost 40% (Burgmann et al. 2009),

so the length was deemed more than sufficient for the experimentation in this work. The same length of pipe and flow straightener was also located downstream of the flow phantom.

$$\frac{L}{D} = (0.619^{1.6} + 0.0567Re^{1.6})^{1/1.6}$$ **Equation 70**

An electromagnetic flow meter[13] (g) and one differential pressure transducer[14] (f1) was located at the inlet of the compliant phantom. The pressure transducer had one port open to atmosphere giving the pressure at the entrance of the phantom. The second differential pressure transducer[15] (f2) had a port connected to the entrance and a port connected to just downstream of the exit, giving the pressure change across the phantom.

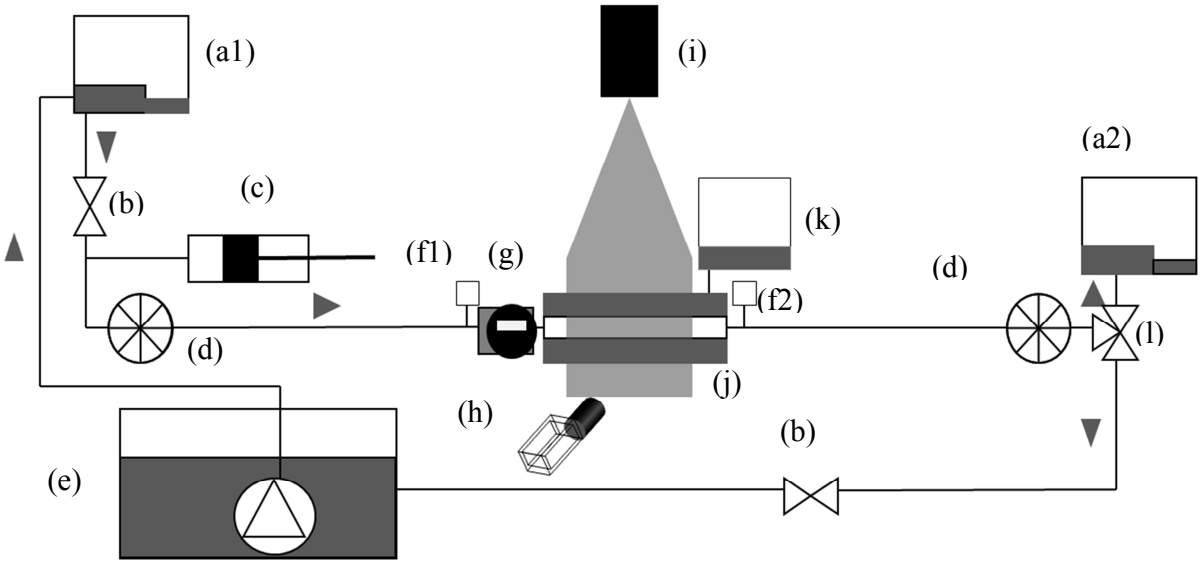

Figure 44 Schematic view of flow system setup, the arrows represent flow direction (a) header tanks with weir for constant pressure (b) ball valves for flow control (c) piston pump (d) flow straightner (e) sump with pump (f) pressure transducers (g) electromagnetic flow meter (h) PIV camera (i) laser and optics (j) model in pressure controlled container (k) external pressure chamber (EPC) (l) three way valve

4.4.1 Recording Error

To assess the error produced by the electromagnetic flow meter used in the experimental setup. The working fluid was passed through the flow meter at several flow rates and the exiting flow was collected over set time periods and weighed. The results showed there to be a relative error of 1.3%. As shown in Figure 42 the kinematic viscosity of the working fluid

[13] Krohne OPTIFLUX 2040 C

[14] RS 286-686 0-5psi

[15] RS 216-6253 0-1psi

is dependent on the working temperature. For the working temperature applied to this system (20ºC) it was common for there to be a fluctuation of ±0.5ºC, leading to an error in the kinematic viscosity of ~1.9%. Combining these two errors leads to an error in the recorded Re of ±2.3%.

4.5 Piston Pump System

In this work, to ensure dynamic similarity, the inlet waveform was matched to the physiological waveform discussed in Section 4.3. To produce an oscillating waveform two piston pump systems were used.

4.5.1 Compressed Air System

The first pump that was used in Chapter 5 consisted of a linear pneumatic actuator controlled by a proportional directional valve. The cylinder had a diameter of 20mm and length of 250mm. The piston was driven by compressed air. To ensure the piston produced the required input flow wave and to enable accurate repeatable motion, feedback was provided by a linear encoder connected to the piston and by the electromagnetic flow meter upstream of the test section. An in house LabVIEW[16] code on a desktop computer[17] gave real time control by closed loop feedback. Piston stroke and cycle frequency were independently controlled allowing for a range of Re and α to be produced.

To produce an oscillatory flow cycle (Q(t)) the required profile was decomposed into its steady (q_0) and unsteady components (q(t)) of the cycle.

$$Q(t) = q_0 + q(t) \qquad \textbf{Equation 71}$$

q_0 was provided by header tank a1 and q(t) was provided by the piston pump. q(t) was found by performing a discrete Fourier analysis (Equation 72) of the required oscillating profile with N data points per cycle over a time period T.

[16] National Instruments

[17] Intel Pentium IV 2.6Ghz

$$q(t) = a_0 + \sum_{n=1}^{N} \left(a_n \cos \frac{n\pi t}{T} + b_n \sin \frac{n\pi t}{T} \right)$$ **Equation 72**

n is the Fourier mode a_n and b_n are the Fourier coefficients. For a physiological flow wave only the first 8 Fourier coefficients are required as Lou and Yang (1992) state that 99% of the energy in a physiological waveform is contained in these components. The coefficients for the physiological flow wave given in Figure 43 are given in Table 12.

Table 12 First 8 Fourier coefficients for the physiological flow wave in l/min

n	0	1	2	3	4	5	6	7
a_n	11.152	-0.849	-0.621	-0.47	0.148	0.194	-0.071	-0.094
b_n	0	1.523	0.416	-0.381	-0.271	0.084	0.148	-0.025

The Fourier components were input into the LabVIEW code which then calculated the time-dependent piston displacement by the ratio of the integral of the oscillatory flow component to the piston cross-sectional area (Equation 73).

$$x(t) = \frac{1}{A} \int_0^T q(t) dt$$ **Equation 73**

This system produced a precise and repeatable flow wave. Theoretically the waveform could be performed on a continuous cycle indefinitely as the piston initial and final cycle displacement was zero. However as experimentation proceeded this was found not to be the case. For the system to work properly the piston had to return to the same starting position after each cycle. This did not happen, so an offset value was implemented into the code to correct the error after each cycle. Even with this offset the piston did not return to the starting location in each cycle. This error propagated over time until after 15-20 cycles it was so big that the system could not resolve the problem and the piston would accelerate and decelerate at unacceptably high rates. This pump system was designed initially with rigid flow phantoms in mind so when this excitation occurred it would not cause any damage and the experiment could be repeated to produce a larger dataset. For compliant phantoms this excitation was a danger to the phantom with the high acceleration gradients causing sharp expansion that could lead to phantom rupture.

4.5.2 Stepper Motor System

A second piston pump (Figure 45) system was adapted from the work of Spence (2011) to suit the needs of this experimental analysis. It consisted of a 140mm nominal bore acrylic cylinder with a conical reduction to 25mm bore. Flexible tubing porting the pump to the flow system was stepped down to the phantom diameter of 20mm before the flow straightener to ensure the flow profile was Poiseuille in nature on entry to the phantom. Two lip seals attached to the front and back of the piston head sealed it to the acrylic cylinder and it was supported by a rail and T slider[18]. The difference between this system and the compressed air system is that the pump was driven by a stepper motor[19]. The motor could produce 200 steps-per-revolution (step angle of 1.8º). To increase the accuracy and resolution of the motor (especially at cycle phases where there is a flow rate transition from acceleration to deceleration) it was driven by a micro-stepper system[20] which increased the steps-per-revolution ratio to a maximum achievable value of 51,200. It should be noted that as steps-per-revolution was increased there was a reduction in torque available from the stepper motor. To convert stepper motor rotational torque to linear translation the stepper motor drove a 5mm precision pitch ball screw and ball nut[21] at a gear ratio of 1:1. A weakness of the stepper motor system compared to compressed air was the reduction of force available to translate the piston head. This was especially evident when reversing the piston head direction, which even with the highest rate of change in direction input, the piston head was momentarily stationary as the motor overcame friction forces. Therefore oscillatory waveforms were produced with a continual forward piston motion. The pump system could produce ~14 physiological flow waves in a single run (1 run constitutes the piston head travelling the length of the pump cylinder). The stepper motor was controlled by an in house LabVIEW code on a desktop computer[22] via a 9401 digital module and 9172 CompactDAQ chassis[23].

---

[18] Rollon Compact 18 series

[19] Astrosyn L259RE Stepper Motor

[20] Astrosyn P808A Stepper Motor Driver

[21] Hiwin®

[22] Intel® Core™ 2 2.13GHz dual core

[23] National Instruments

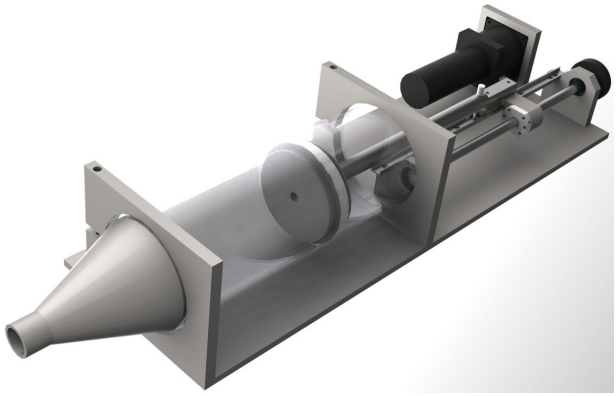

Figure 45 Piston pump developed to produce oscillatory and physiologically realistic flow waves

Adjustment of the Fourier coefficient input to ensure Re and α matching with varying experimental conditions was problematic with this setup as the expected waveform from the Fourier input was never observed from the flow meter output. Therefore the motor step rate was instead calculated using MATLAB for a required oscillatory flow wave and directly input into the LabVIEW code.

Two pump systems that were implemented in the experimentation of this work have been described in this section. The compressed air system can produce more force than the stepper motor system which allowed it to overcome higher friction forces. This was advantageous for running the system on a repeating cycle with the oscillatory component over the steady component. It did however propagate an error over time which could have a destructive force on a compliant model if the system was unable to resolve the error. This did not affect the stepper motor, but the lower power output restricted the system to producing a continuous forward motion due to friction forces opposing the system. This meant the number of cycles than could be performed in one run was restricted by the size of the pump cylinder. Due to the destructive nature of the compressed air system, the stepper motor system was the preferred oscillatory flow input device for compliant flow phantoms.

4.6 Data Acquisition and System Synchronization

Figure 46 gives a schematic of the data acquisition and system synchronization setup for the stepper motor system. The same LabVIEW code designed for the pump control also recorded real time flow rate and pressure data with a sample rate of 2000Hz. To analyse time oscillating flows with a PIV system it was integral to know the time at which the image pairs

were acquired, as well as their position in space (Chapter 3). The LabVIEW code controlled this by sending out a trigger signal to the pulse delay generator[24] at the same point in each oscillatory flow cycle of a data run which was set by the user using the real-time feedback of the flow rate. The pulse generator synchronised the camera shutter to the laser pulses and was set to acquire a predefined number of image pairs per flow cycle using the in-built burst function. The pulse generator was also used to set the time delay between image pairs and images in a pair. The synchronisation system was similar in the LabVIEW code for the compressed air driven pump which did not record pressure data.

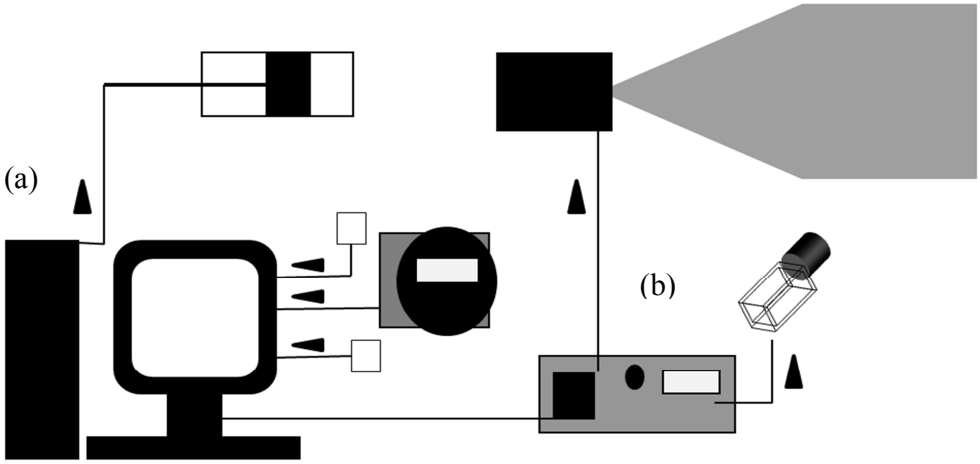

Figure 46 Schematic of data acquisition and system synchronization, the arrows represent signal direction (a) CPU with LabVIEW code (b) pulse delay generator

4.7 Pump Precision

To understand the repeatability and limitations of the stepper motor pump flow system and the variation between system run cycles the pump was tested at three flow conditions of steady, sinusoidal and physiological input. The system was tested on a flow phantom with a symmetric stenosis. Atmospheric pressure was 106.4 kPa (1064mBar) giving an internal static pressure of 125.9 kPa The EPC was pressurised to give an external pressure of 106.6kPa. This gives a static transmural pressure of 19.3 kPa. For ease, in the rest of this document external pressurisation will be referred to as transmural pressure difference with a positive value representing a higher internal than external pressure.

[24] BNC 565 pulse/delay generator

4.7.1 Steady flow

Steady flow was tested at three flow rates that were in the representative range of the minimum, mean and maximum flow rate of a physiological flow wave. Figure 47(a) to (c) gives a comparison of these flow rates over three runs each. There was an initial dynamic response time of ~3 seconds that was demonstrated by the flow waves therefore any experimental analysis should be performed once an equilibrium value was achieved.

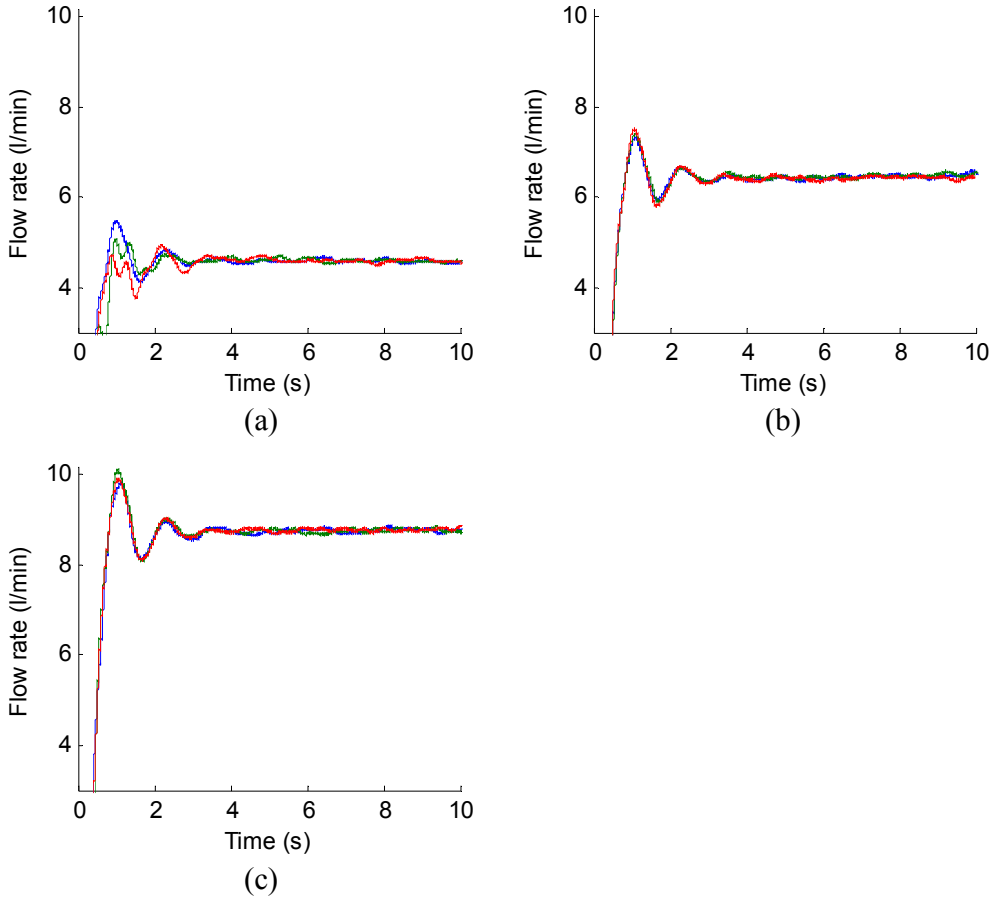

Figure 47 Flow rate comparison for three piston runs (a) Minimum flow rate 4.60 l/min (b) mean flow rate 6.48 l/min (c) maximum flow rate 8.79 l/min. Blue, green and red represents run 1, 2 and 3 respectively

The time averaged flow rate across all three runs for minimum flow, mean flow and maximum flow was 4.60, 6.477 and 8.789l/min respectively. Histogram plots were used show the deviation of the instantaneous flow rate from the time averaged flow rate, giving a Measure of the ability of the pump to hold a constant flow rate. Figure 48 shows the deviation in l/min of data for all three runs from the time averaged flow rate condition. Table

13 provides the median ('middle' data point where 50% of all data points have a lower value) and 85th percentile deviation data point (where 85% of all data points have a lower value) for this data. Percentage error was calculated as a percentage deviation from the time averaged flow rate. Deviation from the mean is in part caused by signal noise in the system.

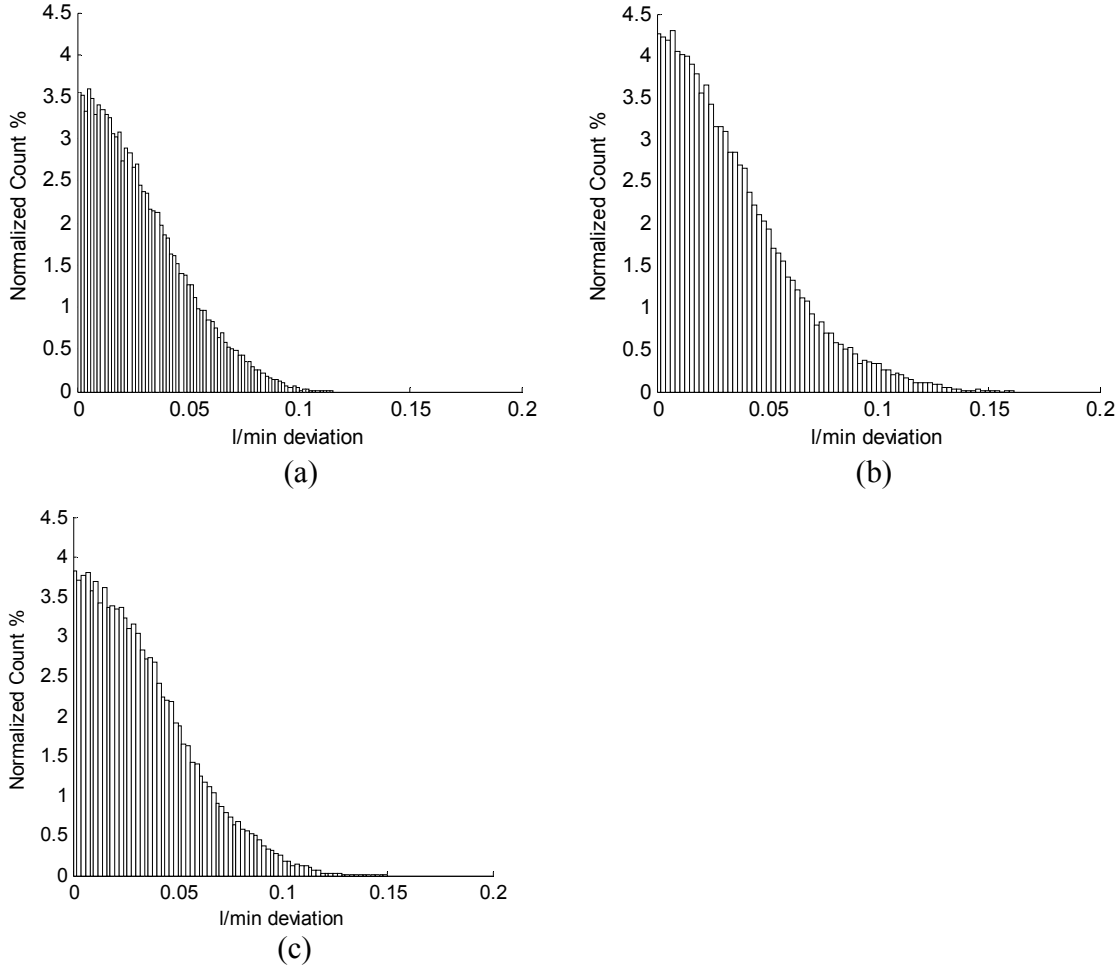

Figure 48 Deviation from the time averaged flow rate of data points for (a) 4.59l/min (b) 6.48 l/min (c) 8.79 l/min

Table 13 Median and 85th percentile results for flow rate deviation of all data sets at three separate flow rates

Steady flow rate (l/min)	Median (l/min)	85th percentile (l/min)
4.600	0.024 (0.52%)	0.051 (1.10%)
6.477	0.028 (0.43%)	0.061 (0.94%)
8.789	0.028 (0.32%)	0.060 (0.67%)

Figure 49 shows the deviation from the time averaged flow rate for a single run. Run two was selected for each flow rate; the deviation was representative of all cases. This gives an

indication of the precision of a single run in comparison to a combination of runs. The time averaged minimum flow rate was slightly lower at 4.596l/min. The time averaged mean flow rate for run two was 6.499l/min; a 0.022l/min increase on the time averaged flow rate for all data sets. For maximum flow rate it was 8.778l/min a 0.011l/min difference. Table 14 provides the median and 85th percentile of this data.

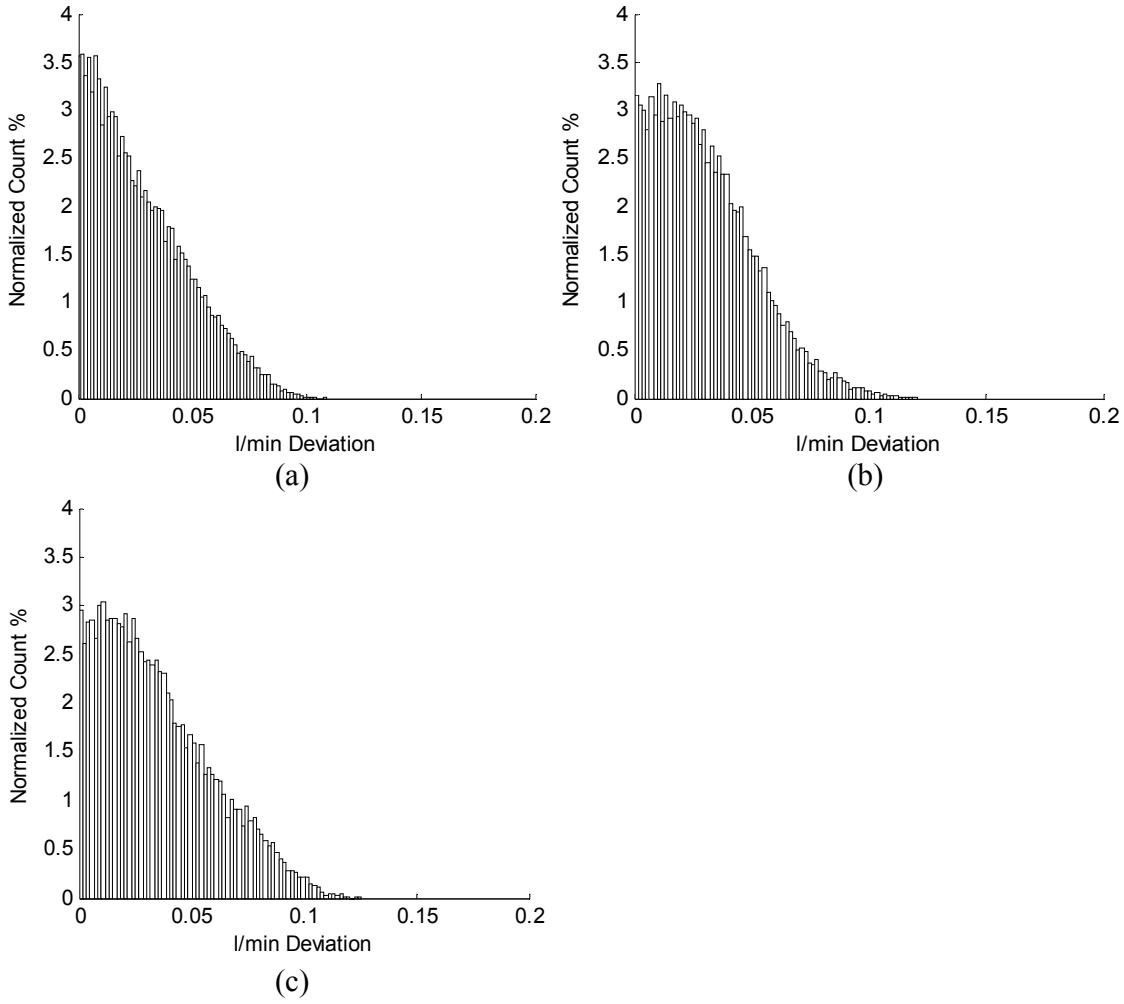

Figure 49 Deviation of all data points from the time averaged flow rates for run 2 of each flow rate only (a) 4.59l/min (b) 6.43l/min (C)8.79l/min

Table 14 Median and 85th percentile results for flow rate deviation of run two for each flow rate only,

Steady flow rate (l/min)	Median (l/min)	85th percentile (l/min)
4.596	0.024 (0.51%)	0.052 (1.12%)
6.499	0.027 (0.41%)	0.053 (0.81%)
8.778	0.030 (0.34%)	0.063 (0.72%)

It can be seen from Table 13 and Table 14 that the percentage deviation of data from the time average of a single run compared to a combination of multiple runs varies minimally with flow rate values varying by only ~0.5% between runs. It is shown that the pump has a high level of precision and repeatability for producing steady flow conditions. For all operating flow rates the median deviation of flow rate from the time averaged value was 0.03l/min or less and 85% of all data points deviated 0.06l/min or less.

4.7.2 Sinusoidal flow

Two sinusoidal inputs were tested, representing the first two Fourier components (Table 12) of the physiological flow waveform. Median and 85th percentile results were calculated for the data sets as the deviation from the respective phase averaged flow, entrance and exit pressure waves.

4.7.2.1 Fourier Coefficient One

Figure 50 provides a comparison of the flow rates recorded for a sinusoidal waveform representing the 1st Fourier component of the physiological waveform each run was 10 cycles long only 4 are shown. It can be seen that similar to the steady flow data that there was a settling time before the pump reaches a state of repeatability in the waveform. From inspection of the waveforms this occurred after cycle two so phase averaging (discussed further in Section 5.3.1) was performed from cycle three onwards. Figure 51 shows the phase averaged flow rate, entrance and exit pressure for the first Fourier coefficient. The time period is 2.92 seconds giving $\alpha = 4.54$.

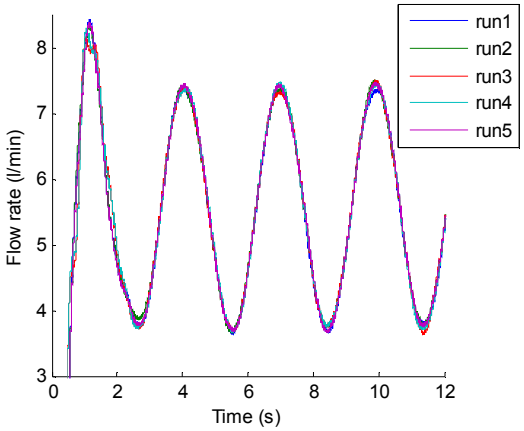

Figure 50 Comparison of 1st Fourier coefficient sinusoidal waveforms for 5 different runs

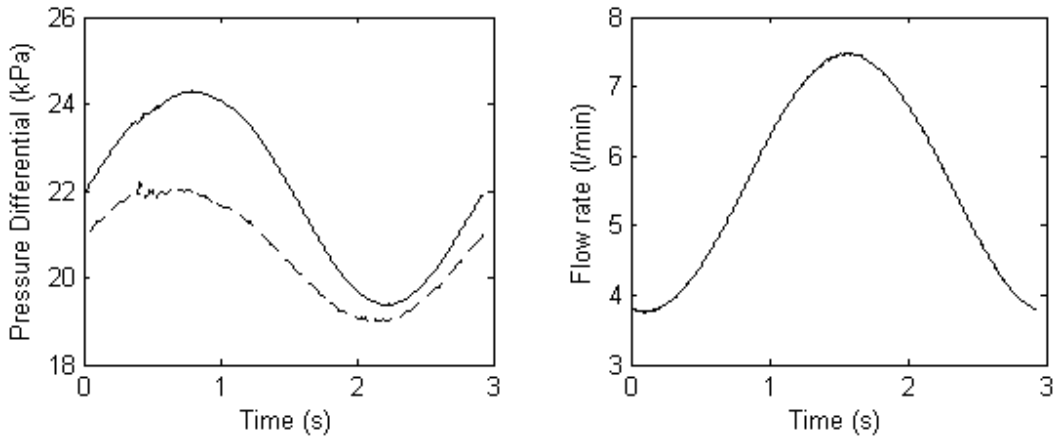

(a) (b)

Figure 51 Phase averaged results for a sinusoidal waveform representing the 1st Fourier component (a) entrance (-) and exit (--) pressure (b) flow rate.

Histograms provided in Figure 52 show how much the data for all experimental runs deviated from the phase averaged waveforms. The median and 85th percentile data points are given in Table 15. The error for all oscillating waveforms was calculated as a percentage of the difference between the peak and trough values of the waveform. For this sinusoidal waveform the peak to trough difference for the flow rate entrance pressure and exit pressure was 3.72l/min, 4.91 kPa and 3.83 kPa respectively. The deviation for a single run from its phase average is also given in Table 15. The histogram plots aren't shown as the distribution is similar to that of Figure 52. Run 2 was selected, the deviation is representative of all cases. The data in Table 15 shows that the ability of the piston pump system to produce the same oscillatory wave form over one cycle was accurate to 0.065l/min for flow rate, 153 Pa

for entrance pressure and 116 Pa for exit pressure. The accuracy over multiple runs reduced, but was still within 2% of the maximum flow rate change and 4% of the maximum pressure change.

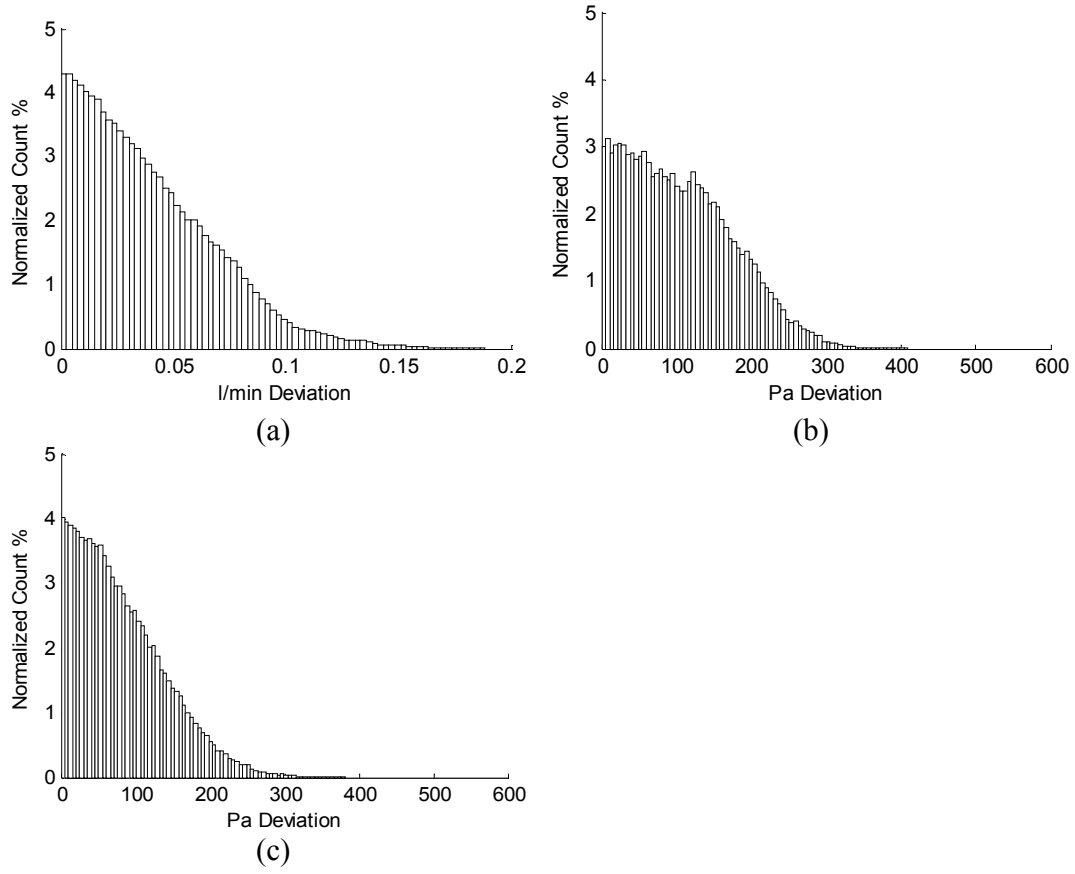

Figure 52 Deviation of all data points from the phase averaged waveforms for a sinusoidal waveform T = 2.92s (a) flow rate (b) entrance pressure (c) exit pressure

Table 15 Median and 85th percentile results for a sinusodal waveform with T=2.92s for flow rate, entrance and exit pressure deviation of all datasets from the phase average

Profile	Median	85th percentile
Deviation of all data recorded		
Flow rate (l/min)	0.033 (0.89%)	0.072 (1.92%)
Entrance pressure (Pa)	96 (1.96%)	185 (3.76%)
Exit pressure difference (Pa)	69 (1.80%)	146 (3.81%)
Deviation of run 2 only		
Flow rate (l/min)	0.032 (0.86%)	0.065 (1.74%)
Entrance pressure (Pa)	92 (1.87%)	153 (3.12%)
Exit pressure difference (Pa)	54 (2.44%)	116 (3.03%)

4.7.2.2 Fourier Coefficient Two

The same analysis was performed for the 2nd Fourier coefficient. Figure 53 gives a comparison of the rate of change of flow rate for five separate 10 cycle runs (only 7 cycles shown). The initial settling time was again deemed to be after the 2nd cycle. Phase averaged waveforms for the flow rate, entrance and exit pressure are given in Figure 54, the oscillation has a time period of 1.46s giving an α of 6.53.

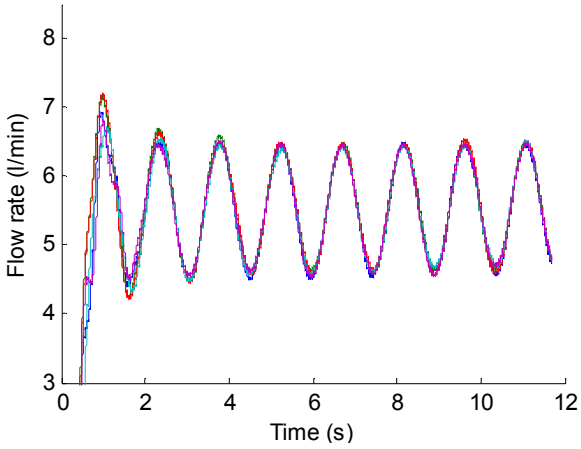

Figure 53 Comparison of 1st Fourier coefficient sinusoidal waveforms for 5 different runs

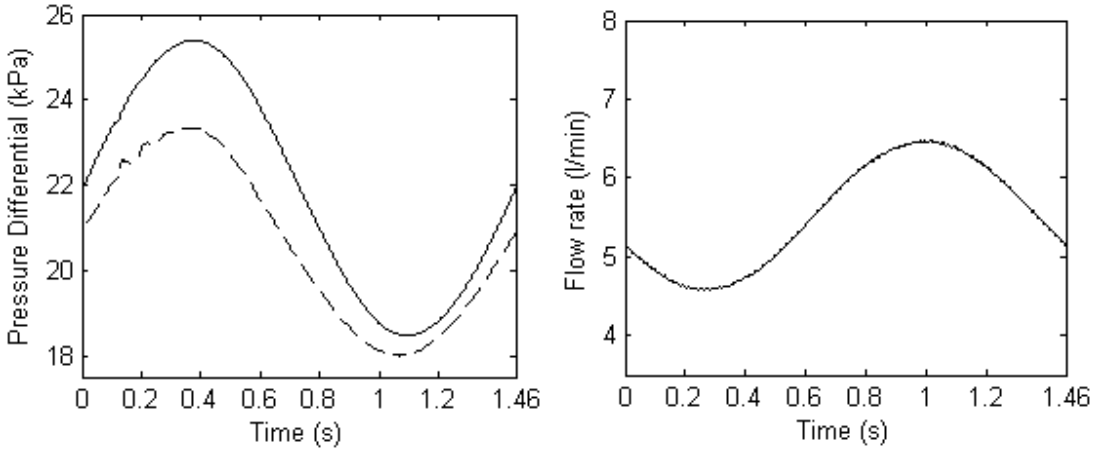

(a) (b)

Figure 54 Phase averaged results for a sinusoidal waveform representing the 2nd Fourier component (a)entrance (-) and exit (--) pressure (b) flow rate.

Histogram plots (Figure 55) show the deviation of all data points from the phase average and the median and 85th percentile data is given in Table 16. The peak to trough difference for the flow rate, entrance pressure and exit pressure was 1.89l/min, 6.93 kPa and 5.86 kPa respectively. Deviation from the phase average of run 2 is also given in Table 16,

distribution of data points is equivalent to Figure 55 and run 2 is representative of the five data runs. The pump was again shown to be more accurate over a single run than multiple runs. There was a slight increase in accuracy in the flow rate form the 1st Fourier coefficient sinusoidal waveform and a decrease in accuracy of the pressure data.

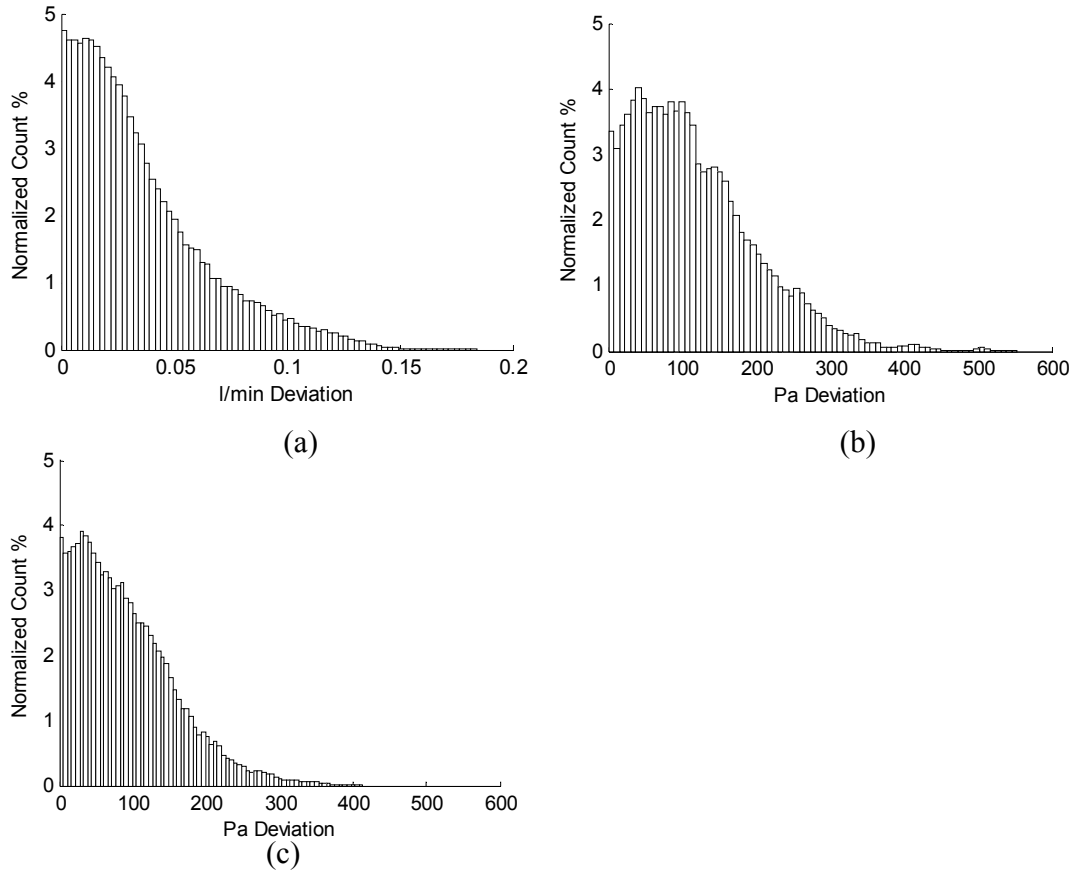

Figure 55 Deviation of all data points from the phase averaged waveforms for a sinusoidal waveform T = 1.46s (a) flow rate (b) entrance pressure (c) exit pressure

Table 16 Median and 85th percentile results for a sinusodal waveform T=1.46s for flow rate, entrance and exit pressure deviation of all datasets from the phase average

Profile	Median	85th percentile
Deviation of all data recorded		
Flow rate (l/min)	0.028 (1.46%)	0.066 (3.48%)
Entrance pressure (Pa)	101 (1.46%)	203 (2.92%)
Exit pressure (Pa)	78 (1.33%)	159 (2.71%)
Deviation of run 2 only		
Flow rate (l/min)	0.026 (1.33%)	0.058 (3.01%)
Entrance pressure (Pa)	106 (1.52%)	193 (2.79%)
Exit pressure (Pa)	69 (1.18%)	137 (2.34%)

4.7.3 Physiological flow

Three separate runs were completed with the pump producing a physiologically realistic flow rate (section 4.3). Figure 56 provides a comparison of the flow rate for this data. Each run lasted for ten cycles but for clarity the first five only are shown. It was noted that there was still a settling time present so experimental analysis should be performed once this has dissipated which was complete after cycle two. The waveform has T = 2.92s and $\alpha = 4.54$. Similar to section 4.7.2 all data sets were phased averaged from cycle three. Phase averaged pressures and flow rate are given in Figure 57.

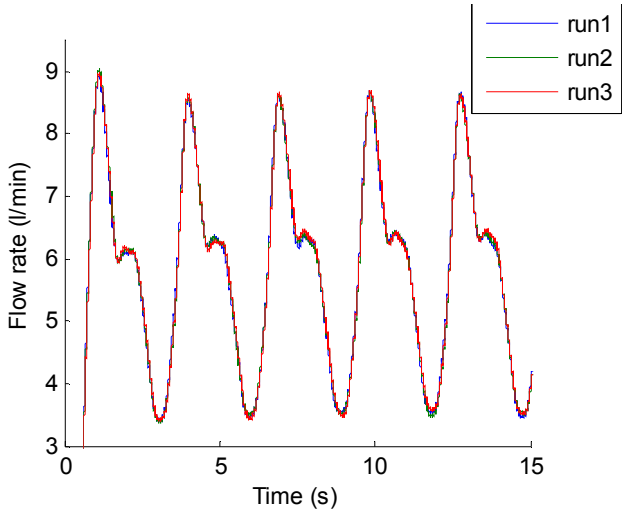

Figure 56 Comparison of physiological flow waves for three separate runs

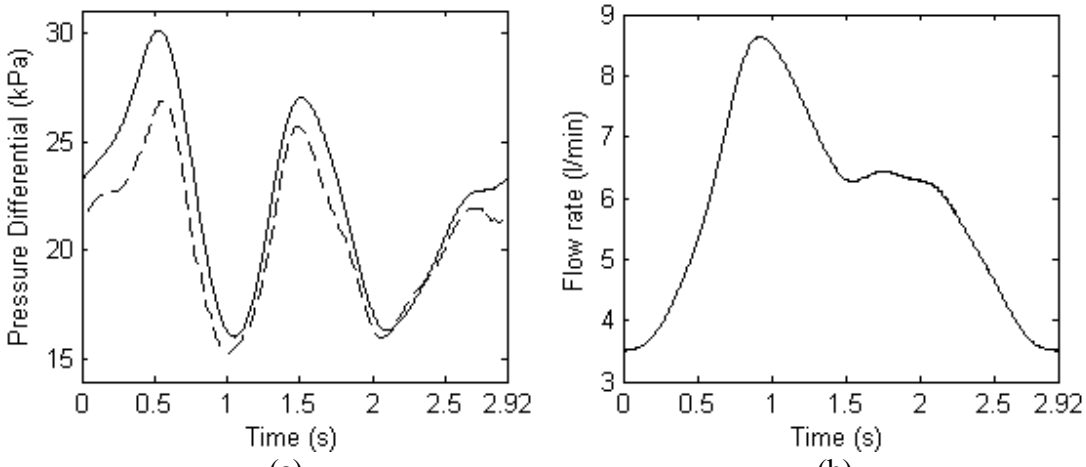

Figure 57 Phase averaged results for the physiological (a) entrance (-) and exit (--) pressure (b) flow rate

Histogram plots given in Figure 58 show the distribution of flow rate deviation for all three runs from the phase averaged waveforms. Median and 85th percentile data points of the

histograms are given in Table 17. The peak to trough values for flow rate, entrance pressure and exit pressure were 5.15l/min, 14.04kPa and 11.55kPa respectively. Accuracy over a single run is also provided in Table 17 for the representative case of run two. The data shows that the flow waveform was repeatable to an accuracy of 0.066 l/min for 85% of all data points and 256 Pa for entrance pressure and 194Pa for exit pressure.

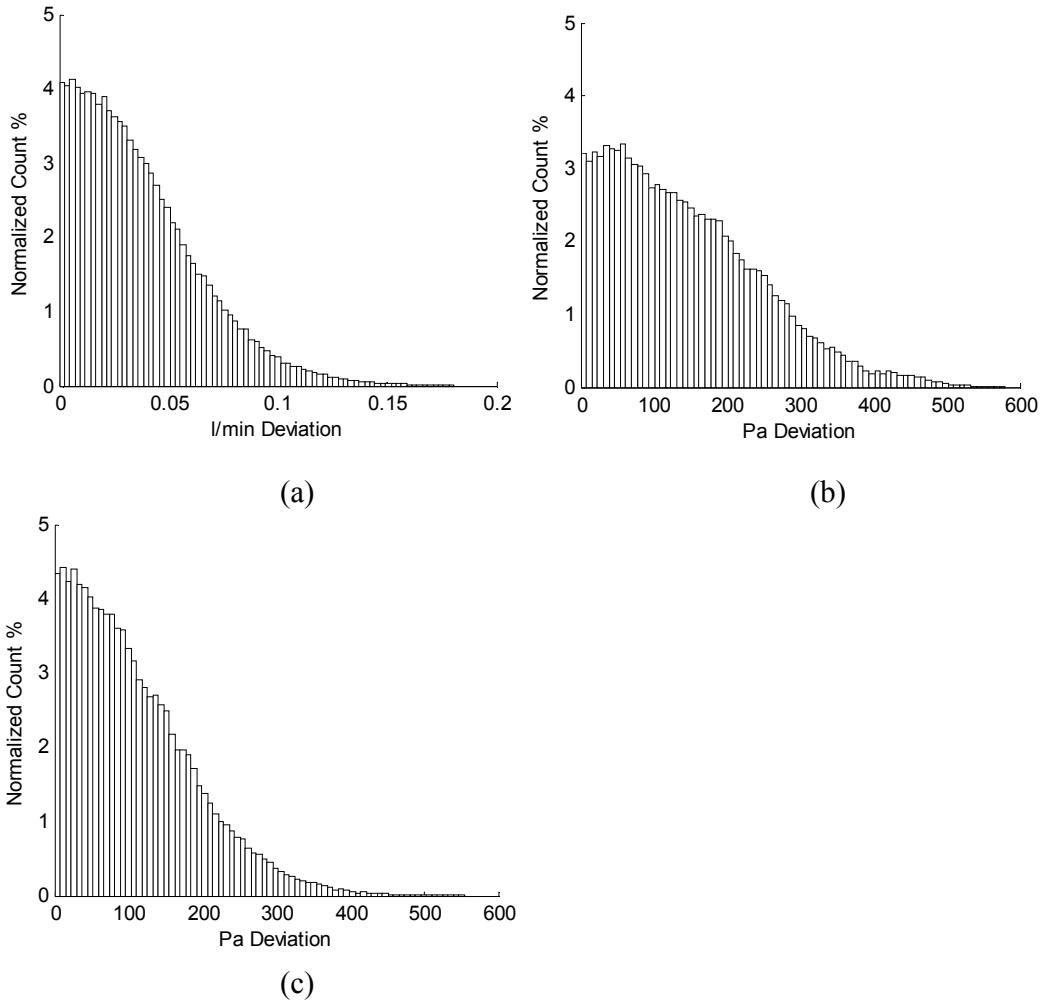

Figure 58 The results show the deviation from the average waveforms from 3 runs and 23 waveforms (a) Flow rate (b) Entrance pressure (c) exit pressure

Table 17 Median and 85th percentile results for flow rate, entrance and exit pressure deviation of all datasets

Profile	Median	85th percentile
Deviation of all data recorded		
Flow rate (l/min)	0.031 (0.61%)	0.066 (1.29%)
Entrance pressure (Pa)	126 (0.90%)	256 (1.82%)
Exit to entrance pressure difference (Pa)	91 (0.79%)	194 (1.68%)
Deviation of run 2 only		
Flow rate (l/min)	0.025 (0.49%)	0.056 (1.08%)
Entrance pressure (Pa)	90 (0.64%)	159 (1.13%)
Exit to entrance pressure difference (Pa)	74 (0.64%)	162 (1.40%)

This section has provided an analysis of the piston pump system and the repeatability it was capable of when producing flow waves over multiple cycles. The quantification of this error is important for all experimental analysis that is performed within this thesis. The results show the pump and experimental system can produce a repeatable oscillating wave form that has a flow wave accurate to ±0.072 l/min, entrance pressure accurate to ±256 Pa and exit pressure to ±194 Pa for 85% of all data points. The difference between entrance and exit pressure is partly due to a different pressure transducers at each location. The entrance pressure was measured with a 0-5psi transducer and exit pressure was measured differentially between entrance and exit with a 0-1psi transducer. On close inspection of the profiles of both flow and pressure, fluctuations in the waveforms from the phase averaged value did increase in areas of change in acceleration, with areas of constant acceleration and deceleration having minimal to no fluctuation. This can be attributed to the friction force opposing the piston head during change in velocities, but as the error values are so small, little to no affect will be seen in experimental data.

4.8 Conclusion

This chapter has laid out the steps required to produce a Newtonian blood analogous liquid that allows similitude between in vivo and in vitro conditions. The liquid selected for this experimentation was a 39:61 aqueous glycerol solution as it has good refractive matching properties which can be easily adjusted due to mismatches occurring from change in silicone refractive index and water evaporation. μ can also be easily controlled by temperature adjustment. A full description of the method for constructing a flow system for producing repeatable physiological flow waveforms and synchronising these to a PIV experimental

system is given. A method for producing time varying flow rates is outlined and the precision of the system is extensively analysed. The system is shown to be highly accurate and produced a repeatable waveform and it was shown that recorded data had a precision of ±0.072 l/min for flow rate, ±256 Pa for entrance pressure and ±194 Pa for exit pressure.

5 Oscillatory flow in a healthy Idealised Geometry Representing the Common Carotid Artery

This chapter presents the results obtained in a flow phantom (Mk.I) representing a healthy idealised carotid artery (CA) experiencing a physiologically realistic input flow waveform produced by the compressed air pump system (Section 4.5.1). Pressure data is omitted from this experimental analysis as at the time of the study pressure transducers were not incorporated into the experimental setup. A comparison is made with a rigid phantom of the same unstressed internal geometry. It is widely accepted that compliance has an effect on the flow field in an arterial geometry, but there is currently very little experimental data available to support this notion and validate computational studies. Some of the results presented in this chapter has been published in Geoghegan et al. (2009a); (2009b).

5.1 Introduction

In-vitro modelling with artificial flow phantoms allows the fluid mechanics of the circulatory system to be studied without the ethical and safety issues associated with animal and human experiments. Zamir (2000) provides an in depth explanation of the analytical solution for the velocity distribution within both a rigid and elastic pipe experiencing an oscillating flow. Much of this theory is based heavily on the previous work by Womersley (1954, 1957). McDonald (1955) went on to extend this theory to incorporate larger deformations of an elastic vessel. Much work has been done on systems with rigid walls (Vétel et al. 2010; Buchmann et al. 2010; Tateshima et al. 2004). Certain systems relevant to circulatory disease have walls which are neither rigid nor static, for example, abdominal and intracranial aneurysms, the coronary arteries, the CA and the heart chambers and valves. Computational methods, in which the equations governing the flow and the elastic walls are coupled, are

maturing. There is a lack of experimental data in compliant arterial systems to validate the numerical predictions.

The chapter firstly presents a review of previous numerical and experimental analysis performed in the CA. The chapter then provides an investigation into the effect compliance plays in an idealised healthy CA. This work provides a stepping stone to developments in the analysis of more complex arterial structures.

5.2 Previous Work

There are two main ways to study biofluid problems relating to the cardiovascular system; in vivo and in vitro experimental and computational analysis. There are several reviews available of the techniques that can be applied to these fields of study (Taylor and Figueroa 2009; Yamaguchi et al. 2006; Taylor and Draney 2004; Ku 1997) in the arterial system, this section provides a brief overview of the work relevant to this thesis. The review primarily concentrates on compliant structures, but rigid structures are referred to when relevant. Several of the studies are also an investigation into larger structures (i.e. the carotid bifurcation); this section however only reviews the relevant information relating to the carotid artery.

5.2.1 In Vivo Analysis

It is currently very difficult to investigate the interaction between blood flow and the vessel wall in vivo. Vennemann et al. (2007) discuss both invasive (laser Doppler velocimetry) and non-invasive (ultrasound PIV) techniques. Elkins and Alley (2007) provide an in depth review of Magnetic resonance velocimetry which utilises the magnetic resonance imaging (MRI) technique to obtain three dimensional velocity fields, but is currently restricted to obtaining mean or phase averaged velocities. A major drawback of all current in vivo techniques is the limitation in temporal and spatial resolution. Ultrasound and echocardiography can be used to obtain in-plane velocity components, but require assumptions to be made of the velocity profiles for flow quantification. The technique is limited by the fact it cannot be performed through bone, restricting analysis in the ribs and cranium (Taylor and Draney 2004). Zhang et al. (2009) developed the ultrasound technique, termed echo particle velocimetry (echoPIV) presenting an investigation into wall shear stress (WSS) with a comparison to results obtained by MRI.

In vitro investigation into techniques that could be used for future in vivo analysis to overcome these drawbacks is currently on going. Jamison et al. (2011) have investigated the application of X-ray velocimetry to study pulsatile blood flow through an optically opaque in-vitro phantom. Further developments are required for this technique to be applied in vivo, as it currently can't account for wall movement.

5.2.2 In vitro Computational

Much work has been performed in developing numerical fluid structure interaction (FSI) codes in relation to biofluid problems. Early work by Perktold and Rappitsch (1995) numerically investigated the effect of compliance on a geometry representing the human CA bifurcation experiencing a physiological realistic waveform. A 25% decrease in WSS was observed in the bifurcation in the compliant model at peak magnitudes, but only a 7% reduction occurred in the CA. The global structure of the flow and stress patterns remained unchanged. A maximum deformation of 16% of the vessel radius was observed with the CA deforming by 6%. This work required development to make the wall mechanics far more physiologically realistic with more attention paid to boundary conditions. Gerbeau et al. (2005) has followed this work by presenting a method that could be used to model the FSI of physiologically realistic arterial geometries from MRI imaging. Tezduyar et al. (2007); (2008), also presents a technique for numerically modelling FSI in biofluid problems presenting test case flow field results, in the CA, abdominal aortic aneurysm (AAA) and cerebral aneurysm. Takizawa et al. (2010) applied this technique in a preliminary study of the WSS experienced in a cerebral aneurysm. Zdravkovic et al. (2010) has presented a method for experimental determination of carotid artery parameters from specimens obtained from a cadaver. It is then shown how to apply this to numerical analysis of the FSI in a carotid bifurcation, with some preliminary analysis completed. Xiong et al. (2011) has looked to develop FSI modelling to incorporate spatially varying wall properties within a physiological geometry. Preliminary results apply the analysis to a straight compliant model with uniform wall properties. It was shown that wall displacement was uniform for the entire length of the geometry.

A restricting factor prevalent in the computational methods previously discussed is the very fine mesh required to obtain accurate WSS results, which in turn require long processing

times to perform analysis. Yamaguchi et al. (2006) presents an overview of different computational techniques being applied and then goes on to discuss the advancement of techniques involving adaptive mesh refinement to improve processing time.

Another restricting factor is the definition of the boundary conditions to provide an accurate representation of arterial hemodynamics. Recently Moireau et al. (2012) has presented a method for the identification of boundary support parameters in a FSI model using patient specific data with the aim that in future work it is applied in complete patient specific vascular modelling. There is extensive progress being made in the field of numerical FSI with direct application to medical problems including Atherosclerosis cerebral aneurysm and AAA. Several studies have produced initial results in complex geometries including the work of Scotti et al. (2005) which studied the effect of symmetry and wall thickness on the stress of an idealised compliant AAA. Ahmed et al. (2007) studied FSI of a physiologically realistic large wide necked cerebral aneurysm. The relevant work in relation to atherosclerosis is discussed in (Chapter 7), but a further review of the other conditions is out with the scope of this thesis.

Even though FSI codes are maturing, it can be seen that there is still a long way to go till they can be readily applied to a cardiovascular problem. They still require experimental validation especially understanding the boundary conditions that should be applied to the geometries, to obtain the correct structural response to the pressure development experienced as this has not been fully clarified in work to date.

5.2.3 In vitro Experimental

There has been extensive in vitro study of the flow field and WSS in rigid geometries representing arteries. The Flow field has been qualitatively visualized in rigid phantoms of arteries (Motomiya and Karino 1984; Zarins et al. 1983) and Laser Doppler Velocimetry (LDV) measurements have yielded quantitative flow fields in idealized models of the carotid artery. Ku et al. (1985) applied LDV to the study of pulsatile flow in a rigid model of the carotid artery bifurcation using the same geometry and input waveform as Perktold and Rappitsch (1995). An investigation was performed looking at WSS and oscillatory shear index (section 5.3.1). Liepsch et al. (1998), (2002) present details of results that study anatomically realistic geometries using LDV. More recently, Bale-Glickman et al. (2003) and

Buchmann et al. (2009) conducted planar PIV measurements in physiologically realistic and diseased models.

Experimental analysis of the fluid structure interaction experienced by an elastic flow phantom using optical techniques has been previously reported for certain flow regimes. As is further discussed in Chapter 6, LDA has been used to study the phenomenon of flow rate limitation (Bertram and Nugent 2005; Bertram and Elliott 2003) found most commonly in the systemic veins.

Eguchi et al. (2003) investigated the applicability of using PIV to study flow in an elastic vessel experiencing a physiological flow waveform in a generic peripheral artery. This waveform varied markedly from the CA waveform studied here as it incorporated a small region of reverse flow. The results were compared to that of a rigid phantom. It was found that estimated flow rate obtained via integration of a 2-D PIV flow field between rigid and compliant phantom varied, especially in regions of maximum growth and shrink rate of the phantom radius. Using numerical analysis it was also shown that there was a reduced variation in WSS magnitude over a periodic cycle as well as a reduction in the magnitude of the time averaged WSS (TAWSS).

Burgmann et al. (2009) produced a review of a construction technique for producing a compliant phantom. A technique for obtaining results in the phantom was presented and results were obtained in a rigid geometry with an input of a sinusoidal oscillating flow waveform about a zero mean in a phantom representing a medium sized artery (equivalent to the CA) using PIV. The mechanical properties of the compliant phantom were well documented, but no results were actually obtained in this geometry and the sinusoidal waveform applied to the rigid geometry is far from physiologically realistic in the CA. Results were also degraded by optical distortion occurring due to a refractive mismatch between the phantom and the working fluid.

Große et al. (2008), used the same experimental facility as Burgmann et al. (2009) to perform a preliminary comparison of a compliant and rigid flow phantom with a near sinusoidal inlet flow waveform. The study investigated the effect of amplitude and α. The results presented show a phase lag between the vessel dilation and centreline velocity when $\alpha<15$, the phase lag disappears when $\alpha\geq15$. The elastic velocity profile was also compared to the Womersley

solution for sinusoidal flow in a rigid pipe, showing a good agreement between the predicted and calculated. The resolution of the waveform produced was questionable, with the plots provided not representing a pure sinusoidal waveform. There is no investigation into WSS and no direct comparison between the compliant and rigid data.

Work has developed to study more complex geometries including stenosis and aneurysm. A further discussion on this is provided in Chapter 7. There have been extensive experimental investigations into rigid geometries representing the carotid artery, with in depth analysis of the flow field and WSS encountered. There however seems to be very little experimental investigation into the affect compliance has on this; especially with respect to a physiologically realistic flow input. A direct comparison needs to be made between a compliant and rigid geometry experimentally to validate numerical work and to ascertain the role compliance plays in the arterial system.

5.2.4 Previous Validation of the Experimental Setup

Buchmann (2010) has previously implemented the PIV and iPIV technique used in this body of work on a similar experimental setup to study both steady and pulsatile flow conditions in a rigid phantom representing the CA and carotid bifurcation. To validate the experimental procedure and PIV analysis a comparison was made with a numerical simulation under steady flow conditions (Buchmann et al. 2010). Only results obtained in the CA are discussed here due to their relevance to this study. Readers should refer to the main body of work (Buchmann et al. 2010) for further discussion of the bifurcation. Comparison was performed at Re = 400 and 800 with an overall difference in peak velocity of 1.23%. A comparison of the WSS in the CA provided an absolute error of 0.02Pa with a relative error (Equation 86) between 1.0-1.5%. Entering the bifurcation differences between numerical and experimental results increased, but overall it was found the differences between numerical prediction and experimental measurement was satisfactory with the percentage differences being similar to experimental and image processing errors.

5.3 Experimental Setup

An analysis of a straight compliant tube (Mk. I phantom) representing the CA experiencing a physiological waveform is compared to the equivalent results obtained from a straight rigid

wall phantom with a radius of 20mm equal to the neutral radius (unstressed) of the compliant phantom. Validation of the rigid phantom results is given in section 5.2.4.

5.3.1 Data Analysis

This section provides an overview of the mathematical operations applied to the analysis in this chapter. The following explanation discusses the averaging operations employed in this study for a data set recorded over a period of time T. It is set out for the x component of velocity (U_x), with the same procedure used for U_y. Figure 59 shows the instantaneous velocity $U_x(t)$ obtained at a constant point in a generic flow system. $U_x(t)$ at any point in time can be described by Equation 74. Where $\overline{U_x}$ is the time average mean velocity calculated by Equation 75 and $u_x'(t)$ is the instantaneous value of the turbulent fluctuation.

$$U_x(t) = \overline{U_x} + u_x'(t) \qquad \textbf{Equation 74}$$

$$\overline{U_x} = \frac{1}{T}\int_{t_0}^{t_0+T} U_x(t)dt \qquad \textbf{Equation 75}$$

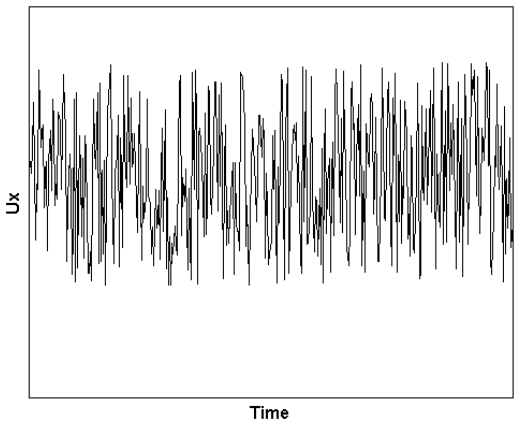

Figure 59 Instantaneous velocity versus time at a point in a steady average flow experiencing turbulence

A pulsatile flow data set can be described as having a time period T=Nτ, where N is the number of cycles recorded and τ is the period of one pulsatile cycle. Following Reynolds and Hussain (1972), the instantaneous velocity $U_x(t)$ (Equation 76) obtained at a given location (x,y) in the flow can be de-composed into a time averaged mean component $\overline{U_x}$, (Equation 77) a periodic component $\tilde{U}(t)$ (Equation 78) and a fluctuating component $u_x'(t)$.

$$U_x(t) = \overline{U}_x + \widetilde{U}(t) + u_x'(t) \quad \textbf{Equation 76}$$

$$\overline{U}_x = \frac{1}{T}\sum_0^T U_x(t) \quad \textbf{Equation 77}$$

$$\widetilde{U}(t) = \langle U_x \rangle(t) - \overline{U}_x \quad \textbf{Equation 78}$$

$\langle U_x \rangle(t)$ is the phase averaged velocity calculated by averaging a large ensemble of points over many cycles with the same phase with respect to the periodic oscillation (Reynolds and Hussain 1972). It can be calculated using Equation 79 (Dec et al. 1991).

$$\langle U_x \rangle(t) = \frac{1}{N}\sum_1^N U_x(t + N\tau) \quad \textbf{Equation 79}$$

For a physiological flow waveform in a straight tube, there is a minimal u_x'(t), therefore it is not analysed in this chapter. Once geometric variations are introduced into the phantom geometry it will play a more important role, with further explanation being presented when relevant (Chapter 8).

All velocities and WSS data in this section are in vivo scaled which was achieved through Reynolds scaling using Equation 80 and Equation 81 respectively, where ν is the kinematic viscosity, μ is the dynamic viscosity, ρ is the density, and 3.2 is the scale factor between the in vitro and in vivo phantom diameter.

$$U(t)_{invivo} = 3.2\frac{\nu_{invivo}}{\nu_{invitro}} U(t)_{invitro} \quad \textbf{Equation 80}$$

$$\tau_{w,invivo} = \frac{\rho_{invivo}}{\rho_{invitro}}\left(\frac{\mu_{invivo}}{\mu_{invitro}} 3.2\right)^2 \tau_{w,invitro} \quad \textbf{Equation 81}$$

A common comparison parameter for WSS (τ_w) in an oscillating flow is the time averaged wall shear stress (TAWSS), which over the course of one cardiac cycle is calculated by Equation 82.

$$TAWSS = \frac{1}{\tau}\int_0^\tau \tau_w d\tau \quad \textbf{Equation 82}$$

It is also important to acknowledge another time dependent WSS index known as the Oscillatory shear index (OSI) (Ku et al. 1985). It is calculated using Equation 83, where

$\tau_{w,mean}$ is the magnitude of the TAWSS (Equation 84) and $\tau_{w,mag}$ is the temporal mean of the WSS magnitude (Equation 85).

$$OSI = \frac{1}{2}\left(1 - \frac{\tau_{w,mean}}{\tau_{w,mag}}\right) \quad \textbf{Equation 83}$$

$$\tau_{w,mean} = \left|\frac{1}{\tau}\int_0^{\tau} \tau_w dt\right| \quad \textbf{Equation 84}$$

$$\tau_{w,mag} = \frac{1}{\tau}\int_0^{\tau} \left|\tau_w\right| dt \quad \textbf{Equation 85}$$

The OSI is a measure used to assess regions that are affected by oscillating WSS and provides a quantification of the oscillatory nature of the WSS being applied to the arterial wall. It can range from 0 (unidirectional flow) and 0.5 (oscillatory flow). It is not a perfect measure by any means including providing no indication of WSS magnitude, but has been shown to have relevance in areas of atherosclerosis progression. Since this particular chapter concentrates on a geometry representing a healthy CA, the flow is assumed to be unidirectional; therefore the OSI will be expected to be 0. Its occurrence is more prevalent in regions of low WSS and flow separation that cause the flow direction to reverse. Its importance will become more apparent in later chapters.

To analyse the difference between compliant and rigid results a relative difference (ε_{rel}) is introduced, which is calculated using Equation 86. It is common to obtain the absolute value of this, but for this work this is not done to allow for an easier understanding of which value has the largest magnitude.

$$\varepsilon_{rel} = \frac{f_r - f_c}{f_r} \quad \textbf{Equation 86}$$

5.3.2 Flow Facility

For this study a previous generation of the flow system discussed in Section 4.4 was used, adapted from the work by Buchmann (2010). A schematic of the experimental flow system is shown in Figure 60. This setup had the phantom enclosed in the external pressurisation chamber (EPC) (Figure 60(g)) orientated in the vertical direction, with no facility available to

record pressure. Steady flow was provided by a header tank with weir (Figure 60(a)). The working fluid passed through a flow straightner in a settling chamber (Figure 60(e)), attached to 1.5m long pipe which reduced flow vorticity providing stable and fully developed flow at the phantom inlet. The same electromagnetic flow meter (Figure 60(f)) discussed in Section 4.4 was attached just upstream of the phantom to provide real-time entrance flow rate data. Temperature stability was controlled by a feedback temperature control system (Figure 60(k)). Downstream from the compliant phantom there was a 0.5m straight section pressurized to a lower value than the upstream header tank. The geometry of the Mk.I phantom is described in Section 2.4. The rigid phantom is of same length and has an internal diameter equivalent to the unstressed diameter of the compliant phantom (20mm).

As discussed in Section 4.1 Re and α matching was applied for data comparison. To ensure Re similarity Equation 87 was applied and to ensure α similarity Equation 88 was applied where Q is the flowrate and T is the time period. The physiological waveform was produced by superimposing the oscillating component of flow provided by a compressed air pump (Section 4.5.1) (Figure 60(c)) over the steady flow rate supplied by the header tank. The resulting in vitro inlet waveform for the compliant and rigid phantom is displayed in Figure 61. Also provided is the in vivo waveform in the CA as obtained through MRI (Section 4.3). The waveforms closely match during the initial acceleration and deceleration phase, as flow rate plateaus the compliant waveform has a higher flowrate with the waveforms converging in late diastole. Overall the match is satisfactory especially in the early phase where many of the interesting fluid phenomena occur (Chapter 8). The waveform had a maximum, minimum and mean Re of 953, 423 and 614 respectively and an α of 4.54.

$$Q_{in\ vitro} = 3.2 \frac{\nu_{in\ vitro}}{\nu_{in\ vivo}} Q_{in\ vitro} \qquad \textbf{Equation 87}$$

$$T_{in\ vitro} = 3.2^2 \frac{\nu_{in\ vivo}}{\nu_{in\ vitro}} T_{in\ vitro} \qquad \textbf{Equation 88}$$

The waveform follows a similar path to that studied by Perktold and Rappitsch (1995) and Ku et al. (1985) in the acceleration phase, but takes longer to return to the minimum value in the deceleration phase. Their work however had a lower peak and mean Re value, which was 800 and 300 respectively. This study had a comparative α of 4.8. This waveform differs from the waveform studied by Große et al. (2008) and Burgmann et al. (2009) which was

sinusoidal around a zero mean, and This waveform also had a smaller α than any of the test cases that were presented in that work. The work of Eguchi et al. (2003) does not explicitly state the flow rate parameters used in the pulsatile waveform, but from what this author can deduce from the information provided, it operated with a maximum, minimum and mean Re of 955, -318 and 212 respectively with an α of 6.27. The initial acceleration phase follows a similar path to this work, but for a period of the waveform there was negative flow rate (reverse) that is not present in this study.

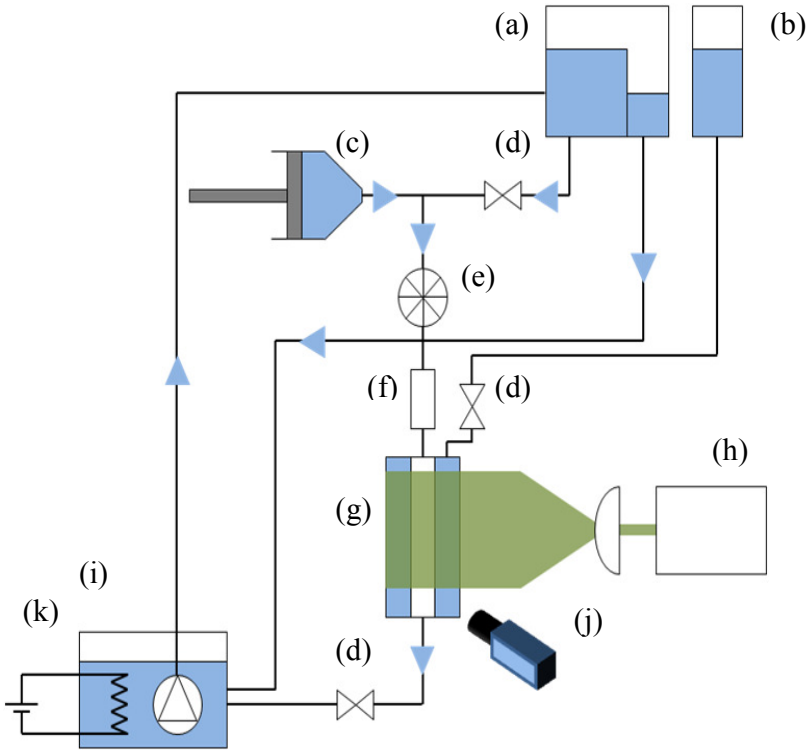

Figure 60 Schematic view of flow system setup, the arrows represent flow direction (a) header tanks with weir for constant pressure (b) external pressure chamber (EPC) (c) Compressed air piston pump (d) ball valves for flow control (e) flow straightner (g) electromagnetic flow meter (h) laser and optics (i) sump with pump and cooling unit (j) PIV camera

The working fluid in this study was a mixture of 39% water and 61% glycerine by weight which provided a refractive index that matched the silicone phantom (n=1.141). It had a kinematic viscosity (ν) of $10.2\times10^{-6}m^2/s$ and a density (ρ) of $1150kg/m^3$ (1. $15g/cm^3$) at 20°C. The Transmural pressure was set to 19.09kPa.

5.3.3 PIV Measurements

Planar digital PIV was used to measure the time varying displacement fields in both the rigid and compliant phantom providing blood flow velocities and WSS data. The PIV technique is extensively discussed in Chapter 3; this section provides only an overview of the experimental setup with Table 18 providing an overview of the measurement parameters. Images were recorded using a single Dantec Flowsense 2MP camera with a CCD array of $1608\times1208 pixel^2$. A 60mm Nikon lens was attached at an aperture of $f^{\#}=8$ and a magnification of 0.25. This gave the experiments an estimated depth of field of 2mm and diffraction limited particle size of 13μm. The flow was illuminated with a 40mm high, 0.5mm thick sheet from a New Wave Solo 120 XT laser with a wavelength of 532nm at 120mJ/pulse using a series of spherical and cylindrical lenses. The flow was seeded with nominally 10 μm diameter hollow glass spheres, which at $1.1 g/cm^3$ were near neutrally buoyant in the water/glycerol mixture. This provided an excellent response to the fluid movement with a response time (τ_s) of ~0.5μs (Equation 24 Section 3.1.1).

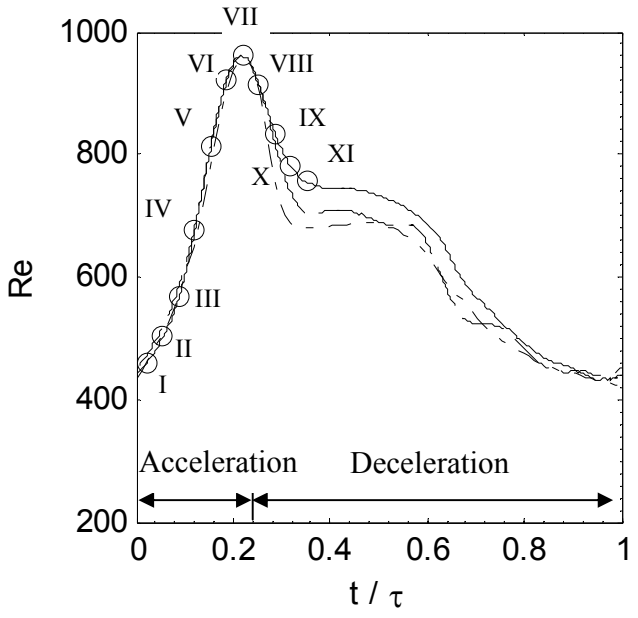

Figure 61 Pulsatile in-vivo (•–), in-vitro rigid phantom (– –) and in-vitro compliant phantom (—) inlet waveform with phase locations at points of interest (t/τ = (I) 0.022, (II)0.055, (III)0.088 (IV)0.121 (V) 0.154, (VI) 0.187, (VII) 0.220, (VIII) 0.253, (IX) 0.286, (X) 0.319 and (XI) 0.352)

The PIV measurements were phase locked, recording 30 image pairs per waveform over 15 waveforms. For time oscillating flow waves the laser pulse time delay selection is a compromise between the variation in maximum pixel displacement for maximum and

minimum flowrate. 1200μs was selected which produced <3% invalid vectors at each phase. After minimum background subtraction, intensity normalisation and masking (Section 3.7), the images were processed with an in-house code implementing 2D FFT cross-correlation (Buchmann 2010) with iterative window sizing (starting at 128x128 and reducing to 32x32 after 2 iterations) and displacement. The data was validated using the signal-to-mean ratio filter and normalised median test (Section 3.6.2.2). In this section phase averaged results of the pulsatile flow are presented. WSS was calculated using the iPIV technique (Section 3.9) with the parameters provided in Table 18.

Table 18 Table of measurement parameters, C and R refer to rigid and compliant respectively

Laser	Type	Nd:YAG, dual cavity
	Thickness (mm)	0.5
Camera	Type	CCD
	Resolution (pix)	1600×1200
	Lens Focal Length (mm)	60
	Lens Aperture (f#)	8
Seeding	Type	Hollow Glass Spheres
	Mean Diameter (μm)	16
	Density (g/cm^3)	1.1
PIV	Window Sizing (pix) Max (Min)	128×128(32×32)
	Resolution (pix/mm)	38.75 (C) 49.95(R)
	Overlap (%)	75
	Vector Spacing (mm)	0.2 (C) 0.16(R)
	Time delay (μs)	1200
iPIV	Interrogation width, M (pix)	32(C) 64(R)
	Interrogation height, N (pix)	80
	Gaussian weight, σ (pix)	10
	Overlap (%)	75
	Vector Spacing (mm)	0.2 (C) 0.32(R)

5.4 Experimental Error

To assess the accuracy of the PIV analysis and the dimensionless scaling applied, Equation 89 was used to calculate the peak flow rate observed in both the compliant and rigid phantom using the velocity profile observed at x/D=0.25. Results were then converted to in vivo scale using Equation 87 and are presented in their Re form. The peak flow rate observed at the inlet from the electromagnetic flowmeter on both the compliant and rigid phantom was Re

953. Applying Equation 89 to the velocity profiles in the compliant and rigid phantom produced a Re of 956 and 950 respectively; in both cases this produces a relative error of 0.3%. When comparing this to the error observed in the work of Buchmann et al. (2010) of 2.7% the results were very favourable indeed. The cause for the increased accuracy observed here was partly due to the attention to detail made in matching the refractive index of the phantoms used, which reduced optical distortions significantly, especially in the regions of high curvature in the vicinity of the phantom walls. It was also due to the increased magnification of the ROI used in this experimental setup. The accuracy of the electromagnetic flow meter as discussed in Section 4.4 was shown to have a relative uncertainty of 1.3%, combining this with an error of 1.9% due to temperature variation in the working fluid (20±0.5ºC) provided a flow system error in Re of ±2.3%.

$$Q = \int u(r) 2\pi r dr \qquad \textbf{Equation 89}$$

It is commonly expected that in PIV there is an error of 0.1 pixel in the calculated displacement (Raffel et al. 2007). For the time delay and resolution given in Table 18, this equated to an error of 0.0021m/s (0.29% of the maximum velocity in the compliant phantom ($U_{max,c}$)) in the compliant phantom and 0.0016m/s (0.21% of the maximum velocity in the rigid phantom ($U_{max,r}$)) in the rigid phantom. The uncertainty in position of the light sheet can also incur an error. A misalignment of the light sheet by half the light sheet thickness (0.25mm) from the plain of symmetry would, for a fully 3D symmetrical flow reduce the centreline velocity by 1%.

Previous error analysis of the iPIV technique has been performed by Buchmann et al. (2010). It was found that with a wall location accurate to ±1pixel the iPIV produced an error in wall shear rate (WSR) of ±0.02pix/pix. This equates to an error in WSS of ±0.15Pa (10% and 6% of the maximum WSS in the compliant and rigid phantom respectively).

5.5 Results and Discussion

5.5.1 Flow Field Analysis

This section provides a quantitative analysis of the flow field in a compliant phantom representing the geometry of an idealised healthy CA. It also presents a quantitative comparison of flow in a compliant geometry against that obtained in a rigid geometry. All

results presented are in vivo scaled. This comparison helps provide a purpose behind producing and studying the more complex compliant geometries and flow field. A schematic of the geometry and the region of interest (ROI) analysed is shown in Figure 62. Experimental analysis was performed at the middle of the compliant phantom, equal distance from the rigid clamped ends. Analysis was performed in the equivalent location of the rigid phantom. Experimental results were obtained in a plane containing the centre axis. The ROI depicted in Figure 62 covered an area 1.5 neutral diameter (unstressed, D) downstream.

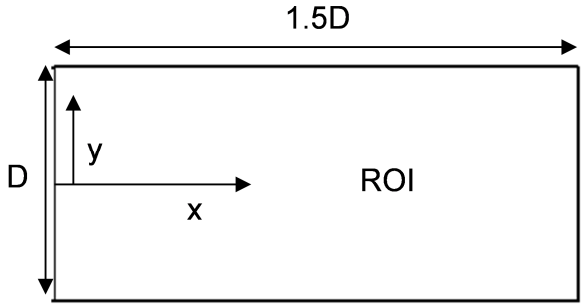

Figure 62 Schematic of flow phantom internal geometry and location of region of interest (ROI)

Figure 63 shows the phase averaged absolute velocity (Equation 90) field and velocity vectors (denoting in-plane velocity magnitude) in the ROI for both the compliant and rigid phantom at peak flow rate (re 953) occurring at phase location VII (Figure 61). Both the radial (y) and longitudinal (x) directions are normalised by D. The flow field results are presented at two locations in the ROI; an upstream (y/D = 0-0.5) and downstream (y/D = 1-1.5) region. At peak flow rate the difference between inlet flow rates for the two phantoms was minimal (±3Re) and the flow rate gradient leading up to the peak flow rate for both phantoms was also equivalent (i.e. the flow acceleration was the same). This allows for a direct comparison of the results obtained at this location.

$$U_{abs} = \sqrt{U_x^2 + U_y^2} \qquad \textbf{Equation 90}$$

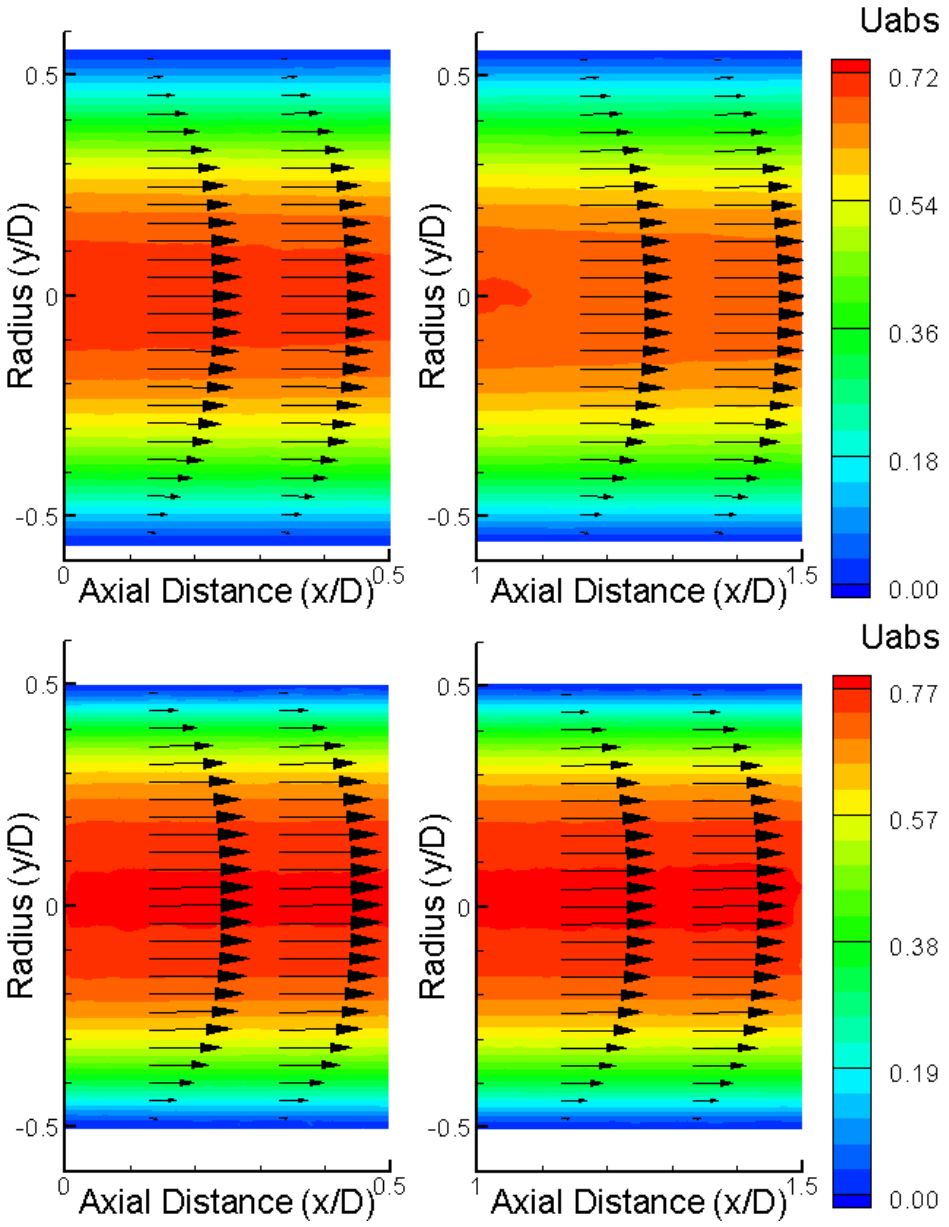

Figure 63 Phase averaged absolute velocity fields (m/s) and velocity vectors for the up (left) and downstream (right) location of a compliant (top) and rigid (bottom) flow phantom at peak flow rate (phase location VII t/τ =0.220 and Re = 953). It should be noted that the difference in contour plot limits between the compliant and rigid flow field

Two distinct differences can be seen between the compliant and rigid phantoms. The first difference observed in Figure 63 is the compliant phantom had a lower maximum velocity of 0.72m/s occurring along the centreline compared to that of 0.77m/s observed in the rigid phantom. This difference at peak flow rate is similar to the observation made by Eguchi et al. (2003). To elucidate further the effect compliance has on the velocity profile of the working fluid through the phantom, Figure 64 presents the comparison of compliant and rigid phase averaged streamwise velocity ($\langle U_x \rangle$) profiles normalised by the maximum velocity in the rigid phantom ($U_{max,r}$) over 1 periodic cycle at the streamwise location x/D = 0.25. The results are shown for phase locations covering the acceleration phase, peak flow rate and the initial deceleration phase (I – VIII), where the flow waveform profiles were equivalent in magnitude. To help further explain these results the phase averaged dilation of the compliant phantom is shown in Figure 65. The phantom wall position at each time step recorded was located using the wall detection technique described in Section 3.7.3. It can be seen that through the acceleration phase the phantom diameter increased in turn increasing the cross sectional area of the phantom increasing the volumetric capacity of the region of interest. Referring to Equation 89, for an equal flow rate input, an increase in cross sectional area will reduce the velocity magnitude across the cross section. This also reduced the gradient of the velocity profile changing the profile when compared to the rigid phantom. At peak flow rate the phantom diameter increase peaked at 22.45mm, this gave the geometry boundary a radial location of y/D = 0.55. This as discussed previously reduced the peak velocity experienced in the compliant phantom when compared to the rigid phantom.

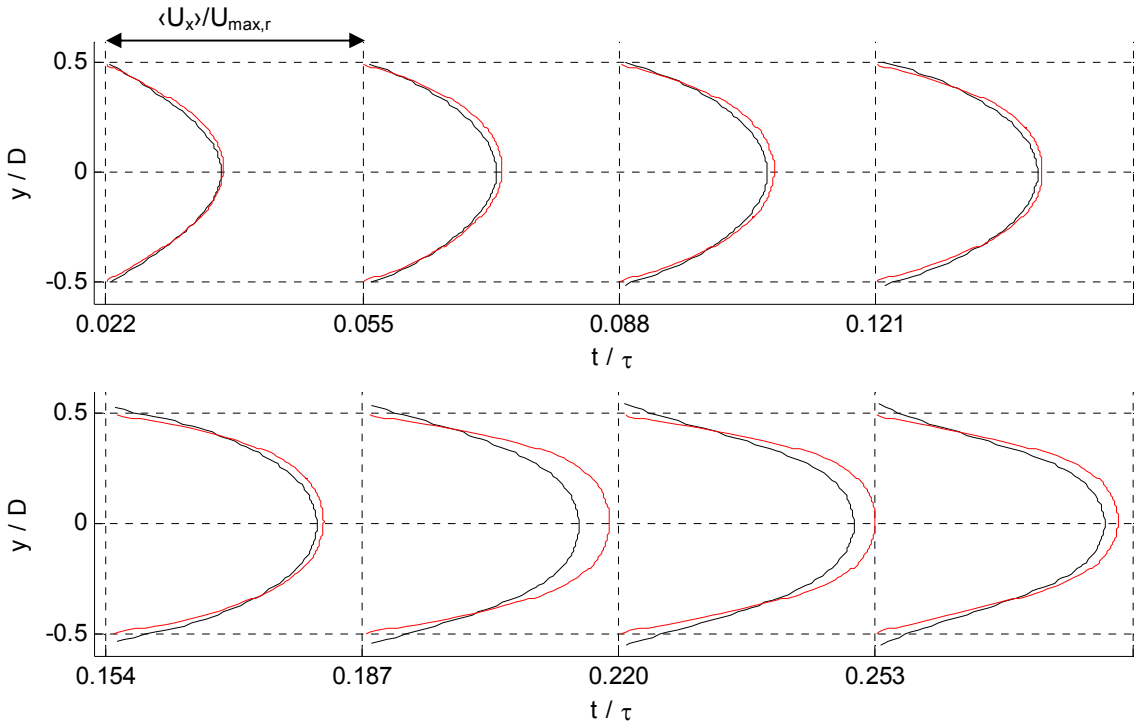

Figure 64 Comparison of normalised phase averaged streamwise velocity profiles ($\langle U_x \rangle / U_{max,r}$) for both compliant (black) and rigid (red) geometry at selected phase locations indicated in Figure 61 (t/τ = (I) 0.022, (II)0.055, (III)0.088 (IV)0.121 (V) 0.154, (VI) 0.187, (VII) 0.220 and (VIII) 0.253) at x/D = 0.25

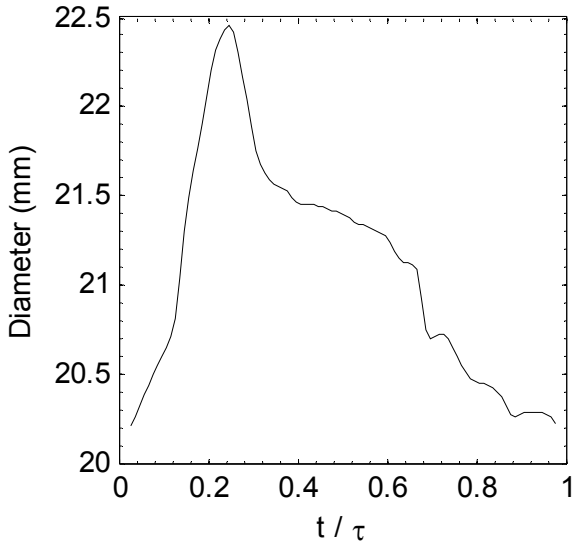

Figure 65 Phase averaged dilation of the compliant phantom at x/D = 0.25.

Figure 66 presents the normalised phase averaged centreline streamwise velocity of both the compliant and rigid flow phantom. To validate whether the variation in centreline velocity is caused by phantom dilation rather than a by-product of the variation in inlet flow wave that

was experienced at the phantom entrances; Figure 67 presents the relative difference (calculated using Equation 86) between the rigid and compliant phantom for both the inlet flow rate and the centreline velocity at x/D = 0.25. It is shown in Figure 67 that between $0.154 \leq t/\tau \leq 0.286$ there was a large variation in the relative difference between centreline velocity and inlet flow rate. The reduction in centreline velocity in the compliant phantom compared to the rigid phantom in this region is therefore produced by the dilation of the phantom. It can be seen in Figure 65 that this was the region of maximum dilation.

From $t/\tau = 0.36$ onwards the compliant centreline velocity is actually larger than the rigid velocity, which is similar to observations made by Eguchi et al. (2003). In this work the difference was actually caused by the difference in inlet flow rate. Between $0.36 \leq t/\tau \leq 0.48$ there was a second deviation of the relative difference of the centreline velocity from the relative difference of the flow rate. This was due to a secondary peak occurring in the rigid phantom flow waveform. Between $0.48 \leq t/\tau \leq 1.00$ the variation in relative difference of centreline velocities and flow rate follow a similar waveform. As flow rate reduced in magnitude, the compliant phantom diameter reduced and any difference observed in centreline velocity observed in this region is dominated by the variation in inlet flow waveform rather than an effect of compliance. It leads to the question of whether the work of Eguchi et al. (2003) actually produced exact replicas between flow waveforms in the rigid and compliant geometries, it is hard to ascertain this from the published data. From the experience of the author it is highly unlikely they were able to produce an exact replica of the waveform due to the complexities of constructing physiological waveforms in compliant models.

The similarity observed in the relative difference in flow rate and centreline velocity also serves as a validity check of the acquired change in velocity, with variation in relative difference calculated via PIV, mirroring that obtained by the electromagnetic flow meter.

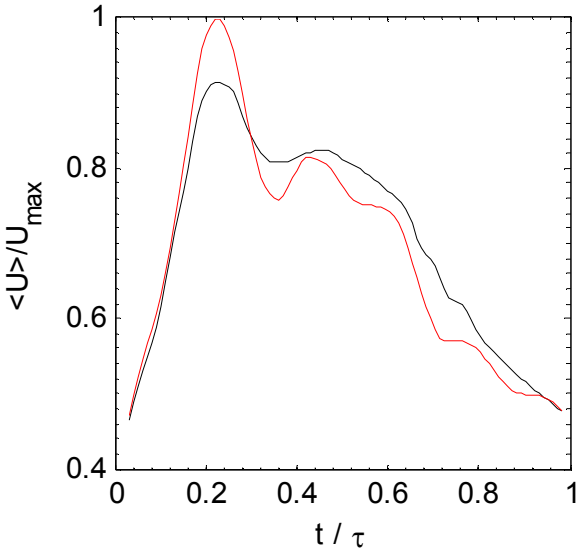

Figure 66 Normalised phase averaged centreline streamwise velocity ($\langle U_x \rangle / U_{max,r}$) of the compliant (black) and rigid phantom (red)

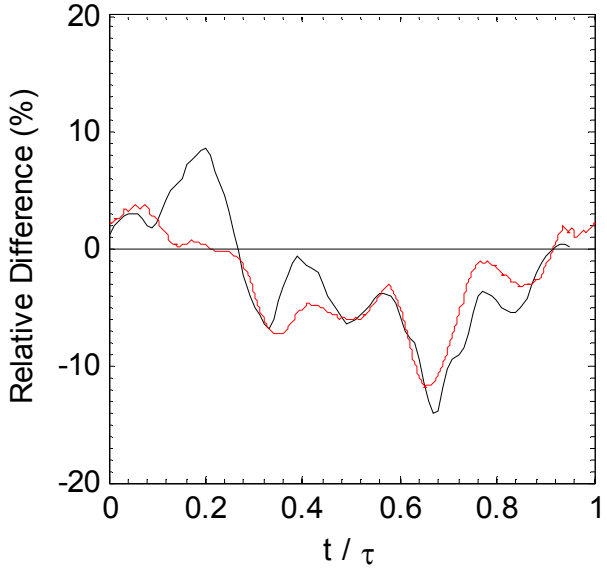

Figure 67 Temporal evolution of the relative difference (calculated using Equation 86) between rigid and compliant data for the inlet flow rate (red) and centreline velocity (black) at x/D = 0.25

The second difference observed in Figure 63 is the change in velocity magnitude observed between the upstream and downstream regions in the compliant flow field that is not observed in the rigid flow field. To understand the temporal variation of this phenomena Figure 68 shows the normalised phase averaged velocity profiles at x/D=0.25 (upstream) and x/D=1.25 (downstream) for the compliant phantom at the phase locations indicated in Figure

61. Figure 69 shows the equivalent phase locations for the rigid phantom. Table 18 presents the difference in centreline velocities obtained from Figure 68 and Figure 69. The results show a 'lag' in the velocity propagation downstream in the compliant phantom as it accelerates to peak flow rate at t/τ =0.220 where the upstream velocity leads the downstream velocity with the difference reaching a maximum of $0.044U_{max,c}$. As flow decelerated from $0.22 \leq t/\tau \leq 0.352$ the 'lag' reversed with the downstream velocity now leading the upstream velocity. The downstream velocity has the largest magnitude with the difference reaching a maximum of -0.29 $U_{max,c}$. Between $0.352 \leq t/\tau \leq 1$ minimal variation in the velocity profiles was observed. In the rigid phantom the difference between upstream and downstream velocity magnitude was minimal, reaching a maximum of $0.005U_{max,r}$. This sort of variation in the rigid data can be attributed to errors occurring due to PIV analysis rather than being an effect of the flow field. This phenomenon to the author's knowledge has not been presented in previous work. It is possible that the alignment of the light sheet along the centre axis could account in part for the variation in velocity, but due to the 'lag' reversal observed in the deceleration phase this is unlikely to be the reason.

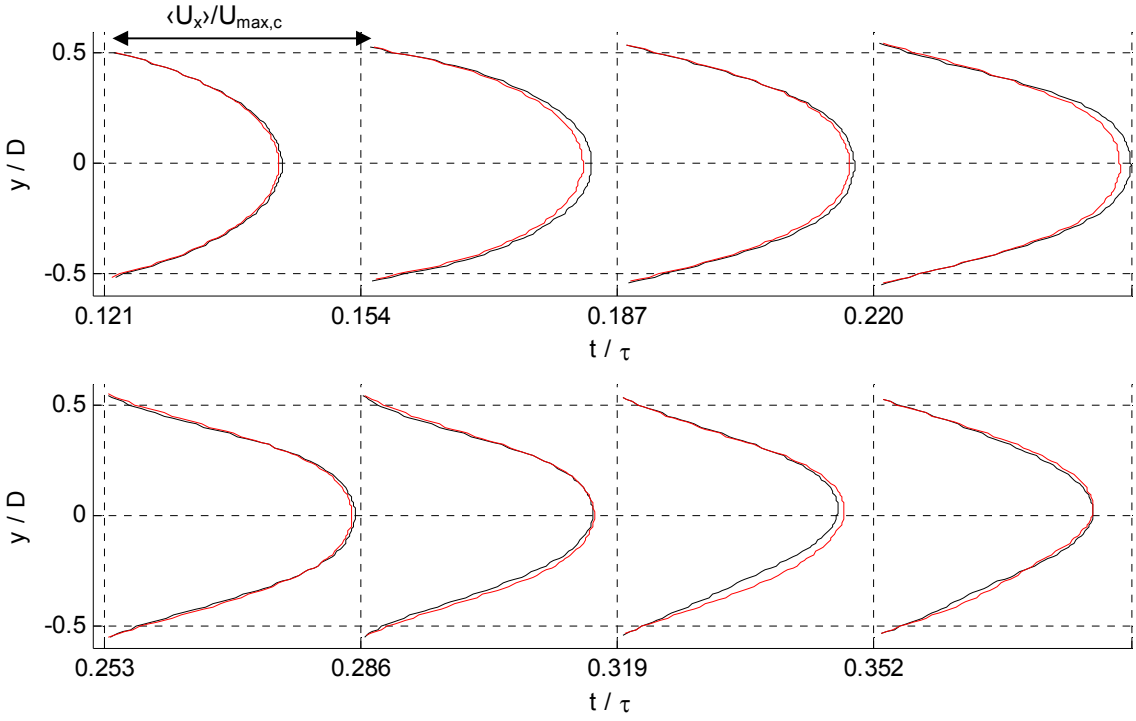

Figure 68 Comparison of upstream (x/D=0.25 (black)) and downstream (x/D=1.25 (red)) Phase averaged stream wise velocity profile normalised by the maximum velocity in the compliant phantom ($\langle U_x \rangle / U_{max,c}$) in a compliant phantom of the CCA at selected phase locations indicated in Figure 61 (t/τ = (IV)0.121 (V) 0.154, (VI) 0.187, (VII) 0.220, (VIII) 0.253 (IX) 0.286, (X) 0.319 and (XI) 0.352)

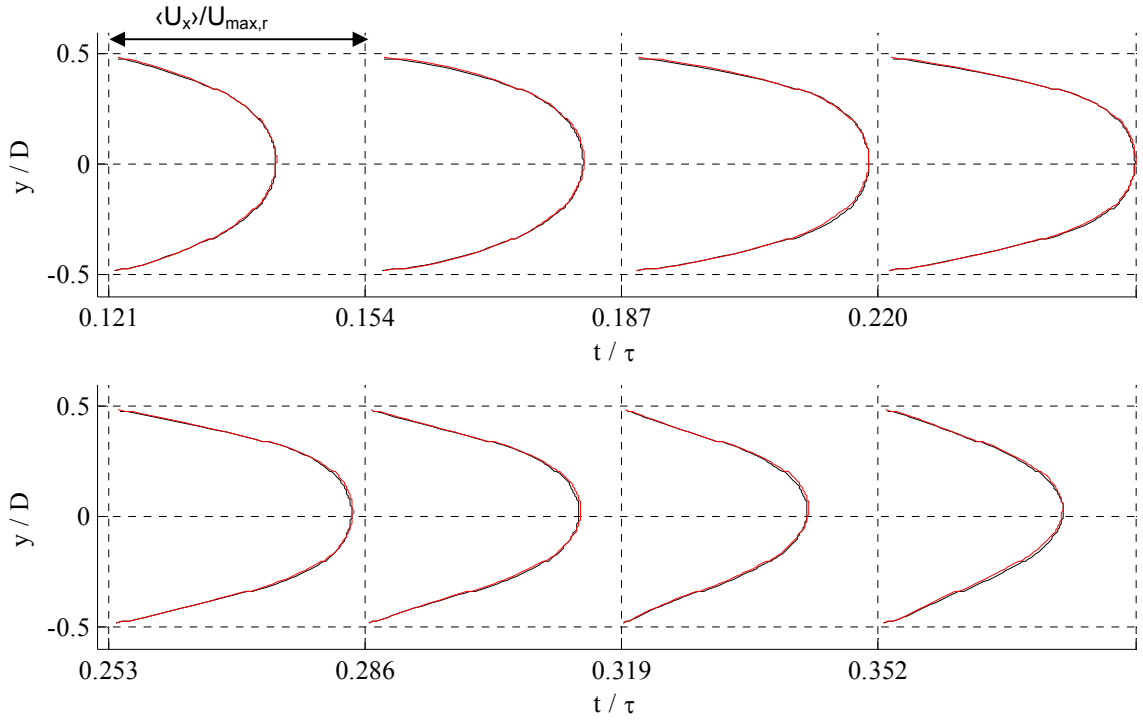

Figure 69 Comparison of upstream (x/D=0.25 (black)) and downstream (x/D=1.25 (red)) Phase averaged stream wise velocity profile normalised by the maximum velocity in the rigid phantom ($\langle U_x \rangle / U_{max,r}$) in a rigid phantom of the CCA at selected phase locations indicated in Figure 61 (t/τ = (IV)0.121 (V) 0.154, (VI) 0.187, (VII) 0.220, (VIII) 0.253 (IX) 0.286, (X) 0.319 and (XI) 0.352)

Table 19 Difference between normalised centreline velocity at x/D=0.25 and x/D=1.25 in a compliant and rigid phantom of the CCA

t/τ	Centreline difference Compliant ($\langle U_x \rangle / U_{max,c}$)	Centreline difference Rigid ($\langle U_x \rangle / U_{max,r}$)
0.121	0.0107	-0.0012
0.154	0.034	-0.003
0.187	0.018	0.001
0.220	0.044	-0.001
0.253	0.0144	-0.0038
0.286	-0.006	-0.005
0.319	-0.029	-0.004
0.352	0.003	0.002

5.5.2 Wall Shear Stress

A comparison of the temporal evolution of the WSS observed in the compliant and rigid phantom at x/D=0.25 is presented in Figure 70(a). Figure 70(b) provides the temporal evolution of the relative difference (Equation 86) between the two results. Results are presented for one wall only as there was minimal difference between the results obtained on

the opposite surfaces. The maximum, minimum and TAWSS in the rigid geometry was 2.3Pa, 0.51Pa and 1.03Pa and in the compliant geometry 1.4, 0.58 and 0.84Pa respectively.

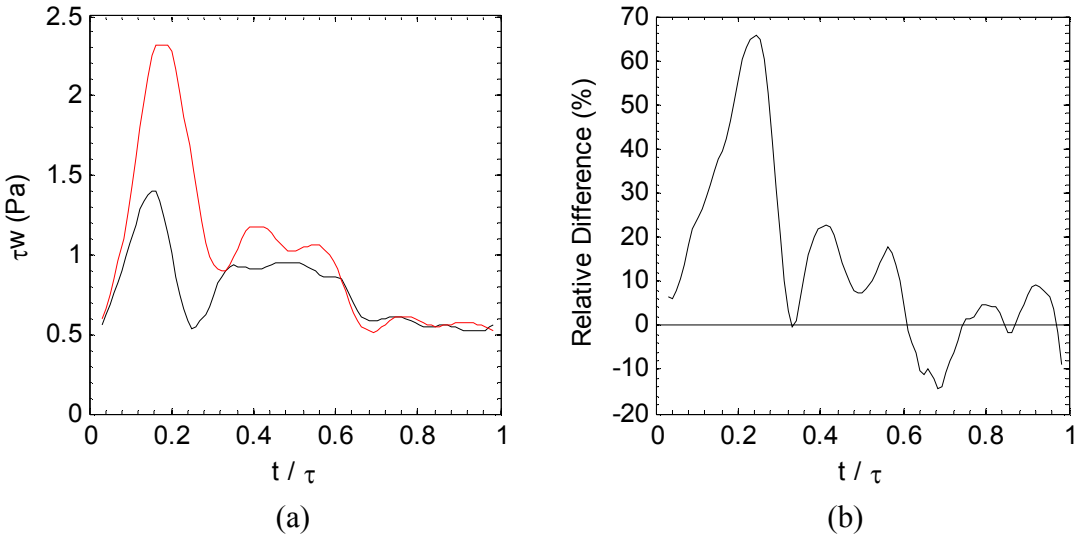

Figure 70 (a) Temporal evolution of the WSS in the compliant (black) and rigid phantom (red) at x/D = 0.25 (b) relative difference of WSS (calculated using Equation 86) between rigid and compliant data

Table 20 presents data on the WSS observed by previous studies in the carotid artery for comparison with the data obtained here, all analyses were performed with a pulsatile inlet flow rate. As previously discussed the work of Buchmann (2010) (chapter 6 section 6.4.2) was performed using the same experimental facility and flow waveform input using iPIV, with the results validated against numerical simulations. Buchmann (2010) performed an analysis of the temporal evolution of WSS in a rigid phantom of the CA which was part of a larger geometry representing the carotid bifurcation. When comparing those results to the results obtained in the rigid structure in Figure 70(a), the waveform is equivalent in Re and the WSS magnitudes are similar. This provides confidence in the data obtained using iPIV and that the correct dimensional scaling of the measurements was applied to this work. The equivalency observed between the results here and the results obtained by Buchmann et al. (2010) in a geometry that led into a carotid bifurcation also shows that the bifurcation downstream of the CA has minimal effect on the flow field dynamics within it and validates the assumption to ignore the geometric change downstream in the current experimental setup. When comparing this result to the three other rigid analysis presented in Table 20, it can be seen the results are in close agreement to the experimental work (Ku et al. 1985), but there is

a variation from the results obtained through numerical simulations (Eguchi et al. 2003; Perktold and Rappitsch 1995).

Table 20 Presentation of WSS data obtained from previous studies in the CA. C denotes results in a compliant geometry, R denotes results in a rigid geometry and N/A is not available.

Study	Condition	Method	WSS (Pa)		
			Max	Min	TAWSS
Ku et al. (1985)	In vitro (R)	LDV	2.8	0.3	0.7
Perktold and Rappitsch (1995)	In vitro (R)	Num	4.44	0.37	1.21
Perktold and Rappitsch (1995)	In vitro (C)	Num	4.15	0.33	1.14
Eguchi et al. (2003)	In vitro (R)	Num	0.01	-0.022	N/A
Eguchi et al. (2003)	In vitro (C)	Num	0.004	-0.018	N/A
Zhang et al. (2009)	In vivo	MRI	1.75	0.45	0.8
Zhang et al. (2009)	In vivo	echoPIV	2.16	0.43	0.92
Buchmann (2010)	In vitro (R)	iPIV	2.4	0.5	1.1
Rigid Phantom	In vitro (R)	iPIV	2.3	0.51	1.03
Compliant Phantom	In vitro (C)	iPIV	1.4	0.58	0.84

In the rigid phantom it is evident that there is a strong temporal variation in the WSS, with the temporal variation following the inlet flow rate waveform closely. A sharp rise can be seen in the acceleration phase with a decrease during the deceleration phase. There was a marked difference between compliant WSS and rigid WSS in this region ($0 \leq t/\tau \leq 0.286$) with a maximum relative difference of 65% occurring at peak flow rate ($t/\tau = 0.22$). This reduction was also observed in the work of Eguchi et al. (2003) however this work only experimentally analysed the difference in velocity profile between a rigid and compliant phantom experiencing a physiological waveform, the WSS results were obtained from the numerical analysis. The numerical geometry had a Young's modulus (E) of $1.13\times10^{6}N/m^{2}$, an internal diameter of 20mm and a wall thickness of 2.5mm; giving it a distensibility (d) (Equation 5 Section 2.2.1) of $7.08\times10^{-6}Pa^{-1}$. The compliant phantom studied in this chapter had a d of $1.29\times10^{-5}Pa^{-1}$ (a lower magnitude d represents a stiffer phantom) therefore would experience a larger dilation for a given input. The numerical prediction presented in the work of Eguchi et al. (2003) showed that for a compliant phantom the WSS was lower compared to a rigid phantom The reduction is however less than that observed in this body of work. The results also showed far lower magnitudes of WSS over an entire periodic cycle. The analysis performed by Eguchi had roughly the same peak flow rate as this body of work and the same diameter; it is questionable to the cause of such low WSS values. The numerical

comparison by Perktold and Rappitsch (1995) also showed a reduction in compliant WSS in this region, but the reduction was shown to be vastly smaller in magnitude at 7% compared to the work in this chapter. The numerical models in Perktold and Rappitsch's work had an in vivo internal diameter of 6.2mm. The compliant model had an in vivo wall thickness of 0.31mm and an E of $3.61\times10^{5}N/m^{2}$; this gave it a d of $5.54\times10^{-5}Pa^{-1}$ (again stiffer than the phantom studied in this chapter). The input peak Re was 800 and the waveform had an α of 4.8. A major factor that accounts for the far smaller reduction in WSS observed in that work is the maximum dilation observed was 50% less than that observed in this chapter.

Between $0.286\leq t/\tau\leq0.64$, when comparing the difference in WSS in Figure 70(a) to the difference in centreline velocity observed, a larger magnitude WSS in the compliant phantom would be expected due to the larger centreline velocity, which is not the case. From $0.64\leq t/\tau\leq1$ the WSS values are relatively similar between compliant and rigid phantoms, which is similar to observations by Eguchi et al. (2003).

When comparing the compliant WSS results to that of previous in vitro and in vivo studies it can be seen the maximum, minimum and TAWSS of 1.4, 0.58 and 0.84Pa in the compliant phantom are in good agreement with the in vivo results obtained through MRI by Zhang et al. (2009) but are lower in magnitude in comparison to data presented obtained using echoPIV. This leads to the point that, echoPIV as stated by Zhang et al., leads to an over prediction of the physiological WSS. When compared to the numerical studies there is again a large difference in magnitudes observed.

To understand the cause of the variation in WSS between the compliant and rigid phantom a comparison of the peak-to-peak normalisation (achieved using Equation 91 where F(t) is the time varying component) of the centreline velocity, dilation and WSS is performed for the compliant phantom (Figure 71(a)). The same comparison between the centreline velocity and WSS in the rigid phantom is also presented (Figure 71(b)). In the rigid phantom a phase shift between the waveforms was observed, with the peak WSS preceding the peak centreline velocity by $0.05t/\tau$. Burgmann et al. (2009) also observed this offset in a rigid phantom for a sinusoidal waveform of Re = 1000 and $\alpha = 5$, but with a difference of $0.15\ t/\tau$ (it should be noted this work was not included in the comparison of WSS magnitude due to their work presenting normalised WSS with no numerical value given to the normalising factor). In

Figure 71(a) the offset is shown to increase in the compliant phantom to 0.07t/τ. The cause of this was due to the dilation of the phantom. It can be seen at peak dilation, there was a severe drop in WSS magnitude. Referring back to Figure 64 it can be seen that as the phantom dilated the velocity gradient in the proximity of the phantom wall reduced when compared to the rigid geometry. Equation 48 Section 3.9.1 shows WSS to be directly proportional to velocity gradient therefore the reduction in gradient reduced the WSS. This goes some way to explain the reason the work of Eguchi et al. (2003) and Perktold and Rappitsch (1995) predicted a lower reduction in WSS in compliant geometries. These geometries were stiffer, therefore dilated less causing a smaller change in velocity gradient between the rigid and compliant geometry. Further it can be seen that the WSS reduced to the minimum value experienced in the cardiac cycle at peak centreline velocity (equivalent to peak flow rate), which is not observed in the rigid results.

$$F(t)_{norm} = \frac{2\left(F(t) - \overline{F}(t)\right)}{\max\left(F(t) - \overline{F}(t)\right) - \min\left(F(t) - \overline{F}(t)\right)} \qquad \textbf{Equation 91}$$

The results presented in this study along with the previous studies that have been discussed show that the peak WSS and TAWSS reduce when compliance is introduced to the experimental analysis. This shows that compliance is integral to the understanding of arterial fluid dynamics, as it provides a preventative measure to the production of large magnitude WSS which can lead to the production of atherosclerosis. The results presented in this section show a severe over prediction in peak WSS by rigid boundary assumptions along with an over prediction of the TAWSS. There is however varying results when looking at the effect compliance has on the minimum WSS. In this work little variation was observed, with previous work showing minimal increases and decreases (Eguchi et al. 2003; Perktold and Rappitsch 1995). It is expected at low Re that WSS predictions between compliant and rigid geometries would be similar as the internal diameter of the compliant geometry would be similar to that of the rigid.

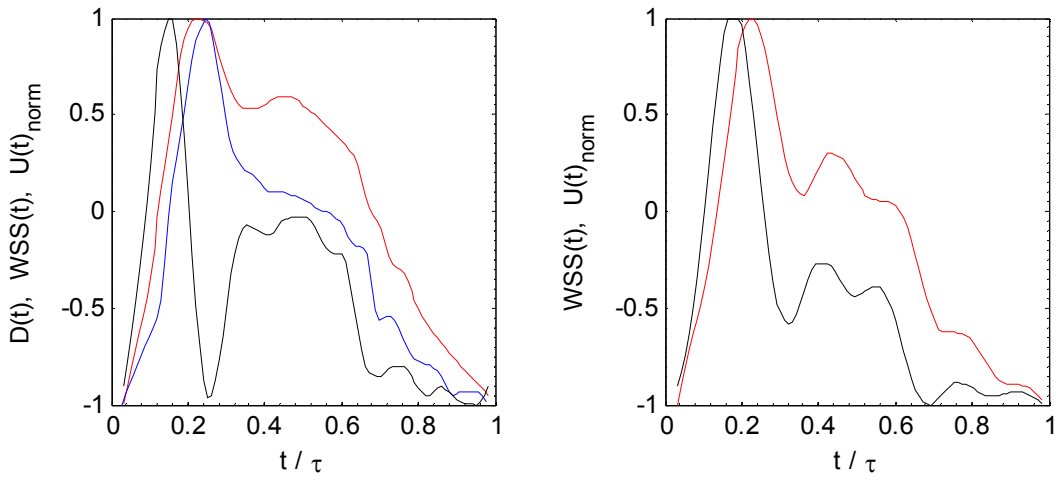

Figure 71 (a) Temporal evolution of the peak-to-peak normalised WSS (black), centreline velocity (red) and diameter (blue) in the compliant phantom. (b) Temporal evolution of the normalised WSS (black), centreline velocity (red) in the rigid phantom

5.6 Conclusion

This section has provided a direct comparison of both the flow field and WSS observed in an experimental phantom of rigid and compliant geometry. Direct comparisons have also been made against previous work. It is evident there is a severe lack of data available on the FSI experienced in the CA. The numerical codes discussed here all present techniques to perform analysis, but only provide preliminary studies. There is an obvious need for their validation. The available experimental data in this area is scarce. This work to the author's knowledge is the first full comparison with quantified differences of a compliant and rigid experimental flow phantom experiencing a physiologically realistic flow wave input. The results have shown the compliant flow field to experience both a temporal and spatial difference to that shown in a rigid geometry. It is also shown that a rigid boundary causes a severe over estimation of the peak WSS and TAWSS experienced. There is however minimal variation shown in minimum WSS, which may not in fact be affected at all. Good agreement in WSS prediction has been shown between the work produced here and the in vivo MRI study by Zhang et al. (2009), along with the experimental analysis by Ku et al. (1985). There is however disagreement with data obtained through numerical simulation (Eguchi et al. 2003; Perktold and Rappitsch 1995).

The experimental setup provided several restrictions and possible sources of error that are accounted for in following studies (Chapter 7 and 8). With the current setup the short exit pipe (0.5m) with subsequent bend in the flow system could be applying unwanted downstream pressure. There was no facility to record pressure, which would help to develop the understanding of physical relationships occurring in the flow field. The design of the EPC was also restricting as it took 24 hours to seal the box, making adjustments to the phantom time consuming.

6 The effect of model compliance on flow and pressure waveforms

The relationship between flow rate and pressure is an important factor to consider when studying the arterial system. Pressure affects wall displacement which as previously discussed is coupled with fluid flow which in turn affects wall shear-stress and the transport of nutrients from blood to the arteries. The main area of concern for this section is the affect transmural pressure (difference between internal and external pressure) has on internal pressure, wall movement and flow rate.

6.1 Introduction

Blood pressure varies throughout the arterial system. The first factor to consider is the hydrostatic pressure acting on the arteries which has a bearing on wall mechanics and transmural pressure. A sphygmomanometer is used by doctors to measure blood pressure in the upper arm; this is approximately in line with the upper chest and the top of the heart which is approximately the location of zero transmural pressure in the human body. The transmural pressure in the arteries of the legs can be up to four times that of the arm raised above chest level with internal pressure increasing in relation to Equation 92.

$$p = \rho g h \qquad \textbf{Equation 92}$$

The transmural pressure experienced by a vessel affects its geometric shape during a cardiac cycle, veins in the arm can collapse due low internal pressure as blood returns to the heart (Caro et al. 1978). A second factor is the driving force of the fluid flow; the unsteady pressure generated by the heart. The shape of the unsteady pressure wave changes throughout the arterial system, due to pressure wave reflections as arteries taper and split off affecting the shape of the pressure profile as it travels through the arterial system (Figure 72). The material properties of an artery affect the relationship between pressure and flow rate.

Hirata et al. (2006) have investigated the effect of arterial stiffening due to increasing age on pressure and flow rate in the carotid artery and have found substantial change in both.

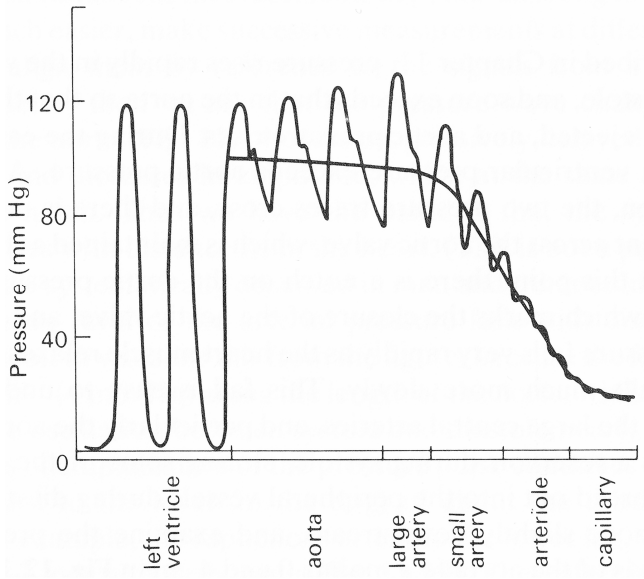

Figure 72 Change in pressure waveform in the arterial system. Figure adapted from (Caro et al. 1978)

Much work has been done experimentally on a phenomenon in compliant phantoms known as flow-rate limitation (Bertram and Tscherry 2006; Bertram and Nugent 2005; Bertram et al. 2004; Bertram and Elliott 2003; Bertram et al. 2001). As previously discussed (Chapter 2), in highly compliant phantoms the flow and the boundary condition are coupled. This causes flow-rate limitation where the flow-rate through the phantom becomes independent of the pressure downstream and can even decrease as pressure drop increases. It is dependent on flow rate and transmural pressure and causes the phantom to execute self-excited oscillations. Bertram et al. (2001) initially studied the velocities just downstream of a phantom experiencing flow-induced oscillations using LDA on a cylindrical phantom with an internal diameter of 12.7mm and wall thickness of 2.4mm. Bertram and Elliott (2003) then went on to compare the effect of flow-rate limitation on thin-walled and thick-walled phantoms and phantoms with tapering thickness. Two stages of collapse were observed, initial buckling from the circular shape and first contact between opposite walls. A hysteresis was observed in results with a difference between behaviour when increasing transmural pressure between runs and behaviour when decreasing it.

Heil and Hazel (2011) provide a review of the experimental advancement in the understanding of phantom collapse. Studies showed that during a particular type of wall oscillation the wall collapses into a figure of eight configuration creating two jet flow structures. The jets impinge on the tube wall near the downstream end of the collapsible segment with the impact creating two regions of elevated axial velocity, with the jets merging further downstream. It is also reported the frequency of oscillation decreased with increased length of the downstream rigid tube, but the change in length does not affect the Re at which the oscillations first develop.

Flow-rate limitation plays a part in the physiological system more prominently in the systemic veins (Bertram and Elliott 2003), in areas of interest in this thesis, like the carotid artery, it is less common but acknowledgement of its occurrence is paramount in the setup of experimentation so as to avoid it affecting the results obtained. This section aims to expand the understanding of the effects phantom geometry and external pressure has on a flow input before flow rate limitation occurs to help define experimental setup conditions for performing physiologically realistic in vitro analysis. There are also questions of the affect tethering of arteries by external tissue like brain tissue for the cerebral arteries has on the artery studied. This effect needs to be taken into account along with the properties of the artery itself. The ultimate goal of this section is to further the argument for creating compliant phantoms as opposed to simpler rigid phantoms to represent arterial structures.

In current work that has studied compliant flow phantoms there seems to be a lack of attention paid or even acknowledgement to the effect the selected external pressure setting (Pielhop et al. 2012; Burgmann et al. 2009; Deplano et al. 2007) of the external pressurisation chamber (EPC) has on the experimental setup. Work has stated that external pressurisation occurs to replicate physiological conditions, but often fails to produce a value of pressurisation used. There is also little to no acknowledgement of the variation with age, with a lot of experimentation being applied to ‘later in life’ diseases it is important for material properties and external pressurisation to reflect this. It is common practice to use Young’s modulus values and (if quoted) external pressure values that are more representative of a young healthy person. Arterial diseases like atherosclerosis are far more likely to occur in middle age to elderly people. The effect of hysteresis should also be considered as the

method of pressurisation either increasing external pressure or reducing external pressure to obtain the required experimental setup needs to be investigated as well.

6.2 Flow wave analysis

The test case waveform input from the stepper motor piston pump in this study was previously discussed in Section 4.7.3. The pump speed programme was set to produce a carotid flow waveform in a 50% symmetric stenosis phantom experiencing a static transmural pressure of 19.09kPa. The peak flow rate was 8.7l/min giving a Re of 954 and the time period was 2.92s giving an α of 4.54. Figure 73 provides the phased averaged entrance flow rate, entrance and exit pressure of this waveform for a single run of 10 cycles.

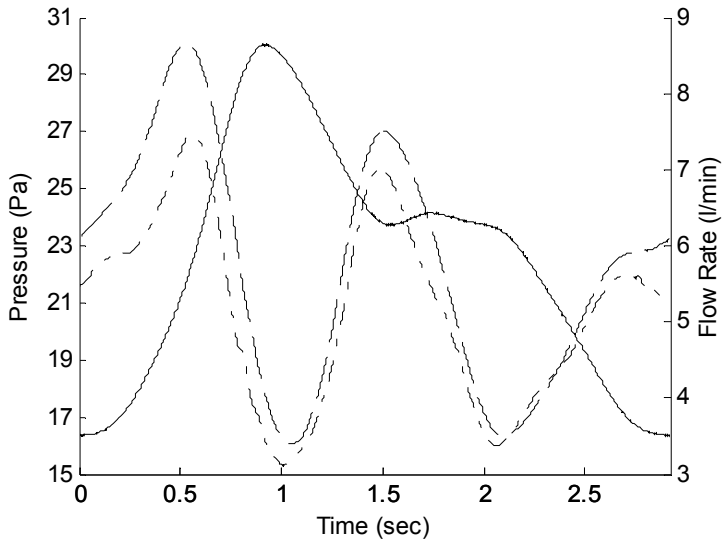

Figure 73 Physiologically realistic waveform average flow rate (-) versus average entrance (- -) and exit pressure (- • -)

The phase lag (θ) of the entrance flow rate to the entrance pressure was calculated using Equation 93

$$\theta = \frac{360\Delta t}{T} \qquad \textbf{Equation 93}$$

The time difference Δt between pressure and flow rate peaks was 0.3875s giving θ = 48º. Referring to previous work by Womersley (1955) and Figure 40 (Section 4.1), it was expected that θ would be ~70º for an α of 4.54. There are several reasons for the large difference between the theoretical Womersley value and the experimental result. In experimentation performed by Womersley (1955) the tube studied was rigid therefore had a

fixed diameter for the entire oscillatory cycle, this obviously is not the case for a compliant phantom. Equation 58 (Section 4.1) shows that α is dependent on diameter so for a compliant phantom it varies as it expands and contracts. Secondly, Womersley (1955) calculated the phase lag for a straight tube with constant diameter in the axial direction. The stenosed phantom used in this study has a constriction in the centre which reduced the diameter by 50%. Haldar (1987) numerically investigated the affect that a symmetric constriction of length two times the unstenosed diameter and of sinusoidal shape had on the θ relationship with α. Figure 74 shows the effect a 12% and 16% reduction in diameter has on the relationship compared to the original (--) Womersley relationship.

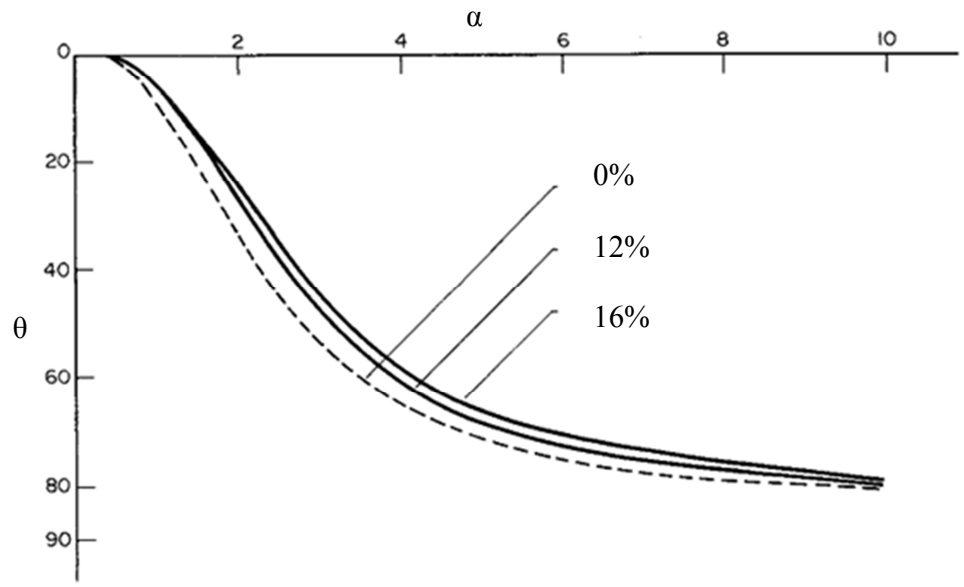

Figure 74 The effect stenosis severity has on the change in phase lag with Womersley number (adapted from (Haldar 1987))

It can be seen that as stenosis severity increases, θ reduces in relationship to α except for the steady flow case (α = 0). At α = 4.54, θ reduces to ~60º. Although it is not possible to deduce from Figure 74 if the reduction of θ is linear with increasing stenosis severity, it can be predicted that for a 50% symmetric stenosis the reduction in θ will increase markedly compared to that of a 16% stenosis. The final point to note is that due to geometric constraints it was impossible to position the pressure transducer and flow meter in the same location in the flow system. The pressure transducer is located ~80mm upstream of the flow meter. The effect this distance has on the phase of the pressure can be regarded as negligible

as it can be seen that there is virtually no phase lag between entrance and exit pressure where the transducers were separated by 350mm.

6.3 Physiological v Sinusoidal

Due to the complexity of producing oscillating waveforms, a common simplification in experimental analysis of physiological problems is to simplify a physiological waveform to a sinusoidal wave with physiologically relevant Re amplitude and α values (Pielhop et al. 2012; Burgmann et al. 2009). Sinusoidal waveforms representing the first two harmonics (0.34Hz and 0.69Hz) of the physiological flow wave presented in Figure 73 are shown in Figure 75. It can be seen that as stated by Womersley (1955), for an increased frequency of oscillation there is a reduction in flow rate produced for a given applied pressure.

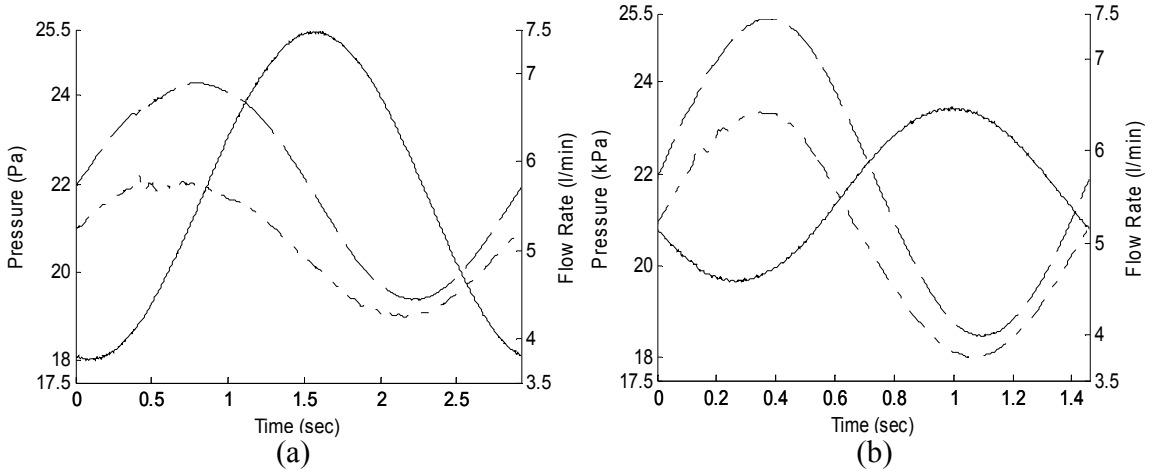

Figure 75 Harmonic 1 (a) and harmonic 2 (b) wave waveform average flow rate (-) versus average entrance (- -) and exit pressure (- • -)

What is apparent from the sinusoidal waveforms is that the shapes of the pressure and flow profiles are almost identical. Producing any sinusoidal waveform with a piston pump requires simply a scaling of the amplitude and frequency of a sinusoidal piston stroke. This is not the case for a physiological waveform as shown in Figure 73 where there is a marked difference in the pressure and flow profiles. The reason for the breakdown in synchronization is due to the arrival of reflected components of the pressure wave. The sinusoidal waveforms have a single dominant frequency which will experience a single dominant wave reflection. The physiological waveform has several prominent frequencies with diminishing power, which produce multiple wave reflections. This increases the complexity of constructing the input required for a piston pump system to produce a physiological waveform.

This restriction that using a sinusoidal waveform as a simplification of the physiological waveform has on experimental results has been demonstrated, especially when wall displacement and pressure are intrinsically linked. The motion of an artery wall is virtually in phase with the pressure waveform (Caro et al. 1978). In vivo invasive measurements of the carotid artery have shown that pressure waveform and artery distension are virtually identical so this relationship is medically used so the carotid artery pressure waveform can be obtained non-invasively using ultrasound to measure the artery distension (Hirata et al. 2006).

6.4 Effect of increasing external pressure

An investigation was performed into the effect varying transmural pressure had on the entrance flow rate, entrance pressure and exit pressure of a physiologically realistic flow wave profile applied to a phantom with 50% stenosis by diameter. Increasing external pressure without inducing flow rate limitation simulates the effect of arterial stiffening that occurs with increasing age. A description of the flow rig is provided in chapter Section 4.4. 10 transmural pressure values varying from 19.09kPa to 3.37kPa were studied. The flow wave was designed for a transmural pressure of 19.09kPa (section 6.2). The piston pump produced the same input piston stroke for each transmural pressure configuration. This was verified by integrating the oscillating flow rate produced by the piston pump at each transmural pressure to obtain the volume of liquid transported (

Table 21). The mean volume was 17.08 litres with a standard deviation of 0.02 litres (0.001%).

Each transmural pressure configuration was void of flow-rate limitation which was verified by physical inspection of the phantom while flow oscillations were applied. Figure 76 shows the phase averaged flow profiles and the effect of increasing transmural pressure. It can be seen with increased external pressure (transmural pressure decreases) and the reduction in phantom dilation this caused, there is a change in the flowrate at the inlet. There is also a change in the entrance pressure waveform. Two hypotheses are put forward to explain this phenomenon.

Table 21 Volume transported by piston pump during a physiological flow cycle at for each transmural test case

Transmural Pressure (kPa)	Volume (l)
19.10	17.06
17.63	17.07
16.45	17.06
14.77	17.06
11.57	17.05
9.60	17.10
8.59	17.10
6.57	17.13
5.11	17.10
3.37	17.10

Knowing that pressure and wall displacement are synchronous it can be hypothesised that as external pressure increases there is a reduction in the expansion of the compliant phantom due to the increased resistance of the phantom to expansion. As previously stated, regardless of transmural pressure the piston produced the same movement of liquid in the system. For higher transmural pressure (lower external pressure) the system has a higher volumetric capacity when flow pressure is high due to increased expansion of the phantom. This acts as a reservoir damping the flow wave and reducing the flow rate at times of high phantom expansion. Phantom expansion reduces as the external pressure increases and the system's instantaneous volumetric capacity reduces resulting in the flow wave progressively synchronising with the pressure wave as there is a reduction in damping effect. This has a greater impact on the second peak as there is a lower flow pressure gradient compared to the first therefore the ability to expand reduces quicker with increasing external pressure. It is theorised for a rigid system the flow wave will match the profile of the pressure wave.

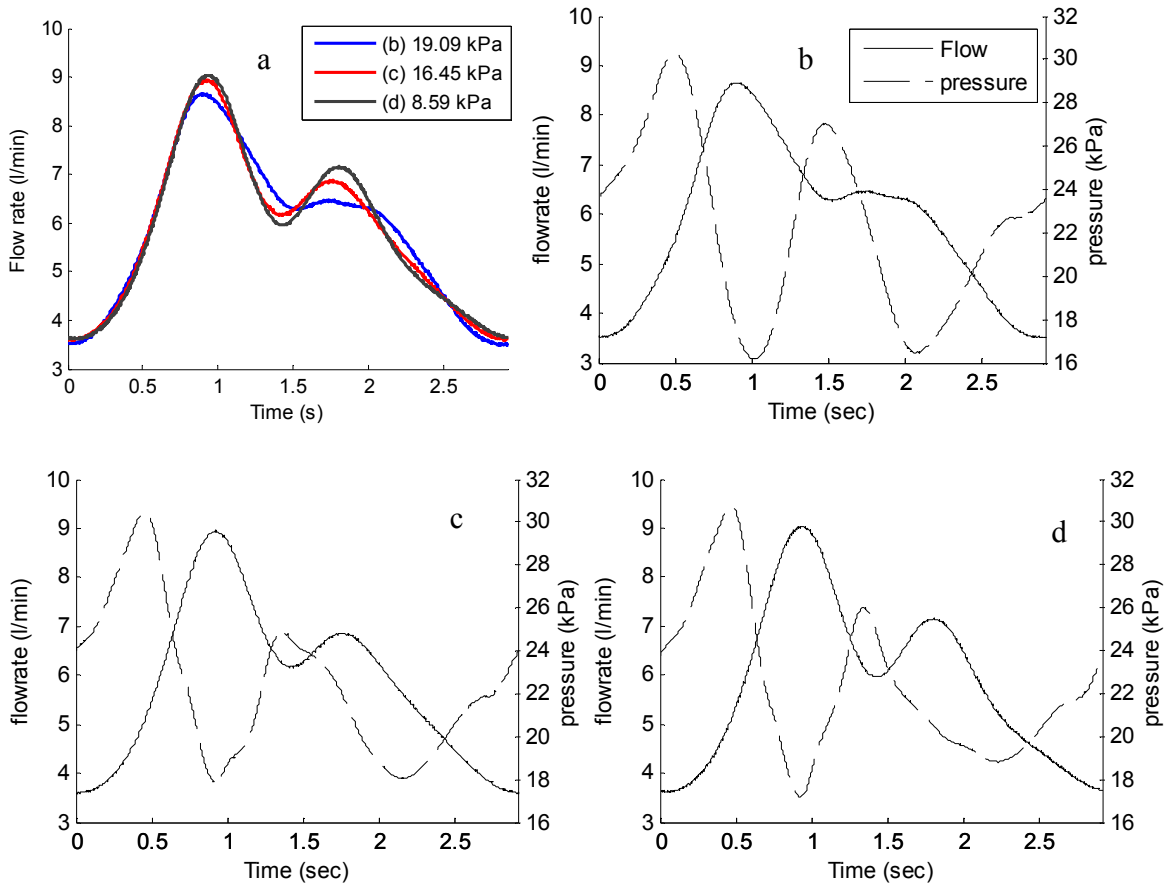

Figure 76 Time averaged profiles of (a) physiological flow rate with increasing transmural pressure and flow rate and entrance pressure for a transmural pressure of (b) 19.9 kPa (c) 16.45 kPa (d) 8.59 kPa

The change in flow rate due to transmural pressure can be quantified by performing a Fourier decomposition of the waveform. The power spectrum provided in Figure 77 shows the first 5 harmonic frequencies of the Fourier series that represent the waveforms. The variation of harmonic strength with changing transmural pressure over all 10 transmural pressure test cases is depicted in Figure 78 (all powers are normalised with respect to the test case waveform (Section 6.2)). Figure 79 provides a Fourier reconstruction of the flow waveform with increasing harmonics from 1-5. Harmonic 1 and 2 vary minimally with increased external pressure. From visual inspection of Figure 79 this result is expected as these harmonics determine the location of the two peaks in the flow waveform, which has minimal change in phase and amplitude with reduction in transmural pressure. The third and fourth harmonics have the highest impact on the waveform shape variation providing an increase in amplitude of the two peaks as transmural pressure reduces. The fifth harmonic, even though

there is a marked variation in its relative size, has little power so there is minimal effect to the overall waveform as can be seen between Figure 79 (d) and (e).

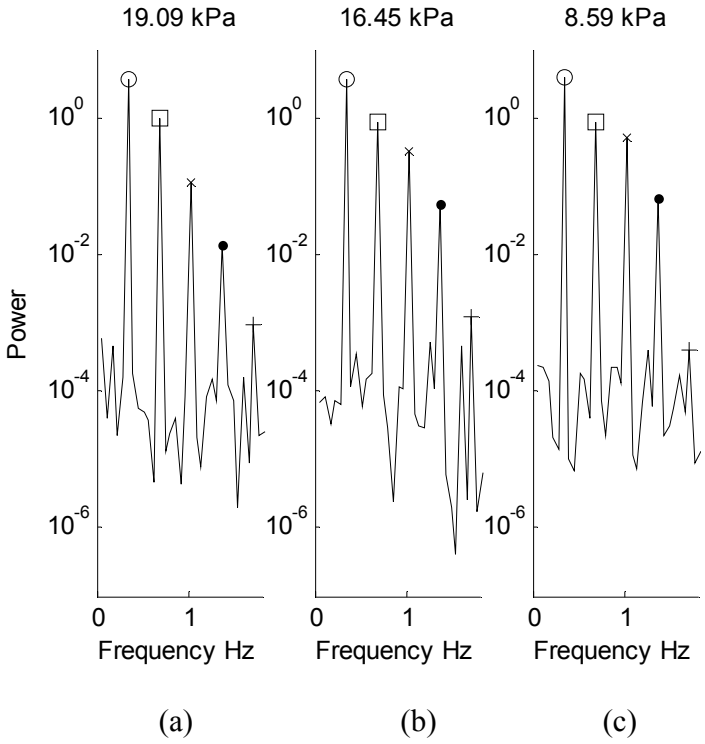

Figure 77 Power spectrums of a physiological waveform in a symmetric stenosis with transmural pressure (a) 19.09kPa (b) 16.45kPa (c) 8.59 kPa

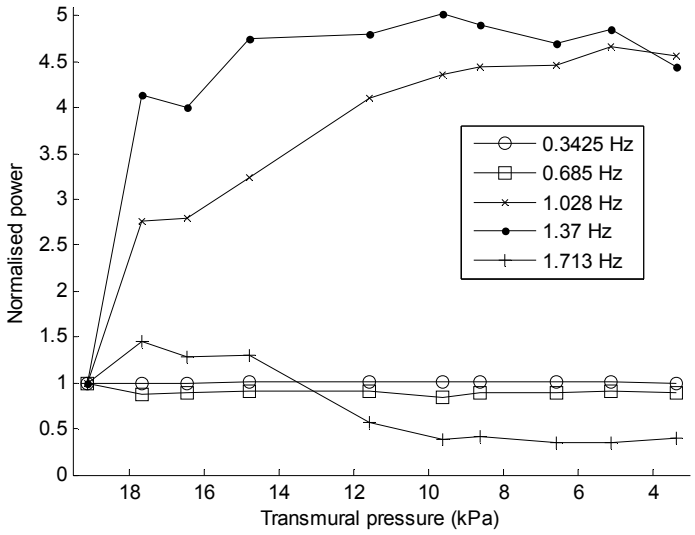

Figure 78 variation of harmonic normalised power spectrum values with transmural pressure

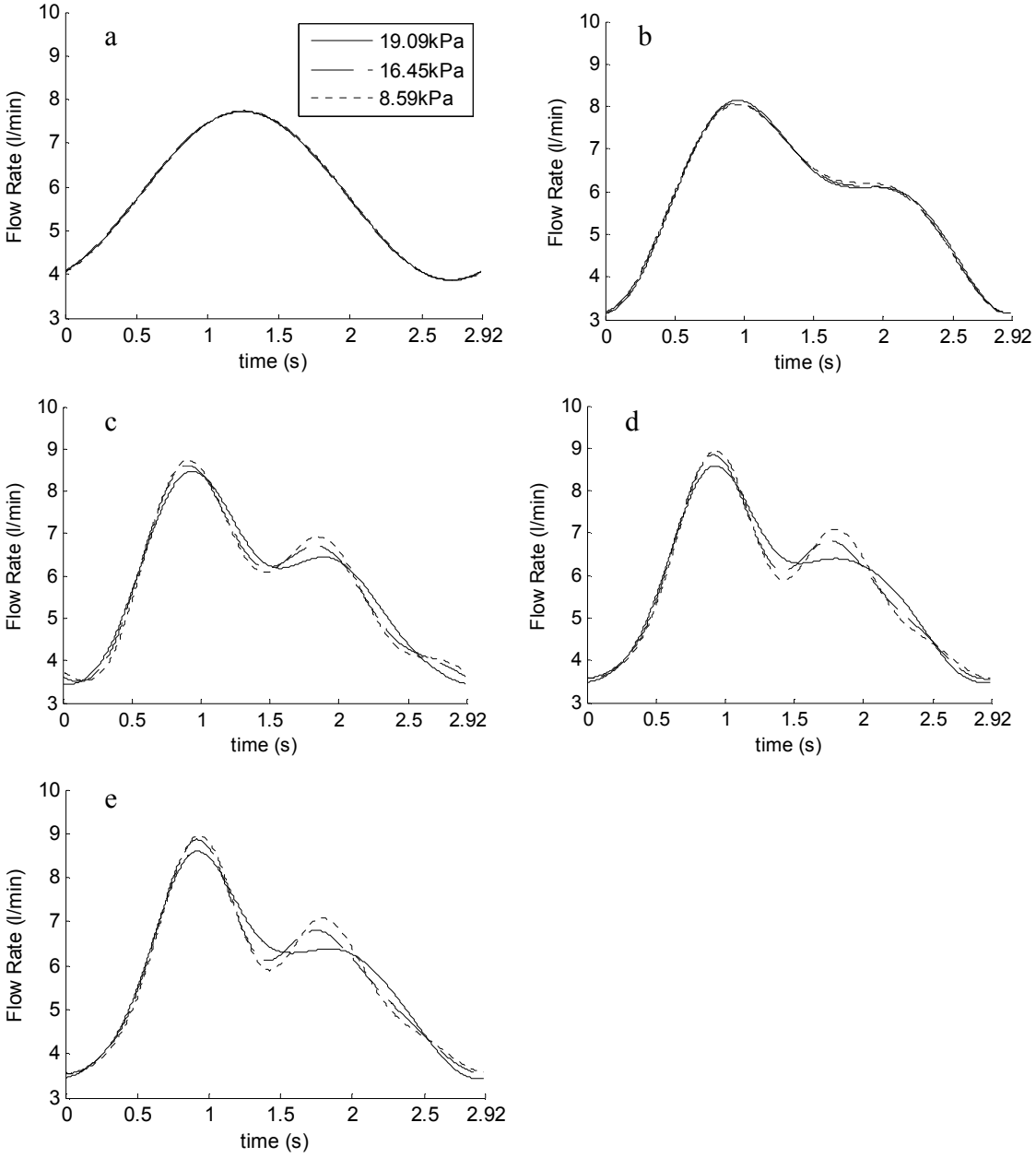

Figure 79 Reconstruction of flow wave from Fourier Harmonics (a) 1 (b) 1-2 (c) 1-3 (d) 1-4 (e) 1-5

The second theory is based on wave reflections, which occur where there is a change in wall properties or geometry, so for the compliant case this is phantom entrance (rigid to compliant), stenosis (reduction and expansion in diameter) and phantom exit (compliant to rigid). As external pressure increases the mechanical properties of the phantom become more 'rigid' therefore reflections at the entrance and exit reduce, bringing the pressure and flow profiles closer to the same shape.

Figure 80 presents the change in phase averaged entrance pressure as transmural pressure is reduced. A definite development pattern can be seen in the profiles especially in the second major peak in the profile. The second peak initially reduces from plot (a) to (b). As transmural pressure reduces further from plot (c) to (j), the peak value of the second peak progressively increases and 'sharpens' in profile. This progression is also shown in the power spectral data shown in Figure 81. The first harmonic (0.3425Hz), which defines the overall peak to trough pressure change, varies minimally. The second harmonic (0.685Hz) gradually reduces as the second peak in the pressure wave occurs at an earlier phase in the flow profile. The observed reduction in the third harmonic followed by a gradual increase describes the initial reduction in the second peak and its gradual increase after plot (b).

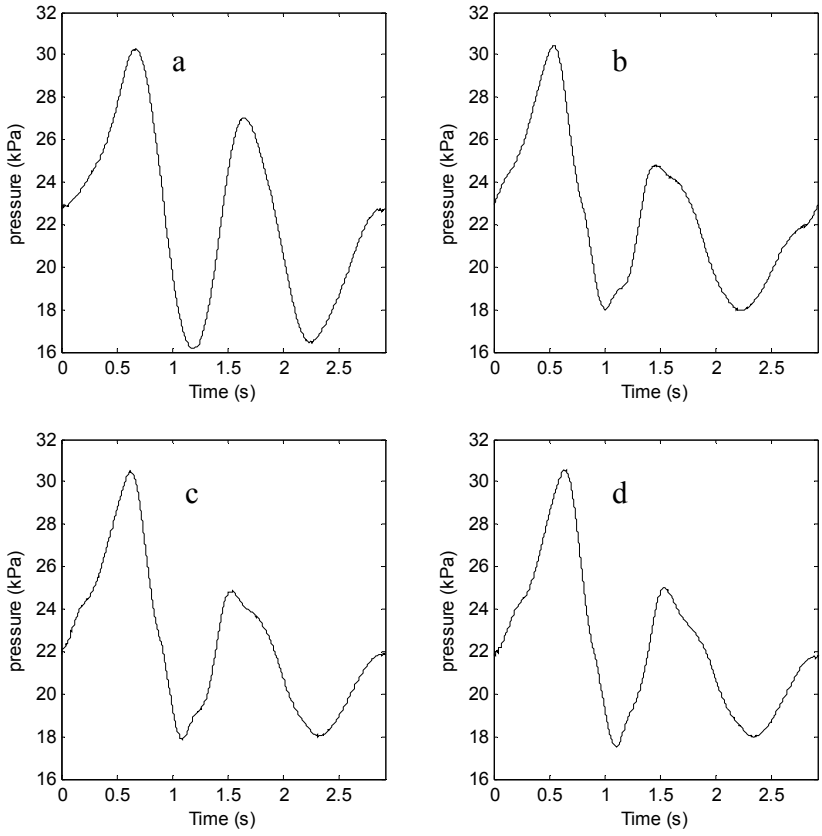

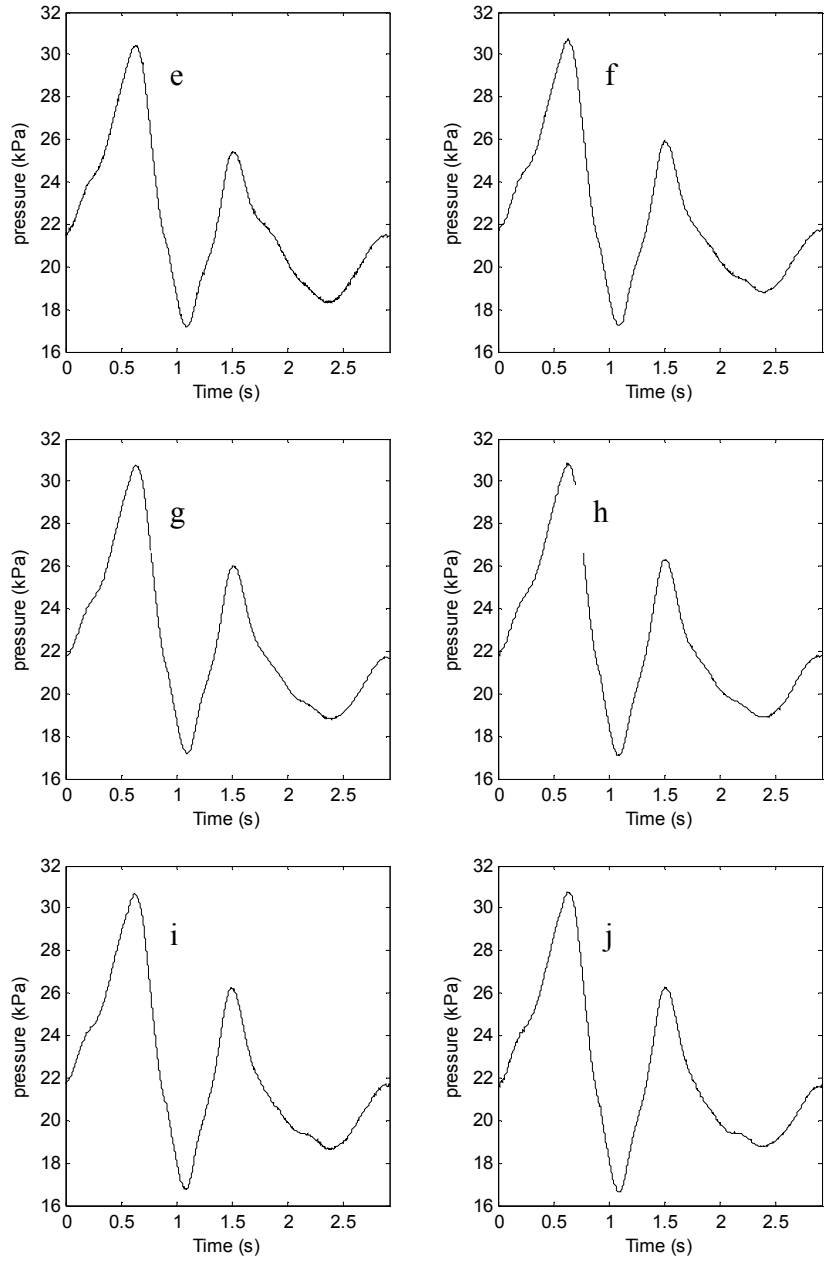

Figure 80 Development of phase averaged entrance pressure profile with decreasing transmural pressure (a) 19.09kPa (b) 17.63kPa (c) 16.45kPa (d) 14.77kPa (e) 11.57kPa (f) 9.60kPa (g) 8.59kPa (h) 6.57kPa (i) 5.11kPa (j) 3.37kPa

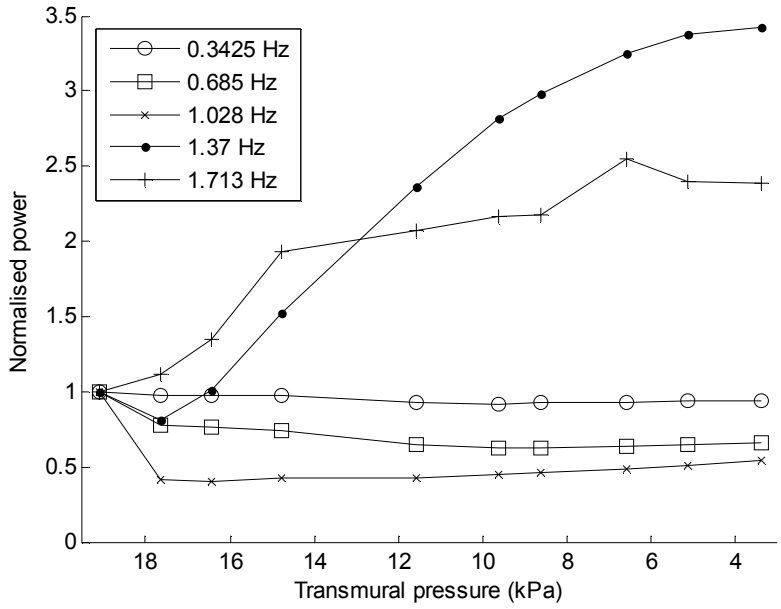

Figure 81 Variation of normalised power spectrum values with transmural pressure for first 5 harmonics

6.5 Effect of Geometric variation

Another assumption that is commonly made to simplify experimental analysis of stenosed geometries is to make the stenosis symmetrical about the axis. In reality in the arterial system it is highly unlikely that atherosclerosis will form a symmetric stenosis and it is important to understand the affect that asymmetry has on experimental analysis. This section compares entrance flow, pressure and exit pressure waveforms for a 50% by diameter asymmetric (Figure 82(a)) and symmetric (Figure 82(b)) stenosis. The waveform input produced by the piston pump is the same one used in the previous section and discussed in section 6.2. Both phantoms experienced the same atmospheric conditions and a static transmural pressure of 19.09kPa.

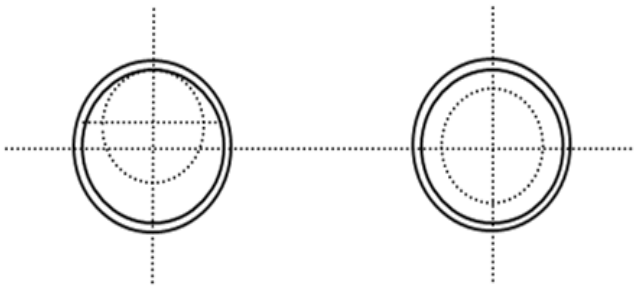

Figure 82 Radial location of stenosis in relation to main phantom centre point (a) Asymmetric stenosis (b) symmetric stenosis

A comparison of the symmetric and asymmetric flow rate (a) and the pressure (b) waveform is shown in Figure 83. There is no change in phase of the flow and pressure between the two geometries and the phase lag of the flow rate to the pressure is 48° in both cases. As previously discussed the oscillating pressure drives flow rate and for $0 < t < 1$ the pressure profiles are almost identical which means that the flow rates are almost symmetrical. There is a smaller reduction in pressure for the asymmetrical geometry from the first pressure peak to the first pressure trough which gives a smaller reduction in flow rate before it enters the plateau region of the waveform. The next pressure rise from trough to peak determines the length of the plateau region; the rise is much shorter for the asymmetric case therefore the plateau in flow rate is markedly reduced.

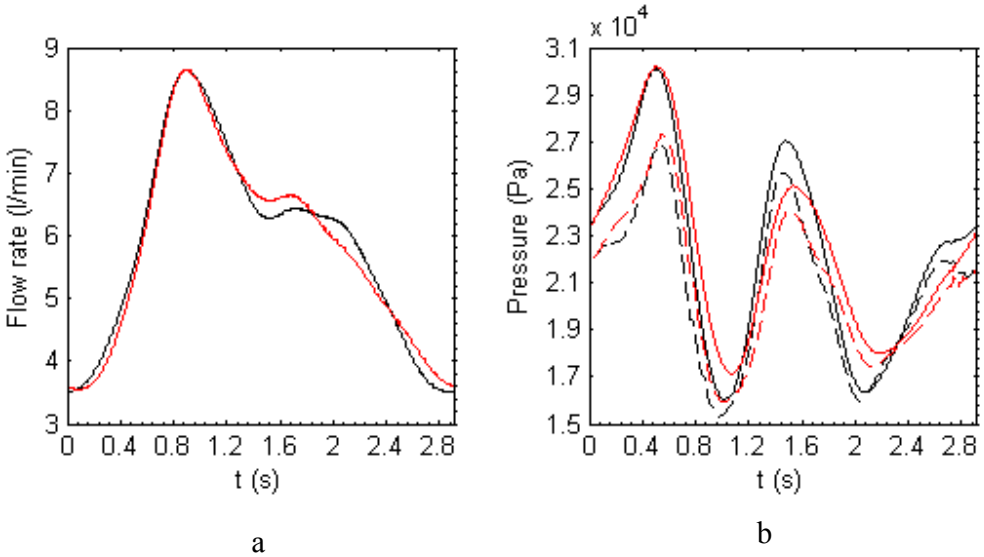

Figure 83 Effect of stenosis geometry on the (a) flow rate and (b) pressure for the symmetric (black) and asymmetric (red) phantom ((-) is the upstream pressure (--) is the downstream pressure)

6.6 Surface Displacement

There needs to be a validation of the theories proposed towards the effect transmural pressure has on flow and pressure waveforms in this chapter. It is also important to produce some quantifiable relationship between wall expansion and transmural pressure. For a straight symmetrical phantom with uniform wall thickness and material properties, PIV images in the centre plane can be used to track wall movement due to an oscillating flow input under the assumption that it will experience a uniform radial expansion. For more complex geometries like an asymmetric stenosis this assumption presents restrictions to the validity of the results. This section provides a preliminary investigation into the use of three-dimensional surface displacement experimental technique that utilises commercially available software[25] to analyse the effect transmural pressure has on wall displacement of stenosis geometries. The analysis technique is primarily designed for deformation and strain analysis of solid, granular and liquid subjects[26]. The aim is to adapt the developed technique of phantom construction so that it can be used in conjunction with this method. For this preliminary study the effect of change in static internal pressure was investigated. Three dimensional surface displacement images were recorded at increasing internal static pressure and compared with an initial zero pressure case.

6.6.1 3D Deformation technique

This section provides a brief overview of the three-dimensional surface displacement mapping technique[27]. The software uses digital image correlation to track surface patterns (natural or applied) as a surface displaces with images coming from a two camera stereoscopic setup. The technique works on a similar principle to SPIV (Section 3.8). The basic process utilises two cameras offset at an angle imaging the displacing surface (Figure 84). The surface is then discretized into interrogation windows and pattern tracking within the window is performed.

[25] LaVision GmbH Strainmaster 3D

[26] www.lavision.de

[27] LaVision GmbH DaVis 7.2 StrainMaster Software Product-Manual

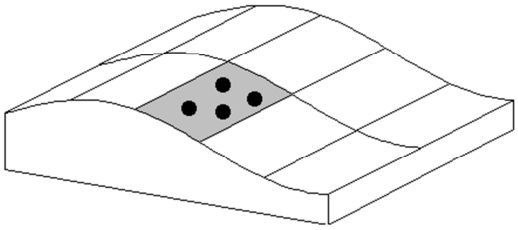

Figure 84 Imaged surface with region of interest

As with PIV a mapping function is obtained through camera calibration to relate the image plane of both cameras with the object plane (Equation 94).

$$\underline{X_i} = \frac{x_i}{\overline{\overline{M}}} \qquad \textbf{Equation 94}$$

To obtain the surface height from images obtained by camera one and camera two the corresponding points between camera one (x_1,y_1) and camera two (x_2,y_2) are found by a correlation process. Combining this with the mapping function the three dimensional object coordinates can be obtained (X,Y,Z) (Equation 95).

$$(X, Y, Z) = f(x_1, y_1, x_2, y_2, M) \qquad \textbf{Equation 95}$$

The above technique works well for smooth surfaces and small variations in surface height. To account for large height variations like the curvature of the phantoms used in this work an iterative process has to be applied. An initial approximation of the surface height is made and the camera images are dewarped into the object plane using the mapping function under the assumption this surface is the correct one. Distortions between the images from camera one and camera two will be due to the difference of the real surface height to the approximate surface height. The residual shift between the dewarped images of camera one and camera two are calculated by cross correlation and then translated into a height correction for the approximate surface height. The new surface height is then used as the initial guess for the loop and the process is repeated until distortion between images is below a predefined tolerance.

After the surface height of the region of interest (ROI) is calculated, vector displacement calculations are performed between image time steps (t and t+Δt) for the individual cameras. Cross-correlation is performed in the image plane of each camera. The mapping function

and calculated surface height distribution for each time step is used to produce the three dimensional surface displacement vectors (Figure 85).

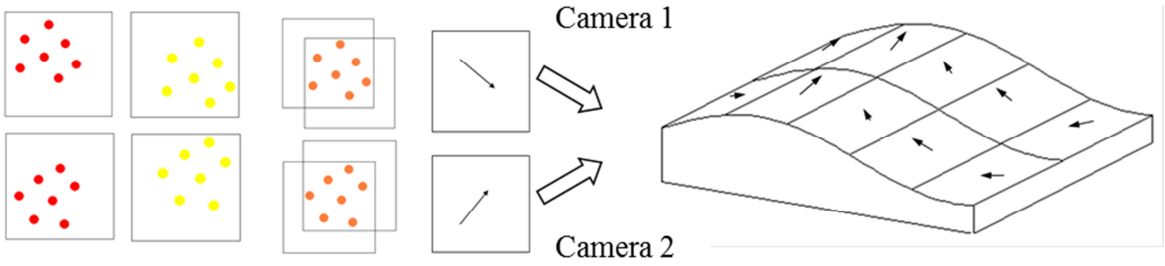

Figure 85 Schematic of surface displacement vector mapping

6.6.2 Experimental Setup

A schematic of the experimental setup is shown Figure 86. The investigation was performed on the mark II flow phantoms (Section 2.4), with both the 30% symmetric and asymmetric stenosis analysed. Phantom and EPC (a) were mounted in a vertical orientation. A straight copper pipe (b) was ported upstream of the phantom and a flexible exit tube with ball valve was ported downstream (c). A water manometer (d) was attached just downstream of the phantom to obtain the internal pressure. Static pressure was varied by increasing the height (h) of working fluid in the inlet copper pipe and the experiment was performed with the EPC void of liquid providing zero external pressurisation of the flow phantom (the purpose of the study was to ascertain the viability of the technique rather than produce physiologically realistic data).

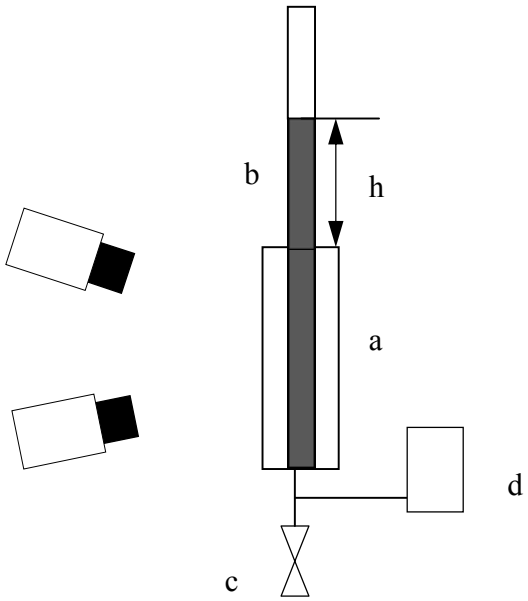

Figure 86 Schematic of surface displacement experimental setup

Refractive matching between solid and working fluid would be detrimental to this experimental analysis as the phantom surface is required to be visible to allow for deformation tracking. The working fluid was therefore distilled water rather than the aqueous glycerol solution used in PIV experimentation. This provides a restriction to the ability to run surface displacement and PIV simultaneously.

The flow phantom was illuminated with a uniform LED light source. Images were obtained with twin LaVision Imager Intense 2 mega pixel CCD cameras with Scheimpflug adapters, the specifications of which can be found in Table 22. The cameras were fitted with the same 60mm Nikon AF Micro-Nikkor lenses used in the PIV experimentation (Table 8 Section 3.4). The cameras were separated by an angle of 36º in the vertical direction and at a 450mm standoff from the EPC. The cameras were calibrated with a calibration routine built-in to the DaVis 7.2 software using a 105 x 105mm LaVision two-level circular marker calibration target plate and a 3rd order polynomial reconstruction. The calibration was performed with the calibration plate inside the EPC with the compliant phantom removed. This calibration utilises the improvement alluded to in Section 3.8.1 with the three-dimensional nature of the calibration target plate negating the need to traverse it through multiple z-planes to obtain a mapping function reducing the experimental error.

Table 22 Surface displacement camera specifications

Specifications	LaVision Imager Intense
Sensor type	CCD progressive scan monochrome
Sensing area (mm)	8.3 x 6.6
Cell size (μm)	6.45
Effective pixels	1280 x 1024
Frame rate (Hz)	10
Output quantization (bit)	12
Frame separation (μs)	0.5

An initial attempt was made to track natural features of the flow phantom surface which would allow the phantoms to be used multiple times for PIV and surface displacement analysis, results from this were poor and the images did not provide enough pattern definition to perform a surface displacement analysis. Two methods of surface treatment of the flow phantom were trialled to produce adequate surface patterns. The first method and was the light application of black spray paint. A single pass of the spray can across the phantom surface produced a contrast pattern of ≈200μm black spots. The drawback to this method was the challenge to obtain an even coat of spray paint. The second method was the application of stone textured spray paint[28]. This produced a well-defined surface pattern for tracking, but the paint requires reapplying every 50 experimental runs due to cracking and peeling. The second method was the technique ultimately used for experimentation as it provided the best pattern for tracking. Figure 87 provides images of the two surface treatment methods.

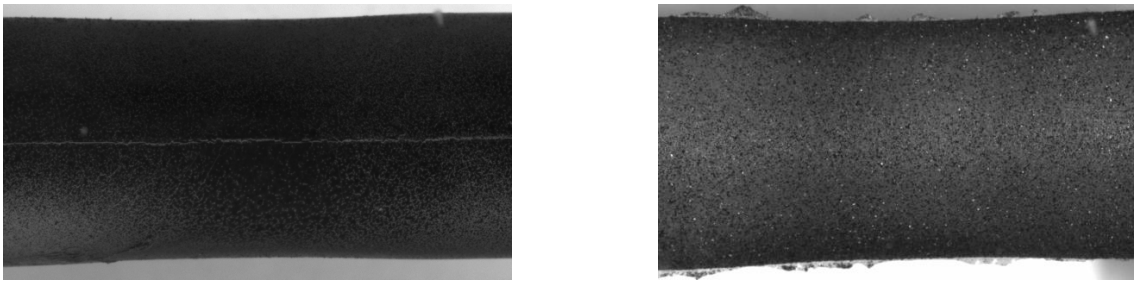

(a) (b)

Figure 87 Spray paint surface treatment (a) black spray paint (b) textured spray paint

[28] Krylon Make It Stone!® Textured Paint

Ten images were acquired at each loading condition. For static (zero flow) tests, images were taken with the flow circuit empty and then filled to a given height. Background subtraction and masking routines built-in to the DaVis 7.2 software similar to those discussed in Section 3.7 were applied to each image data set. Three-dimensional surface displacement due to static loading was then calculated using DaVis 7.2 StrainMaster (LaVision GmBH) software.

6.6.3 Results and Discussion

Figure 88 shows the surface displacement map for a 30% stenosed symmetric and asymmetric geometry experiencing a static pressure change of h=955mmH_2O (9.365kPa). The Asymmetric results provide two viewing directions, one with the maximum wall thickness located on the opposite side from the camera (Figure 89(a)) and one with the maximum wall thickness on the same side as the camera (Figure 89(b)). The vector arrows are scaled up by a factor of 10 to make them more pronounced in the image.

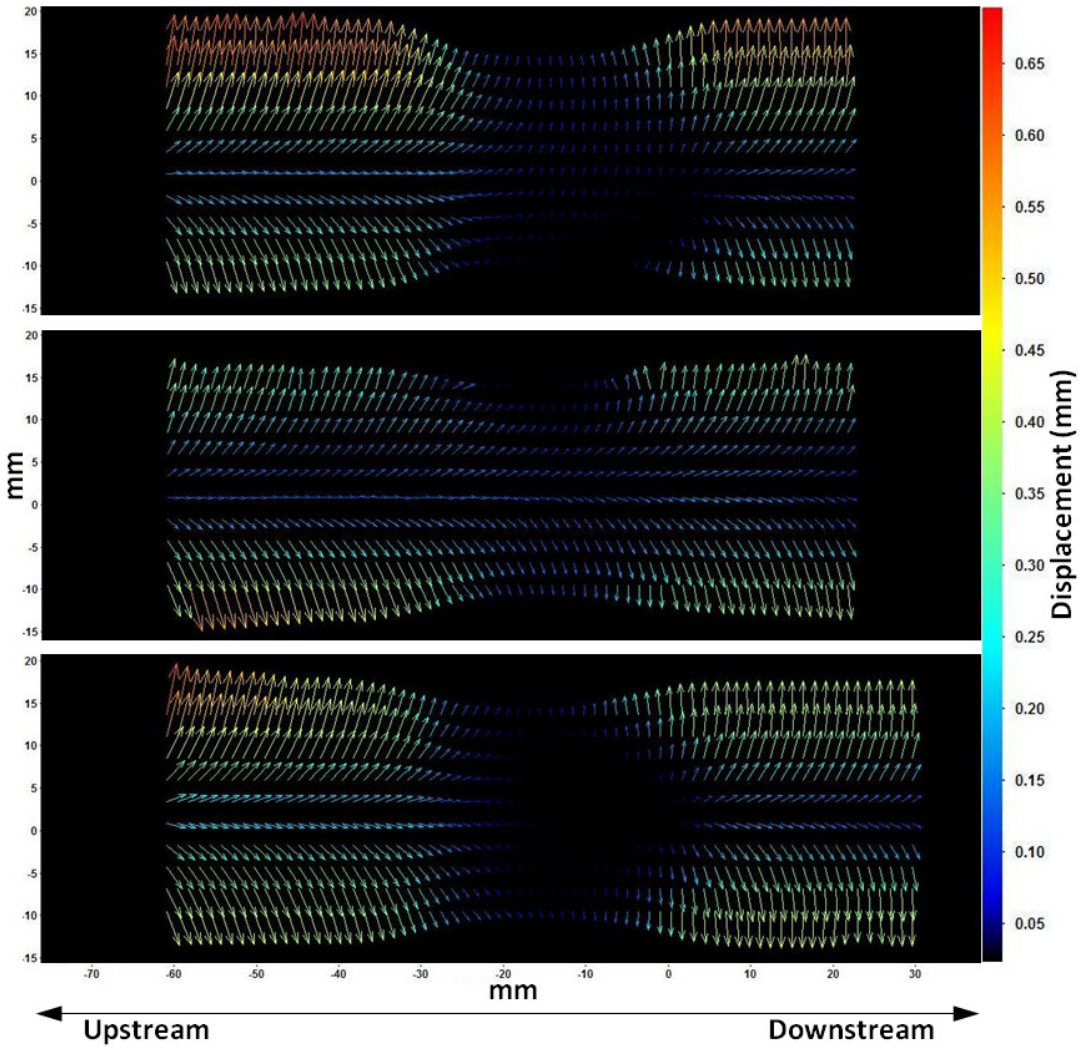

Figure 88 Surface displacement results for an applied internal static pressure of 9.365kPa (top) symmetric stenosis (middle) asymmetric stenosis camera orientation 1 (bottom) asymmetric stenosis camera orientation 2 (refer to Figure 89)

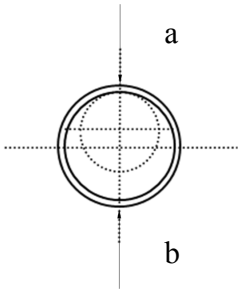

Figure 89 Asymmetric stenosis, centre lines show location of the centre of the main phantom and the centre of the stenosed section at its smallest radius. The viewing directions were (a) Camera orientation 1 (b) Camera orientation 2

The symmetric stenosis displacement field shows a progressive reduction in displacement as the thickest part of the stenosis is approached from the upstream direction, as expected.

Above the stenosis displacement vectors display both axial and radial components. Below the stenosis the axial component reduces to near zero. The hydrostatic pressure has caused the phantom above the stenosis to bulge and sag. The sagging occurs due to a propagation of expansion axially along the phantom from the entrance due the internal pressure and the weight of the filled phantom above the stenosis. There is no axial component (sagging) below the stenosis as phantom expansion was restricted by the stenosis and has to reinitiate. It is expected that as the phantom exit is approached, sagging would increase again due to a second axial propagation of the phantom expansion. This phenomenon will only occur for a constant applied pressure to the phantom wall, for oscillating flows the phantom experiences an oscillating internal pressure and the phantom expansion is related to the propagation wave (Section 2.2.2).

The asymmetric stenosis presents the same sagging upstream of the stenosis as experienced in the symmetric stenosis. For camera orientation 2 with the thickest section of the phantom orientated towards the camera there is similar response downstream with axial displacement near zero. For camera orientation 1 the wall thickness in the stenosis region increases radially from an initial unstenosed value. This equates to less restriction on radial expansion as evident with vectors present across the stenosed region. There is also an increased radial expansion from the first two cases discussed.

Further investigation needs to be performed with a time oscillating flow to ascertain if this technique can provide a full understanding of wall displacement due to oscillating pressure. It would also be preferential to be able to perform the experimentation simultaneously with PIV analysis. This would require a method of tracking the wall displacement while the fluid is refractively matched to the silicone. A technique that should be investigated is adding fluorescence to the silicone phantom during curing similar to Pielhop et al. (2012).

6.7 Conclusion

This section highlights the importance transmural pressure has on experimental results produced when analysing a compliant flow phantom. The shortcomings associated when idealising a physiological flow wave as a sinusoidal flow wave were presented. It has been found that as external pressure increased (increasing the stiffness of the phantom) the pressure and flow waveform shape becomes similar. It is therefore a sensible assumption to

make that any experimentation performed in a rigid phantom (Buchmann et al. 2011; Tateshima et al. 2003a) will have pressure and flow waveform of similar shape, which is not physiologically realistic. This gives further validation to the importance of modelling the compliance of an artery when performing in vitro analysis. A method has also been trialled for the development of a technique to track the surface displacement of asymmetrical structures to help quantify the affects dilation of a compliant model has on the pressure waveform.

7 Oscillatory Flow in a Constricted Geometry Representing the Carotid Artery

The next two chapters present results obtained in the Mk.III flow phantom representing an idealised stenosed carotid artery (CA) experiencing a physiologically realistic input flow waveform produced by the stepper motor pump system (Section 4.5.2). The literature review provided at the beginning of this chapter is relevant to both, so there will be no literature review present in the next chapter.

7.1 Introduction

As previously discussed in Chapter 1 a stenosis is a restriction in the artery caused when it becomes severely diseased. Velocity increase thorough the stenosis depends on the square of the reduction in diameter (Ku 1997). Downstream of the stenosis a shear layer occurs between the jet issuing from the constricted passage and a recirculating region. The upstream Reynolds number (Re) that induces turbulence downstream of the stenosis has been shown to be Re>300 with turbulence intensities that have been observed to be up to 100% of the upstream velocity values and can be found to be high for $1.5 \leq x/D \leq 6$ (x/D represents streamwise location non-dimensionalised by the neutral unstenosed diameter) downstream (Ku 1997). The Re at which recirculation starts to occur for a stenosis severity >70% by diameter is 10 therefore it will occur in nearly all flow conditions (Ku 1997). The throat of the stenosis is also a region where high wall shear stress (WSS) occurs.

The chapter firstly presents a review of previous numerical and experimental analysis performed in a stenosed geometry. The chapter then presents an investigation into the effect a restriction in the arterial geometry causes on the flow field and WSS. The analysis predominantly concentrates on a phantom with an axis symmetric stenosis, but some comparisons will be made to a geometry with an asymmetric stenosis.

7.2 Previous Work

As previously discussed, the two main avenues of research for biofluid problems are in vivo and in vitro. The techniques for in vivo analysis of biofluid problems has been presented in Section 5.2.1, the body of this literature review provides the analysis of the in vitro computational and experimental techniques that have been used to study compliant and rigid stenosed geometries

7.2.1 In Vitro Computational

Several investigations have been made numerically into arterial geometries with a stenosis with a rigid wall assumption. Long et al. (2001) numerically studied pulsatile flow in both symmetric and asymmetric idealised rigid geometries with varying degrees of stenosis severity (25-75% by diameter) with a laminar flow assumption. The constriction in geometry is far more dramatic than other studies. Rather than a stenosis with a sinusoidal geometry, these models had a throat of constant diameter with two regions of changing diameter on either side. It was found in all asymmetric geometries that WSS reached a positive peak just downstream of the stenosis exit on both the stenosed and unstenosed wall. It was found that there was a difference in flow recirculation zone length between symmetric and asymmetric geometry, with the symmetric stenosis zone being more stable and lasting longer. Sherwin and Blackburn (2005) investigated a rigid straight tube with a 75% reduction by diameter, symmetric stenosis experiencing steady, single-harmonic sinusoidal and a two harmonic more physiologically relevant flow using DNS. For steady flow at Re 722 a linear instability was observed that had a Coanda-type wall attachment characteristic, with the shear layer perturbed towards the pipe wall. The flow was observed to become turbulent downstream of the stenosis occurring between $4 \leq x/D \leq 10$. It was found that reducing Womersley number (α) increased the instability of the waveform. Vortex ring formation was observed in the shear layer. Mao et al. (2011) continued this work with a pulsatile waveform that was more physiologically realistic, through the same rigid 75% symmetric stenosis geometry. They presented further results demonstrating instabilities in the shear layer.

Varghese et al. (2007a) firstly studied a 75% reduction in diameter in a rigid wall symmetric and asymmetric stenosis with fully three-dimensional time dependent calculations using

direct numerical simulation (DNS) under steady flow conditions (Re 500 and 1000). For the symmetric case a laminar flow field was predicted downstream. The introduction of a 5% offset of the stenosis centre to the artery centre caused a breakdown in the symmetry downstream from the stenosis directing the jet towards the side of the eccentricity. At Re 1000 the jet broke down with flow transitioning to turbulence ~5D (unstenosed diameter's) downstream. Varghese et al. (2007b) went on to study the same geometries experiencing a pulsatile sinusoidal inlet waveform (Re mean, maximum and minimum 600, 1000, and 200 respectively and $\alpha = 7.5$) using DNS. Predictions again showed a laminar post-stenotic flow field. The asymmetric stenosis experienced periodic localized transition to turbulence occurring around peak flowrate with instabilities occurring in the shear layer. Turbulence was observed between x/D=4-7. Lovald et al. (2009) studied an idealised rigid geometry of the carotid bifurcation using 3D CFD, experiencing a physiologically realistic flow waveform, to investigate the effect of stenosis severity. It was found that each 10% increase in stenosis severity, increased the peak WSS by a factor of two. Dhahbi et al. (2012) recently studied the dynamics of solid particles downstream from an idealised rigid symmetric stenosed geometry with a 75% reduction by area experiencing a steady flow input. The purpose was to understand the dynamics of particles that could break away from a partially occluded thrombus.

As previously discussed there are inherent difficulties in modelling the fluid structure interaction (FSI) in compliant geometries. Tang et al. (1999b) numerically modelled the FSI in a 3-D thin walled symmetric and asymmetric stenosis to understand the wall deformation and flow properties under steady flow conditions. The elastic properties of this computational model were obtained experimentally from a silicone phantom. It was found that a severe symmetric stenosis can produce a non-symmetric flow field. It was found asymmetry causes 50% higher maximum WSS and 6% lower maximum velocity. Following this Tang et al. (2003) studied the effect of stenosis asymmetry and severity looking at 50 and 70% diameter reductions and 0% and 50% offset from the artery centre axis. The mechanical properties were this time obtained from a PVA hydrogel phantom, which were stated to be closer to that of the human CA. Steady flow conditions were again applied in the analysis. It was found that asymmetry reduced the maximum velocity present in the flow field. Asymmetry also leads to a larger separation region downstream of the stenosis. It was

found that WSS varied minimally circumferentially in the symmetric stenosis, but was found to vary by up to 38% in the asymmetric stenosis. Increase in stenosis severity was shown to increase maximum wall shear stress experienced. Tang et al. (2004) then went on to study a physiologically realistic geometry obtained via magnetic resonance imaging (MRI) with a multi component plaque structure experiencing a physiologically realistic flow input. Large cyclic stress/strain variations in the plaque under pulsating pressure were observed.

Li et al. (2007) studied compliant, idealised geometries of symmetric stenosis with varying degrees of stenosis severity (30-70% by diameter), experiencing physiologically realistic flow waveforms. It was found that for a stenosis with a 50% restriction, wall movement is reduced by 85%. The work of Xiong et al. (2011) which has previously been mentioned in Section 5.2.2, developed FSI modelling to incorporate spatially varying wall properties within a physiological geometry. Preliminary results looked at increasing Young's modulus in the central region of the phantom. The occurrence of stenosis will produce a similar increase in stiffness due to increase in wall thickness. Dilation was shown to reduce with increased wall stiffness. It was also shown that, when comparing the geometry with the increased E in the centre to the geometry with uniform E, the areas of the increased geometry that had the same E as the uniform geometry experienced the same dilation magnitude. It was found that there was a higher pressure pulse occurring in a geometry with an increased E in the central region compared to a geometry with uniform E. This is consistent with cardiovascular theory where stiffer geometries have higher pressure pulses.

As stated in Section 1.5 an assumption made in the work of this thesis was that due to the large diameter of the arteries being studied, blood could be modelled as a Newtonian fluid. There have however been some studies into the effect the non-Newtonian nature of blood has on the flow field dynamics of a stenosed geometry using blood viscosity prediction models. Buchanan Jr et al. (2000) studied the effects of the non-Newtonian behaviour of blood in an idealised rigid asymmetric geometry experiencing a sinusoidal input waveform around a zero mean with varying Womersley numbers (α). The non-Newtonian models affect the ability of entrained particles downstream of the stenosis to exit the recirculation zone. Increasing α was found to delay the formation of the primary vortex downstream of the stenosis. Molla and Paul (2012) used large eddy simulation (LES) to study pulsatile flow in an idealised rigid geometry of an asymmetric stenosis with five different blood viscosity models, looking at the

effect of a non-Newtonian fluid. It was found that the non-Newtonian models increase the length of the recirculation zone downstream from the stenosis exit. The shear stress drop on the wall with the stenosis is larger for the non-Newtonian model. The pressure drop downstream of the stenosis was also predicted to be slightly smaller.

7.2.2 In Vitro Experimental

Ahmed (1998) studied the flow field of a rigid wall symmetric stenosis with varying degrees of stenosis severity (25, 50 and 75% reduction by area) by laser Doppler velocimetry experiencing a sinusoidal waveform input. It was found that an increase in stenosis severity increased the size of recirculation region downstream of the stenosis. During flow acceleration vortices are shed downstream of the stenosis with their interaction with the flow field being dependent on the degree of constriction.

Vétel et al. (2008) provided an in depth study of a rigid model symmetric stenosis with a 75% reduction in area (50% reduction in diameter) under steady flow (Reynolds number (Re) range 110-1100) conditions using both stereoscopic particle image velocimetry (PIV) and time-resolved PIV (TRPIV). For low Re, steady flow results showed a flow asymmetry downstream from the stenosis resulting from a Coanda-type wall attachment, with the jet exiting the stenosis causing a one sided recirculation region. It was found that above a critical Re = 400 the separation surface no longer remained attached and an unsteady flow regime commenced downstream. Vétel et al. (2008) found that there were low frequency axial oscillations of the reattachment point in conjunction with a slow swirling motion of the jet. Above Re = 900 vortex rings downstream of the stenosis were observed before breaking down into turbulence.

Kung et al. (2011) studied a compliant flow phantom representing a healthy and stenosed artery using phase contrast MRI flow velocity data, a technique that could be used in the future for in vivo analysis. A physiologically realistic flow input was applied at the phantom inlet. The results were then compared to analysis performed using CFD. The average difference between the measured and simulated results was 13% of the mean for flow velocity and 1.8% of the mean for flow pressure. This showed the CFD produced accurate wall motion and wave reflections.

Pielhop et al. (2012) studied the flow field and WSS in a compliant stenosed model experiencing a sinusoidal oscillating flow wave around a zero mean with varying amplitude and time period using planar TRPIV. It was shown that oscillating WSS was induced by vortices produced in the separated shear layer of the jet emanating from the stenosis. Local static pressure and dilation, when analysed with respect to phase and amplitude, was shown to have phase lags and deviations in the temporal distributions from the imposed bulk flow at the maximum and minimum pressure and dilation points. This result was dependent on frequency.

As previously stated in Section 5.2.3 although there is some experimental work available in compliant geometries representing stenosis, further work needs to be done to provide data that can be used to validate computational results. It has become evident during the extensive literature search performed that varying locations of stenosis are analysed with varying inputs from steady to physiologically realistic. There is however little that concentrates on the carotid artery (CA) and a physiologically realistic input into that geometry. An in depth experimental investigation needs to be performed into the effect a stenosis has on a compliant geometries flow field and the WSS experienced. This can then be used to validate numerical studies that are currently on going.

7.3 Experimental Setup

The body of this chapter provides an analysis of a straight compliant phantom (Mk.III phantom) representing the CA with a 50% axis-symmetric (from now on referred to as symmetric) stenosis by diameter. Certain aspects of the analysis will provide a comparison to results obtained in non-axis-symmetric (from now on referred to as asymmetric) stenosis. The mathematical operations applied to this analysis have already been set out in Section 5.3.1.

7.3.1 Flow Facility

A schematic of the experimental flow system used in this investigation is shown in (Figure 44 Section 4.4). The system recorded both inlet flow rate and pressure and outlet pressure. The pulsatile waveform was provided by the more stable stepper motor pump system. Re and α matching was again applied to ensure similarity between the in vivo and experimental in vitro conditions. The physiological waveform was produced by the continuous forward

movement of the piston head, allowing for ~14 waveform cycles per experimental run. With the implementation of the new piston system it was impossible to replicate the input provided to the compliant straight tube studied in Chapter 5 due to the change in waveform input method into the control software (Section 4.5.2). Figure 90 provides a comparison of the measured average inlet flow waveform entering the compliant straight tube, symmetric and asymmetric phantom scaled to in vivo conditions. It was decided to match the symmetric stenosis input as closely to physiologically realistic waveform and input the exact same piston stroke to the asymmetric geometry (shown in Figure 91).

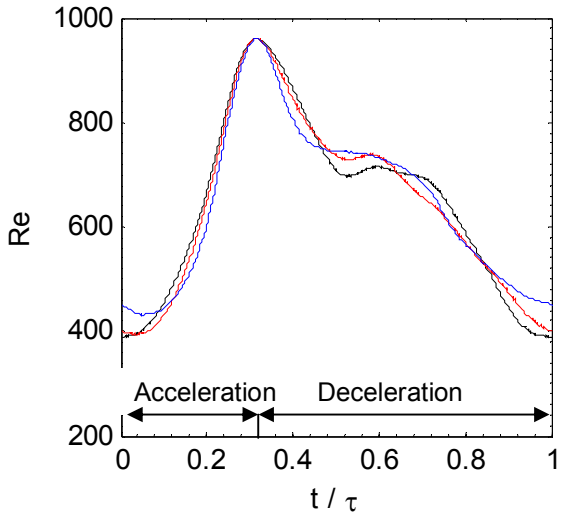

Figure 90 Comparison of the measured average inlet flow waveform entering compliant straight tube (Chapter 5) (blue), in-vitro symmetric stenosis phantom (black) and in-vitro asymmetric stenosis phantom (red)

When comparing to the waveform input to the healthy geometry, it can be seen that the input into the symmetric phantom has a lower minimum Re (383). The initial acceleration phase closely matches up to an equivalent peak Re (954). The flow rate drops to a lower plateau value with a similar rate of deceleration in the late deceleration phase. There is a higher overall mean Re (644), and matching α (4.54). Figure 91 provides a comparison with the original in vivo waveform. The larger drop in flowrate just after peak flow rate shows the new waveform to return to a more physiologically relevant value. There are some differences observed in the early deceleration phase and at the end of the waveform. The match between the two waveforms was, overall, satisfactory especially in the early acceleration phase and at peak flow rate, where the most interesting fluid phenomena occur.

The piston pump system can produce a repeatable wave form with a precision of ±0.072l/min (Re±8 for the experimental conditions used for this study).

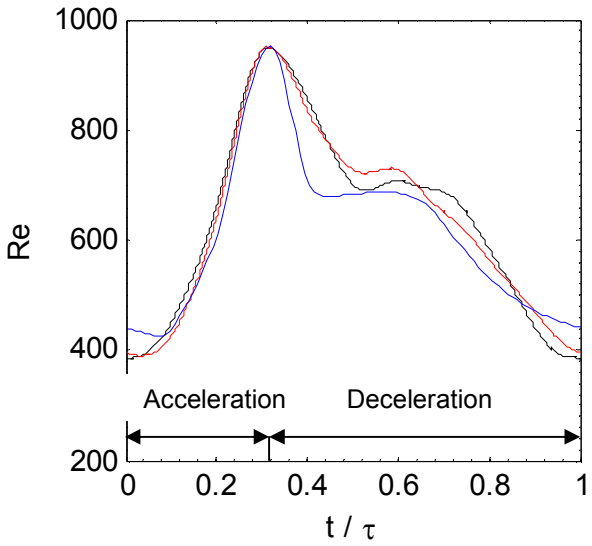

Figure 91 Pulsatile in-vivo (blue), in-vitro symmetric stenosis phantom (black) and in-vitro asymmetric stenosis phantom (red) inlet waveform

As discussed in Chapter 6 geometric changes have an effect on inlet flow conditions. This can be seen to manifest between the symmetric and asymmetric mainly in the deceleration phase, where the asymmetric geometry demonstrates a reduction in the plateau in flow rate experienced in the symmetric geometry. Figure 92 presents the phase averaged inlet flow and pressure waveform and outlet pressure waveform along with specific points of interest where analysis was performed. The geometric effect of asymmetry on pressure can be seen to produce a reduction in the first pressure minimum and a reduction on the subsequent pressure peak and minimum. These reductions coincide with the reduction in the flow rate in that phase.

The symmetric waveform follows a similar path to the work of Long et al. (2001), which has a similar α (5.31), but a reduced maximum, mean and minimum Re (700, 300 and 200 respectively). Lovald et al. (2009) used a similar model with a physiological waveform with a mean inlet Re of 298 and an α of 5.5. The physiological waveform in the work by Sherwin and Blackburn (2005) was more idealised than the one used in this work and had a larger α (7.2-18.6) and smaller Re (250-550). The follow on work from that group (Mao et al. 2011) used a waveform that followed a more realistic path similar to this work, with similar Re and

α values. The mean Re was 450 with a peak of 1426 and an α of 5.04. The work of Li et al. (2007) concentrated on the external iliac artery with a higher maximum inlet Re (1206) and smaller α (~4.19), it was also shown that stenosis severity altered inlet waveform. The input waveform used by Molla and Paul (2012) is similar to that used in this work, but has a larger peak Re of 2000 and an α of 10.5. The waveform in the study by Kung et al. (2011) varied from this one as it had a phase of reverse flow.

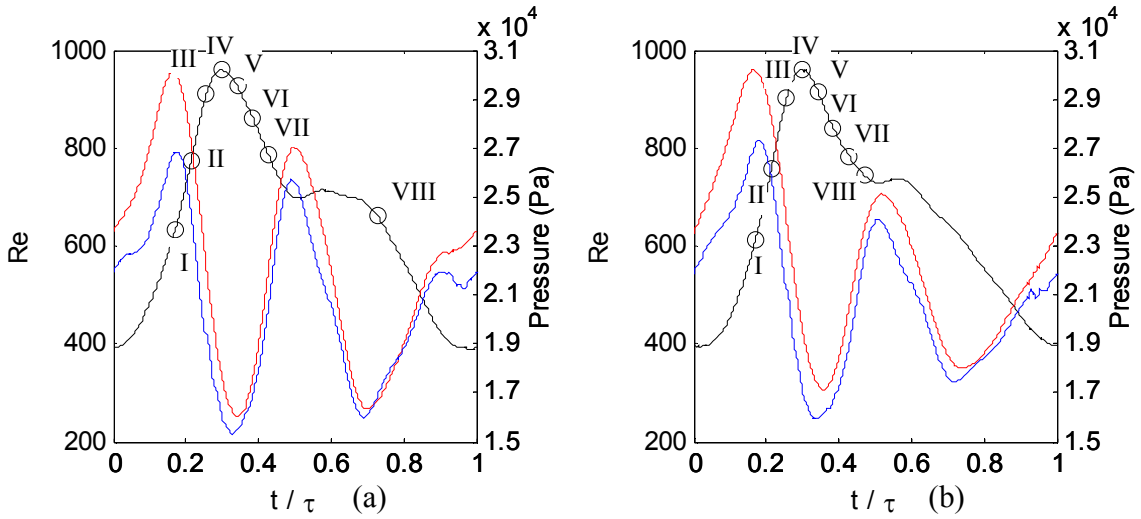

Figure 92 In vitro inlet pressure (red), outlet pressure (blue) and inlet flow (black) and waveform. (a) Symmetric flow phantom with points of interest at t/τ = (I) 0.09 (II) 0.13 (III) 0.19, (IV) 0.23, (V) 0.26 (VI) 0.31, (VII) 0.34, (VIII) 0.44 and (IX) 0.75. (b) Asymmetric flow phantom with points of interest at t/τ = (I) 0.13 (II) 0.19 (III) 0.23 (IV) 0.27 (V) 0.31, (VI) 0.36, (VII) 0.40 and (VIII) 0.44) (note variation in range of pressure axis)

This waveform differs from the waveform studied by Ahmed (1998), Buchanan Jr et al. (2000), Varghese et al. (2007b) and Pielhop et al. (2012) who used a sinusoidal input. Ahmed (1998) studied a waveform with a Re range of 200-1000 and a mean Re of 600, with an α of 7.5. The work of Buchanan Jr et al. (2000) had a maximum, minimum and mean Re of 400, 0 and 200 respectively and looked at 3 values of α 4, 7.5 and 12.5. Re values in this work are comparative to the sinusoidal study of Varghese et al. (2007b) (maximum, minimum and mean Re of 1000, 200 and 600 respectively), but had a smaller α in comparison to that work (7.5). The work of Pielhop et al. (2012) studied a sinusoidal flow around a zero mean with all test cases having a larger α than this work, 7.5, 9.5 and 13. As shown in Chapter 6 the sinusoidal assumption affects the input pressure wave, which in turn effects the wall displacement. For a sinusoidal input around a zero mean there is a reverse flow rate phase that isn't evident in the physiological waveforms studied here.

The working fluid was a mixture of 39% water and 61% glycerine by weight which provided a refractive index that matched the silicone phantom (n=1.141). It had a kinematic viscosity (ν) of $10.2\times10^{-6}m^2/s$ and a density (ρ) of $1150kg/m^3$ (1. $15g/cm^3$) at 20°C. The Transmural pressure was set to 19.09kPa.

7.3.2 PIV Measurements

Planar digital PIV was used to measure the time varying displacement fields in both a symmetric and asymmetric stenosed phantom providing both flow velocities and WSS data. Table 23 provides an overview of the measurement parameters. Images were recorded using a single Dantec Flowsense 2MP camera with a CCD array of $1608\times1208pixel^2$. A 60mm Nikon lens at an aperture of $f^{\#}=8$ and a magnification of 0.2 to 0.15. This gives the experiments an estimated depth of field of 3 to 4.9mm and diffraction limited particle size of 12.5 to 11.9μm. The flow was illuminated with a 40mm high, 0.5mm thick sheet from a New Wave Solo 120 XT laser with a wavelength of 532nm at 120mJ/pulse using a series of spherical and cylindrical lenses. The flow was seeded with nominally 10 μm diameter hollow glass spheres with a density of $1.1g/cm^3$.

The PIV measurements were phase locked, recording 22 image pairs per waveform over 24 waveforms. For time oscillating flow waves the laser pulse time delay selection is a compromise between the variation in maximum pixel displacement for maximum and minimum flowrate. With a higher flow velocity occurring in a stenosed geometry through the constricted section compared to the geometry of a straight tube; a far smaller time delay is required. For this analysis in region of interest 1 (ROI 1) a time delay of 350μs and for region of interest 2 (ROI 2) a time delay of 650μs was selected, which produced <3% invalid vectors at each phase. After minimum background subtraction, intensity normalisation and masking (Section 3.7), the images were processed with an in-house code implementing 2D FFT cross-correlation (Buchmann 2010) with iterative window sizing and displacement. The data was validated using the signal-to-mean ratio filter and normalised median test (Section 3.6.2.2).

7.4 Experimental Error

To assess the accuracy of the PIV analysis and the dimensionless scaling applied, Equation 89 (Section 5.4) was used to calculate the peak flow rate observed in both the geometries

using the velocity profile observed at x/D=-1.1, upstream of the stenosis entrance. Results were then converted to in vivo scale using Equation 87 (Section 5.3.2) and are calculated as Reynolds number i.e. the Reynolds number corresponding to a flow of the same average velocity and neutral diameter. The peak flow rate observed at the inlet from the electromagnetic flow meter on both the symmetric and asymmetric geometry was Re=954. Applying Equation 89 (Section 5.4) to the velocity profiles in the symmetric and asymmetric geometry produced a Re of 933 and 961 respectively; which equates to a relative error of 2.2% and 0.7%. This is an increase in error compared to the work in Chapter 6, but still presents a favourable result. The reduction in magnification on the ROI would have been a factor in the increased error. As previous the electromagnetic flow meter has a relative uncertainty of 1.3%, temperature variation (20±0.5ºC) caused an error of 1.9% giving the system an error in Re of ±2.3%.

For an error in calculated displacement of 0.1 pixel (Raffel et al. 2007) and time delays used (Table 23), in ROI 1, this gives an error of 0.0092m/s (0.49% of the maximum velocity). In ROI 2 this gives an error of 0.0084m/s (0.44% of the maximum velocity). The uncertainty in position of the light sheet can also cause an error. A misalignment of the light sheet by half the light sheet thickness (0.25mm) from the plain of symmetry would, for a fully 3D symmetrical flow reduce the centreline velocity by 1%. In the asymmetric geometry where the flow is asymmetric this error increases. Wall location could be measured to an accuracy of 1 pixel, giving an error of ±0.06mm in diameter calculation (0.3%D). The error in WSS calculation has previously been discussed in Section 5.4.

Table 23 Table of measurement parameters, S and A refer to symmetric and asymmetric respectively

Laser	Type	Nd:YAG, dual cavity
	Thickness (mm)	0.5
Camera	Type	CCD
	Resolution (pix)	1600×1200
	Lens Focal Length (mm)	60
	Lens Aperture (f#)	8
Seeding	Type	Hollow Glass Spheres
	Mean Diameter (μm)	16
	Density (g/cm^3)	1.1
PIV ROI 1	Window Sizing (pix) Max (Min)	64×64(16×16)
	Resolution (pix/mm)	30.93
	Overlap (%)	75
	Vector Spacing (mm)	0.13
	Time delay (μs)	350
PIV ROI 2	Window Sizing (pix) Max (Min)	64×64(32×32)
	Resolution (pix/mm)	18.2
	Overlap (%)	75
	Vector Spacing (mm)	0.44
	Time delay (μs)	650
iPIV ROI 1	Interrogation width, M (pix)	64
	Interrogation height, N (pix)	80
	Gaussian weight, σ (pix)	10(S) 14(A)
	Overlap (%)	75
	Vector Spacing (mm)	0.26

7.5 Results and Discussion

A schematic of the symmetric phantom is shown in Figure 93; D represents the neutral diameter (20mm in vitro) of the main artery. There were two regions of interest (ROI) investigated within this phantom, both were in a plane containing the centre axis. ROI 1 covered a region $-1.1 \leq x/D \leq 1.1$, where a negative value represents a location upstream of the stenosis throat (x/D=0) and a positive value represents a region downstream of the throat. ROI 2 covered an area starting at the stenosis exit and extending 2.75D downstream.

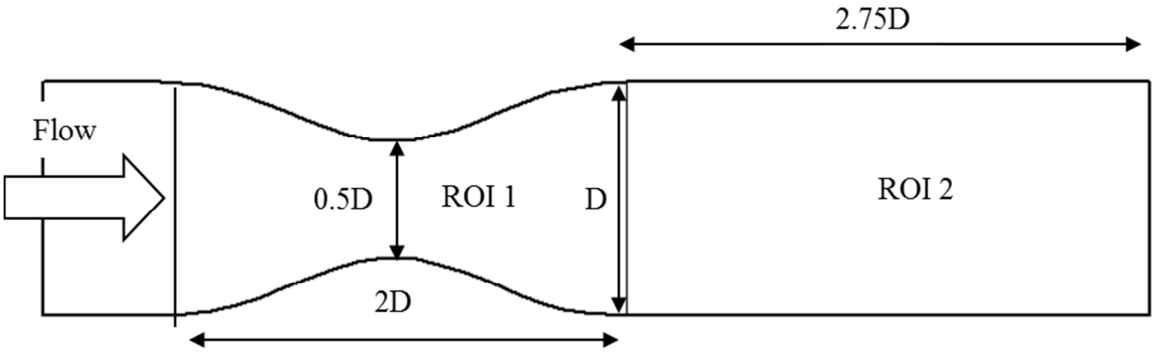

Figure 93 Schematic of the symmetric flow phantom internal geometry and location of region of interest 1 (ROI 1) and region of interest 2 (ROI 2)

A schematic of the asymmetric geometry is shown in Figure 94. Only one region was investigated (ROI 1), which was equivalent in location to ROI 1 in the symmetric phantom ($-1.1 \leq x/D \leq 1.1$). All results presented are in vivo scaled.

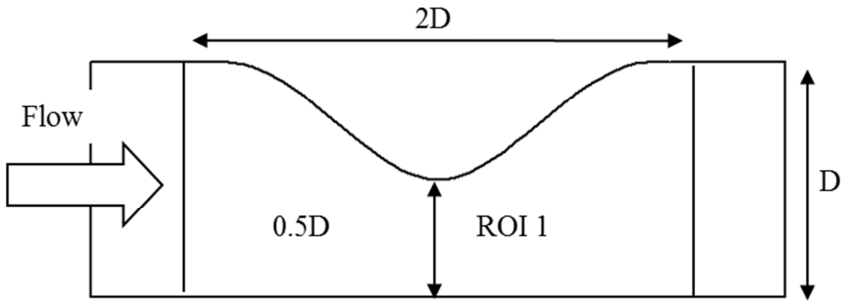

Figure 94 Schematic of the asymmetric flow phantom internal geometry and location of region of interest 1 (ROI 1)

7.5.1 Region of Interest 1 Flow Field Analysis

Figure 95 and Figure 96 present the phase averaged absolute velocity $\langle U_{abs} \rangle(t)$ fields and velocity vectors (denoting in-plane velocity magnitude) obtained during the initial acceleration phase up to the peak inlet flowrate (Figure 92a IV) and the initial deceleration thereafter (Figure 92a V-VII). Between $-1.1 \leq x/D \leq 0$ there was an increase in centreline ($y/D=0$) velocity due to the decrease in cross sectional area of the phantom geometry. As flow passed through the stenosis throat ($x/D = 0$) two distinct flow regimes were observed to begin. A central high velocity jet and a low velocity recirculation region either side of the jet. These two regimes were separated by a shear layer. The peak flow velocity of 1.9m/s observed in the symmetrically stenosed phantom occurred in the centre line at $x/D=0$, which is 2.6 times larger than the 0.72m/s observed in the straight healthy geometry in Section 5.5.1. The peak velocity at $x/D=-1.1$ at this phase is 0.71m/s which was similar to the

straight healthy geometry peak velocity. The work of Li et al. (2007) in the iliac artery which has a smaller healthy unstenosed in vivo diameter (0.0058m) and a larger peak inlet Re showed the peak velocity in a 50% stenosis to be 2.3m/s from 0.78m/s in a healthy geometry. The higher velocities are expected dues to the smaller diameter and higher Re. Steady flow results by Dhahbi et al. (2012) at Re 1000 in larger in vivo diameter (0.008m) showed a lower peak velocity of 1.77m/s at the stenosis throat. Steady flow results by (Tang et al. 1999b) at an Re 840 with an in vivo diameter of 0.004m produced a peak velocity of 5.36m/s. The work of Varghese et al. (2007b) in a rigid geometry of similar dimensions at a peak Re of 1000 observed a peak velocity at the stenosis throat of 4.5 times the mean inlet centreline velocity. In this work at y/D= 0 at x/D=-1.1 the mean centreline velocity was 0.55m/s which giave a peak velocity of 3.45 times the mean centreline velocity. The larger result observed by Varghese et al. (2007b) was expected due to the increased Re and as discussed in Section 5.5 the rigid wall assumption. The peak velocities observed in this work are in the range expected when compared to other bodies of work.

Figure 97(a) presents the peak-to-peak normalised (Equation 91 Section 5.5.2) phase averaged centreline velocity at three streamwise locations (x/D = -1.0, -0.5 and 0). A shift in the timing of the peak velocity can be seen as the stenosis throat is approached. Results from between $0 \leq x/D \leq 1.1$ are not displayed as there was no further observation of temporal shift. The peak flow rate occurred at $t/\tau=0.31$, which was equivalent to the peak velocity location at x/D=0. At x/D=-1 peak velocity occurred one time step later at $t/\tau=0.34$. The cause of this was the dilation of the geometry. Referring to Figure 101, which presents the wall dilation, there was a much larger variation at x/D=-1 compared to x/D=0. The minimal change in diameter during the entire cardiac cycle at x/D=0 meant it had minimal effect on centreline velocity. At x/D=-1 the phantom radius was larger at $t/\tau=0.31$ (1.114D), than at $t/\tau=0.34$ (1.103D), referring again to Equation 89 (Section 5.4) a reduction in diameter would increase velocity. The path of the centreline waveform is also observed to alter with increased downstream location. The corresponding temporal spectra presented in Figure 97(b-d) show there to be a reduction in the first harmonic and an amplification of the 2^{nd} harmonic. This caused the velocity path to shift from one closely resembling the inlet flow rate to one starting to bear the attributes of the pressure waveform.

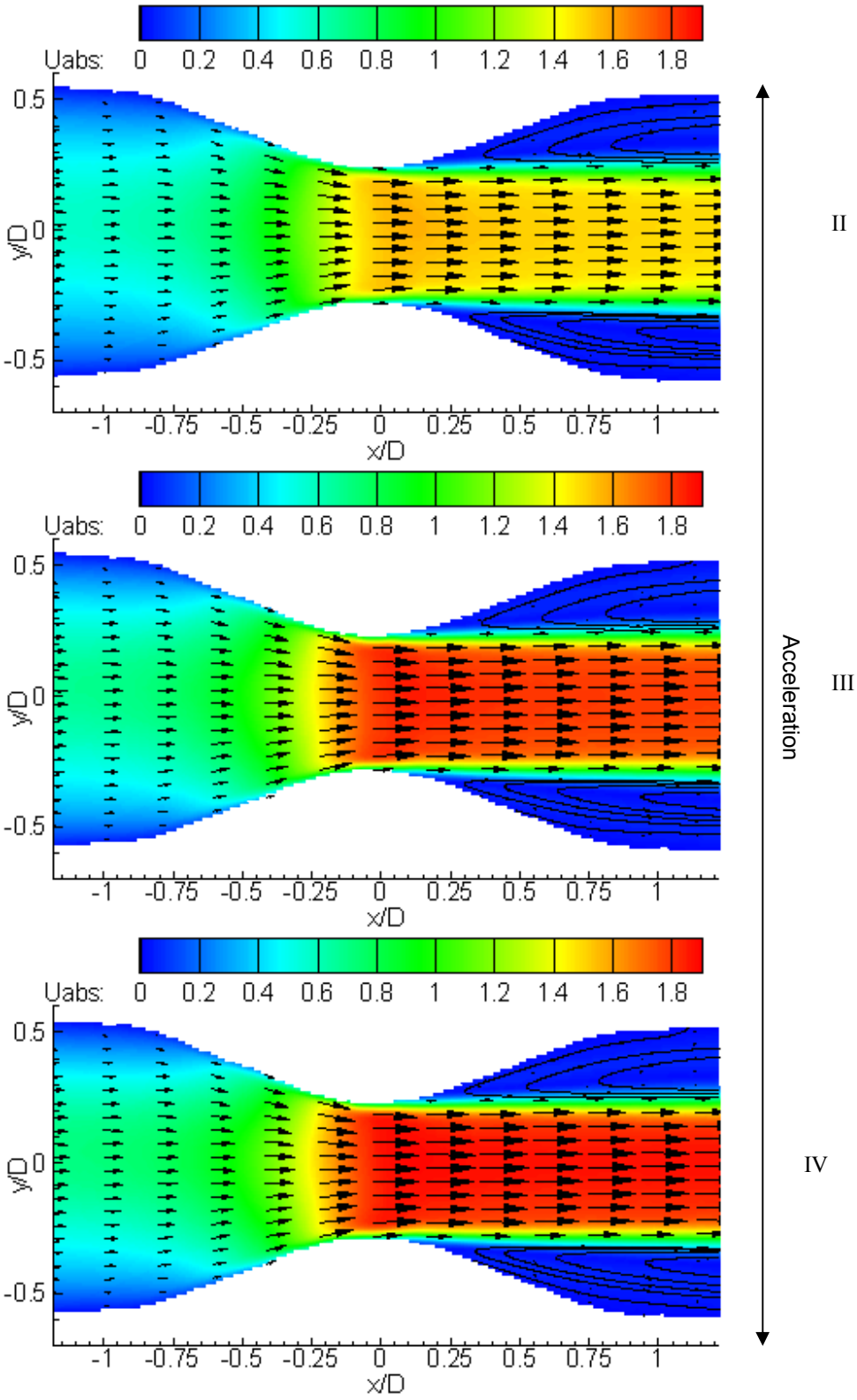

Figure 95 Phase averaged absolute velocity fields (m/s) and velocity vectors in the symmetric stenosed phantom at phase locations indicated in Figure 92(a) (t/τ = (II) 0.23 (III) 0.26 and (IV) 0.31)

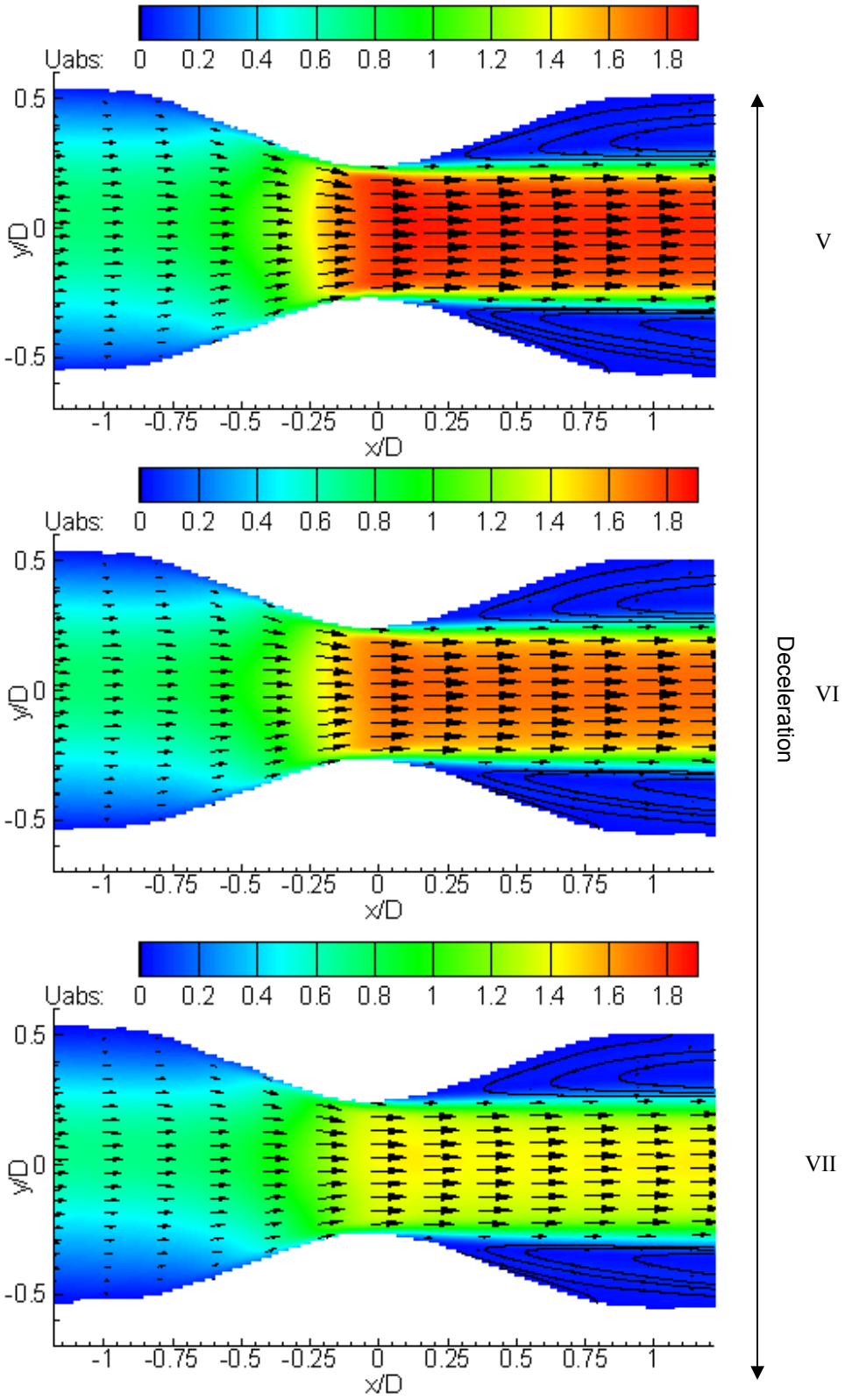

Figure 96 Phase averaged absolute velocity fields (m/s) and velocity vectors in the symmetric stenosed phantom at phase locations indicated in Figure 92(a) (t/τ = (V) 0.34 (VI))

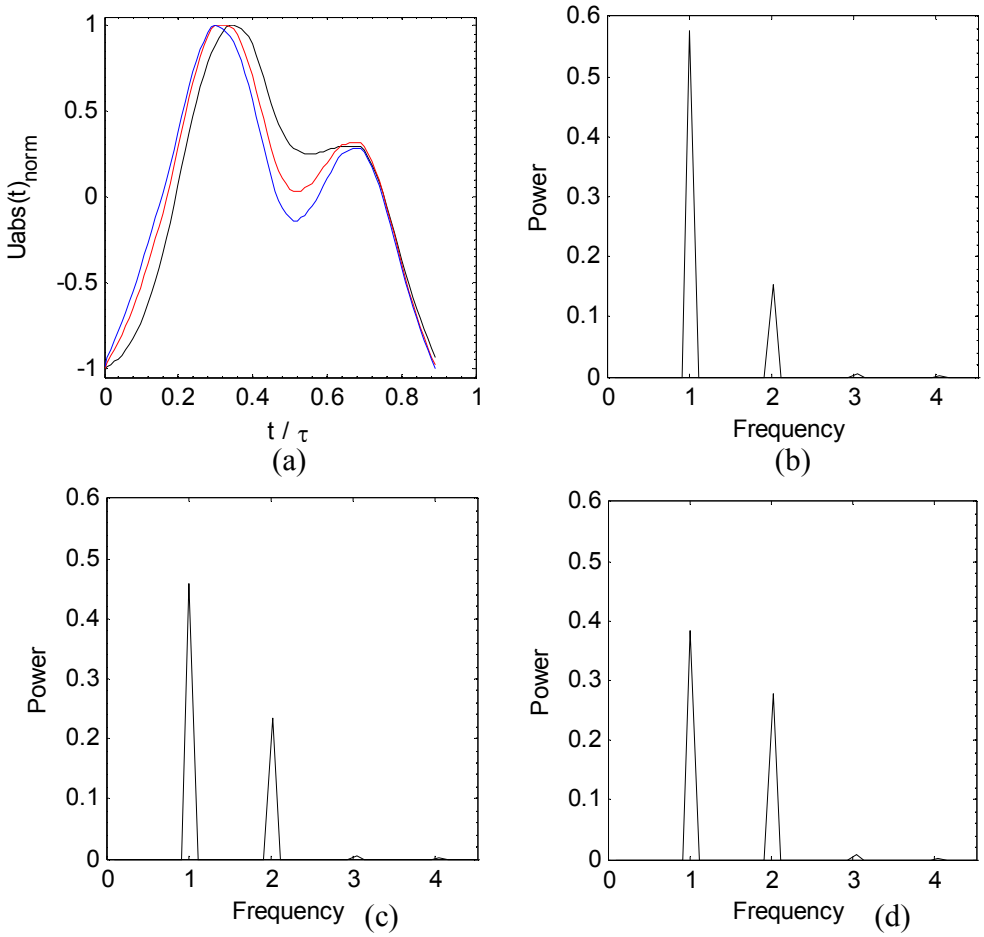

Figure 97 (a) Normalised phase averaged centreline velocity in the symmetric stenosis at x/D (black) -1.0, (red) -0.5 and (blue) 0.0. Corresponding temporal spectra at x/D = (b) -1.0, (c) -0.5 and (d) 0.0.

Figure 98, Figure 99 and Figure 100 show the phase averaged absolute velocity fields and velocity vectors (denoting in-plane velocity magnitude) obtained during the initial acceleration phase up to peak inlet flowrate and the initial deceleration thereafter (Figure 92(b) (I-VIII)) in the asymmetric geometry. This portion of the asymmetric flowrate waveform closely followed the path of the symmetric flowrate waveform. As observed in the symmetric geometry there was an increase in peak cross sectional velocity between $-1.1 \leq x/D \leq 0$ due to the decrease in cross sectional area. Both geometries experienced an equal peak flow rate of Re 954. However, the peak velocity experienced in the asymmetric geometry was 1.77m/s; lower than the peak velocity of 1.9m/s experienced in the symmetric geometry. Figure 101(a) shows the temporal evolution of the diameter at the stenosis throat (x/D=0) for both the symmetric and asymmetric geometry. At this location it can be seen

that the asymmetric geometry had a larger diameter throughout the cardiac cycle. The symmetric stenosis wall had a uniform increase in thickness of 0.25D compared to the unstenosed section around the entire circumference at this location. In the asymmetric stenosis, the lower wall had an increase in thickness of 0.5D, but this reduced around the circumference to the upper wall where the thickness is the same as that in the main unstenosed portion of the artery. This thin wall section in the asymmetric stenosis caused an increased dilation at the stenosis throat and therefore an increased cross sectional area. Referring to Equation 89 (Section 5.4), for an equal flow rate value, an increase in cross sectional area would reduce the velocity magnitude across the cross section, therefore explains the reduction in velocity experienced in the asymmetric geometry. This reduction was also observed by Tang et al. (1999a); (1999b).

As flow passed through the stenosis throat two flow regimes were again evident. There was the main jet that exited the restriction separated from a low velocity recirculation zone behind the stenosis by a shear layer. The fluid dynamics within the low velocity recirculation zone can be seen to be time dependent. As flow accelerated from phase I-IV a vortex developed within this region. At phase I, the bulk of the recirculation zone flow moves in a reverse direction opposite to the main jet, it then travels up the downstream stenosis wall and reverses, following the main jet direction. It is noted that in this 2 dimensional 2 component (2D2C) analysis the streamlines observed can resemble a closed loop system. The work of Buchmann (2010) when investigating similar flow structures using 2D3C analysis observed these apparent closed loop systems to be helical flow. It is expected for this asymmetric geometry that there is a nonzero out of plane velocity component that cannot be resolved from the presented analysis. The stream lines are also shown to originate from the wall which is not realistic. This in part could be due to the out of plane velocity. There is also a limitation in the resolution of the PIV technique at the wall interface, which led to the requirement of the implementation of the iPIV technique to obtain WSS data. Noise in the measured vectors could also give rise to the occurrence of spurious streamlines. The intent to present the streamline data is to help graphically represent the bifurcation of the flow that occurred.

At phase location II the reverse flow in the recirculation zone separated when it hit the downstream stenosis wall (location signified by the red dot in Figure 98(II)). The upper

section of the separated flow followed the direction observed in phase I; the lower section travelled down the stenosis wall and back in the forwards direction along the main phantom wall. Between phase III and IV this separation region moved up the stenosis wall and combined with the increased forward flow in the lower section with an accelerated reverse flow, caused the vortex to occur in a small region in space. The streamlines here again can be misleading, with the results seeming to show the vortex to spiral out from a point. This is not the case, they are merely meant to represent the rotational nature of the flow, due to the low velocity experienced in this region the vectors are too small to visualise. What is occurring is a counter clockwise vortex in the lower half of the flow bifurcation.

As the main jet decelerated in phase V and VI the vortex in the recirculation zone broke down. The work of Buchanan Jr et al. (2000); Long et al. (2001) observed a vortex to occur downstream of an asymmetric stenosis and show for low flow rates the recirculation zone expanded beyond the limits of ROI 1 ($x/D>1.1$). They did not note the movement of the stagnation point observed here as these studies concentrated on a larger ROI, with little of the small scale detail, unlike in the present work. The recirculation zone can cause the advancement of arterial thrombus by keeping platelets 'trapped' in the same region for several cycles rather than allowing free travel through the artery(Cao and Rittgers 1998).

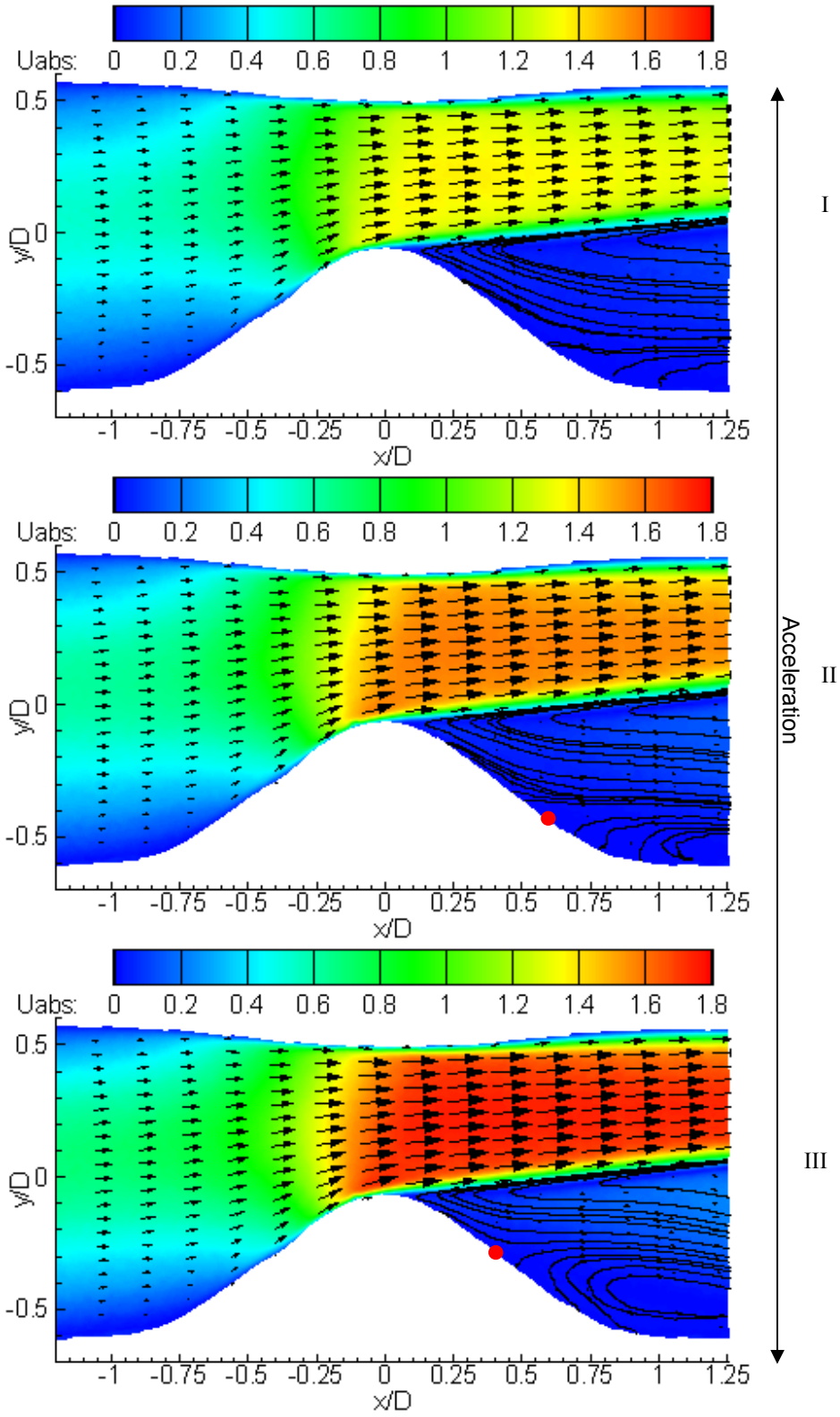

Figure 98 Phase averaged absolute velocity fields (m/s) and velocity vectors in the asymmetric stenosed phantom at phase locations indicated in Figure 92 (t/τ = (I) 0.13 (II) 0.19 and (III) 0.23)

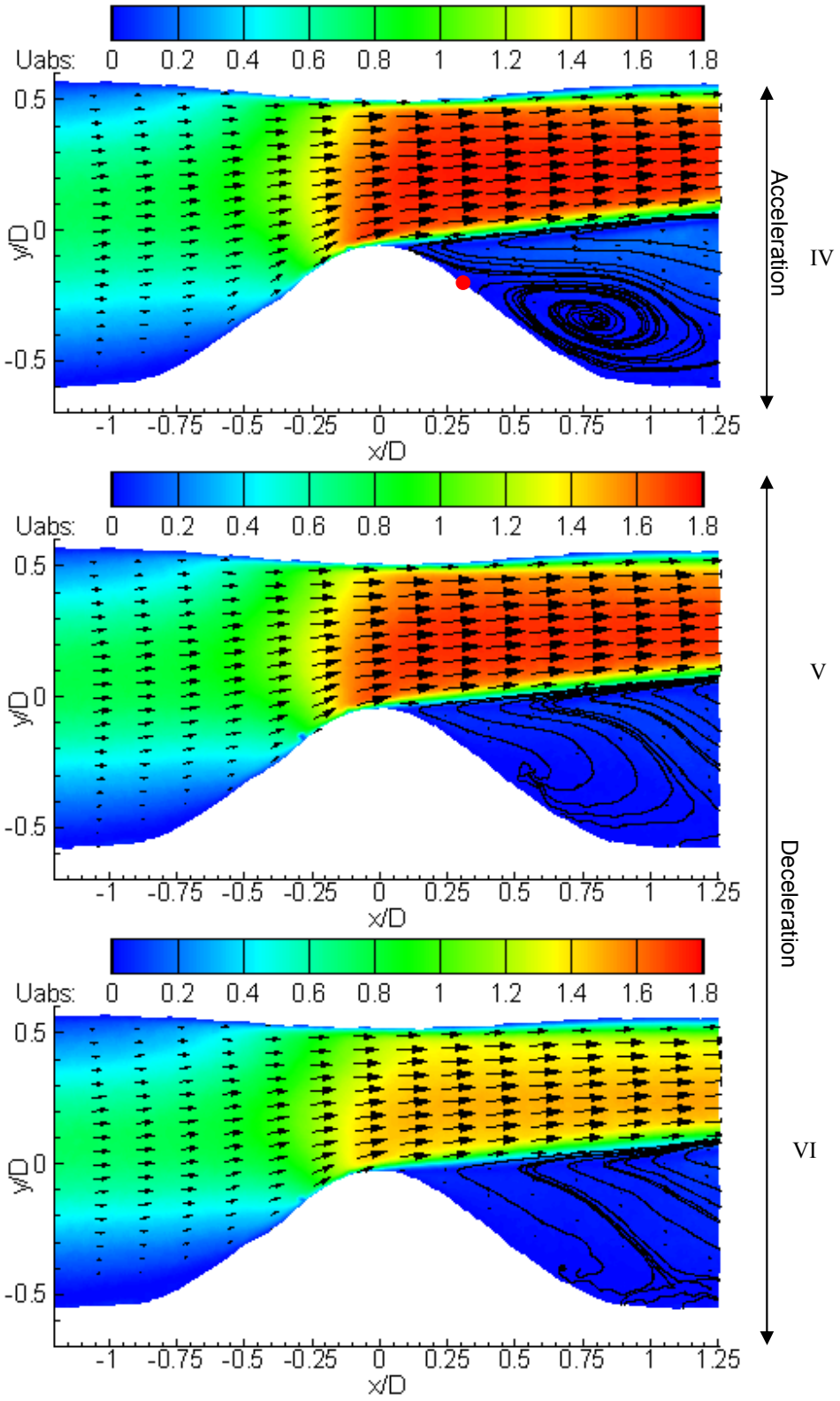

Figure 99 Phase averaged absolute velocity fields (m/s) and velocity vectors in the asymmetric stenosed phantom at phase locations indicated in Figure 92(b) (t/τ = (IV) 0.27 (V) 0.31 and (VI) 0.36)

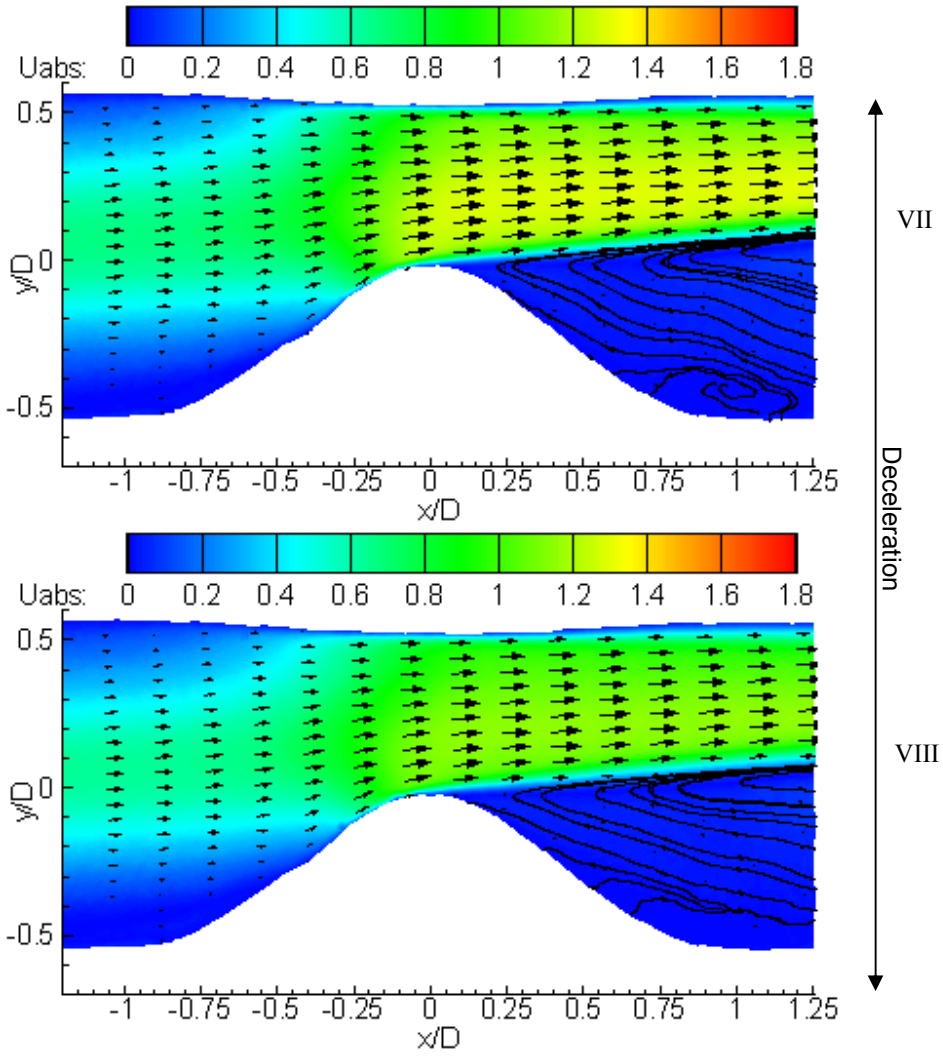

Figure 100 Phase averaged absolute velocity fields (m/s) and velocity vectors in the asymmetric stenosed phantom at phase locations indicated in Figure 92(b) (t/τ (VII) 0.40 and (VIII) 0.44)

Figure 101 presents the temporal evolution of both the symmetric and asymmetric geometries diameter at streamwise location x/D=-1.0:0.5:1.0. At all locations throughout both stenoses it can be seen that there was a larger time averaged diameter observed in the asymmetric stenosis. This occurred due to the increased compliance in the unstenosed wall of the asymmetric geometry causing a greater expansion due to internal pressure. In the symmetric stenosis the maximum difference in diameter observed over the cardiac cycle was 0.043D at the stenosis entrance (x/D=1), this reduced by 79% to 0.0091D at the stenosis throat. This is similar to the 85% reduction observed by Li et al. (2007) in a symmetric geometry with 50% stenosis by diameter. In the asymmetric stenosis the maximum difference in diameter was 0.06D at the stenosis entrance, this reduced by 77% to 0.014D at the stenosis throat. This

shows that the asymmetric geometry experienced not only a larger time averaged diameter, but also a larger variation in diameter over the cardiac cycle.

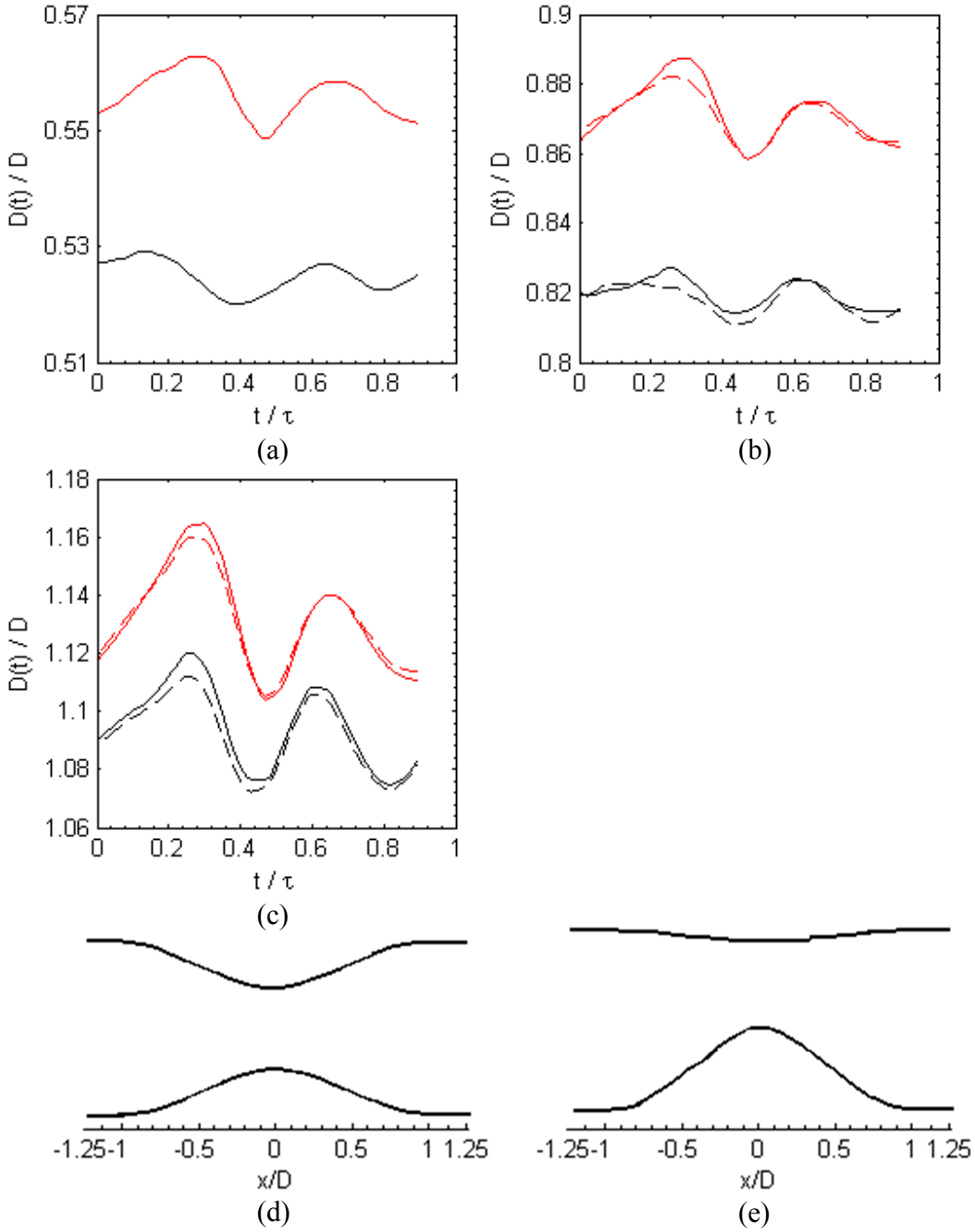

Figure 101 Phase averaged dilation of the symmetric (black) and asymmetric (red) stenosed phantom at stream wise locations (x/D) (a) 0.0, (b) ±0.5 and (c) ±1.0 (-) signifies the upstream location (negative) and (--) signifies the downstream location (positive). Schematics of the symmetric (d) and asymmetric (e) geometries are given for reference

The second observation in both geometries is that a larger dilation occurred upstream of the stenosis throat, compared to the equivalent downstream location. One theory that is proposed to explain this is that due to the increase in velocity exiting the stenosis there was a reduction in internal pressure which in turn reduced the dilation experienced downstream. To test this hypothesis a positive steady flow was applied at the symmetric phantom inlet. External pressure was incrementally increased until the phantom experienced collapse. The main phantom wall downstream of the stenosis collapsed first, signifying a lower internal pressure compared to the main phantom geometry upstream of the stenosis. To confirm this was not due to imperfections in the thin walls of the constructed phantom; it was removed from the external pressurisation chamber and outlet and inlet positions were swapped (i.e. the outlet was now placed in the inlet position and experienced the input steady flow). Again collapse was observed to occur downstream of the stenosis first. A smaller pressure loss would have also occurred due to the expected frictional loss over the phantom length. This reduction was similar to the observation made by Li et al. (2007), but that work did not go on to explain the cause.

It can be seen when comparing the wall displacement in both the symmetric and asymmetric geometry to that in the straight tube phantom in Figure 65 (Section 5.5.1), there is a marked difference in the path the wall displacement followed. As discussed in section 7.3.1, both experiments had a similar inlet flow waveform. In the straight tube study the wall displacement profile follows a similar path to the inlet flow rate. For the stenosed geometries the wall displacement profile follows a similar path to the inlet pressure profile. As there was no pressure recording facility available in the straight tube experiment, the shape of the pressure waveform profile can only be theorised. As this experiment showed that wall displacement is driven by pressure waveform, which is similar to the predictions of theory (Caro et al. 1978), it is expected that the pressure waveform profile in the straight phantom was similar to the flowrate waveform. Referring to Figure 102 which shows the temporal spectra of the inlet flowrate (a) and pressure (b) and noting that the introduction of the stenosis to a geometry alters the pressure waveform for a given inlet flowrate waveform, it can be seen the stenosis caused a reduction in the 1st harmonic and amplified the 2nd and 3rd harmonic. The fact the axial location of the stenosis centre is shown to affect the pressure waveform (Figure 92) provides further validity to this argument. A restriction to this

experimental analysis is the number of data points recorded per waveform was relatively low at 22, due to the limited frame rate of the cameras used. An increased temporal resolution would provide a better representation of the phantom dilation.

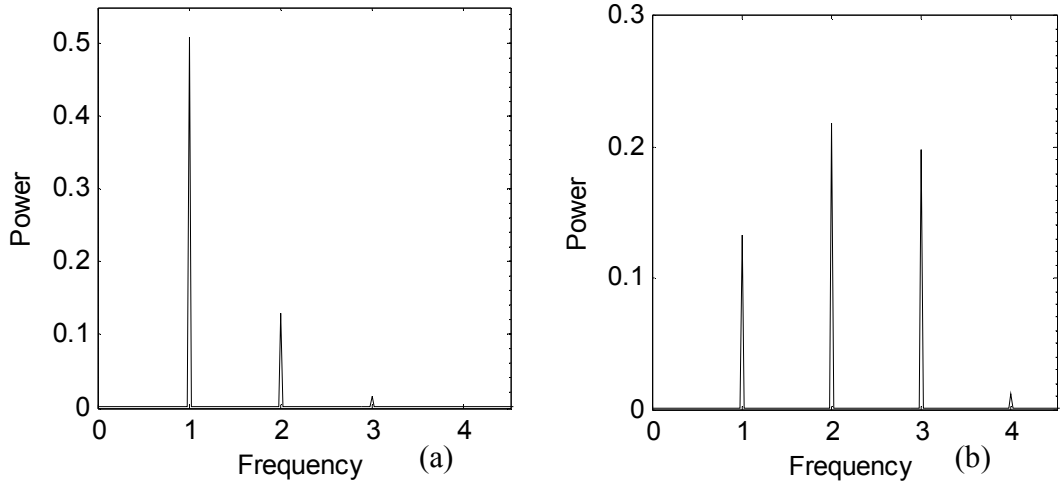

Figure 102 Temporal spectra of the peak-to-peak normalised (Equation 91 (Section 5.5.2)) (a) inlet flowrate and (b) inlet pressure

7.5.2 Region of Interest 1 Wall Shear Stress analysis

Figure 103(a) presents the temporal evolution of the WSS between $-1.1 \leq x/D \leq 1.1$ for the symmetric stenosis and Figure 103(b) presents the TAWSS in the same region. Results are presented for one wall only as there was minimal difference between the results obtained on the opposite surfaces. The peak WSS occurs just before the stenosis throat at $x/D = -0.1$. Between $0.1 \leq x/D \leq 0.75$ there was also a region of negative WSS that lasts for nearly the entire cardiac cycle; this is caused by the reverse flow observed in the recirculation region in Figure 95 and Figure 96.

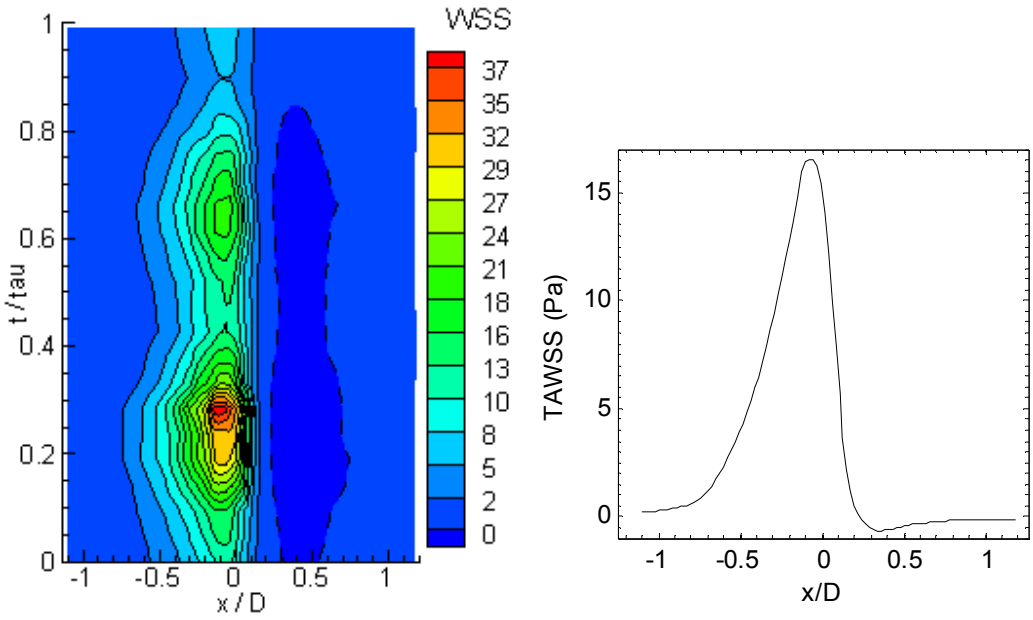

Figure 103 (a) Time variation of WSS in the symmetric stenosed phantom (--) represents a region of negative WSS (b) TAWSS along the wall of the symmetric phantom

To elucidate further on the temporal variation of the WSS over the cardiac cycle; Figure 104(a-c) presents the temporal evolution of the WSS at several streamwise locations along the phantom wall (x/D = -1.0:0.25:1 and the point of peak WSS -0.1). For locations upstream of the stenosis throat the temporal variation of the WSS was seen to follow the path of the centreline velocity closely (Figure 97a). A sharp rise can be seen in the acceleration phase with a decrease during the deceleration phase, similar observations were made by Li et al. (2007). Peak WSS rose between -1.0≤x/D≤-0.1, to a value of 33.39Pa, this dropped to 29.51Pa at the stenosis throat (x/D=0). The WSS observed by Li et al. (2007) at the stenosis throat in a geometry that had a smaller starting healthy diameter (0.0058m) and experienced a higher centreline velocity was shown to be ~100Pa, there was no mention of peak WSS occurring before the stenosis throat. The peak WSS observed by Tang et al. (1999b) was 196.1Pa, this work also observed a much larger centreline velocity. The work of Varghese et al. (2007b) observed WSS values at a higher Re of 1000 to be ~55Pa and observed the location of peak WSS to be similar to this work. As shown in the TAWSS plot (Figure 103(a)) after this point there was a dramatic drop in WSS magnitude. On the downstream wall of the stenosis (0.25≤x/D≤1) the reverse flow of the recirculation region caused a negative WSS, similar to observations made in previous computational studies (Varghese et

al. 2007b; Li et al. 2007; Tang et al. 1999b). In this work WSS was shown to reduce to -0.71Pa at x/D=0.5 then increase to -0.17Pa at x/D=1. The path the WSS waveform followed was an inverted image of the WSS waveform path of the upstream locations; this indicates that the reverse flowrate is driven by the forward jet. When comparing to the maximum, minimum and time averaged WSS magnitude (1.4, 0.58 and 0.84 respectively) observed in the straight tube phantom, it can be seen that the acceleration of flow caused by the reduction in diameter, severely increases the WSS along the upstream wall of the stenosis which can lead to endothelial cell erosion (Cao and Rittgers 1998). Downstream of the stenosis throat the recirculation zone caused a reduction from the WSS values observed in the healthy artery geometry.

Figure 104(d) presents the oscillatory shear index (OSI) along the wall, which was calculated using Equation 83 (Section 5.3.1). The main spike, when referring to Figure 103(b) is in a region of low TAWSS just after the peak TAWSS. The OSI is a very low value which indicates that the flow was mainly unidirectional. The small OSI values occurring between $-1.1 \leq x/D \leq -0.8$ are in a region where complete unidirectional flow is expected (OSI=0). There are two sources of error that account for this result; firstly light reflections at the fluid wall interface could be producing erroneous WSS values. Secondly, due to the large variation in WSS magnitude in both space and time in this region of interest, a time delay had to be selected that was a compromise to obtain the best possible results for both low and high WSS magnitudes. Repeating the experimental analysis in this region at a larger time delay would increase the validity of the results.

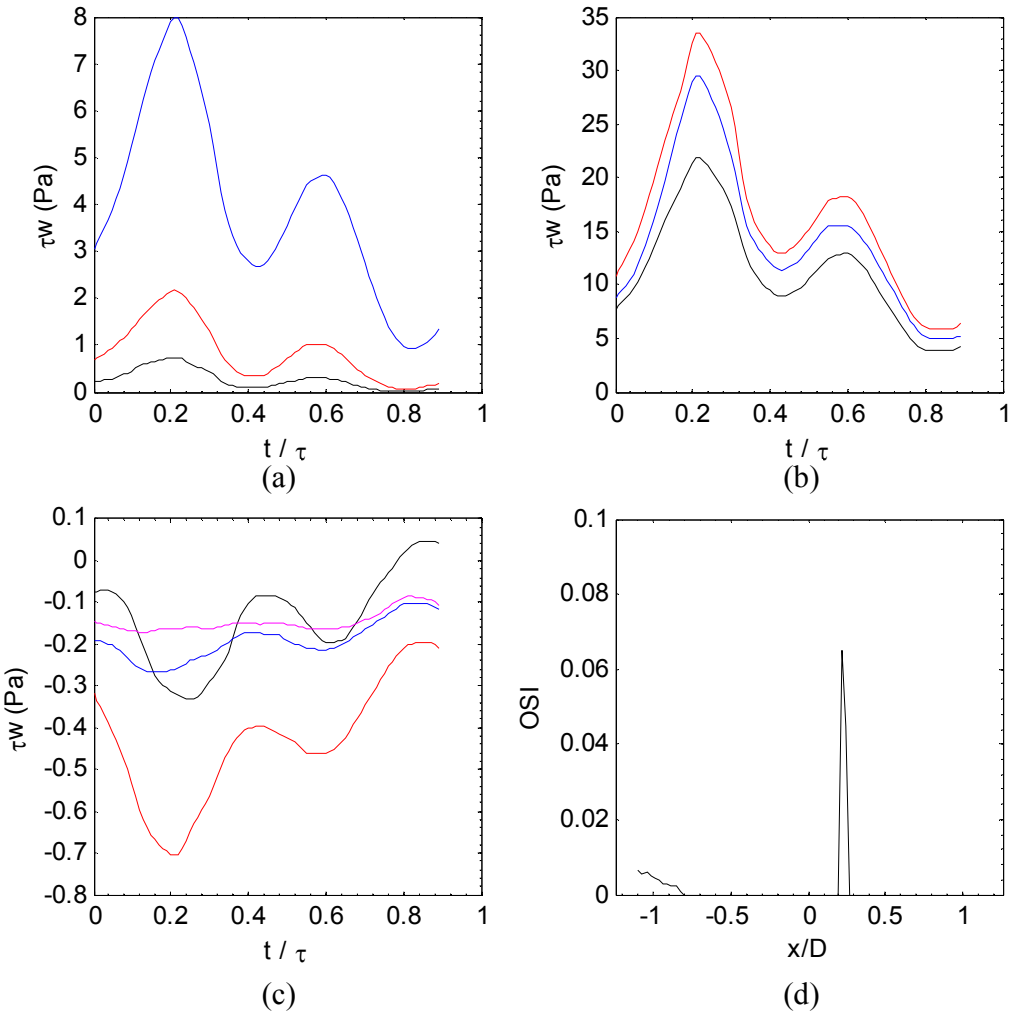

Figure 104 Temporal evolution of the WSS on the wall of the symmetric phantom at x/D (a) -1.0 (black), -0.75(red) and -0.5 (blue). (b) -0.25 (black), -0.1 (red) and 0.0 (blue). (c) 0.25 (black), 0.5(red) and 0.75 (blue) and 1.0 (purple). (d) Oscillatory Shear index along the wall (OSI).

Figure 105(a) presents the temporal evolution of the WSS between -1.1≤x/D≤1.1 for the unstenosed wall of the asymmetric stenosis and Figure 105(c) presents the respective TAWSS. Figure 105(b) presents the temporal evolution of the WSS between -1.1≤x/D≤1.1 for the stenosed wall of the asymmetric stenosis and Figure 105(d) presents the respective TAWSS. The peak WSS on the unstenosed wall occurred just downstream of the stenosis throat at x/D=0.1. Between 0.1≤x/D≤1.1, the WSS reduced in magnitude, but was a larger than that observed at the stenosis entrance (x/D=-1). The peak WSS on the stenosed wall occurs in a similar location as the symmetric geometry at x/D=0.08. There was a much smaller negative WSS region between 0.1≤x/D≤0.5 which occurred over a shorter interval in

the cardiac cycle compared to the symmetric geometry. The upstream location of peak WSS is different to the findings of Long et al. (2001), but the geometric differences of the stenosis in that study accounts for this variation.

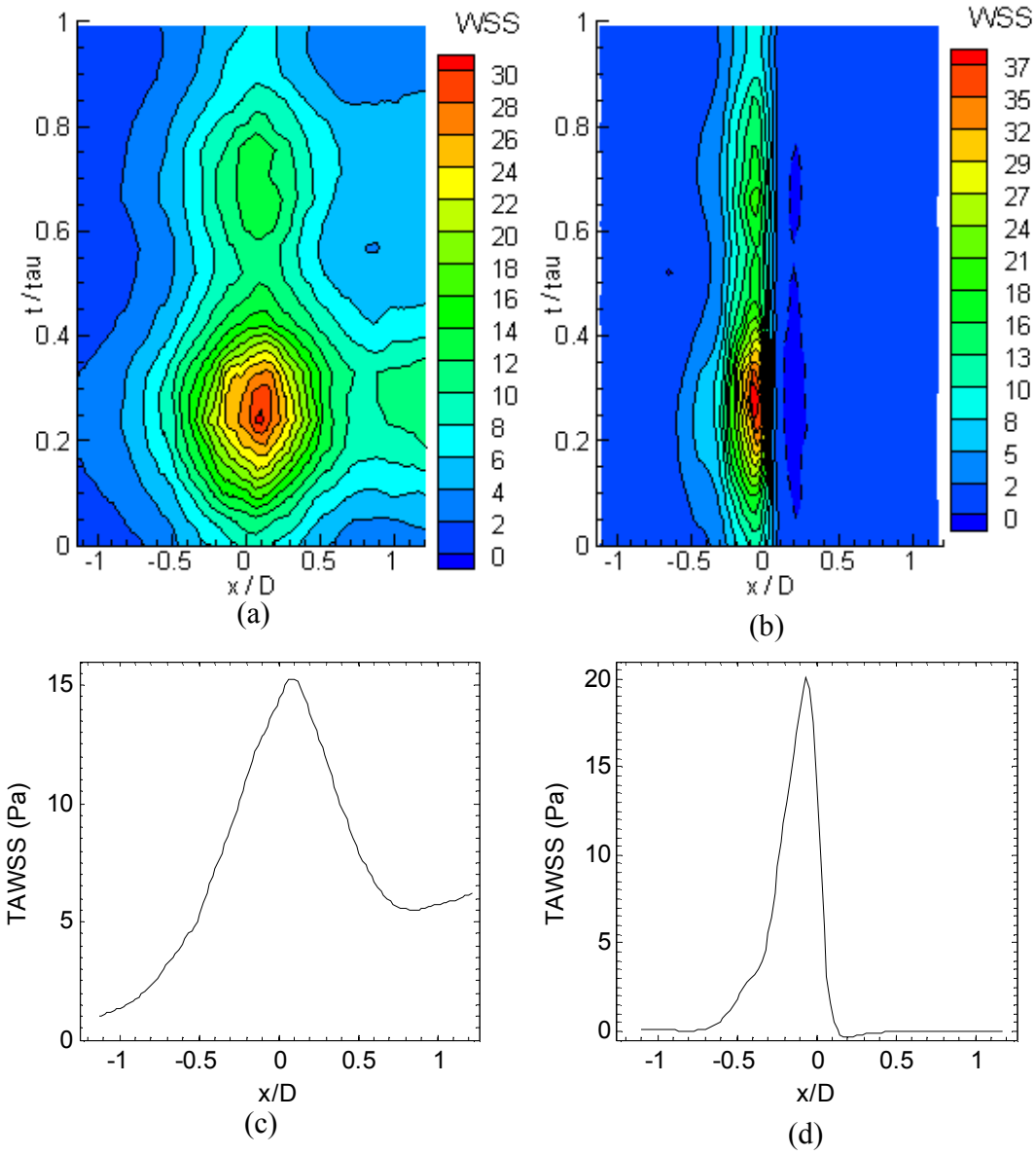

Figure 105 Contour plot showing the time variation of WSS in the asymmetric stenosed phantom plotted along (a) the unstenosed wall and (b) the stenosed wall. TAWSS as a function of location in the (a) unstenosed and (d) stenosed wall of the asymmetric phantom.

Figure 106 presents the temporal evolution of the WSS on the unstenosed wall of the asymmetric geometry at several streamwise locations (x/D = -1.0:0.25:1 and the point of peak WSS 0.1). As previously discussed the peak WSS increased between -1.0≤x/D≤0.1, to

a maximum value of 28.75Pa. Downstream of this point the magnitude of the WSS dropped, but stayed at a relatively high value across the cardiac cycle with a TAWSS ranging between 5-7Pa. This was caused by the asymmetry of the geometry forcing the main jet to be relatively close to the wall unlike the symmetric geometry. The path of the waveform is the same along the entire length of the wall following a similar path to the inlet flowrate.

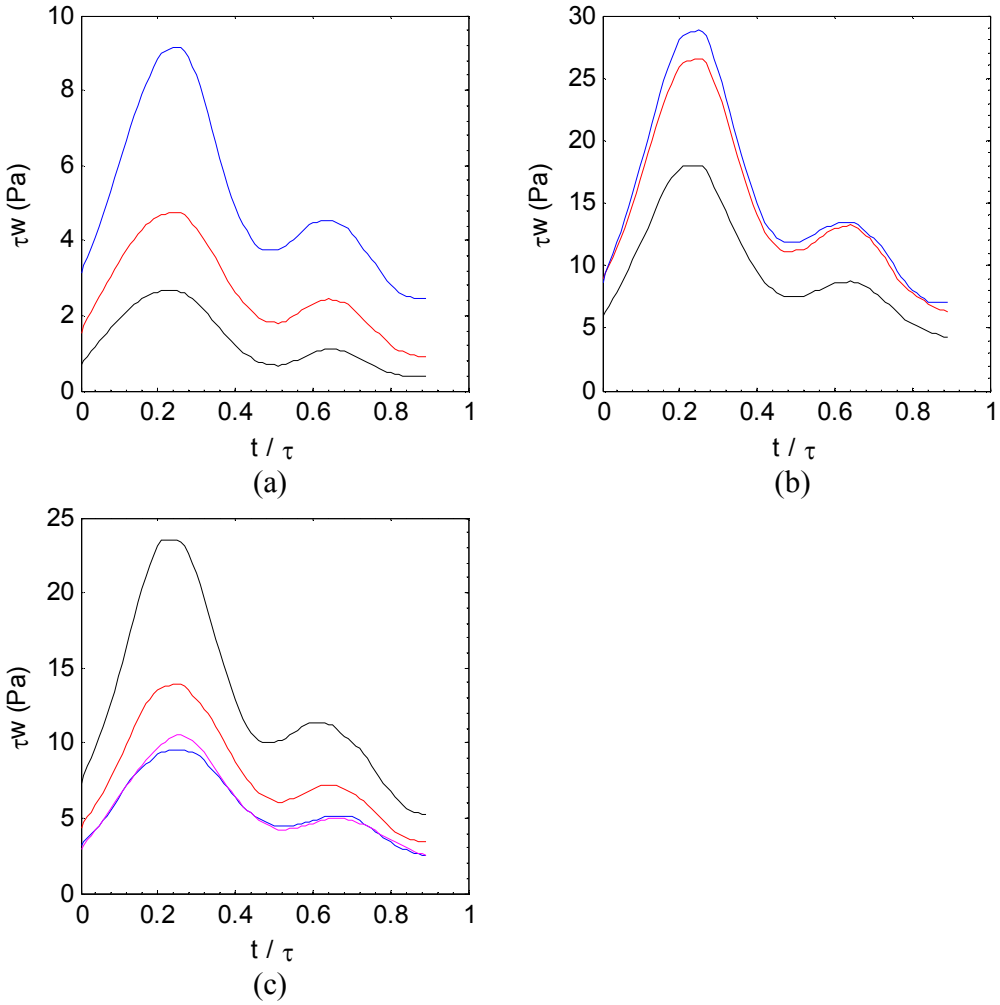

Figure 106 Temporal evolution of the WSS on the unstenosed wall of the asymmetric phantom at x/D (a) -1.0 (black), -0.75(red) and -0.5 (blue). (b) -0.25 (black), 0.0 (red) and 0.1 (blue). (c) 0.25 (black), 0.5(red) and 0.75 (blue) and 1.0 (purple).

Figure 107 presents the temporal evolution of the WSS on the stenosed wall of the asymmetric geometry at several streamwise locations (x/D=-1.0:0.25:1 and the point of peak WSS 0.08). In the initial section of the upstream stenosis wall (-1.0≤x/D≤-0.75) the WSS is low compared to the equivalent position on the unstenosed wall. Referring to Figure 98 to

Figure 100, it can be seen that the asymmetry of the geometry had already shifted the bulk of the flow up from the centreline (y/D=0), which increased the flow on the unstenosed wall (increasing the WSS) and reduced the flow on the stenosed wall, which in turn created a lower WSS. As the flow started to impinge on the upstream stenosis wall ((-0.5≤x/D≤-0.08) there was a marked increase in WSS to a maximum of 36.2Pa. This was higher than the peak WSS experienced in the symmetric geometry, this finding is similar to that observed by Tang et al. (2003). It can be attributed to the fact that the asymmetric wall had a larger gradient compared to the symmetric geometry causing an increased velocity experienced in that localised region. At the stenosis throat the WSS magnitude drops to 25.43Pa. On the downstream wall of the stenosis at x/D=0.25, the WSS waveform path was similar to that observed in the same location in the symmetric geometry; it followed an inverted image of the upstream profiles. At x/D=0.5 the WSS transitioned between positive and negative values during the cardiac cycle. The cause of this was the movement of the separation point discussed in section 7.5.1. x/D=0.5 initially experienced the reverse flow regime in the upper section of the recirculation zone which caused the negative WSS. As the flow accelerated the separation point passed across it and x/D=0.5 entered the lower section forward flow region producing a positive WSS. When the vortex dissipated in the deceleration phase of the cardiac cycle x/D=0.5 returned to the reverse flow region re-establishing the negative WSS. At x/D=0.75 and 1, as expected the shift from negative to positive WSS occurred earlier in the cycle due to these locations experiencing the transition from reverse flow region to forward flow region earlier. It also occurred at a lower magnitude.

Figure 107(d) provides the OSI on the stenosed wall. This data is not provided for the unstenosed wall as the WSS was unidirectional for the entire length (OSI=0). Referring to Figure 105(b) and (d) the OSI spike at x/D=0.1 is in a region of low TAWSS which is shown to fluctuate between positive and negative values. There is also evidence of a region upstream and downstream experiencing high OSI magnitudes, which occurred at low magnitude TAWSS. This result highlights the limitation of OSI, in that it is independent of WSS magnitude. The experimental errors of course affect the data in these two regions, which as discussed before include, light reflections at the fluid wall interface and the compromise in time delay selection arising from the variation in WSS magnitude in both space and time.

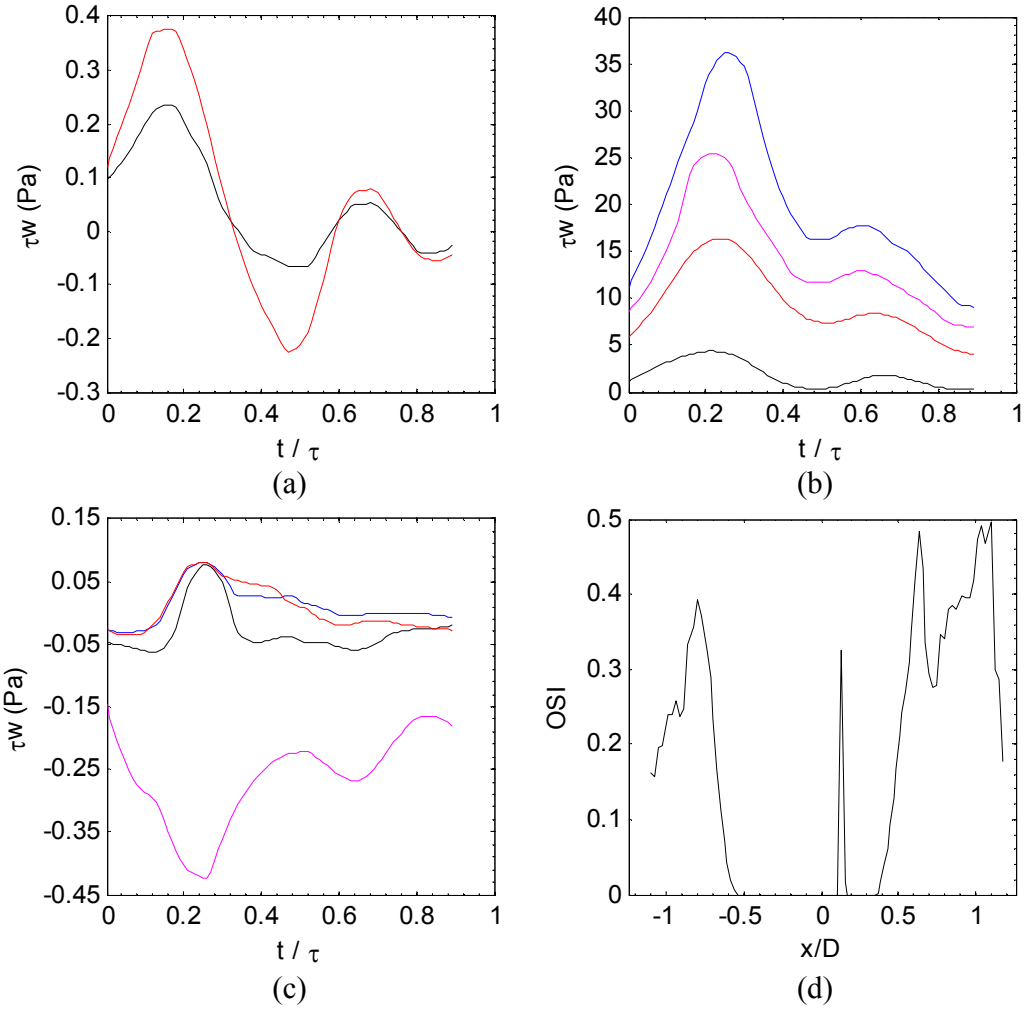

Figure 107 Temporal evolution of the WSS on the stenosed wall of the asymmetric phantom at x/D (a) -1.0 (black), -0.75(red). (b) -0.5 (black), -0.25 (red), -0.08 (blue) and 0.0 (purple). (c) 0.25 (purple), 0.5(black) and 0.75 (blue) and 1.0 (red). (d) Oscillatory Shear index along the wall (OSI).

7.5.3 Region of Interest 2 Flow Field Analysis

This section provides an initial analysis into the flow field experienced in ROI 2 in the symmetric phantom. This ROI is investigated in depth in the next chapter using a novel experimental illumination technique replacing the expensive high powered laser system, with, in relative terms, a cheaper Light Emitting Diode (LED) system. The results here will be used to validate the flow field observed using the LED system. Figure 108 shows the phase averaged streamwise velocity $\langle U_x \rangle(t)$ normalised by the mean free-stream velocity (U_m) for phase locations (I), (II), (IV), (VII) and (VII) in the symmetric waveform (Figure 92(a)). Two distinct flow regimes are evident; a high velocity forward flow central jet

emanating from the constriction and a separation region of low speed reversed or zero flow located from between y = ±0.35D and the phantom wall. This is quite different to the parabolic profile observed in the healthy straight geometry. In the initial flow acceleration phase up to phase IV the core jet entering the expansion downstream of the stenosis exit shows a 'flattening' of the flow profile in the centre which propagated downstream with increased flow rate. The length of this jet in this stenosed compliant phantom is vastly reduced compared to the inviscid core of a flow entering a rigid pipe as discussed by Durst et al. (2005). In the present case the core boundary is determined by the shear layer between the forward and reverse flow rather than the artery wall which reduces jet length. It is also shown for an oscillating flow system that core length is reduced by up to 40% (Burgmann et al. 2009). It still holds true, though, that core length will increase with increase in flow rate as shown here. In the outer region there was an increase in the velocity of the reverse flow as the central jet accelerated to peak flow rate. As the flow decelerated the 'flattening' of the velocity profile reduced and it assumed a more parabolic nature. It can also be seen in this ROI that during the acceleration phase of the cycle here is a lower peak velocity downstream (x=2.25D) compared to the upstream region (x=0.25D) with a difference ranging from 0.40-0.53U_m as flow accelerated to the peak value. In the deceleration phase this 'lag' is greatly reduced to a difference of 0-0.17U_m.

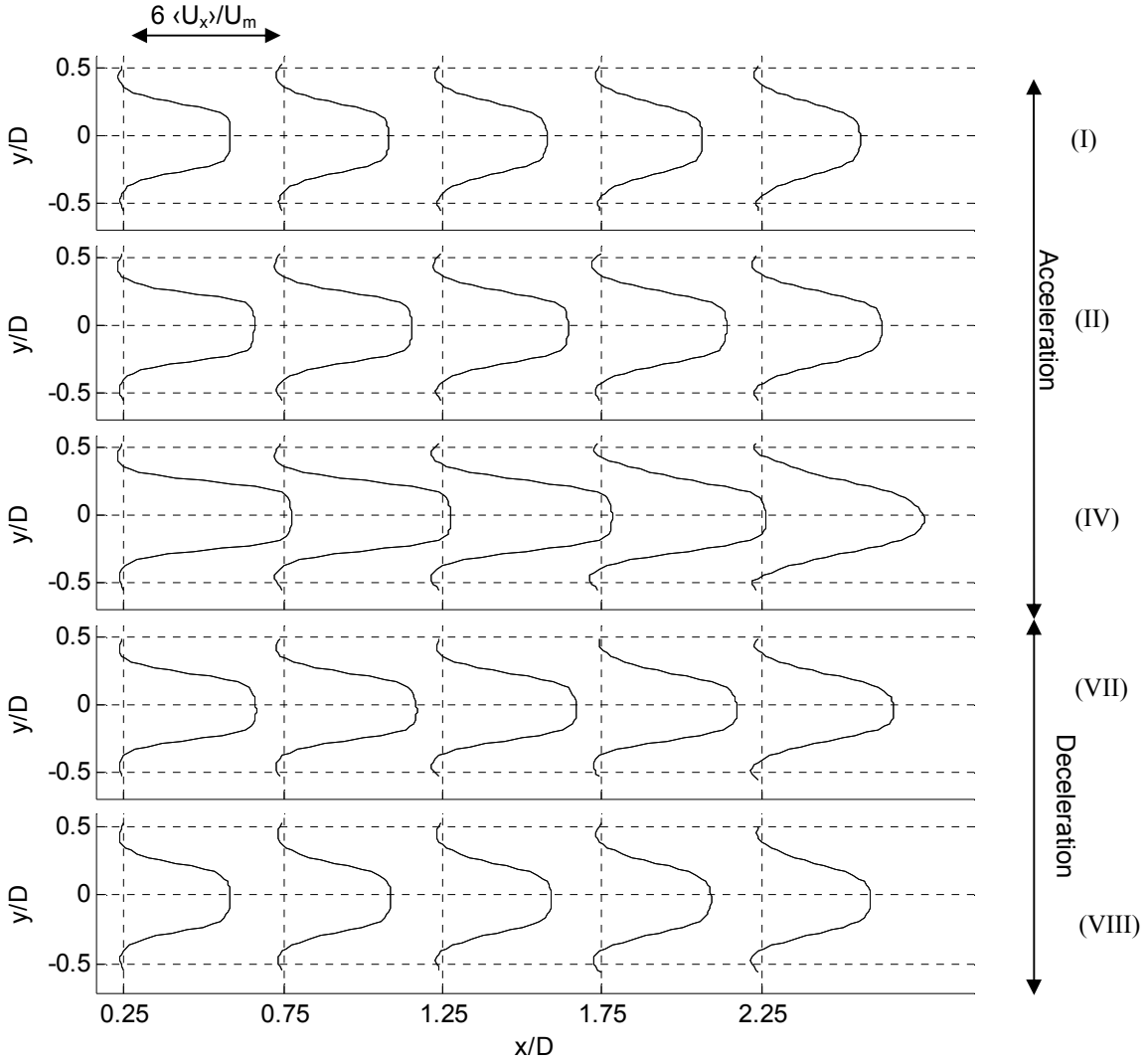

Figure 108 Phase averaged streamwise velocity profiles normalised by mean entrance velocity (‹U_x›/U_m) at phase locations indicated in Figure 92 (t/τ = (I) 0.09, (II) 0.13, (IV) 0.23, (VI) 0.31 and (VII) 0.34)

Figure 109 presents the instantaneous evolution of the velocity field between phase locations (II) and (V) for the 4th period of the entire captured series. It is representative of observations made over all data sets. Vortices can be observed to occur reminiscent of a street of Kelvin-Helmholtz instabilities. This observation requires further investigation to understand the evolution of these observed vortices. To do this a higher resolution analysis of the waveform needs to be done (i.e. more data points in one cardiac cycle studied). This is performed in the next chapter which provides an in depth study of ROI 2.

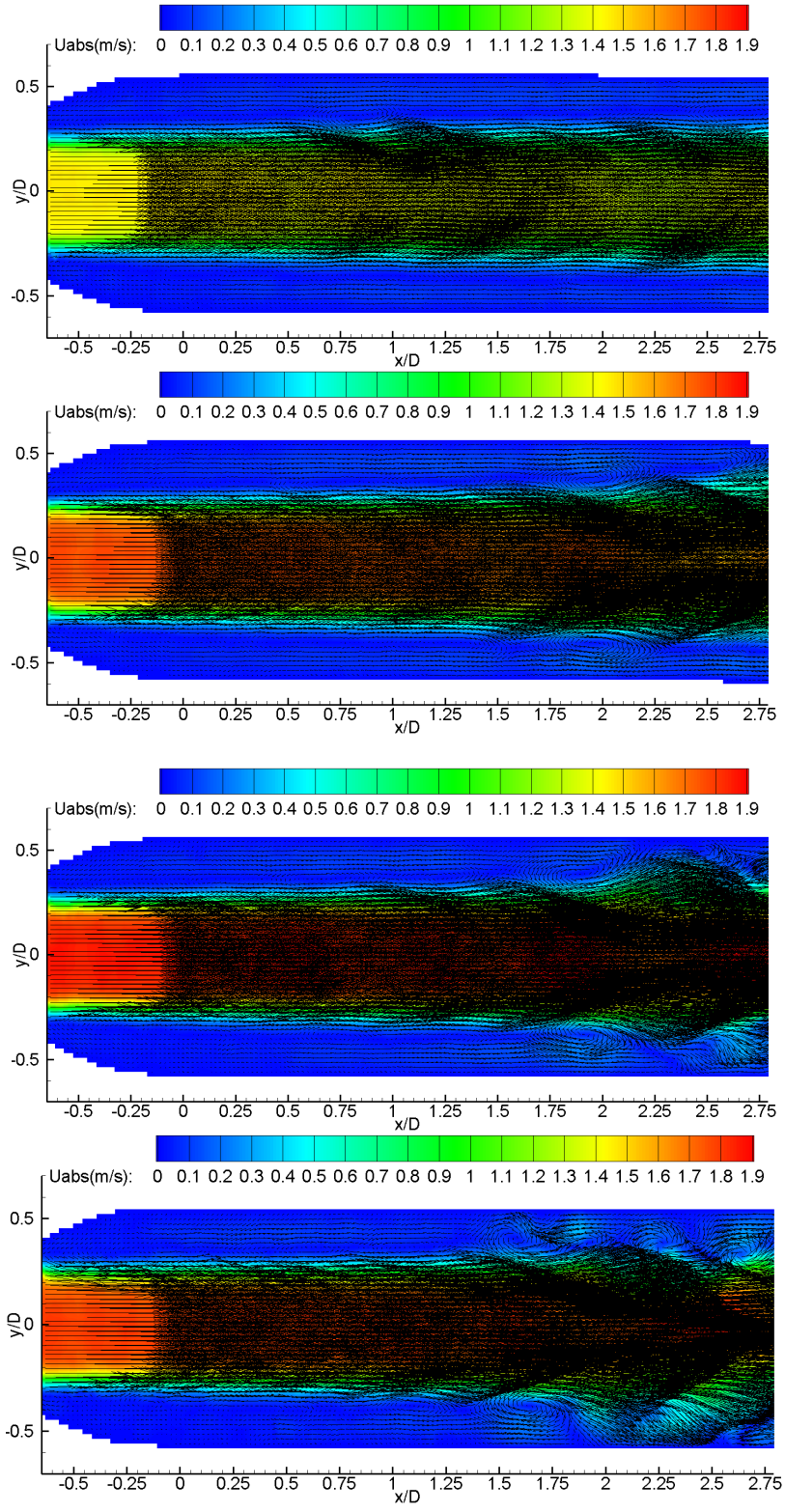

Figure 109 Instantaneous velocity vectors with contours of the absolute velocity component $U_{abs}(t)$ (m/s) at phase locations t/ τ=(II) 0.13, (III) 0.19, (IV) 0.23 and (V) 0.26

7.6 Conclusion

This section provides an in depth analysis into the WSS observed through both a symmetric and asymmetric stenosis, with an analysis of the cause of the differences observed. There is also an analysis of the flow field downstream of the symmetric stenosis. It is clear there is very little experimental work with a physiologically realistic flow waveform input into stenosed compliant geometry. This work to the author's knowledge is the first full experimental analysis of WSS in the stenosis region using this geometry and waveform input. A huge increase in WSS can be seen to occur in the stenosis throat in both a symmetric and asymmetric stenosed geometry. It is also evident that stenosis axial position is important, with asymmetry producing a major change in WSS and flow field. This is important in medical terms as a stenosed artery is very rarely going to be symmetric in appearance. It is also shown that stenosis geometry effects input flow and pressure waveform. The velocity magnitudes presented here have shown good agreement with other bodies of work. There is agreement in how WSS develops along the artery wall but disagreement in WSS magnitude, this however was highly dependent on variations in geometry and flow rates experienced.

The work in this chapter applied a physiologically realistic waveform from a healthy artery to a stenosed geometry as it is difficult to obtain cardiac waveforms for diseased arteries. This may affect the validity of the results and future work should look to applying a more realistic wave input. It is also evident that especially for the asymmetric stenosis the flow field will present variation in the axial direction. Stereoscopic or tomographic PIV should be used in future investigation to understand the effect the 3-D flow field has within the geometry. The restriction of only recording 22 data points per waveform should be investigated, with high speed data analysis. This is however further investigated in the following chapter. There is also a high variation of WSS across the artery wall from very low to quite high values; it would be prudent to repeat the WSS analysis at regions of low WSS to ensure that data presented here isn't over or underestimating the magnitude due to pixel displacement being too low to get a fully resolved result.

8 Time Resolved PIV measurements of the flow field in a stenosed, compliant arterial model

PIV is extensively used to experimentally analyse transparent flow phantoms of physiological systems. These experimental set ups can be extremely costly with low repetition rate double pulsed lasers costing in the region of $US 50,000. High-power Light Emitting Diodes (LEDs) have recently become available due to developments in solid-state illumination see Buchmann et al. (2012) for more details. Willert et al. (2010) investigated the feasibility of using LED illumination as an alternative to laser-based illumination for planar PIV experimentation in both air and water. Buchmann et al. (2012) further investigated this technique for application with Tomographic PIV. Willert et al. (2012) then went on to investigate LED application in high frame rate schlieren (MHz) imaging. The relevant review of the literature relating to the analysis of a stenosed carotid artery (CA) is presented in Section 7.2. This section presents results obtained using the high-power LED set up applied by Buchmann et al. (2012), with the light sheet produced by an optical fibre system. The LED illumination is used to obtain high speed planar PIV measurements in a compliant symmetrically stenosed flow phantom experiencing a physiological flow wave input representative of the carotid artery waveform.

8.1 Experimental Setup

This chapter provides an analysis of a straight compliant phantom (Mk.III phantom) representing the CA with a 50% symmetric stenosis by diameter. A novel LED illumination system is implemented in the experimental technique.

8.1.1 Data Analysis

Most of the mathematical operations applied to this analysis have already been set out in Section 5.3.1. There are also two types of root mean square (r.m.s) fluctuations that will be presented in this work; time averaged (Equation 96) and phase averaged (Equation 97).

$$u_x{}'_{rms,T} = \sqrt{\frac{1}{T}\sum_0^T \left(u_x'(t)\right)^2} \qquad \textbf{Equation 96}$$

$$u_x{}'_{rms,N} = \sqrt{\frac{1}{N}\sum_1^N \left(u_x'(t+N\tau)\right)^2} \qquad \textbf{Equation 97}$$

8.1.2 Flow Facility

This experimental investigation was performed on the Mk. III symmetric stenosis phantom with the region of interest (ROI) depicted in Figure 110 (same region as ROI 2 in section 7.5.3). A schematic of the experimental flow system used in this investigation is shown in (Figure 44 Section 4.4). Reynolds number (Re) and Womersley number (α) matching was again applied to ensure similarity between the in vivo and experimental in vitro conditions. The same physiological waveform with a maximum, minimum and mean Re of 954, 383 and 644 respectively was applied at the inlet. Section 7.3.1 should be referred to for the relevant flow and pressure profiles. Figure 111 shows the relevant phases of the cardiac cycle where analysis in this chapter was performed.

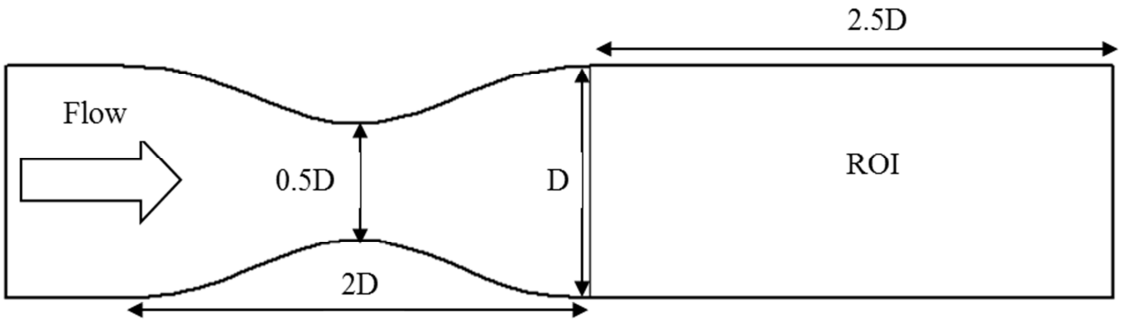

Figure 110 Schematic of flow phantom internal geometry and location of region of interest (ROI)

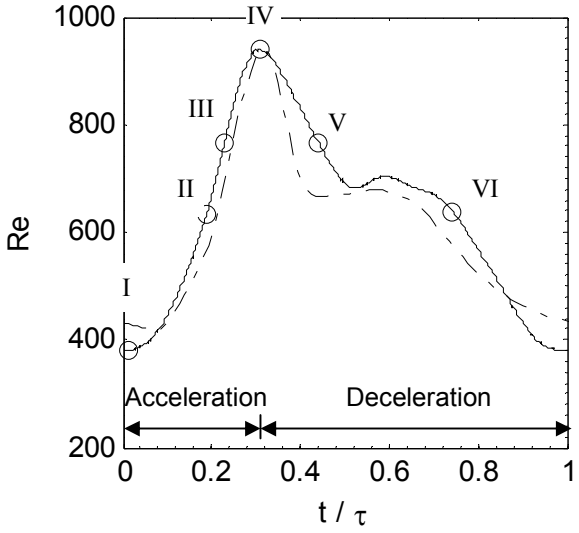

Figure 111 In vivo (•–) scaled carotid artery and phase averaged in vitro (–) inlet physiological flow waveform with phase locations at points of interest t/τ = (I) 0.01 (II) 0.19 (III) 0.23 (IV) 0.31 (V) 0.44 and (VI) 0.75).

8.1.3 LED Illumination and Camera Setup

The flow was illuminated with a custom built high power LED system. The light from the LED was fed through a fibre optic system with the fibres clamped in a linear pattern to produce a light sheet (Figure 112). A full explanation of the LED circuit and fibre optic coupling is given by Willert et al. (2010) and Buchmann et al. (2012), this section provides a brief overview. The system used a green PT-120 LED (Luminus Devices Inc.); Table 24 gives performance data supplied by the manufacturer for pulsed operation at a duty cycle of 50%. This type of LED was designed for projector systems and they are surface emitters with a near constant distribution of light per unit area. The LED was driven by short-duration high current pulses from an electronic circuit system. A power supply charged capacitors with the charge released to the LED by a TTL triggered MOSFET power transistor. This circuit could provide current pulses of up to 150A at a pulse duration between $1\mu s \leq \tau_p \leq 250\mu s$ at ~kHz repetition rates. LED light emission duration was directly proportional to the input drive current which was controlled precisely by the width of the TTL signal. The LED light emission lags behind the initial TTL signal by ≈200ns.

Table 24 Specification of green PT-120 LED in pulsed operation with 50% duty cycle (Luminus 2009)

Wavelength (nm)	Maximum drive current (A)	Maximum recommended current (A)	Luminous Flux (lm)	Radiometric flux (W)	Light Emitting area (mm^2)
525	36	30	3500	7.3	4.6×2.6

Willert et al. (2010) and Buchmann et al. (2012) have shown that reducing τ_p allowed for an increased maximum drive current and that mean light emission was proportional to the drive current, therefore an increased light emission can be achieved. Willert et al. (2010) provide damage threshold data and safe operation settings and their dependence on pulse width. In this setup the LED had a pulse width of 80µs.

Images were captured by a 1280×1024pix megapixel Motion Studio MotionPro X3 with a Nikon 60mm lens attached. The resolution recorded by the camera was 24 pix per mm. Each image pair was processed with a multi pass cross-correlation algorithm (Buchmann and Jermy 2007) which started with an initial window size of 128×128pix reducing to 32×32pix at the final iteration. A 75% overlap was used giving a final vector spacing of 1/3mm. The camera recorded at a rate of 100Hz and the time delay between image pairs was set at 500µs with a CCD exposure time of 499µs. The LED circuitry and camera were synchronised using a BNC pulse delay generator, which was in turn triggered with a TTL signal from the pump system for synchronisation with the time oscillating flow wave. 50 flow wave cycles were recorded.

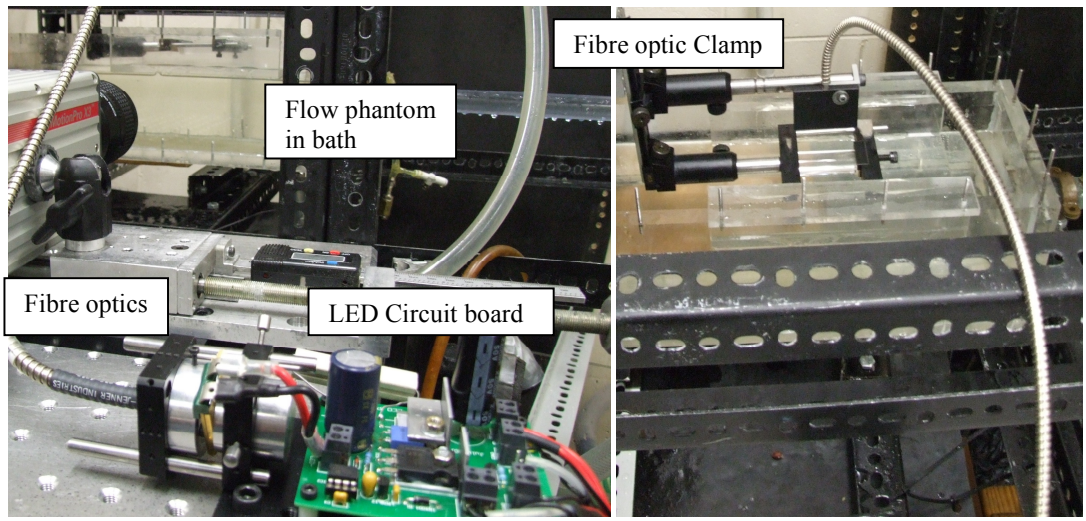

Figure 112 Camera and LED set-up

8.1.4 Limitations of the experimental setup

The light sheet produced by the LED illumination setup in this experimental analysis experienced rapid reduction in intensity as it diverged and propagated outwards. The flow phantom experimental setup used in this analysis was adapted from the previous work in the thesis. The External pressurisation chamber (EPC) shown in the experimental schematic (Figure 44 Section 4.4) served two purposes; firstly it contained the same liquid as the flow phantom to reduce optical distortion from the curvature of the phantom and minimising buoyancy forces. Secondly it was sealed and attached to a header tank to allow for accurate control of transmural pressure (the pressure difference across the compliant wall between the internal working fluid and external fluid). Due to the distance between the compliant phantom and the EPC external wall, the light sheet intensity in the ROI when the fibre optic clamp was located outside the EPC was too weak to produce useable PIV data. To position the light sheet close enough to perform PIV the EPC had to be unsealed as shown in Figure 112 and filled with just enough liquid to remove refractive distortions. Pressurisation control of the flow phantom was therefore not possible. It should be noted that other authors do not report the value of external pressurisation applied to experimentation (Pielhop et al. 2012; Burgmann et al. 2009; Deplano et al. 2007), but acknowledge that it was controlled.

The width of the light sheet produced was also a restricting factor in the experimental setup compared to that of a conventional PIV laser which can easily produce a width of 150mm. For the LED setup the vector validity rate was greatly reduced at the extremity of the light sheet. Invalid vectors increased from 3% in the central section, to 30% in the final 10% extremities of the light sheet. This limited the ROI to a length of 50mm (2.5 neutral diameters (D)).

8.2 Image Preprocessing

The light intensity recorded by the high speed CCD camera from 10μm diameter silver coated glass sphere seeding particles under LED illumination (Figure 113(b)) was much less than that which can be typically obtained from a standard PIV setup with a double shutter camera (Dantec Flow Sense 2M) and double pulse laser (120mJ Nd:YAG) (Figure 113(a), taken on the same flow). Figure 114 presents resulting images of pre-processing techniques applied to images obtained in this study along with the corresponding PIV analysis. Invalid

vectors are evident where large displacement vectors occur with respect to nearby vectors. To extract as much information as possible from the available signal, the images were pre-processed with an average background intensity subtraction (Wereley et al. 2002) (Figure 114(b)), as opposed to a minimum subtraction (Figure 114(a)) since with the low illumination level provided by the LED system minimum subtraction would leave a substantial amount of image noise in the final pre-processed image, which was found to produce 20-30% invalid vectors in the main body of the flow. Average subtraction does remove more information from the images, but when processed with a dynamic histogram filter and Gaussian smoothing with a 3×3 kernel to enhance image contrast (Raffel et al. 2007) (Figure 114(c)) there were enough particles per interrogation window (greater than the 15 recommended by (Keane and Adrian 1990) for an invalid vector rate of less than 10%) to obtain a resolvable correlation peak with a final invalid vector rate between 2 and 5%.

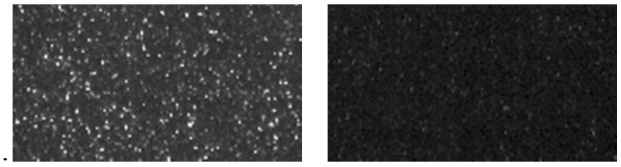

Figure 113 (a) 120mJ Nd:YAG illuminated raw image (b) LED illuminated raw image

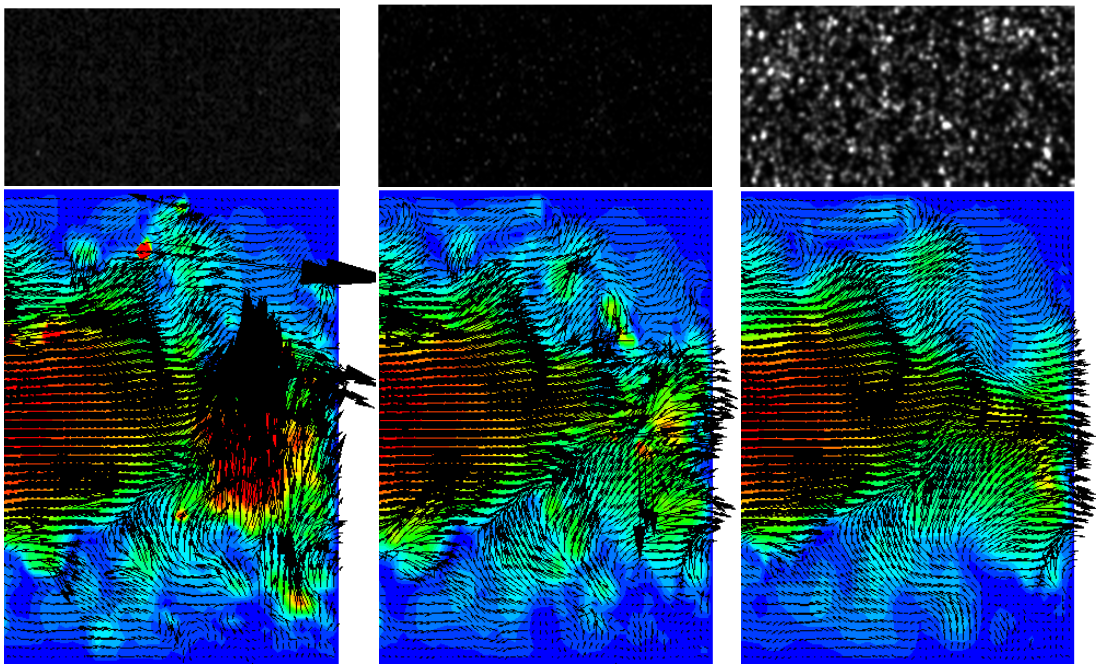

Figure 114 (top) Sample images pre-processed with (a)Minimum background subtraction (b) Average background subtraction (c) Average background subtraction with a dynamic histogram filter and Gaussian smoothing with a 3×3 filter and (bottom) corresponding Instantaneous PIV map with velocity vectors and contour map

8.3 Results and Discussion

Experimental results were obtained in a plane containing the centre axis of the compliant flow phantom. The ROI depicted in Figure 1 covered an area starting at the stenosis exit and extending 2.5 neutral diameters (D) downstream, which is the same ROI as ROI 2 in Section 7.5.3.

8.3.1 Mean Flow Statistics

Figure 115 shows the phase averaged streamwise velocity $\langle U_x \rangle(t)$ profiles calculated using Equation 79 (Section 5.3.1) normalised by the inlet mean free-stream velocity (U_m) for the six phase locations depicted in Figure 111. Phase (II) to (VI) in Figure 115 have the same phase location in the cardiac cycle as those depicted in Figure 108 (ROI 2 Section 7.5.3). The same two distinct flow regimes are evident; a high velocity forward flow central jet emanating from the constriction and a separation region of low speed reversed or zero flow located from between y = ±0.35D and the phantom wall. Figure 116 presents the shear strain for the time averaged velocity field ($\overline{U}$), calculated by Equation 98. It shows the shear layer that separated the flow regimes covering a region from y = ±(0.2 to 0.35)D from the centre.

$$\gamma_{xy} = \left(\frac{\partial U_x}{\partial y} + \frac{\partial U_y}{\partial x} \right) \qquad \textbf{Equation 98}$$

To validate the results obtained using the new LED illumination system the peak velocity at x/D=0.25 at several phase locations was compared to the equivalent data obtained using laser illumination (Table 25). At peak flow rate the relative difference between the results was extremely low (-0.08%). The maximum relative difference was -8.57% observed at phase (III). The difference between the results is acceptable and a possible cause to the larger variations could be due to a slight mismatch between the phase locations where the data was obtained.

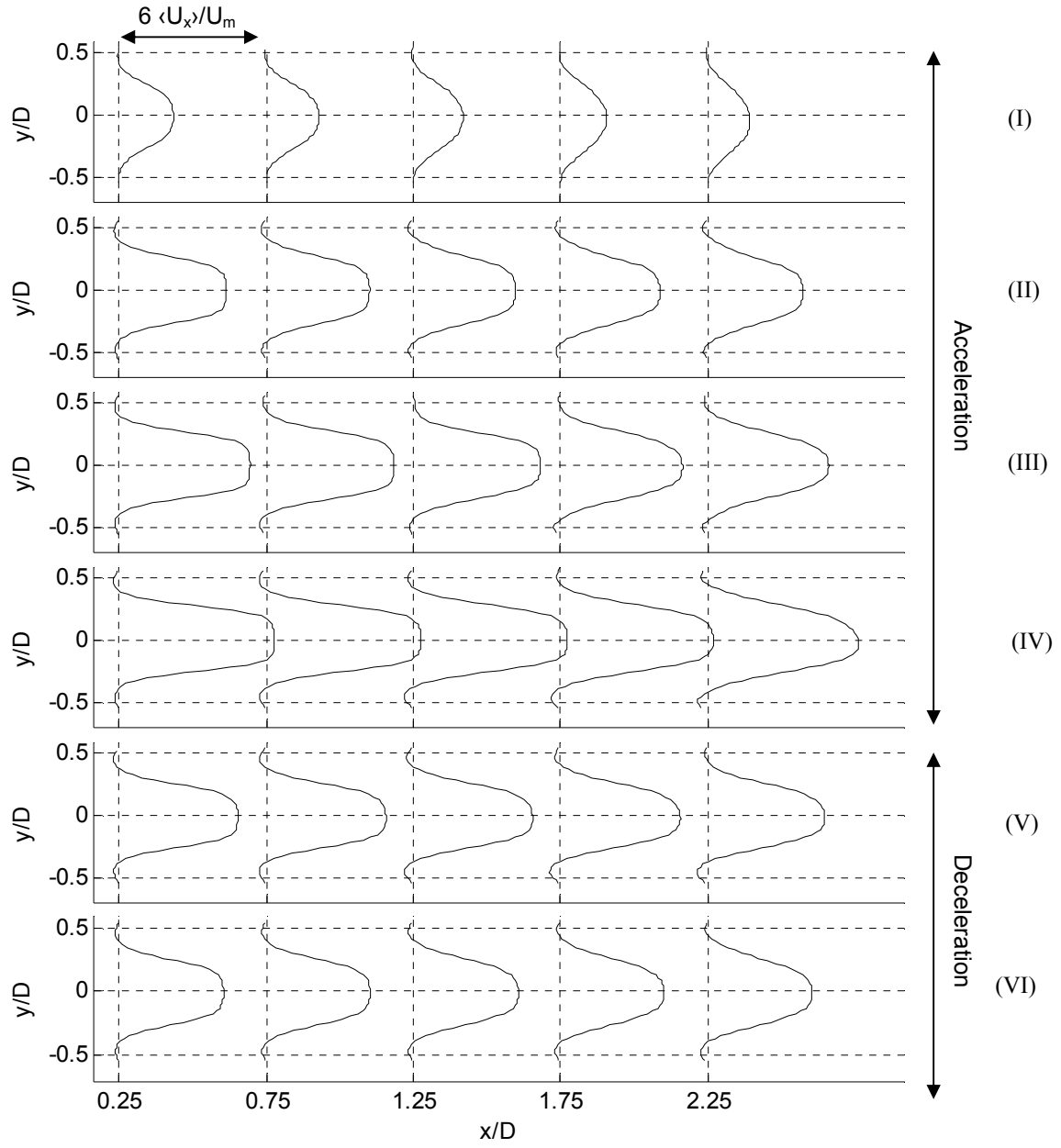

Figure 115 Normalised phase averaged streamwise velocity profiles ($\langle U_x \rangle / U_m$) at phase locations indicated in Figure 111 (t/τ = (I) 0.01 (II) 0.19 (III) 0.23 (IV) 0.31 (V) 0.44 and (VI) 0.75)

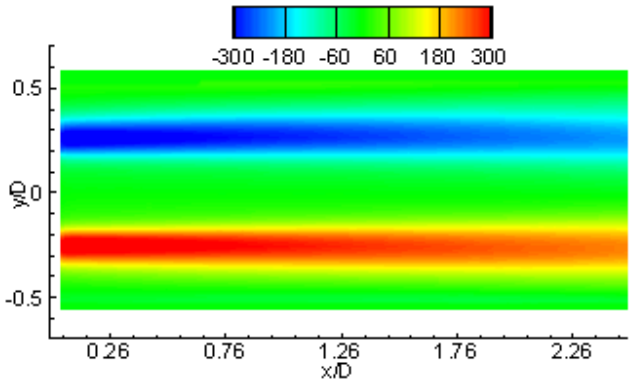

Figure 116 Time averaged shear strain (γ) downstream from the stenosis exit

Table 25 Peak velocity at phase locations indicated in Figure 115 (equivalent to those shown in Figure 108 (Section 7.5.3) at x/D=0.25 for results obtained using laser and LED illumination. Relative difference between the two results calculated using Equation 86 (Section 5.3.1).

Phase location (Figure 115)	Peak Velocity (Laser) ($\langle U_x \rangle / U_m$)	Peak Velocity (LED) ($\langle U_x \rangle / U_m$)	Relative Difference (%)
II	4.026	4.363	-8.37
III	4.912	5.333	-8.57
IV	6.315	6.32	-0.08
V	4.959	4.851	2.18
VI	4.026	4.26	-5.81

8.3.2 Instantaneous Flow Statistics

As discussed in Section 7.5.3, some interesting fluid phenomena occur downstream of the stenosis exit. Figure 117 to Figure 120 present the instantaneous evolution of the flow field at the phase locations depicted in Figure 111. The results were obtained from the 4th period of the series of 50 captured, but were representative of observations made across all data sets. The shear layer observed between the central jet exiting the stenosis and the separated flow led to Kelvin-Helmholtz instabilities. From $0.01 \leq t/\tau \leq 0.19$ this generated small vortices with minimal effect on the forward jet. At $t/\tau=0.19$ (phase location (II)) the vortices increased in size. Figure 117 shows the velocity vectors superimposed on a colour-contour plot of the radial velocity U_y at phase location II for t/τ = 0.190, 0.193, 0.197 and 0.2. The Re at this flow rate was 644 which is equivalent to the physiological waveform mean flow rate. The velocity fields show an axis-symmetric system (with regards to physical location) of vortex rings propagating downstream from the stenosis (yellow box), causing a repetitive fluctuation in the U_y component of velocity longitudinally in the forward jet in close proximity and within the shear layer. Even though the fluctuation location is axis-symmetric, there was an

asymmetry in the velocity magnitude with the fluctuations in the upper half ($0 \leq y/D \leq 0.5$) being larger than the lower ($0 \leq y/D \leq -0.5$). This shows an asymmetry in vortex strength coming from the stenosis exit.

Figure 118 concentrates on the region of interest depicted by the large red box in Figure 117 at the edge of the shear layer (y/D=0.35). It shows that the change in the U_y component of velocity of the main jet was caused by a street of Kelvin-Helmholtz vortices between forward and reverse flow. The small red boxes in Figure 118 show how the same vortex traversed longitudinally downstream. The vortices drew fluid from the jet as they tracked its trajectory downstream causing the fluctuation in U_y. Vétel et al. (2008) observed in a rigid phantom, under steady flow conditions at Re = 630, a variation in the symmetry and length of recirculation zone, which was not seen in the results presented here.

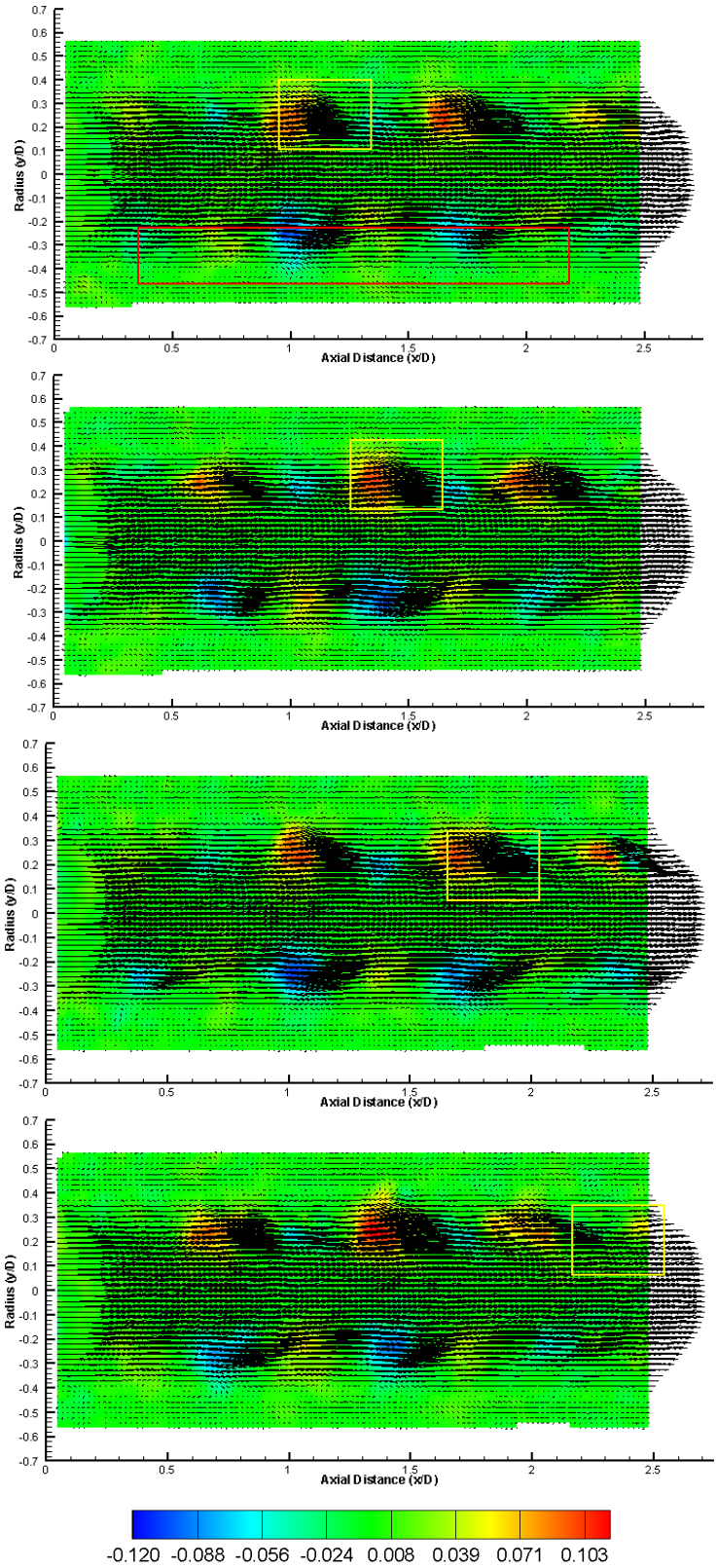

Figure 117 Instantaneous velocity vectors with contours of the radial velocity component $U_y(t)$ (m/s) at phase location II, showing 4 sequential time steps t/ τ (a) 0.190 (b) 0.193 (c) 0.196 and (d) 0.199

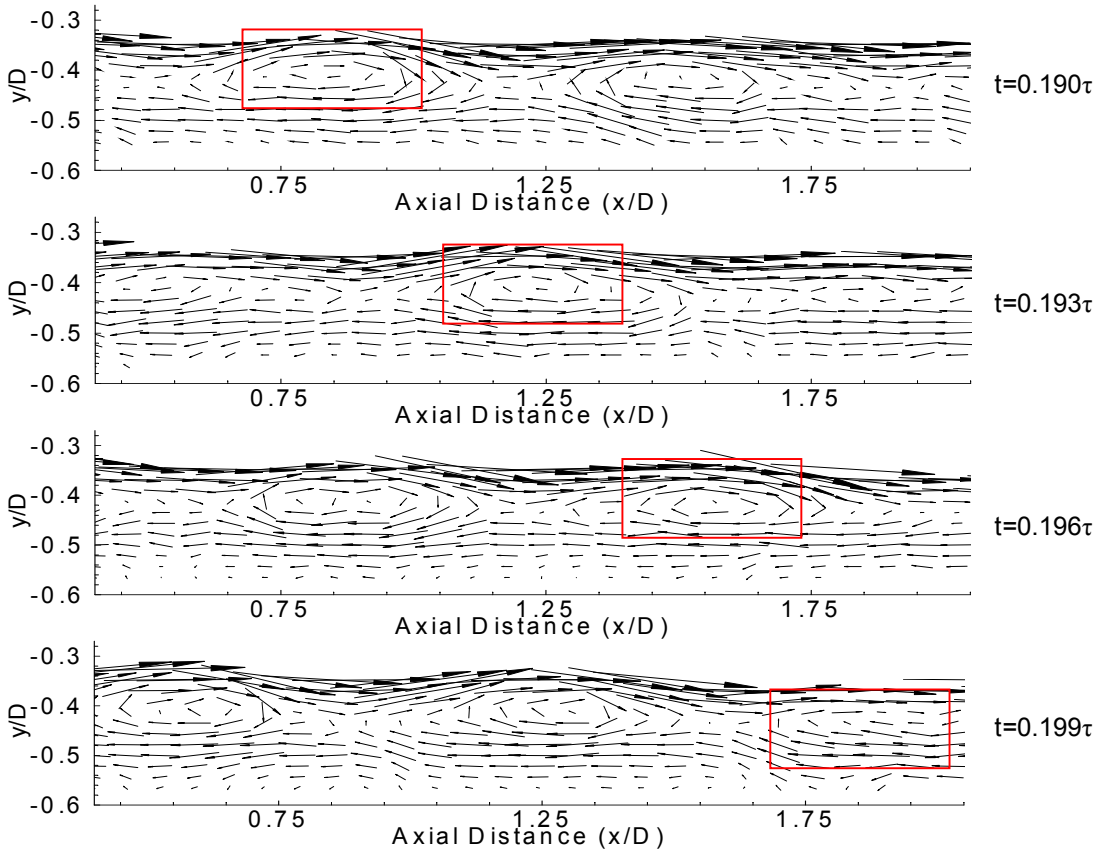

Figure 118 Instantaneous velocity vectors from large red box region of Figure 117 at equivalent time steps t/ τ (a) 0.190 (b) 0.193 (c) 0.197 and (d) 0.2 (vector length has been increased by a factor of 2 for ease of understanding)

Figure 119 shows the velocity field 1.75D to 2.5D downstream of the stenosis exit, for t/τ=0.231, 0.234, 0.237 and 0.240 (phase location (III) with Re=766). It shows an increase in the size of the shear layer vortices and an asymmetry starting to appear in the spatial field in the upper and lower regions. The red and green boxes track two vortices as they travel downstream. Vétel et al. (2008) showed this system to occur further downstream (x=3D onwards) at an equivalent Re. The discrepancy with our findings may be due to the rigid wall used in Vétel's work. The instability in the velocity field shown in Figure 119 continued to manifest as flow rate accelerated towards the peak flow rate. Vortex size continued to increase leading to the increase in fluctuation magnitude observed between phase locations (III) and (IV).

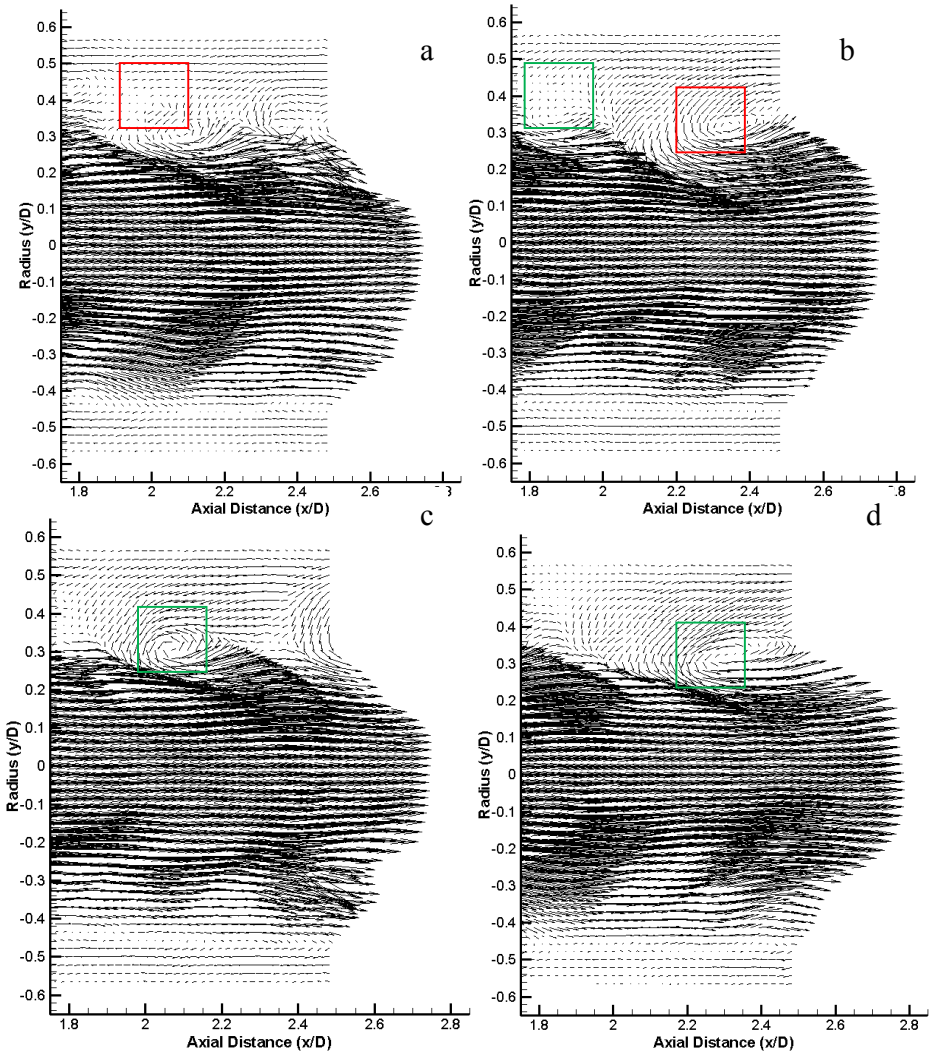

Figure 119 Instantaneous velocity vectors at at phase location III, showing 4 sequential time steps t/ τ (a) 0.231 (b) 0.234 (c) 0.237 and (d) 0.240

The instantaneous velocity fields in the same spatial region as Figure 119, at phase location (V) (Re 766) between t/τ =0.445, 0.448, 0.451 and 0.454 are shown in Figure 120. An assumption that is commonly made in arterial experimental and numerical simulation is that the flow is quasi-steady (Buchmann et al. 2010; Vétel et al. 2010; Varghese et al. 2007a), therefore steady flow simulation gives a good representation of the flow field dynamics. The instantaneous flow rate at the phase locations analysed in Figure 119 and Figure 120 was equivalent (Re 766), but the flow rate acceleration and deceleration at these locations differed, i.e. the magnitude of the flow rate gradient in the acceleration phase at phase location III (Figure 119) was larger than the gradient in the deceleration phase at phase location V (Figure 120). Figure 120 shows a large reduction in the intensity of the vortices,

compared to Figure 119. Therefore the strength of the vortices depended not only on the instantaneous flow rate but also on the rate of change of flow rate. The flow cannot be assumed to be quasi steady. The Kelvin-Helmholtz vortices were weaker in the deceleration phase. From phase location V to the end of the cycle the Kelvin-Helmholtz vortices in the shear layer reduced markedly in strength and the propagating wave system seen in Figure 117 dissipated completely.

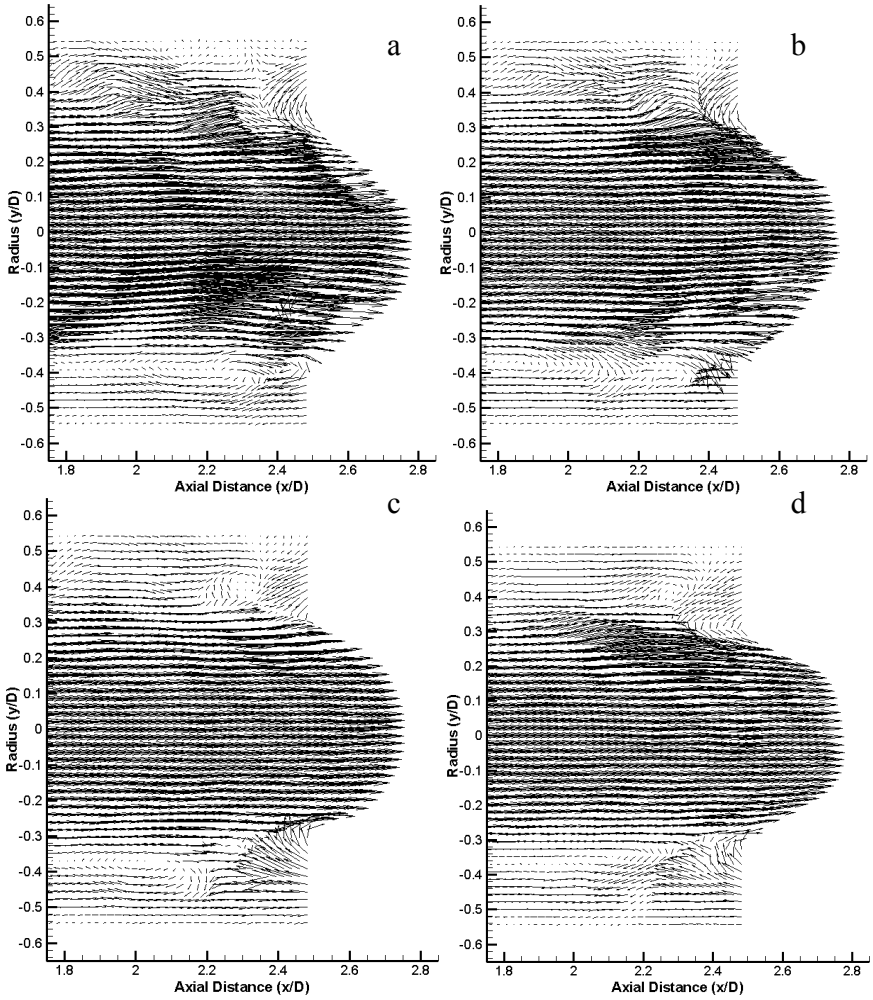

Figure 120 Instantaneous velocity vectors at at phase location V, showing 4 sequential time steps t/ τ (a) 0.445 (b) 0.449 (c) 0.452 and (d) 0.455

8.3.3 Temporal Evolution

To better understand the temporal evolution of the flow field Figure 121(a) presents the time history of the instantaneous streamwise velocity, normalised by U_m, at three longitudinal locations (x/D=0.25, 1.25 and 2.25) each at five radial locations (y/D=0, 0.17, 0.26, 0.35 and

0.43) from the centreline to the phantom wall. The results show a contiguous set of 4 cycles. Corresponding phase average waveforms for the whole dataset are shown in Figure 121(b). Figure 121(c) presents the corresponding time history for the radial velocity. The results show the temporal evolution of the disturbances in the flow was largely periodic and coherent, with some cycle to cycle fluctuation superimposed. Along the centre line (y/D=0), at the stenosis exit (x=0.25D) there was minimal fluctuation in velocity over a cycle period. Further downstream the frequency of the fluctuations in velocity increased in the vicinity of the peak flow rate. The cause of this was the downstream vortex system shown to occur between phase III and IV (Figure 119). The velocity fluctuations at the subsequent radial locations occurred at the same phase of the flow cycle as the centreline fluctuations when the flow was accelerating to the peak flow rate and in the initial deceleration phase thereafter (phase location II to V). The fluctuation intensity increased with increasing radial location with maximum fluctuation occurring within the region of the shear layer (y/D=0.2-0.35). Within the reverse flow region, where the flow velocity is low, there was a reduction in intensity of the fluctuation.

8.3.4 Velocity disturbance

Figure 122 presents the time averaged turbulence intensity calculated by Equation 99. The fluctuation resolution is limited to 50Hz by the recording rate and Nyquist sampling considerations therefore if any fluctuations occurred above that frequency they were not recorded in this work. There was an increase in the turbulence intensity in the shear layer as the distance downstream from the stenosis exit increased. Due to the interaction between the shear layer, the jet exiting the stenosis and the vortex system it created between x/D=2.25 to 2.5 there was an increase in turbulence intensity across the entire phantom radius.

$$Ti = \frac{u_{x'rms,T}}{U_m} \qquad \textbf{Equation 99}$$

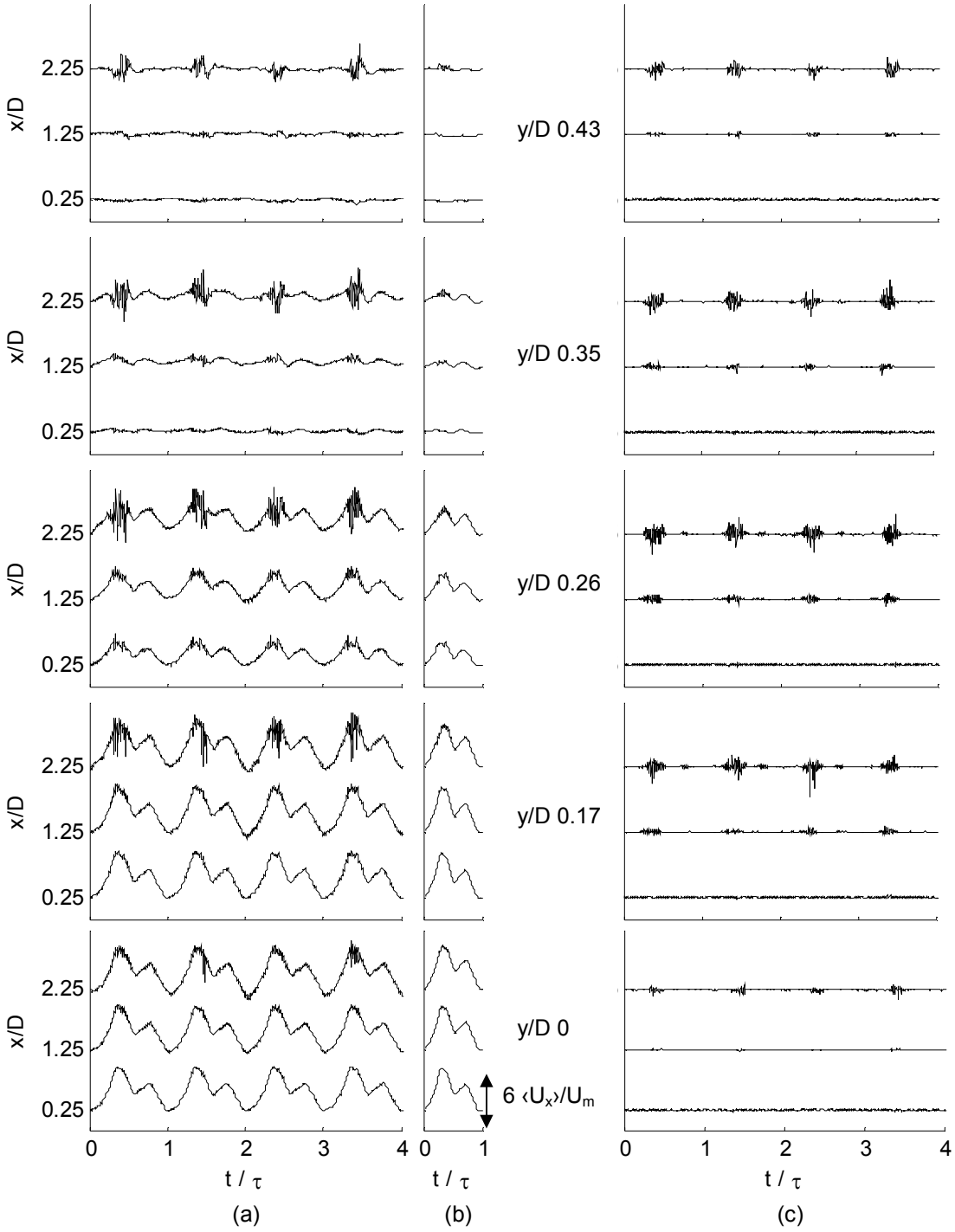

Figure 121 (a) Time history (4 cycles shown of the 50 used for phase averaging) of normalised streamwise velocity (U_x/U_m) as a function of streamwise distance (x/D) at radial location (y/D) (from bottom to top) 0, 0.17, 0.26, 0.35 and 0.43 (b) Corresponding normalised phase averaged velocity ($\langle U_x \rangle/U_m$) (c) Corresponding normalised radial velocity (U_y/U_m)

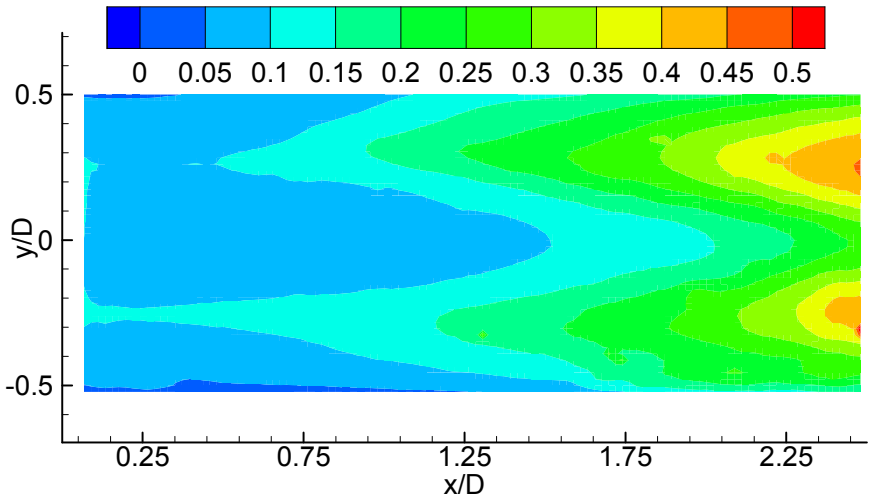

Figure 122 Time averaged turbulence intensity

To elaborate on the temporal and spatial evolution of the velocity disturbances; Figure 123 and Figure 124 present the spatial evolution of the phase averaged fluctuation r.m.s velocities (Equation 97 Section 8.1.1) in both the streamwise $u_x'_{rmsN}$ and radial $u_y'_{rmsN}$ directions for the six phase locations depicted in Figure 111. There was a significant variation in the profile shape of both velocity fluctuation components with phase and streamwise location. At the minimum flow rate (phase location I) where the phase averaged velocity profile in the central region (Figure 115(a)) was parabolic with near zero reverse flow near the wall, there was a minimal disturbance in the radial velocity of less than $0.02U_m$. In the streamwise velocity the disturbance ranged from 0.04-$0.2U_m$ from x/D=0.25D to 2.25. The disturbance increased with increasing downstream location. This corresponded to the reduction in maximum velocity in the flow profile that was observed in Figure 115. Midway through the initial acceleration at phase location II there was significant amplification of the disturbances. Initially, downstream from the stenosis exit at x/D = 0.25 and 0.75, there was symmetry about the central axis in both $u_x'_{rmsN}$ and $u_y'_{rmsN}$ r.m.s levels. The disturbance in $u_x'_{rmsN}$ peaked in the centre at ~$0.15U_m$ and in $u_y'_{rmsN}$ disturbance the peaks were located within the shear layer (y/D=0.28) at a value of ~$0.2U_m$. This was caused by the Helmholtz instabilities drawing the fluid from the central jet as shown in Figure 117. Further downstream an asymmetry in velocity disturbance magnitude occurred around the central axis with a significant increase in $u_x'_{rmsN}$ to ~$0.5U_m$ in the shear layer between x/D = 1.26D and 2.26 and $u_y'_{rmsN}$ increasing to ~$0.25U_m$.

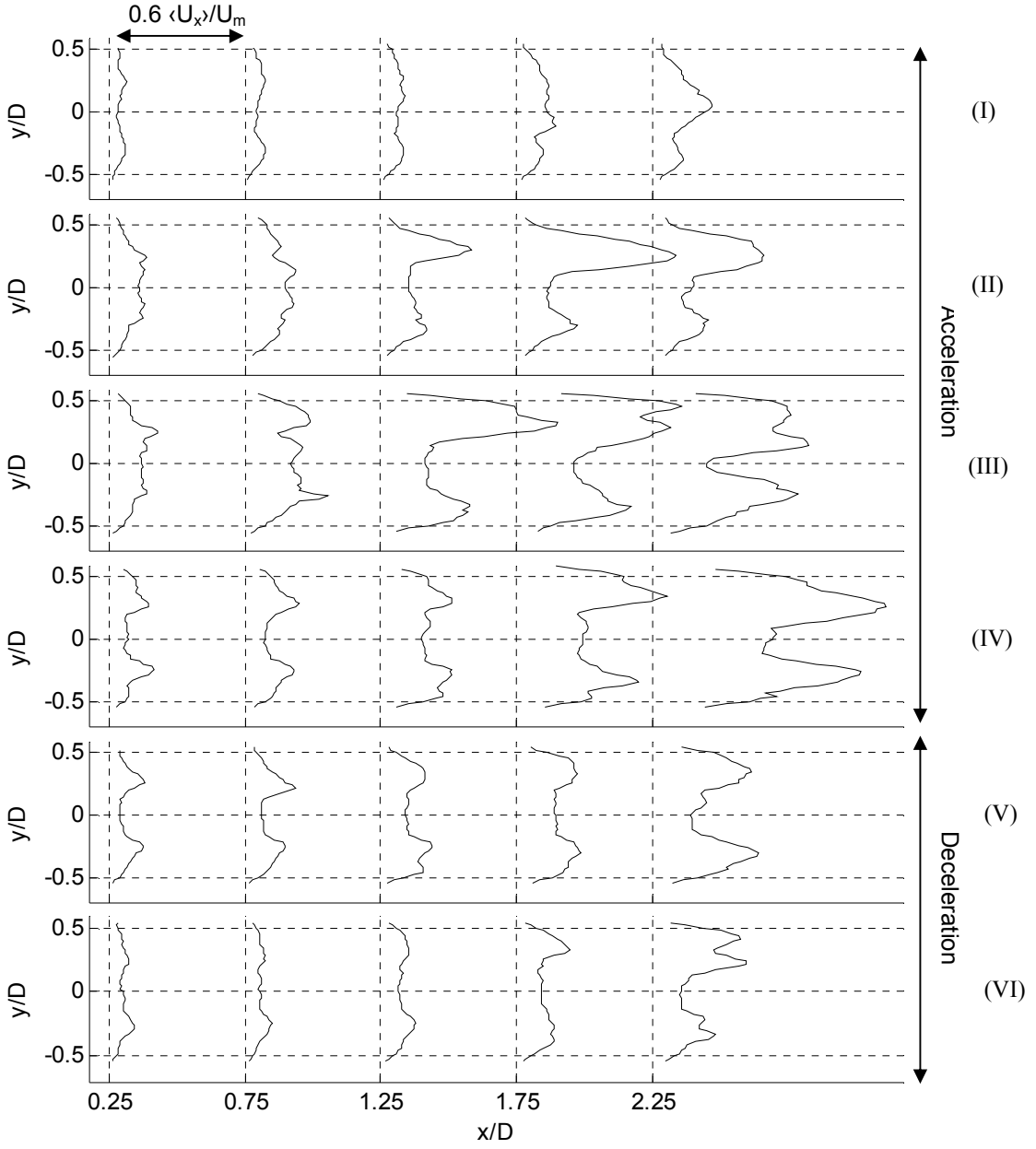

Figure 123 Normalised streamwise phase averaged r.m.s ($u_x'_{rmsN}$/ U_m) velocity profiles at phase locations indicated in Figure 111 (t/τ = (I) 0.01 (II) 0.19 (III) 0.23 (IV) 0.31 (V) 0.44 and (VI) 0.75)

In the final quarter of the initial flow acceleration at phase location III, velocity disturbance amplitudes continued to increase within the shear layer. The magnitude of fluctuation in both the streamwise and radial components increased with increasing downstream location and began to occur in the main jet. This increase in central jet fluctuation was caused by the vortex system shown in Figure 119. Peak $u_x'_{rmsN}$ increased to $0.64U_m$ and peak $u_y'_{rmsN}$ increased to $0.4U_m$. Comparing $u_x'_{rmsN}$ with $\langle U_x \rangle$ in Figure 115 at phase location III it is evident that there was an increase in the disturbance levels occurring in the reverse flow

zones either side of the main jet (y/D=±0.35 to 0.5). At peak flow rate at phase location IV the magnitude of velocity disturbances reached peak values. $u_x'_{rmsN}$ at x/D=2.25 is significantly larger than at other locations, which corresponded to a large reduction in peak magnitude of the streamwise phase averaged velocity profile (Figure 115 (IV)). As flowrate decelerated (phase location V and VI), the disturbance magnitude reduced for $u_x'_{rmsN}$ and $u_y'_{rmsN}$ with the largest magnitudes located at x/D=1.75 and 2.25D.

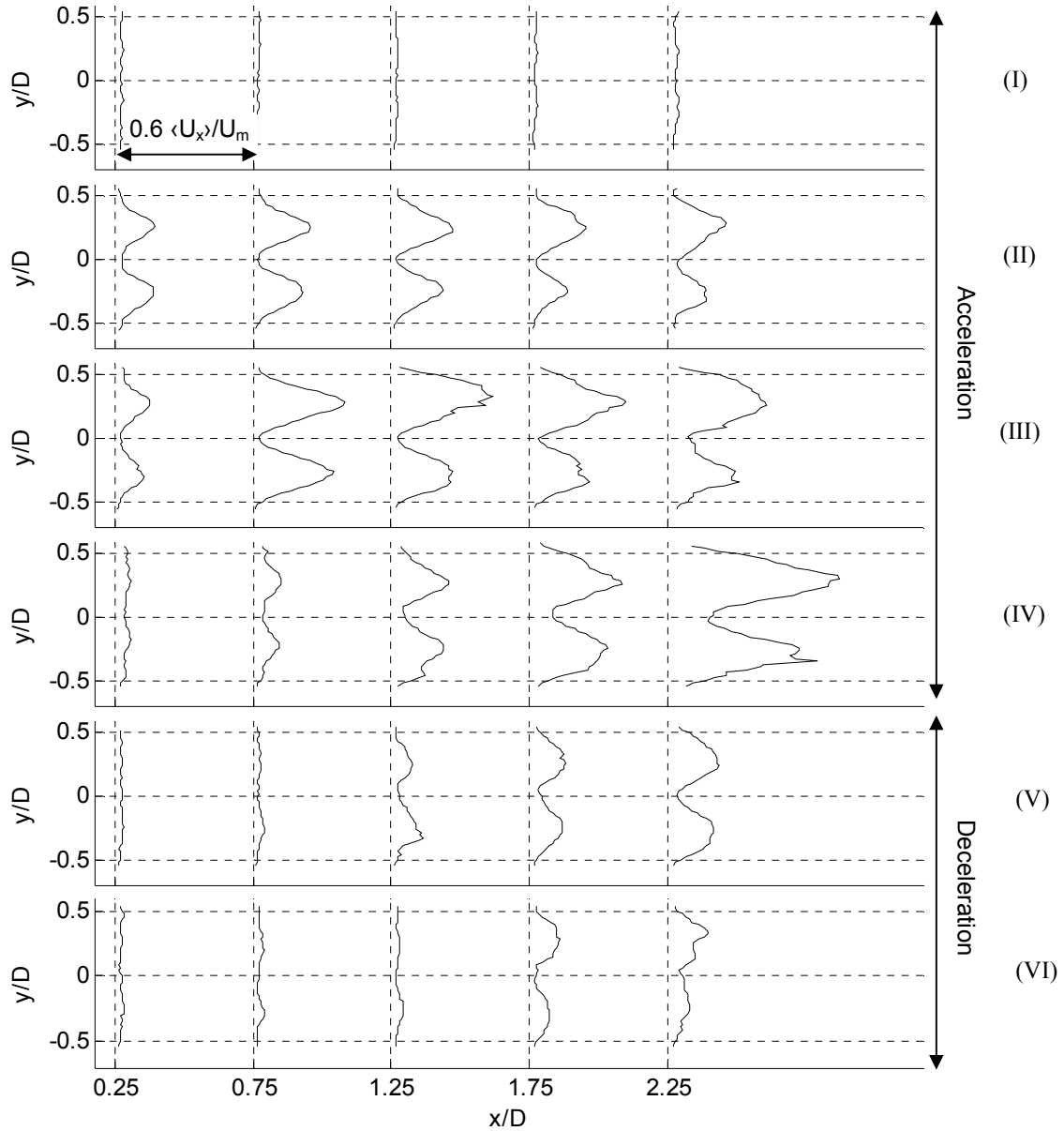

Figure 124 Normalised radial phase averaged r.m.s ($u_y'_{rmsN}$/ U_m) velocity profiles at phase locations indicated in Figure 111 (t/τ = (I) 0.01 (II) 0.19 (III) 0.23 (IV) 0.31 (V) 0.44 and (VI) 0.75)

To further understand the disturbance in velocity with time and the periodicity it displays in Figure 121, Figure 125 shows the temporal evolution of both the streamwise and radial r.m.s velocities at 3 longitudinal locations (x/D=0.25, 1.25 and 2.25) each at 5 radial locations (y/D=0, 0.17, 0.26, 0.35 and 0.43). As discussed previously there was an increase in disturbance magnitude at all radial locations with increased streamwise location. At x/D=1.25 velocity disturbance was localised to the late initial acceleration phase and peak flow rate, at x/D=2.25 the disturbance is evident in the initial deceleration phase as well. The magnitude of the disturbance increase was equivalent in its physical location in both the streamwise and radial direction, which rather than signify a turbulent breakdown (this would be shown by a randomness rather than equivalency) of the flow, suggests the movement of coherent vortex structures through the system.

8.3.5 Structural Response

To understand the effect compliance has on the flow field it is important to investigate the dilation of the phantom and its relation to the phase of the flow wave. The phantom wall position at each time step recorded was located using the wall detection technique described in Section 3.7.3. The peak-to-peak normalised phase averaged vessel dilation (Equation 91 Section 5.5.2) is shown in Figure 126. Previous work by Pielhop et al. (2012) as discussed in Section 7.2 has shown that for a sinusoidal waveform there was a phase difference in the dilation between locations upstream and downstream of the stenosis. This created a secondary bulk flow that was superimposed onto the piston bulk flow, affecting the characteristics in the flow field.

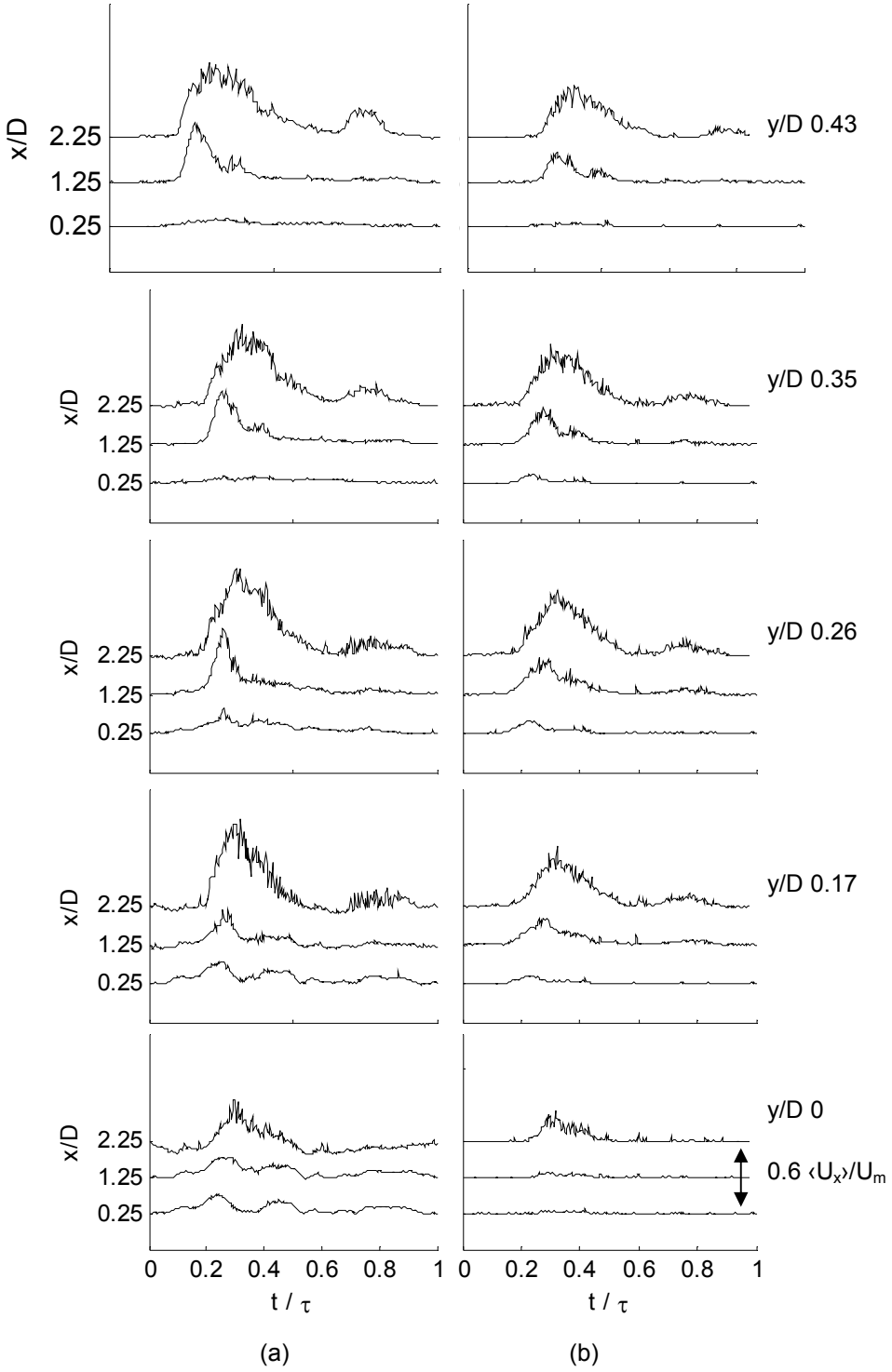

Figure 125 Temporal evolution of normalised (a) streamwise ($u_x'_{rmsN}/ U_m$) and (b) radial ($u_y'_{rmsN}/ U_m$) phase averaged r.m.s velocities a function of streamwise distance (x/D) at radial location (y/D) (from bottom to top) 0, 0.17, 0.26, 0.35 and 0.43

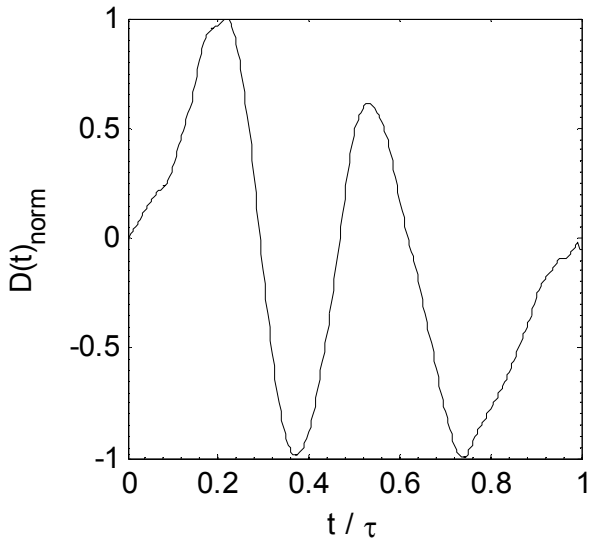

Figure 126 Phantom Dilation at x = 1.25D

Figure 127 presents temporal spectra of results peak-to-peak normalised in both space (calculated using Equation 91 Section 5.5.2 where F(t) is the time varying component) and time for the inlet flow rate, pressure, phantom dilation and centreline velocity at x/D = 1.25. Since the data was normalised by τ the peak powers occurred at integer values representing the Fourier components of the waveforms. For pressure and dilation the peak power was located in the second component, which when comparing Figure 92(a) (Section 7.3.1) and Figure 126 was expected as the waveforms follow a similar path. For flow rate and centreline velocity the peak power was located in the first component. from this it can be deduced that inlet pressure was controlling the frequency of oscillation of the phantom dilation, which was expected from theory (Caro et al. 1978), and that the frequency of oscillation of centreline velocity at x/D = 1.25 was highly dependent on the frequency of the inlet flow rate.

Knowing that dilation is coupled with pressure and combining this data with the findings of Pielhop et al. (2012) it is evident that a change in compliance would have an effect on entrance pressure. The centreline velocity would also experience a change due to the secondary bulk flow oscillation described above. This, with the correlation between centreline velocity and inlet flow rate shown in Figure 127, would cause a change in inlet velocity. This is verified by the results provided in Section 6.4. This result presents a limitation to the physiological accuracy of the experimental analysis presented here which

was performed with no external pressure applied. It also shows that in future work greater attention needs to be applied in experimental setup when replicating physiologically realistic tethering of a compliant geometry.

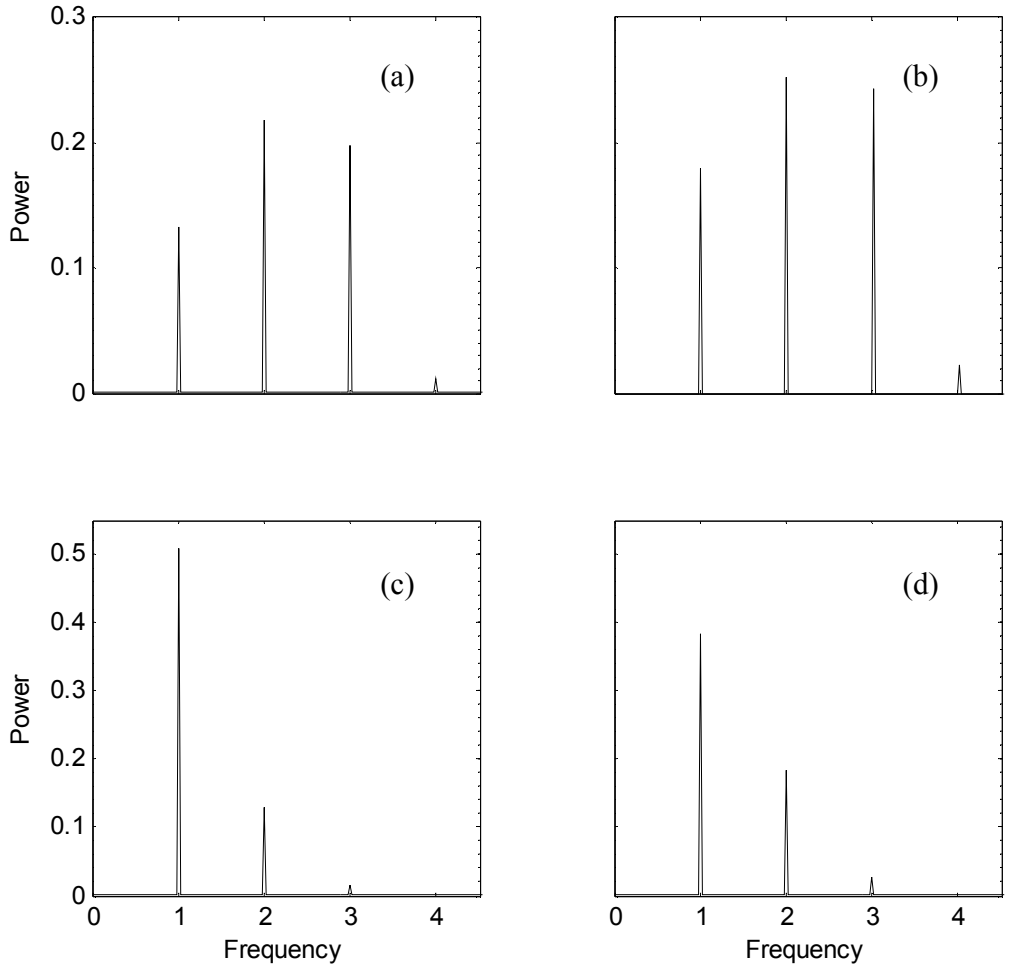

Figure 127 Temporal spectra of normalised (a) inlet pressure (b) vessel dilation at x = 1.25D (c) inlet flowrate (d) centreline velocity at x = 1.25D

8.3.6 Symmetry of the flow field

The results from the experimental work presented here, and those of Vétel et al. (2008), show asymmetry in the flow field downstream of an axis-symmetric stenosis, whereas the numerical results of (Varghese et al. 2007b) show the flow field to be axis-symmetric for central, axis-symmetric stenoses. It is important to define the experimental errors which could lead to an asymmetric flow field being obtained by experimental analysis in what was, or should have been, a symmetric field. Varghese et al. (2007b) showed that an offset of the

stenosis from the central axis of 1mm introduced an asymmetry into the flow, therefore slight variation in the axis symmetry of the manufactured phantom would introduce an asymmetry in the downstream flow field. The manufacturing tolerance of ±0.05mm for the compliant flow phantom used in this work could lead to an offset of 0.1mm. The asymmetry experienced in the flow field is markedly less than that shown in an asymmetric stenosis by Varghese et al. (2007b), which could suggest a very small misalignment in the manufacturing process. Secondly, the small variation in external pressurisation of the compliant phantom with height could lead to slight asymmetries in the phantom configuration. Thirdly, a small misalignment in the light sheet off the centre axis of the phantom could lead to an asymmetry in the velocity predicted radially across the region of interest.

8.4 Conclusion

Phase averaged and instantaneous PIV data using LED illumination was obtained in a compliant flow phantom representing an idealised stenosed carotid artery experiencing a physiologically realistic carotid artery flow waveform. The LED system is a low cost alternative to a double pulsed laser system. For a region of interest of 50x25mm^2 it was possible to obtain results at a resolution of 32x32pix^2 producing only 3% invalid vectors for instantaneous analysis. The rapid reduction in LED illumination prevented any increase in region of interest in the current experimental set up. Further investigation into light intensity enhancement is required. Future work will investigate fluorescent seeding.

The PIV results showed there to be two distinct flow regions directly downstream of the stenosis exit. There was a main high velocity jet exiting the restriction and low velocity reverse flow region at a distance y/D = 0.35 from the axis of symmetry. These two flow regimes were separated by a shear layer that produced a Kelvin-Helmholtz vortex ring system. As flow rate increased the vortices increased in size and the shear layer boundary between the flow regimes became unstable and broke down. It was shown that the flow structure was dependent on the rate of temporal acceleration and the flow cannot be assumed to be quasi-steady. Fluctuation intensity caused by the periodic change in flow field structure was dependent on both spatial and temporal location. There was an increase in magnitude of fluctuation with increased downstream location. Velocity disturbances also displayed a periodicity and were localised to the end of the initial acceleration phase, peak flow rate and

initial deceleration. Vessel dilation has been shown to determine the structure of the oscillating flow wave, which in turn has an effect on the flow field as a whole.

9 Conclusions and Future Work

9.1 Phantom Construction

A technique to produce compliant flow phantoms representing idealised geometries of both a healthy and a stenosed carotid artery (CA) from a silicone based material was developed. To ensure in vitro conditions represented those experienced in vivo, dynamic similarity had to be preserved. For the construction of the flow phantom this was achieved by matching both the circumferential and longitudinal response. Several evolutions of the phantom construction technique occurred. The final design provided a unique endplate design for porting it to the flow system that allowed for a smooth transition between the system and the phantom, markedly reduced the chance of structural failure in that region. The custom designed bottom up silicone injection method also provided a final phantom that was void of any bubbles, which can affect both the flow field analysis and the structural integrity of the phantom. The core casting technique presented in this work has the potential to be highly adaptable for the production of more complex geometries. The final phantom constructed was at a scale of 3.2 times life size and had a wall thickness of 1.3±0.05mm; the wall thickness was shown to vary 1.44-8.00% with a standard deviation of 4.99%.

9.2 Experimental Facility and Analysis Techniques

A flow system was constructed to provide a physiologically realistic oscillating flow waveform input to the flow phantom. Preservation of dynamic similarity was also required in the flow system; this was achieved by matching both the Reynolds and Womersley numbers. Flow field analysis was performed in geometries representing healthy, symmetrically and asymmetrically stenosed CAs using planar particle image velocimetry (PIV). A wall detection method was implemented that allowed wall displacement to be tracked from the same PIV images. Wall shear stress (WSS) analysis was performed using interfacial PIV (iPIV). This technique provides a reduction in error in near wall velocity

estimation that occurs with PIV analysis. For part of the study analysing the fluid phenomena downstream of a symmetric stenosis, a novel Light Emitting Diode (LED) illumination system was used to obtain high speed planar PIV measurements. The combined set up of the LED light source, driver unit components and fibre optics for high speed imaging costs in the region of $US 650 which provides a far cheaper option in comparison to the pulse laser system that is commonly used in PIV analysis (In the region of $US 50,000). Inlet flow and pressure and outlet pressure were also recorded, with the effect compliance has these properties studied.

9.3 Experimental Results in a Healthy Arterial Geometry

To test the assumption made in previous work, that the compliance of an artery could be ignored in experimental and computational studies, a comparison of the phase averaged flow field and WSS between a compliant and rigid geometry representing an idealised healthy CA experiencing a physiologically realistic input was performed. It was shown that peak velocity observed in the compliant phantom during the cardiac cycle (0.72m/s) was lower than that observed in the rigid phantom (0.77m/s). Comparison of the WSS and the time averaged WSS (TAWSS) showed the rigid boundary condition to cause a severe over estimation of the peak magnitudes observed (A relative difference of 65% was observed at peak WSS), as the increased diameter in the compliant geometry caused a reduction in the velocity gradient experienced at the fluid-wall interface. This shows that compliance is integral to the understanding of arterial fluid dynamics, as it provides a preventative mechanism, ameliorating the production of large magnitude WSS which can lead to atherosclerosis. Good agreement in WSS prediction has been shown between the work produced here and the in vivo MRI study by Zhang et al. (2009), along with the experimental analysis by Ku et al. (1985). There is however disagreement with data obtained through numerical simulation (Eguchi et al. 2003; Perktold and Rappitsch 1995). To this authors knowledge this is the first full experimental comparison of a rigid and compliant geometry representing the CA experiencing a physiologically realistic input.

9.4 The Effect of Compliance on Flow and Pressure Waveforms

Another common assumption made in computational and experimental analysis is to apply a sinusoidal inlet waveform rather than physiologically realistic waveform. For a stenosed

geometry it has been shown in this work that the pressure and flow waveform follow a similar path with a phase shift for a sinusoidal input. When a physiological input was applied however, a marked difference in the waveform paths occurred. Varying the transmural pressure applied to the flow system was shown to also affect the flow and pressure waveform. For a geometry with a symmetric stenosis it has been found that as external pressure increased (increasing the stiffness of the phantom) the pressure and flow waveform shape become more similar. This gives further validation to the importance of modelling the compliance of an artery when performing in vitro analysis. Stenosis eccentricity (an offset of the stenosis centre and the vessel centre) was also shown to affect the flow and pressure waveform.

9.5 Experimental Results in Stenosed Arterial Geometries

A study comparing the phase averaged flow field and WSS in a compliant symmetric and asymmetric stenosis geometry with a 50% constriction by diameter was performed. The introduction of a stenosis to the phantom geometry caused an increase in the observed peak velocity (1.9m/s and 1.77m/s in the symmetric and asymmetric geometry respectively). Both geometries presented two distinct flow regimes downstream of the stenosis exit; a central high velocity jet and a low velocity recirculation region, which were separated by a shear layer. For the symmetric geometry the 2 dimensional 2 component (2D2C) data presented by the planar PIV analysis provides a good representation of the flow field dynamics as it is expected the flow field will be symmetric. For the asymmetric geometry it is expected that there is a variation in the out of plane component of velocity and requires a 2D3C/3D3C analysis using either stereoscopic or tomographic PIV to obtain a full understanding of the flow field. At all locations throughout both stenoses it can be seen that there was a larger time averaged diameter observed in the asymmetric stenosis. This occurred due to the greater compliance in the unstenosed wall of the asymmetric geometry causing a greater expansion due to internal pressure. For both geometries a larger dilation occurred upstream of the stenosis throat, compared to the equivalent downstream location. This was caused by the pressure drop downstream of the stenosis throat due the increased velocity that exited it. Wall displacement was shown to be driven by the pressure waveform. This is further evidence that the assumption of a sinusoidal inlet flow wave leads to invalid results. A large increase in WSS can be seen to occur in the stenosis throat in both a

symmetric and asymmetric stenosed geometry. It is also evident that stenosis eccentricity is important, with asymmetry producing a major change in WSS magnitude in time and space. This is important in medical terms as a stenosed artery is very rarely going to be concentric with the artery. This work to the author's knowledge is the first full experimental analysis of WSS in the stenosis region using this geometry and waveform input.

The LED illumination system allowed for a high speed imaging analysis to be performed. The illumination system is an emerging technology, which presented a restriction in light sheet intensity and size that could be obtained. After extensive image preprocessing the number of invalid vectors were reduced to between 2 and 5% of the total. Comparing phase averaged results of the peak velocities at the stenosis exit to those obtained using a conventional laser illumination system, there was shown to be a relative difference ranging from 0.08 to 8.57%. High speed imaging allowed for an elaboration on some of the fluid phenomena present downstream of the stenosis exit. The shear layer was shown to produce a Kelvin-Helmholtz vortex ring system. As flow rate increased the vortices increased in size and the shear layer boundary between the flow regimes became unstable and broke down. The strength of these vortices varied between the acceleration and deceleration phase therefore the flow cannot be assumed to be quasi-steady. Fluctuation intensity caused by the periodic change in flow field structure was dependent on both spatial and temporal location. There was an increase in magnitude of fluctuation with increased downstream location. Velocity disturbances also displayed a periodicity and were localised to the end of the initial acceleration phase, peak flow rate and initial deceleration. This again provides evidence that the quasi-steady assumption lacks validity.

9.6 Future Work

The work presented in this thesis has provided new techniques for the experimental design of compliant studies to be used in conjunction with optical imaging analysis, primarily for PIV, but can also be applied to other flow visualisation analysis. Knowledge has been contributed to the advancement of understanding arterial hemodynamics and the role compliance plays in the flow field dynamics and WSS. New knowledge has been provided that can be used for validation of both future experimental and computational results. A novel illumination technique has been implemented in this study which provides a cheaper alternative to the

conventional laser systems used. There is however the potential for further improvement that can be applied to both the techniques use for experimental analysis and experimental design.

First and foremost, the area that provides the largest scope for future work is the improvement of the accurate replication of in vivo conditions. The justification to study an idealised geometry provides a general result that can be used to give an overview of the hemodynamic effects occurring. It has however been shown that the variation in arterial geometry from person to person will cause variation in the flow field and WSS (Buchmann 2010). Compliance also plays a major part in far more complex geometries like the abdominal aortic aneurysm and cerebral aneurysm. Therefore the phantom construction technique needs to be developed further to produce physiologically realistic geometries.

A technique for obtaining realistic geometries from MRI data has been presented in Geoghegan et al. (2012a); Spence (2011); Buchmann (2010). Scans are available as a collection of 2D grey-scale images, in DICOM format, with different pixel intensities representing different tissue properties. Extraction of the arterial geometry is achieved from a data set by using a marching cubic algorithm implemented by in-house software developed by Moore (2007). This document should be referred to for a full explanation of the technique. The resolution of the MRI data can be limited and along with the presence of noise can cause the final geometry to appear coarse. To alleviate this, Gaussian smoothing and interpolation algorithms are applied to flatten the surface and increase the spatial resolution. A physiologically realistic geometry of an abdominal aortic aneurysm from an anonymous male[29] produced using the technique discussed is presented in Figure 128. The model is solidified and then exported to STL format. The same rapid prototyping technique discussed in Section 2.5.1 can then be applied to produce the sacrificial model. Models of equal complexity to this have previously been produced by Spence et al. (2011a). The work of Doyle et al. (2008) has also shown that CNC machined aluminium can be easily used to produce more complex geometries, which can be used to produce the external female mould.

[29] Data provided by St. Georges hospital

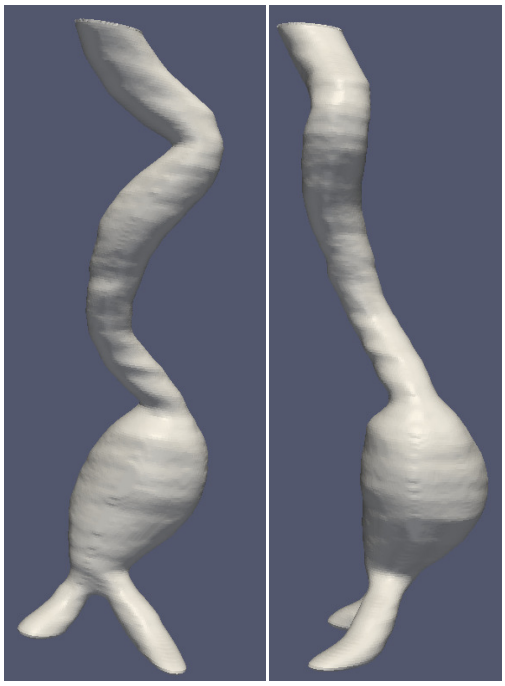

Figure 128 Physiologically realistic geometry of the aortic artery with an abdominal aortic aneurysm

As discussed in Section 1.1, an artery is made up of several different layers, which have varying mechanical properties, although neglecting the effect this variation has is justified; it would be prudent to investigate this further. It is also acknowledged that the material properties of the stenosis can vary in comparison to the main unstenosed artery. Implementing this into an experimental design could be achieved by using multiple female moulds with increasing mould diameter. This would require multiple pouring phases with each layer having varying mechanical properties. For each layer added there would be a 48 hour increase in construction time. The mechanical properties of live tissue are not known very accurately, but techniques like magnetic resonance elastography are increasing the knowledge in this area.

Introducing a non-Newtonian blood-mimicking liquid into the experimental setup that would match the shear thinning properties would further the physiological realism of the analysis. The justification of using a Newtonian liquid was based on the high shear rates that were expected in the arterial geometry. This is however only really relevant for the mean results in the centre of the geometry. Time oscillating flow and flow in the vicinity of the wall could be affected by the non-Newtonian behaviour due to the far lower shear rates experienced. Some computational work has been performed to investigate this (Buchanan Jr et al. 2000;

Molla and Paul 2012) , but experimental studies are required to provide validity to the non-Newtonian fluid models applied. Some experimental studies have developed non-Newtonian blood analogues for optical measurements such as aqueous solutions of KSCN and Xanthan gum (Gray et al. 2007; Gijsen et al. 1999) or polyacrylamide (Liepsch 2002) to match both the shear thinning behaviour of blood and the refractive index of the phantom, but these techniques also require further study.

Further improvements can be made to the design of the phantom construction and experimental setup. Improvements to the final mould design include improving the alignment between the endplate mould and the main external mould to reduce the error in wall thickness obtained. The use of the intricate retrofitted alignment tool should be designed out and alignment should come from a locking mechanism between the end plate moulds and the main aluminium mould. A site specific improvement would be to increase the stability of the final mould/alignment tool/plunger system as systematic failure occurs during a magnitude 7.2 on the Richter scale earthquake. The external pressurisation chamber (EPC) design can be improved by replacing the threaded rod/wing nut clamp system for the removable surface with a hinge attaching the surface to the main EPC and a latch to clamp it in place. This would reduce phantom changeover time by ~1 hour. To increase the number of cardiac cycles recorded in one experimental run the pump cylinder length could be increased.

Although the PIV and iPIV algorithms applied to the analysis of the data in this thesis are at a highly advanced level, there are still improvements that can be made to improve the quality of results that are obtained. Further wild vector detection techniques can be applied to improve the validity of the results including the method discussed in Section 3.6.2.2 (Green et al. 2000). A forward window is slightly offset from the original window in the direction of the calculated vector and a reverse window placed on the same path in the reverse direction. Cross correlation is then performed on the new windows and compared with the original. If a vector is invalid the offset windows will produce a different result and can be used to adjust the original. For a test case analysing a synthetic image pair, the technique was shown to reduce a vector field with 15% invalid vectors to 5%. It must be noted though that this method would increase processing time 3 fold. Adaptive window sizing (i.e. larger window sizes in regions of high displacement) within the image pair being analysed introduced to

both the PIV and iPIV technique would provide more flexibility to the final analysis, especially in flows that experience a large variation in displacement across the region of interest like a stenosed geometry.

The first steps were taken in this thesis to obtain surface displacement data of a compliant geometry experiencing a change in internal pressure. The initial results were promising, but a much more in depth study needs to be performed to ascertain the viability of the technique for a time oscillating flow. The technique currently also requires an opaque surface applied to the compliant geometry, which stops simultaneous PIV and surface displacement analysis being performed. Methods to address this is issue should be investigated, with one possible avenue being the addition of fluorescent material to the silicone phantom in the curing stage (Pielhop et al. 2012).

The novel LED illumination system used for high speed PIV analysis presented in this thesis is currently in its infancy. To this author's knowledge, this is the first application of the technique to the study of a refractive matched liquid flow system in a compliant phantom. It provides a versatile illumination facility that is relatively safe and cheap, which could lead to more widespread use of PIV. It is thought that the technique provides a good avenue to implementing the use of PIV at an undergraduate level in the university system. Combining the technique with some of the advancements being made in using graphical processing units to process PIV images (Tarashima et al. 2010), could help progress the development of PIV as a live demonstration experimental analysis technique. For the application to this experimental setup the LED system presented a major drawback in the available light intensity, to improve this it is suggested that fluorescent seeding particles should be trialled to ascertain any possible improvements.

The final avenue that presents scope for future work to be performed is further analysis of the phantoms and the data presented. With the introduction of the longer phantom to account for the longitudinal response, it would be interesting to produce a healthy geometry with this length to see what differences the results present when compared to the analysis of the shorter geometry presented here. Chapter 6 presented the effect transmural pressure had on inlet and outlet flow and pressure conditions. The understanding of the causes behind these changes needs to be further developed so that the data has more tangible significance. The study of stenosed geometries was performed with a physiologically realistic waveform input

from a healthy artery, as it is difficult to obtain cardiac waveforms for diseased arteries. This may affect the validity of the results and future work should look to applying a more realistic wave input. It is also discussed that for an asymmetric stenosis the flow field will present variation in the axial direction. Stereoscopic or tomographic PIV should be used in future investigation to understand the effect the 3-D flow field has within the geometry. There was also a high variation of WSS across the artery wall from very low to quite high values; it would be prudent to repeat the WSS analysis at regions of low WSS to ensure that data presented here isn't over or underestimating the magnitude due to the pixel displacement being too low to get a fully resolved result. The introduction of high speed PIV analysis of the downstream region of a symmetric stenosis has shown there to be a lot of interesting fluid phenomena throughout the cardiac cycle. This technique should be applied to further study in the same region of interest in the asymmetric geometry to help develop the understanding of the fluid phenomena that may occur. There was evidence in this work of flow instabilities, but the relatively low data samples (50) available limited the level of investigation that could be performed. Increasing the number of data samples (>1000) will provide a greater insight into the flow field dynamics. Some preliminary images taken downstream of this region of interest (streamwise locations >3D) by the author have demonstrated there to be a complete breakdown of the streamwise direction of the flow, this needs extensive study experimentally to help validate the current computational turbulent models that are being applied in this region.

10 Appendix A – Refractive Index

When light passes through different mediums the light will experience refraction when the propagation velocity is different. A quantification of a medium's refraction is its refractive index (n) shown in Equation 100

$$n = \frac{c}{v_{phase}}$$ **Equation 100**

Where c is the speed of light and v_{phase} is the phase velocity.

Snell's law (Equation 101) can then be used to quantify the relationship between the angle of incidence of a wave and the mediums refraction.

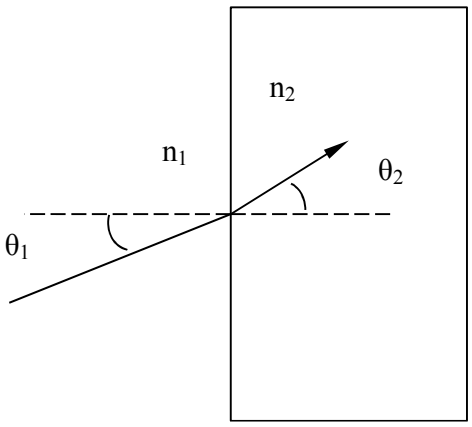

$$n_1 sin\theta_1 = n_2 sin\theta_2$$ **Equation 101**

11 Appendix B - Stereoscopic PIV measurement of airflow in human speech during pronunciation of fricatives

This appendix presents a supplementary study that was performed during the course of this thesis. Its purpose was to develop the applicability of the Canterbury University PIV system to different experimental studies. It presents stereoscopic PIV (SPIV) measurements taken in a rigid geometry representing the human vocal tract. The body of this work was presented in Geoghegan et al. (2012b) and partially in Spence (2011).

11.1 Introduction

The speech production process involves manipulating airstream into audible sounds. The lungs generate the force to drive the air in and out of the airway. On leaving the lung, the air passes through the trachea and enters the upper airway where speech sounds are produced. Generally speaking, it can be viewed as a tubular tract filled with air and surrounded by muscular and passive soft tissues. The human vocal tract (Figure 129) may be divided into four cavities: the laryngeal, pharyngeal, oral and nasal cavities. Before entering the larynx, the air has to pass through a narrow opening called the glottis which is an orifice bounded by the vocal folds. The pharynx which connects the nose, mouth and throat can be subdivided into three regions: the nasopharynx which forms the superior portion of the pharynx and connects to the posterior portion of the nasal cavity; the oropharynx which extends between the soft palate and the base of the tongue at the level of hyoid bone; and the larynxgopharynx which includes the area between the hyoid bone and the entrance of the oesophagus (Martini et al. 2006). The nasal cavity can be decoupled from the vocal tract by raising the soft palate. The hard palate is bony and separates the oral cavity from the nasal cavity. The tongue is a highly mobile muscular structure, owing to its complex intrinsic and extrinsic muscle groups.

Its surface extends from the hyoid bone at the back of the mouth upward and forward to the lips, which means it forms almost two-thirds of the lower surface of the vocal tract. Adjusting the vocal tract's shape to produce different sounds is called "Articulation" (Dense and Pinson 1963).

Fricatives are a group of noise-like consonants such as 's' and 'sh', where the sound is made by forcing the air stream through a narrow constriction mainly located in the oral cavity. They are both `unvoiced' which means the glottis does not vibrate during their phonation's therefore such sound is believed to be the direct product of unsteady flow motion. Modulation of the sound is achieved by altering the position and speed of the vocal articulators. 's' and 'sh' can be characterised by their place-of-constriction, as dental (teeth) and palatal (hard palate) sound respectively.

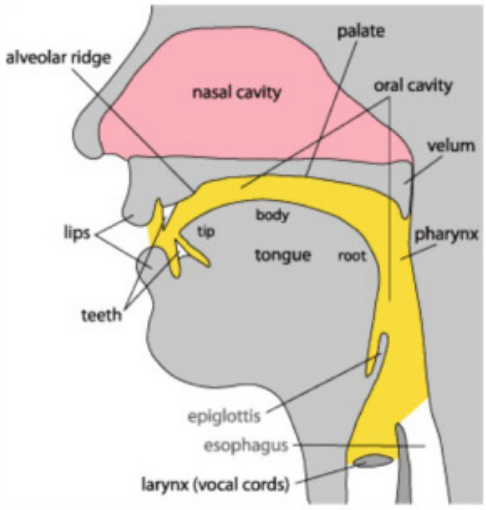

Figure 129 Schematic illustrating the key vocal articulators. Figure adapted from (Spence 2011)

This appendix provides results obtained in-vitro using stereo particle image velocimetry (SPIV) for two geometries; one representing vocal tract producing a 's' sound and one producing a 'sh' sound. Experimental investigation was performed in rigid walled phantoms with the assumption that there is minimal movement in the vocal tract for the duration of production of these sounds. This work is part of a programme to develop a model of the motion of human vocal articulators and the accompanying airflow during the production of vowels and consonants, using articulator shape and position data from magnetic resonance imaging (MRI), articulatory kinematics from electromagnetic articulography (EMA), video

imaging of the face, and CFD (Lu et al. 2009). All results presented are in-vivo scaled to ensure their physiological relevance with the purpose of the investigation providing validation of computational data to be used in the construction of the talking head model.

11.2 Experimental Methodology

11.2.1 Model Construction

In this study, simplified 3D models of the articulators (lips, teeth, tongue, hard palate, and larynx) were constructed from MRI scans of a subject pronouncing ‘s’ and ‘sh’. Cross – sections through the central plane of the geometries are shown in Figure 130. There are two main differences between the two geometries. Firstly there is a slight narrowing of the passage in the ‘s’ configuration as the geometry transitions from the oesophagus to the epiglottis region that doesn’t occur in the ‘sh’ configuration. For the ‘s’ sound, in the main body of the oral cavity, the cross section is relatively large until it constricts dramatically in close proximity with the tip and teeth. Conversely for ‘sh’ there is a more gradual constriction in cross section through the body of the cavity. There is also a geometric difference at the lips. For the ‘s’ configuration the lips are spread further apart causing a near instant increase in cross section as air exits past the teeth to the lip region. For the ‘sh’ configuration there is only a slight gradual expansion through the tip/teeth/lip region.

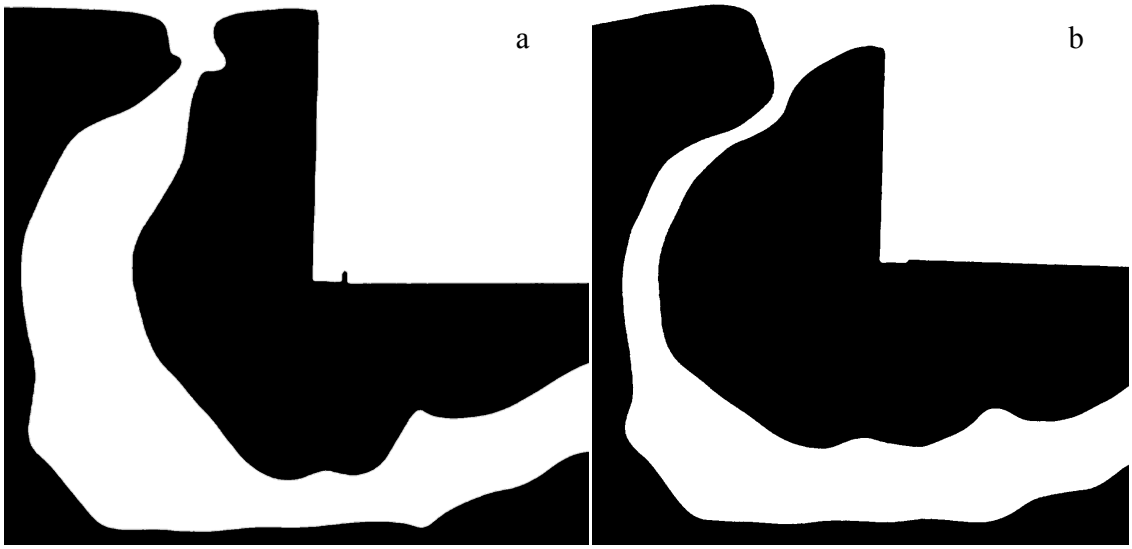

Figure 130 Cross section of vocal tract geometry in the mid-sagittal plane for a geometry producing the sound (a) ‘s’ and (b) ‘sh’ (subject lying supine, lips to the top)

Rigid transparent silicone flow phantoms of these models (Figure 131) were cast at a scale of 1.55 times using an investment casting technique (Section 2.5.4.1). The soft palate is assumed to be closed to the nasal cavity.

CT scans of the constructed flow phantoms were obtained to compare against the original 3D computer model. The RMS discrepancy between the two surfaces was 0.5 and 0.57mm for the 's' and 'sh' models respectively which corresponds to approximately 2% of the throat diameter (25.4mm in in vitro scale).

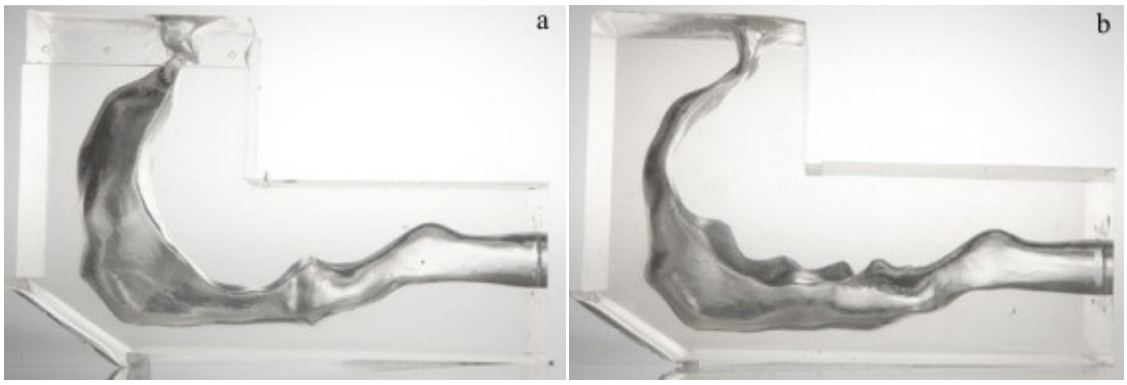

Figure 131 Silicone flow phantoms with geometries (a)"s" and (b)"sh"

11.2.2 Flow Circuit

A schematic of the recirculating flow circuit used during experimentation is shown in Figure 132. To minimise optical distortion due to refraction at the fluid-silicone interface the working fluid was refractive matched to the silicone phantom. A 39% water and 61% glycerine mixture by weight was found to be the optimal mixture to match the silicone refractive index of 1.43. The phantom is placed in a reservoir tank (b) containing the same water/glycerol mixture used in the flow circuit. The reservoir surface area and phantom depth were such that at the required flow rate there was minimal movement in the free surface providing a constant exit pressure from the mouth. Steady flow was provided by a header tank with weir (f), giving a constant head of pressure. Flowrate control was provided by a ball valve (e2) and was measured with an electromagnetic flown meter (c) (Tigermag FM626). Return flow was pumped (d) back up to the header tank with return and overflow controlled by two ball valves (e1 and 3) to ensure flow over the weir and constant head. An in vivo steady expiration flow rate of 12 l/min was applied in vitro using Reynolds number

matching (Table 26). The fluid system was seeded with near neutrally buoyant 10µm hollow silver coated spheres.

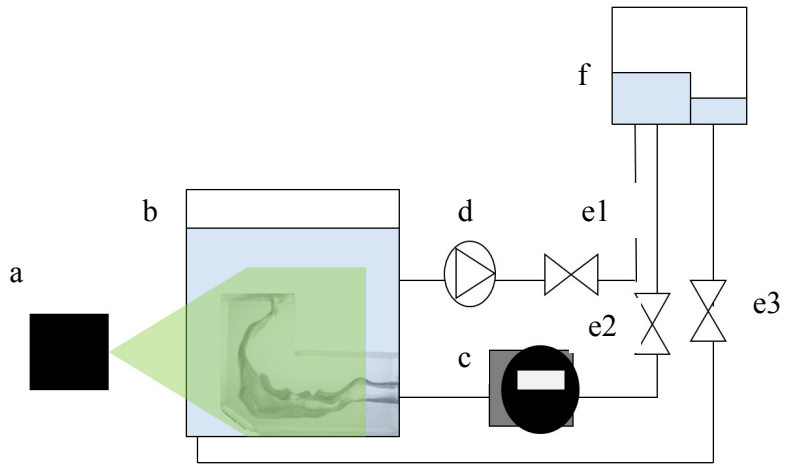

Figure 132 Schematic view of experimental setup (a) laser and optics (b) reservoir containing silicone flow phantom (c) electromagnetic flow meter (d) return pump (e) ball valves for flow control (f)) header tank with weir to ensure constant pressure

Table 26 In vivo and in vitro flow parameters

	In Vivo (Dry Air)	In Vitro (Water/Glycerine at 25ºC)
ρ (kg/m^3)	1.177	1154
µ (kg/ms)	1.846x10^{-3}	9.27x10^{-3}
Flowrate (l/min)	12	9.2
Velocity (m/s)	1.07	0.36
Inlet Re	1060	

11.2.3 PIV Measurements

SPIV measurements were obtained using a system comprising a 15Hz dual-head 120 mJ Nd:YAG laser (New Wave Solo XT), two digital 2 megapixel CCD cameras (Dantec Flowsense) and collimated optics producing a light sheet approximately 2mm thick. Laser and camera timings were synchronised using a BNC 565 pulse delay generator. To take advantage of the Lorenz-Mie scatter pattern the left camera was positioned at a small stereo angle of -2.3º and the right camera positioned at 30.4º in forward scatter. A sliding background subtraction technique was applied to remove background noise. The corresponding image pair of either the following or the previous was subtracted depending on which provided the minimum image. This technique was preferred over an average or minimum background subtraction since, with the geometry used, the light sheet would be

near to a parallel wall for several measurement planes. This meant stationary particles adhered to the model wall would be illuminated appearing to be in plane. As attached particles remain in place longer than the time between consecutive image pairs but less than the time to acquire the date set, the subtraction methods would not remove the particles from the image. The images were then processed with a dynamic histogram filter and Gaussian smoothing with a 3x3 kernel to enhance image contrast (Raffel et al. 2007). A zero flow condition was applied to the non-flow regions by way of a masking technique. Mask geometries were obtained from the CT scan of the flow phantom and by extracting the cross-sections at measurement planes analysed using an open source software package (Paraview).

Camera calibrations were made at each measurement plane with a self calibration routine applied to correct for misalignments of the laser sheet and the calibration target plate. Correlation was performed on an initial window size of 80x80pix^2 using an iterative window refinement technique to 40x40pix^2. An average overlap factor of 73% was obtained using a grid spacing of 1.4mm. Window deformation and displacement were also applied. The light sheet and CCD cameras were fixed and the reservoir traversed in increments of 2mm to obtain 26 sagittal slices per phantom. Mean flow fields and a reconstructed volume were produced from ensemble correlation averaging 200 image pairs. Time delays ranged from 200-2000μs through the planes to ensure a maximum particle displacement of about 8 pixels in any one plane.

11.3 Results and Discussion

Ensemble averaged SPIV results in a series of traversed planes were reconstructed into a 3D 3C volume using the Kriging interpolation algorithm in Tecplot 360. All velocities are scaled to in vivo conditions and only every second vector is shown for clarity. Figure 133 shows the absolute velocity (U_{abs}) field calculated from all three velocity components with velocity vectors super imposed on top through the mid sagittal plane for both the ‘s’ (a) and ‘sh’ (b) case. As discussed in Section 11.2.1 the main variation internally between the geometries is located between the epiglottis and the main body of the oral cavity. It can be seen from the masked outline in Figure 133 showing the absolute velocity through the mid-sagittal plane that this is caused by the location of the tongue which in the ‘s’ case is set back into the throat. Figure 136 and Figure 137 also provide a good visualisation of the variation

in the internal geometry. The restricted glottis in the 's' case initially accelerates the flow before expanding into the oral cavity where as shown by the stream traces some flow recirculation occurs. The flow is then accelerated rapidly by the sharp narrowing of the flow domain at the teeth. Conversely the 'sh' configuration has less constriction at the glottis with very little variation in cross section until the oral cavity: therefore, without a dramatic change in geometry no recirculation occurs in the main cavity. There is then a gradual constriction of the main body of the oral cavity from its midway point to the teeth creating a gradual increase in velocity. As the internal jet exits the mouth into the atmosphere there is a distinct difference in exit trajectory. The difference in direction of the external jets in both cases can be experienced by feeling the air direction by hand while producing the 's' and 'sh' sound. Both jets entrain flow into the system from the surroundings as they propagate outwards from the mouth.

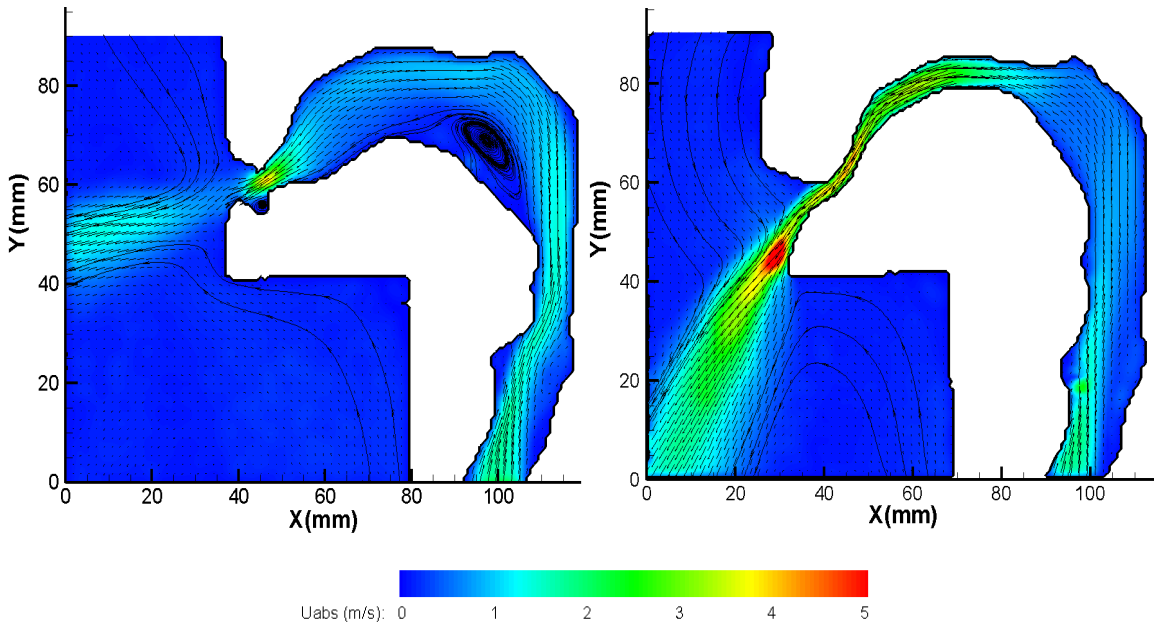

Figure 133 Absolute velocity (m/s) map through a mid-sagittal cross-section with 12l/min flow of the (a) "s' and (b) 'sh' geometry

A magnified view of the region in the vicinity of the mouth exit for the results in Figure 133 is shown in Figure 134. There is a distinct difference in the exit geometry between the two configurations. For the 's' geometry (Figure 134(a)) there is a cavity present between the teeth and the lip on the lower section of the mouth. In this cavity the streamlines show there to be recirculation in the flow. The protrusion of the lip into the flow causes a change in the

exit flow trajectory from the inferior direction exiting the teeth to an anterior trajectory. For the ‘sh’ geometry (Figure 134(b)) there is no cavity present therefore there is no recirculation zone in the flow. The lip also provides a smooth transition from the teeth region into the atmosphere. This smooth transition ensures the jet follows the inferior trajectory that is experienced at the exit of the teeth section. The Coanda effect can also be seen as the jet is attached to the curved exit of the lip section as it exits the mouth

Another feature observed in teeth-lip region of the ‘s’ geometry is the sharp deceleration of the absolute velocity of the flow as the geometry expands into the area of the lips. The jet expands with an increased out of plane component (u_z) as shown in Figure 135(a) (with positive out of the page). The velocity leading into the teeth boundary in the central plane of the geometry is dominated by the in plane velocity (u_x,u_y) components, but as it exits the teeth a lower magnitude out of plane velocity component (u_z) dominates. Neighbouring planes also show this increased u_z component thus continuity is satisfied. The u_z component in the lip region is asymmetric with a predominantly positive u_z value across the planes in the lip expansion region. This asymmetry can be explained by the asymmetry of the geometry.

An interesting feature observed in the exit jet of the ‘sh’ geometry in this plane is the maximum velocity of 6.3m/s occurs outside of the mouth. This velocity is dominated by the traverse velocity component as shown in Figure 135. Neighbouring planes again also show this region of high transverse velocity and this maximum appears to be genuine, but requires the experimental analysis to be repeated for confirmation. The jet’s asymmetry can again be explained by the asymmetry of the geometry. The exit jet of the ‘s’ geometry has the same asymmetric nature in u_z component but it has a far lower magnitude with a highest magnitude of 0.7m/s across all planes. The u_z component of velocity is very low throughout the internal geometry except for a small region where the flow is disturbed by the irregular geometry of the larynx and as the geometry constricts to the teeth exit.

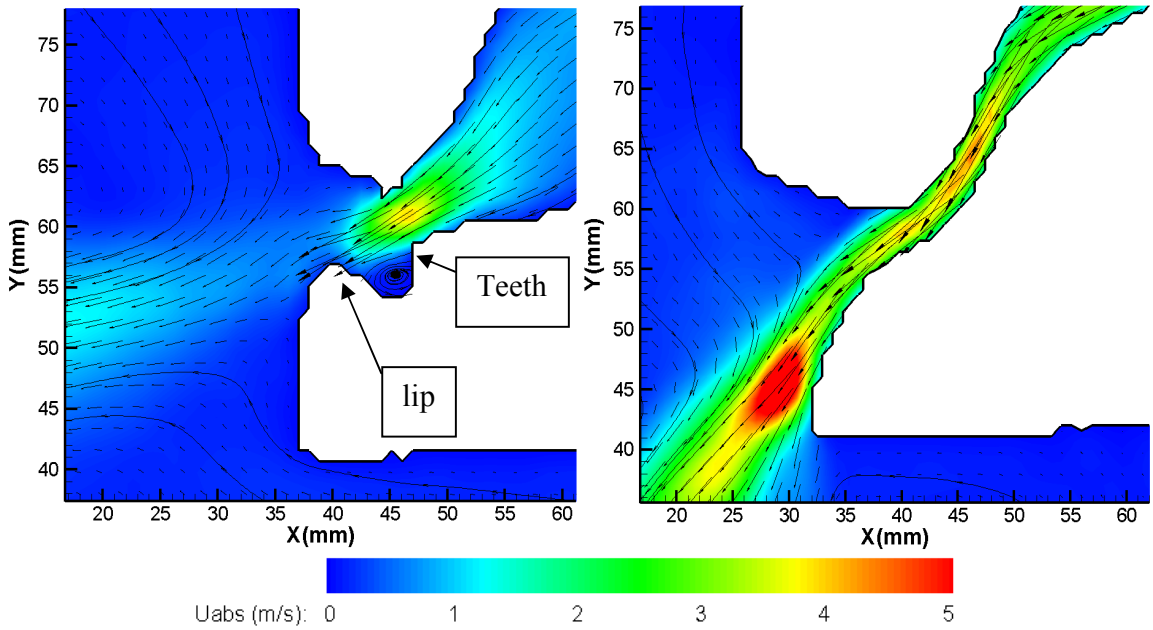

Figure 134 Magnified mouth exit region for (a) "s' and (b) 'sh' geometry

Coronal, axial and the mid-sagittal plane cross-sections through the reconstructed velocity volume are shown in Figure 136 for the 'sh' geometry and Figure 137 for the 's' geometry. In the 'sh' geometry the flowrates through 10 coronal and 10 axial cross-sections were calculated by integrating the orthogonal velocity component over each respective cross-sectional area. Calculated flow rates ranged from 8.3 to 11.3, whereas the true flowrate is 12 l/min. Lower flowrates were calculated in the narrower regions of the model where the interrogation windows and 2 mm traverse increments were relatively larger. The width of the model's narrowest region for example was equal to the width of the smallest correlation window, which would have resulted in velocity bias towards zero displacement due to the non-slip boundary condition imposed by the mask images and cross-correlation algorithm. The same analysis was performed in the 's' geometry. The calculated flow rates varied between 10.9 and 12.5 l/min in the main body of the geometry and produced a value of 9.3l/min and the constriction. With the constriction of the 's' geometry covering a much smaller area than the 'sh' the results were less affected by the no slip boundary condition. In the main body of the flow the flow rate was comparable to the imposed 12l/min.

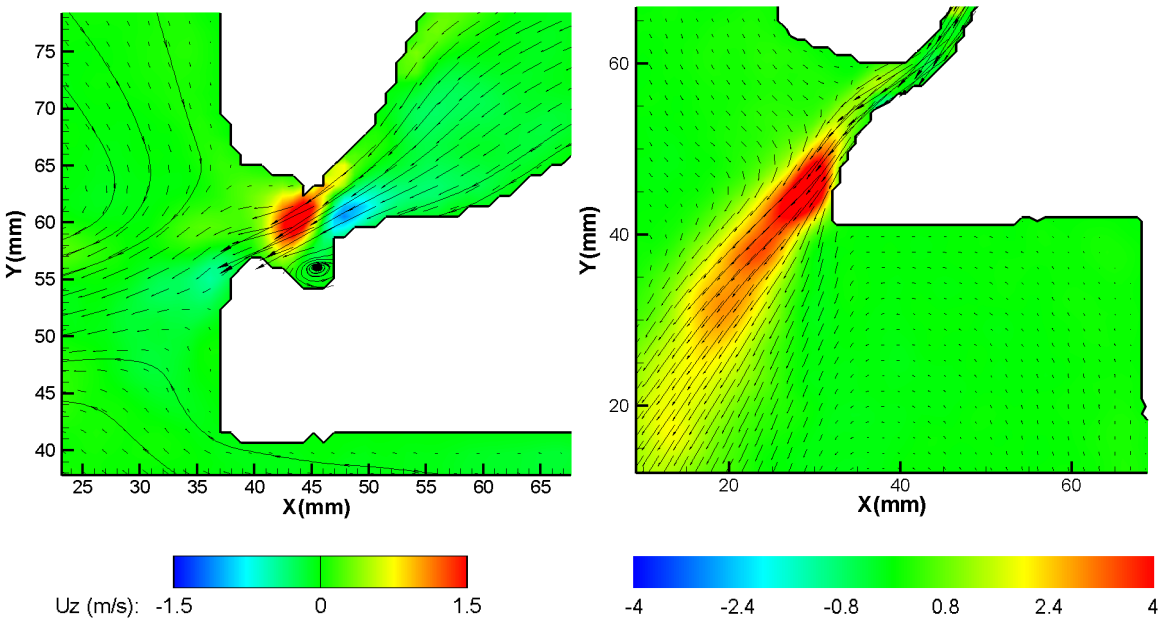

Figure 135 Orthogonal velocity (u_z(m/s)) component contour through a mid-sagittal cross-section in the magnified mouth region of the (a) 's' and (b) 'sh' geometry (Note the difference in scale between the results)

11.4 Conclusion

Time averaged SPIV data was obtained in idealised vocal tract geometries that represent the production of the fricatives 's' and 'sh'. Results show that tongue position and lip configuration are major contributors to the production of these two sounds. In the production of the 's' fricative there are two regions of recirculation that occur, but which do not appear in the production of the 'sh' fricative. Due to high variation in oral cavity cross section and the teeth exit for the 's' configuration it was difficult to find a time delay that could accurately obtain the low magnitude velocities in the oral cavity along with the high magnitude velocities in the constricted region. To improve the accuracy of the results experimental analysis should be repeated in the oral cavity with larger time delays used. To improve the accuracy of the results in the narrow regions of the 'sh' geometry the measurements should be repeated with a higher resolution camera, and/or magnification in order to allow a smaller final interrogation window size.

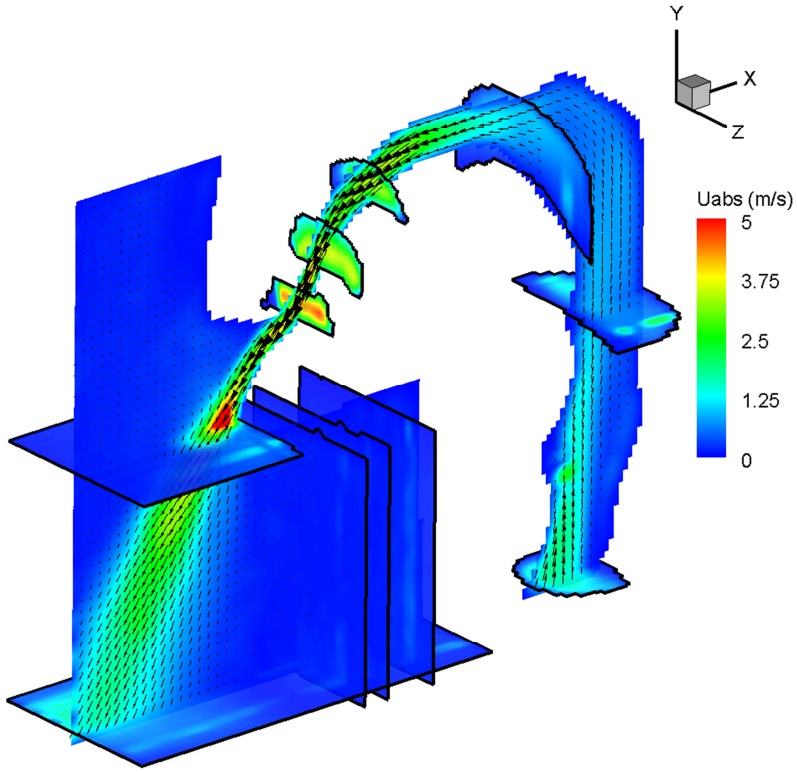

Figure 136 Absolute velocities on coronal, axial and the centre sagittal plane cross-sections through the reconstructed 'sh' fricative velocity volume

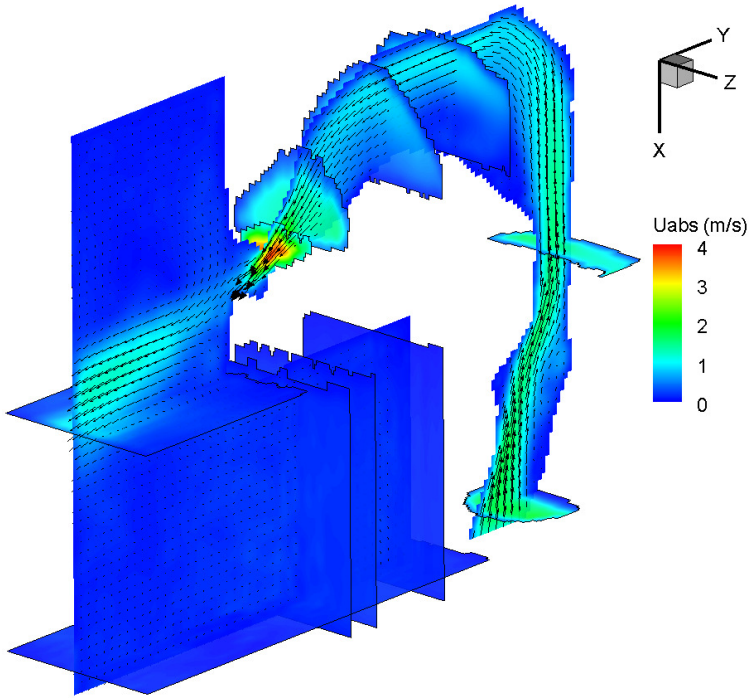

Figure 137 Absolute velocities on coronal, axial and the centre sagittal plane cross-sections through the reconstructed 's' fricative velocity volume

12 References

Adrian RJ (1984) Scattering particle characteristics and their effect on pulsed laser measurements of fluid flow: speckle velocimetry vs particle image velocimetry. Appl Opt 23 (11):1690-1691

Adrian RJ (2005) Twenty years of particle image velocimetry. Experiments in Fluids 39 (2):159-169. doi:10.1007/s00348-005-0991-7

Ahmed S, Sutalo ID, Kavnoudias H, Madan A Fluid Structure Interaction Modelling of a Patient Specific Cerebral Aneurysm Effect of Hypertension and Modulus of Elasticity. In: Jacobs P, McIntyre T, Cleary M et al. (eds) 16th Australasian Fluid Mechanics Conference, Crown Plaza, Gold Coast, Australia, 2007. pp 75-81

Ahmed SA (1998) An experimental investigation of pulsatile flow through a smooth constriction. Experimental Thermal and Fluid Science 17 (4):309-318. doi:10.1016/s0894-1777(98)00009-0

Bale-Glickman J, Selby K, Saloner D, Savas O (2003) Experimental Flow Studies in Exact-Replica Phantoms of Atherosclerotic Carotid Bifurcations Under Steady Input Conditions. Journal of Biomechanical Engineering 125 (1):38-48

Bertram CD, de Tuesta GD, Nugent AH (2001) Laser-Doppler Measurements of Velocities Just Downstream of a Collapsible Tube During Flow-Induced Oscillations. Journal of Biomechanical Engineering 123 (5):493-499

Bertram CD, Elliott NSJ (2003) Flow-rate limitation in a uniform thin-walled collapsible tube, with comparison to a uniform thick-walled tube and a tube of tapering thickness. Journal of Fluids and Structures 17 (4):541-559

Bertram CD, Nugent AH (2005) The Flow Field Downstream of an Oscillating Collapsed Tube. Journal of Biomechanical Engineering 127 (1):39-45

Bertram CD, Timmer J, Muller TG, Maiwald T, Winterhalder M, Voss HU (2004) Aperiodic flow-induced oscillations of collapsible tubes: a critical reappraisal. Medical Engineering & Physics 26:201–214

Bertram CD, Tscherry J (2006) The onset of flow-rate limitation and flow-induced oscillations in collapsible tubes. Journal of Fluids and Structures 22 (8):1029-1045

Buchanan Jr JR, Kleinstreuer C, Comer JK (2000) Rheological effects on pulsatile hemodynamics in a stenosed tube. Computers & Fluids 29

Buchmann N (2010) Development of Particle Image Velocimetry for In Vitro Studies of Arterial Haemodynamics. University of Canterbury, Christchurch

Buchmann NA, Atkinson C, Jermy MC, Soria J (2011) Tomographic particle image velocimetry investigation of the flow in a modeled human carotid artery bifurcation. Experiments in Fluids 50 (4):1131-1151. doi:10.1007/s00348-011-1042-1

Buchmann NA, Jermy MC (2007) Particle image velocimetry measurements of blood flow in a modeled carotid artery bifurcation. Paper presented at the In Proceedings of the 16th Australasian Fluid Mechanics Conference, Gold Coast, Australia,

Buchmann NA, Jermy MC, Nguyen CV (2009) Experimental investigation of carotid artery haemodynamics in an anatomically realistic model. Int J Exp Comp Methods in Biomechanics 1 (2):172-192

Buchmann NA, Willert C, Soria J (2012) Tomographic Particle Image Velocimetry with Pulsed High-Power LED Illumination. Laboratory of Turbulence Research in Aerospace and Combustion, Department of Mechanical and Aerospace Engineering Monash University, Melbourne, Australia

Buchmann NA, Yamamoto M, Jermy M, David T (2010) Particle Image Velocimetry (PIV) and Computational Fluid Dynamics (CFD) Modelling of Carotid Artery Haemodynamics under Steady Flow: A Validation Study. Journal of Biomechanical Science and Engineering 5 (4):421-436

Burgmann S, Große S, Schröder W, Roggenkamp J, Jansen S, Gräf F, Büsen M (2009) A refractive index-matched facility for fluid–structure interaction studies of pulsatile and oscillating flow in elastic vessels of adjustable compliance. Experiments in Fluids 47 (4):865-881

Cao J, Rittgers S (1998) Particle Motion Within In Vitro Models of Stenosed Internal Carotid and Left Anterior Descending Coronary Arteries. Annals of Biomedical Engineering 26 (2):190-199. doi:10.1114/1.131

Caro CG, Pedley TJ, Schroter RC, Seed WA (1978) The mechanics of circulation. Oxford University Press,

Chatzizisis YS, Coskun AU, Jonas M, Edelman ER, Feldman CL, Stone PH (2007) Role of Endothelial Shear Stress in the Natural History of Coronary Atherosclerosis and Vascular Remodeling: Molecular, Cellular, and Vascular Behavior. Journal of the American College of Cardiology 49 (25):2379-2393

Collaborators NASCET (1991) Beneficial Effect of Carotid Endarterectomy in Symptomatic Patients with High-Grade Carotid Stenosis. New England Journal of Medicine 325 (7):445-453. doi:doi:10.1056/NEJM199108153250701

Dec JE, Keller JO, Hongo I (1991) Time-resolved velocities and turbulence in the oscillating flow of a pulse combustor tail pipe. Combustion and Flame 83 (3–4):271-292. doi:10.1016/0010-2180(91)90075-m

Dense PB, Pinson EN (1963) The speech chain: the physics and biology of spoken language. Bell Telephone laboratories, Baltimore

Deplano V, Knapp Y, Bertrand E, Gaillard E (2007) Flow behaviour in an asymmetric compliant experimental model for abdominal aortic aneurysm. Journal of Biomechanics 40 (11):2406-2413

Dhahbi M, Ben Chiekh M, Gilles B, Béra JC, Jemni A (2012) Numerical simulations of particle dynamics in a poststenotic blood vessel region within the scope of extracorporeal ultrasound stenosis treatment. Medical Engineering & Physics 34 (7):982-989. doi:10.1016/j.medengphy.2011.11.003

Ding Z, Wang K, Li J, Cong X (2001) Flow field and oscillatory shear stress in a tuning-fork-shaped model of the average human carotid bifurcation. Journal of Biomechanics 34 (12):1555-1562

Doyle BJ, Morris LG, Callanan A, Kelly P, Vorp DA, McGloughlin TM (2008) 3D Reconstruction and Manufacture of Real Abdominal Aortic Aneurysms: From CT Scan to Silicone Model. Journal of Biomechanical Engineering 130 (3):034501-034505

Durst F, Ray S, Unsal B, Bayoumi OA (2005) The Development Lengths of Laminar Pipe and Channel Flows. Journal of Fluids Engineering 127 (6):1154-1160

Eguchi T, Satoshi W, Hisasada T, Akinori F (2003) Development of Pulsatile Flow Experiment System and PIV Measurement in an Elastic Tube. Memoirs of the Faculty of Engineering, Kyushu University 63 (3)

Elkins C, Alley M (2007) Magnetic resonance velocimetry: applications of magnetic resonance imaging in the measurement of fluid motion. Experiments in Fluids 43 (6):823-858. doi:10.1007/s00348-007-0383-2

Elkins JS, Johnston SC (2003) Thirty-Year Projections for Deaths From Ischemic Stroke in the United States. Stroke 34 (9):2109-2112. doi:10.1161/01.str.0000085829.60324.de

Elsinga G, Scarano F, Wieneke B, van Oudheusden B (2006) Tomographic particle image velocimetry. Experiments in Fluids 41 (6):933-947. doi:10.1007/s00348-006-0212-z

Fung YC (1993) Biomechanics: Mechanical Properties of Living Tissues, 2nd ed. Springer-Verlag New York, Inc., 175 Fifth Avenue, New York, NY 10010, USA

Galdi GP, Rannacher R, Robertson AM, Turek S (2008) Hemodynamical Flows Modelling, Analysis and Simulation, vol 37. Oberwolfach Seminars. Birkhäuser, Basel

Gawenda M, Knez P, Winter S, Jaschke G, Wassmer G, Schmitz-Rixen T, Brunkwall J (2004) Endotension is Influenced by Wall Compliance in a Latex Aneurysm Model. European Journal of Vascular and Endovascular Surgery 27 (1):45-50

Geoghegan P, Buchmann N, Spence C, Moore S, Jermy M (2012a) Fabrication of rigid and flexible refractive-index-matched flow phantoms for flow visualisation and optical flow measurements. Experiments in Fluids:1-17. doi:10.1007/s00348-011-1258-0

Geoghegan PH, Buchmann N, Jermy M, Nobes D, Spence C, Docherty PD (2010) SPIV and image correlation measurements of surface displacement during pulsatile flow in models of compliant, healthy and stenosed arteries. Paper presented at the 15th International Symposium of Laser Techniques to Fluid Mechanics, Lisbon, Portugal, 5th-8th July

Geoghegan PH, Jermy MC, Buchmann N, Spence CJ (2009a) Experimental investigation of flow in compliant tubes to validate numerical models of aneurysms. Paper presented at the 4th Asia Pacific Conference on Biomechanics Christchurch, New Zealand,

Geoghegan PH, Jermy MC, Buchmann NA, Spence CJ, Freitag T (2009b) Experimental investigation of flow in a compliant tube using particle image velocimetry. Paper presented at the 8th International Symposium on Particle Image Velocimetry, Melbourne Australia,

Geoghegan PH, Spence C, Ho WH, Jermy M, Hunter P, Cater JE (2012b) Stereoscopic PIV measurement of airflow in human speech during pronunciation of fricatives. Paper presented at the 16th International Symposium of Laser Techniques to Fluid Mechanics, Lisbon, Portugal, 9th-12th July

Gerbeau J-F, Vidrascu M, Frey P (2005) Fluid–structure interaction in blood flows on geometries based on medical imaging. Computers & Structures 83 (2–3):155-165. doi:10.1016/j.compstruc.2004.03.083

Gijsen FJH, van de Vosse FN, Janssen JD (1999) The influence of the non-Newtonian properties of blood on the flow in large arteries: steady flow in a carotid bifurcation model. Journal of Biomechanics 32 (6):601-608

Gimbrone MA, Topper JN, Nagel T, Anderson KR, Garcia-CardeÑA G (2000) Endothelial Dysfunction, Hemodynamic Forces, and Atherogenesis. Annals of the New York Academy of Sciences 902 (1):230-240. doi:10.1111/j.1749-6632.2000.tb06318.x

Gonzalez RC, Woods RE (2009) Digital Image Processing Third Edition. 3rd edn. Dorling Kindersley (India) Pvt. Ltd.,

Gray H (1918) Anatomy of the Human Body. 12th edn. Lea & Febiger, Philadelphia

Gray J, Owen I, Escudier M (2007) Dynamic scaling of unsteady shear-thinning non-Newtonian fluid flows in a large-scale model of a distal anastomosis. Experiments in Fluids 43 (4):535-546. doi:10.1007/s00348-007-0317-z

Green RB, Doolan CJ, Cannon RM (2000) Measurements of the orthogonal blade–vortex interaction using a particle image velocimetry technique. Experiments in Fluids 29 (4):369-379

Große S, Burgmann S, Schröder W (2008) Time-resolved PIV measurements of oscillating flow in a non-collapsing flexible pipe. 14th Int Symp on Applications of Laser Techniques to Fluid Mechanics

Guyton AC, Hall JE (2000) Textbook of Medical Physiology. W. B. Saunders Company,

Haldar K (1987) Oscillatory flow of blood in a stenosed artery. Bulletin of Mathematical Biology 49 (3):279-287. doi:10.1007/bf02460120

Heil M, Hazel AL (2011) Fluid-Structure Interaction in Internal Physiological Flows. Annual Review of Fluid Mechanics 43 (1):141-162. doi:doi:10.1146/annurev-fluid-122109-160703

Heros RC, Kistler JP (1983) Intracranial arterial aneurysm--an update. Stroke 14 (4):628-631. doi:10.1161/01.str.14.4.628

Hirata K, Yaginuma T, O'Rourke MF, Kawakami M (2006) Age-Related Changes in Carotid Artery Flow and Pressure Pulses. Stroke 37 (10):2552-2556. doi:10.1161/01.STR.0000242289.20381.f4

Honkanen M, Nobach H (2005) Background extraction from double-frame PIV images. Experiments in Fluids 38 (3):348-362

Hopkins LM, Kelly JT, Wexler AS, Prasad AK (2000) Particle image velocimetry measurements in complex geometries. Experiments in Fluids 29 (1):91-95. doi:10.1007/s003480050430

Isnard RN, Pannier BM, Laurent S, London GM, Diebold B, Safar ME (1989) Pulsatile diameter and elastic modulus of the aortic arch in essential hypertension: A noninvasive study. Journal of the American College of Cardiology 13 (2):399-405. doi:10.1016/0735-1097(89)90518-4

Jamison R, Dubsky S, Siu K, Hourigan K, Fouras A (2011) X-ray Velocimetry and Haemodynamic Forces Within a Stenosed Femoral Model at Physiological Flow Rates. Annals of Biomedical Engineering 39 (6):1643-1653. doi:10.1007/s10439-011-0260-2

Kähler C, Scharnowski S, Cierpka C (2012) On the uncertainty of digital PIV and PTV near walls. Experiments in Fluids 52 (6):1641-1656. doi:10.1007/s00348-012-1307-3

Keane RD, Adrian RJ (1990) Optimization of particle image velocimeters. I. Double pulsed systems. Measurement Science and Technology 1 (11):1202

Keane RD, Adrian RJ (1992) Theory of cross-correlation analysis of PIV images. Applied Scientific Research 49 (3):191-215

Koenig W, Khuseyinova N (2007) Biomarkers of Atherosclerotic Plaque Instability and Rupture. Arteriosclerosis, Thrombosis, and Vascular Biology 27 (1):15-26. doi:10.1161/01.ATV.0000251503.35795.4f

Ku DN (1997) Blood flow in arteries, vol 29. Annual Reviews, Palo Alto, CA, ETATS-UNIS

Ku DN, Giddens DP, Zarins CK, Glagov S (1985) Pulsatile flow and atherosclerosis in the human carotid bifurcation. Positive correlation between plaque location and low oscillating shear stress. Arteriosclerosis, Thrombosis, and Vascular Biology 5 (3):293-302. doi:10.1161/01.atv.5.3.293

Kung E, Les A, Figueroa C, Medina F, Arcaute K, Wicker R, McConnell M, Taylor C (2011) In Vitro Validation of Finite Element Analysis of Blood Flow in Deformable Models. Annals of Biomedical Engineering 39 (7):1947-1960. doi:10.1007/s10439-011-0284-7

Li MX, Beech-Brandt JJ, John LR, Hoskins PR, Easson WJ (2007) Numerical analysis of pulsatile blood flow and vessel wall mechanics in different degrees of stenoses. Journal of Biomechanics 40 (16):3715-3724

Liepsch D (2002) An introduction to biofluid mechanics--basic models and applications. Journal of Biomechanics 35 (4):415-435

Liepsch D, Pflugbeil G, Matsuo T, Lesniak B (1998) Flow visualization and 1- and 3-D laser-Doppler-anemometer measurements in models of human carotid arteries. Clinical Hemorheology and Microcirculation 18 (1):1-30

Long Q, Xu XY, Ramnarine KV, Hoskins P (2001) Numerical investigation of physiologically realistic pulsatile flow through arterial stenosis. Journal of Biomechanics 34 (10):1229-1242

Lou Z, Yang WJ (1992) Biofluid dynamics at arterial bifurcations. Critical reviews in biomedical engineering 19 (6):455-493

Lovald S, Heinrich J, Khraishi T, Yonas H, Pappu S (2009) The role of fluid dynamics in plaque excavation and rupture in the human carotid bifurcation: a computational study. International Journal of Experimental and Computational Biomechanics 1 (1):76-95. doi:10.1504/ijecb.2009.02286

Lowe ML, Kutt PH (1992) Refraction through cylindrical tubes. Experiments in Fluids 13 (5):315-320. doi:10.1007/bf00209503

Lu XB, Thorpe W, Foster K, Hunter P (2009) From Experiments to Articulatory Motion - A Three Dimensional Talking Head Model Paper presented at the INTERSPEECH 2009 10th Annual Conference of the International Speech Communication Association, Brighton, United Kingdom, September 6-10, 2009

Luminus (2009) Product Data Sheet, PhlatLight PT120 Projection Chipset. Luminus Devices Inc

Mao X, Sherwin S, Blackburn H (2011) Transient growth and bypass transition in stenotic flow with a physiological waveform. Theoretical and Computational Fluid Dynamics 25 (1):31-42. doi:10.1007/s00162-009-0167-9

Martini FH, Timmons MJ, Tallitsch RB (2006) Human Anatomy. 5th edn. Pearson Education Inc, San Francisco

Mautner SL, Mautner GC, Froehlich J, Feuerstein IM, Proschan MA, Roberts WC, Doppman JL (1994) Coronary Artery Disease; Prediction with In Vitro Electron Beam CT. 192:625-630

Mayer FB, Morita A, Puumala MR, Nichols DA (1995) Medical and Surgical Management of Intercranial Aneurysms. Mayo Clinical Proceedings 70:153-172

McDonald DA (1955) The relation of pulsatile pressure to flow in arteries. The Journal of physiology 127 (3):533-552

Melling A (1997) Tracer particles and seeding for particle image velocimetry. Measurement Science and Technology 8 (12):1406

Meynart R (1983) Instantaneous velocity field measurements in unsteady gas flow by speckle velocimetry. Appl Opt 22 (4):535-540

Moireau P, Bertoglio C, Xiao N, Figueroa C, Taylor C, Chapelle D, Gerbeau JF (2012) Sequential identification of boundary support parameters in a fluid-structure vascular model using patient image data. Biomechanics and Modeling in Mechanobiology:1-22. doi:10.1007/s10237-012-0418-3

Molla MM, Paul MC (2012) LES of non-Newtonian physiological blood flow in a model of arterial stenosis. Medical Engineering & Physics 34 (8):1079-1087. doi:10.1016/j.medengphy.2011.11.013

Moore S (2007) Computational 3D Modelling of Hemodynamics in the Circle of Willis. University of Canterbury, Christchurch

Motomiya M, Karino T (1984) Flow patterns in the human carotid artery bifurcation. Stroke 15 (1):50-56. doi:10.1161/01.str.15.1.50

Nguyen C, Nguyen T, Wells J, Nakayama A (2010) Interfacial PIV to resolve flows in the vicinity of curved surfaces. Experiments in Fluids 48 (4):577-587. doi:10.1007/s00348-010-0824-1

Nguyen TT, Biadillah Y, Mongrain R, Brunette J, Tardif JC, Bertrand OF (2004) A Method for Matching the Refractive Index and Kinematic Viscosity of a Blood Analog for Flow Visualization in Hydraulic Cardiovascular Models. Journal of Biomechanical Engineering 126 (4):529-535

O'Brien T, Morris L, O'Donnell M, Walsh M, McGloughlin T (2005) Injection-Moulded Models of Major and Minor Arteries: The Variability of Model Wall Thickness Owing to Casting Technique. Proceedings of the Institution of Mechanical Engineers, Part H: Journal of Engineering in Medicine 219 (5):381-386

Palmen DEM, Gijsen FJH, van de Vosse FN, Janssen JD, van Dongen MEH Lda measurements in a non-stenosed and a stenosed model of the carotid artery bifurcation. In: The International Society for Optical Engineering, 1993. pp 219-226

Parker K, Ellenrieder vK, Soria J (2004) Stereoscopic PIV measurements of the flow past a circular cylinder at reynolds number 15000. Paper presented at the 15th Australasian Fluid Mechanics Conference, Sydney, Australia,

Perktold K, Rappitsch G (1995) Computer simulation of local blood flow and vessel mechanics in a compliant carotid artery bifurcation model. Journal of Biomechanics 28 (7):845-856

Perry JH (1950) Chemical engineers' handbook. Journal of Chemical Education 27 (9):533-null. doi:10.1021/ed027p533.1

Pielhop K, Klaas M, Schröder W (2012) Analysis of the unsteady flow in an elastic stenotic vessel. European Journal of Mechanics - B/Fluids (0). doi:10.1016/j.euromechflu.2012.01.010

Potter MC, Wiggert DC (2002) Mechanics of Fluids 3rd Edition. Brooks/Cole,USA,

Prasad AK (2000) Stereoscopic particle image velocimetry. Experiments in Fluids 29 (2):103-116

Prasad AK, Jensen K (1995) Scheimpflug stereocamera for particle image velocimetry in liquid flows. Appl Opt 34 (30):7092-7099

Raffel M, Willert CE, Wereley ST, Kompenhans J (2007) Particle image velocimetry: a practical guide second edition. 2nd edn. Springer (Berlin and New York),

Reynolds WC, Hussain AKMF (1972) The mechanics of an organized wave in turbulent shear flow. Part 3. Theoretical models and comparisons with experiments. Journal of Fluid Mechanics 54 (02):263-288. doi:doi:10.1017/S0022112072000679

Riley W, Barnes R, Evans G, Burke G (1992) Ultrasonic measurement of the elastic modulus of the common carotid artery. The Atherosclerosis Risk in Communities (ARIC) Study. Stroke 23 (7):952-956

Scarano F (2002) Iterative image deformation methods in PIV. Measurement Science and Technology 13 (1):R1

Scarano F, Riethmuller ML (2000) Advances in iterative multigrid PIV image processing. Experiments in Fluids 29 (0):S051-S060

Scotti C, Shkolnik A, Muluk S, Finol E (2005) Fluid-structure interaction in abdominal aortic aneurysms: effects of asymmetry and wall thickness. BioMedical Engineering OnLine 4 (1):64

Seeley RR, Stephens TD, Tate P (2003) Anatomy and Physiology. 6th edn. McGraw-Hill, Boston

Sherwin SJ, Blackburn HM (2005) Three-dimensional instabilities and transition of steady and pulsatile axisymmetric stenotic flows. Journal of Fluid Mechanics 533:297-327. doi:doi:10.1017/S0022112005004271

Soloff SM, Adrian RJ, Liu ZC (1997) Distortion compensation for generalized stereoscopic particle image velocimetry. Measurement Science and Technology 8 (12):1441

Spence C (2011) Experimental Investigations of Airflow in the Human Upper Airways During Natural and Assisted Breathing University of Canterbury, Christchurch

Spence C, Buchmann N, Jermy M (2011a) Unsteady flow in the nasal cavity with high flow therapy measured by stereoscopic PIV. Experiments in Fluids:1-11. doi:10.1007/s00348-011-1044-z

Spence C, Buchmann N, Jermy M, Moore S (2011b) Stereoscopic PIV measurements of flow in the nasal cavity with high flow therapy. Experiments in Fluids 50 (4):1005-1017. doi:10.1007/s00348-010-0984-z

Stanislas M, Monnier JC (1997) Practical aspects of image recording in particle image velocimetry. Measurement Science and Technology 8 (12):1417

Steiger HJ, Aaslid R, Keller S, Reulen H-J (1989) Strength, elasticity and viscoelastic properties of cerebral aneurysms. Heart and Vessels 5 (1):41-46. doi:10.1007/bf02058357

Stitou A, Riethmuller ML (2001) Extension of PIV to super resolution using PTV. Measurement Science and Technology 12 (9):1398

Takizawa K, Christopher J, Tezduyar TE, Sathe S (2010) Space–time finite element computation of arterial fluid–structure interactions with patient-specific data. International Journal for Numerical Methods in Biomedical Engineering 26 (1):101-116. doi:10.1002/cnm.1241

Tang D, Yang C, Huang Y, N. Ku D (1999a) Wall stress and strain analysis using a three-dimensional thick-wall model with fluid–structure interactions for blood flow in carotid arteries with stenoses. Computers & Structures 72 (1–3):341-356. doi:10.1016/s0045-7949(99)00009-7

Tang D, Yang C, Kobayashi S, Zheng J, Vito RP (2003) Effect of Stenosis Asymmetry on Blood Flow and Artery Compression: A Three-Dimensional Fluid-Structure Interaction Model. Annals of Biomedical Engineering 31 (10):1182-1193. doi:10.1114/1.1615577

Tang D, Yang C, N. Ku D (1999b) A 3-D thin-wall model with fluid–structure interactions for blood flow in carotid arteries with symmetric and asymmetric stenoses. Computers & Structures 72 (1–3):357-377. doi:10.1016/s0045-7949(99)00019-x

Tang D, Yang C, Zheng J, Woodard PK, Sicard GA, Saffitz JE, Yuan C (2004) 3D MRI-Based Multicomponent FSI Models for Atherosclerotic Plaques. Annals of Biomedical Engineering 32 (7):947-960. doi:10.1023/B:ABME.0000032457.10191.e0

Tarashima S, Tange M, Someya S, Okamoto K (2010) GPU accelerated direct cross-correlation PIV with window deformation Paper presented at the 15th International Symposium of Laser Techniques to Fluid Mechanics, Lisbon, Portugal, 5th-8th July

Tateshima S, Grinstead J, Sinha S, Nien Y-L, Murayama Y, Villablanca JP, Tanishita K, Vinuela F (2004) Intraaneurysmal flow visualization by using phase-contrast magnetic resonance imaging: feasibility study based on a geometrically realistic in vitro aneurysm model. Journal of Neurosurgery 100

Tateshima S, Murayama Y, Villablanca JP, Morino T, Nomura K, Tanishita K, Vinuela F (2003a) In Vitro Measurement of Fluid-Induced Wall Shear Stress in Unruptured Cerebral Aneurysms Harboring Blebs. Stroke 34 (1):187-192. doi:10.1161/01.str.0000046456.26587.8b

Tateshima S, Murayama Y, Villablanca JP, Morino T, Takahashi H, Yamauchi T, Tanishita K, Vinuela F (2001) Intraaneurysmal flow dynamics study featuring an acrylic aneurysm model manufactured using a computerized tomography angiogram as a mold. Journal of Neurosurgery 95:1020-1027

Tateshima S, Vinuela F, Villablanca JP, Murayama Y, Morino T, Nomura K, Tanishita K (2003b) Three-dimensional blood flow analysis in a wide-necked internal carotid artery–ophthalmic artery aneurysm. Journal of Neurosurgery 99:526-533

Taylor CA, Draney MT (2004) EXPERIMENTAL AND COMPUTATIONAL METHODS IN CARDIOVASCULAR FLUID MECHANICS. Annual Review of Fluid Mechanics 36 (1):197-231. doi:doi:10.1146/annurev.fluid.36.050802.121944

Taylor CA, Figueroa CA (2009) Patient-Specific Modeling of Cardiovascular Mechanics. Annual Review of Biomedical Engineering 11 (1):109-134. doi:doi:10.1146/annurev.bioeng.10.061807.160521

Tezduyar TE, Sathe S, Cragin T, Nanna B, Conklin BS, Pausewang J, Schwaab M (2007) Modelling of fluid–structure interactions with the space–time finite elements: Arterial fluid mechanics. International Journal for Numerical Methods in Fluids 54 (6-8):901-922. doi:10.1002/fld.1443

Tezduyar TE, Sathe S, Schwaab M, Conklin BS (2008) Arterial fluid mechanics modeling with the stabilized space–time fluid–structure interaction technique. International Journal for Numerical Methods in Fluids 57 (5):601-629. doi:10.1002/fld.1633

Tortora GJ, Derrickson B (2009) Principles of Anatomy and Physiology. 12th edn. John Wiley & Sons Inc.,

Traub O, Berk BC (1998) Laminar Shear Stress : Mechanisms by Which Endothelial Cells Transduce an Atheroprotective Force. Arterioscler Thromb Vasc Biol 18 (5):677-685

Varghese SS, Frankel SH, Fischer PF, Mathematics, Science C, Univ. P (2007a) Direct numerical simulation of stenotic flows, Part 1 : Steady flow. Journal Name: J Fluid Mech; Journal Volume: 582; Journal Issue: Jul 10, 2007:Medium: X; Size: 253-280

Varghese SS, Frankel SH, Fischer PF, Mathematics, Science C, Univ. P (2007b) Direct numerical simulation of stenotic flows, Part 2 : Pulsatile flow. Journal Name: J Fluid Mech; Journal Volume: 582; Journal Issue: Jul 10, 2007:Medium: X; Size: 281-318

Vennemann P, Lindken R, Westerweel J (2007) In vivo whole-field blood velocity measurement techniques. Experiments in Fluids 42 (4):495-511. doi:10.1007/s00348-007-0276-4

Vétel J, Garon A, Pelletier D (2010) Vortex identification methods based on temporal signal-processing of time-resolved PIV data. Experiments in Fluids 48 (3):441-459. doi:10.1007/s00348-009-0749-8

Vétel J, Garon A, Pelletier D, Fasinas M-I (2008) Asymmetry and transition to turbulence in a smooth axisymmetric constriction. Journal of Fluid Mechanics 607 (-1):351-386. doi:doi:10.1017/S0022112008002188

Vlaardingerbroek M, Boer J (1996) Magnetic Resonance Imaging. Springer-Verlag Berlin-Heidelberg,

Wereley ST, Gui L, Meinhart CD (2002) Advanced algorithms for microscale particle image velocimetry. AIAA Journal 40 (6)

Westerweel J (1993) Digital particle image velocimetry: Theory and application. Delft University, Delft, Netherlands

Westerweel J (1994) Efficient detection of spurious vectors in particle image velocimetry data. Experiments in Fluids 16 (3):236-247

Westerweel J (1997) Fundamentals of digital particle image velocimetry. Measurement Science and Technology 8 (12):1379

Westerweel J (2008) On velocity gradients in PIV interrogation. Experiments in Fluids 44 (5):831-842

Westerweel J, Dabiri D, Gharib M (1997) The effect of a discrete window offset on the accuracy of cross-correlation analysis of digital PIV recordings. Experiments in Fluids 23 (1):20-28

Westerweel J, Scarano F (2005) Universal outlier detection for PIV data. Experiments in Fluids 39 (6):1096-1100

Widmaier EP, Raff H, Strang KT (2004) Human physiology the mechanisms of body function 9th edn. The McGraw-Hill Companies Inc, New York

Wieneke B (2005) Stereo-PIV using self-calibration on particle images. Experiments in Fluids 39 (2):267-280

Willert C (1997) Stereoscopic digital particle image velocimetry for application in wind tunnel flows. Measurement Science and Technology 8 (12):1465

Willert C, Stasicki B, Klinner J, Moessner S (2010) Pulsed operation of high-power light emitting diodes for imaging flow velocimetry. Measurement Science and Technology 21 (7):075402

Willert CE, Gharib M (1991) Digital particle image velocimetry. Experiments in Fluids 10 (4):181-193. doi:10.1007/bf00190388

Willert CE, Mitchell DM, Soria J (2012) An assessment of high-power light-emitting diodes for high frame rate schlieren imaging. Experiments in Fluids 53 (2):413-421. doi:10.1007/s00348-012-1297-1

Womersley JR (1954) XXIV oscillatory motion of a viscous liquid in a thin walled elastic tube. Philosophical Magazine 7

Womersley JR (1955) Method for the calculation of velocity, rate of flow and viscous drag in arteries when the pressure gradient is known. Journal of Physiology:553

Womersley JR (1957) Oscillatory Flow in Arteries: the Constrained Elastic Tube as a Model of Arterial Flow and Pulse Transmission Physics in Medicine and Biology 2:178-187

Xiong G, Figueroa CA, Xiao N, Taylor CA (2011) Simulation of blood flow in deformable vessels using subject-specific geometry and spatially varying wall properties. International Journal for Numerical Methods in Biomedical Engineering 27 (7):1000-1016. doi:10.1002/cnm.1404

Yagi T, Kamoda A, Sato A, Yang W, Umezu M (2009) 3D volume flow visualization for vascular flow modelling using stereo PIV with fluorescent tracer particles. Paper presented at the 8th International Symposium on particle image Velocimetry (PIV 09), Melbourne, Australia,

Yamaguchi T, Ishikawa T, Tsubota K-i, Imai Y, Nakamura M, Fukui T (2006) Computational Blood Flow Analysis —New Trends and Methods. Journal of Biomechanical Science and Engineering 1 (1):29-50

Yamamoto M (2011) Coupling of Arterial Wall Cell Dynamics and Blood Flow. University of Canterbury, Christchurch

Zamir M (2000) The Physics of Pulsatile Flow. Springer-Verlag New York Inc.,

Zarins C, Giddens D, Bharadvaj B, Sottiurai V, Mabon R, Glagov S (1983) Carotid bifurcation atherosclerosis. Quantitative correlation of plaque localization with flow velocity profiles and wall shear stress. Circ Res 53 (4):502-514

Zdravkovic ND, Kojic MR, Rosic MA, Filipovic ND Numerical modeling of fluid-structure interaction of the carotid artery based of experimental stress-stretch curves. In: Information Technology and Applications in Biomedicine (ITAB), 2010 10th IEEE International Conference on, 3-5 Nov. 2010 2010. pp 1-4. doi:10.1109/itab.2010.5687678

Zhang F, Barker AJ, Gates PE, Strain WD, Fulford J, Mazzaro L, Shore AC, Bellenger NG, Lanning C, Shandas R Noninvasive wall shear stress measurements in human carotid

artery using echo particle image velocimetry: Initial clinical studies. In: Ultrasonics Symposium (IUS), 2009 IEEE International, 20-23 Sept. 2009 2009. pp 562-565. doi:10.1109/ultsym.2009.5441616